

On the adhesion between aluminium and polymers

Jeroen van den Brand

On the adhesion between aluminium and polymers

Proefschrift

Ter verkrijging van de graad van doctor
aan de Technische Universiteit Delft,
op gezag van de Rector Magnificus prof. dr. ir. J.T. Fokkema,
voorzitter van het College voor Promoties,
in het openbaar te verdedigen
op woensdag 6 oktober 2004 om 10.30 uur

door

Jeroen VAN DEN BRAND

Ingenieur in de Materiaalkunde
Technische Universiteit Delft
geboren te Tilburg

Dit proefschrift is goedgekeurd door de promotoren:

Prof. dr. J.H.W. de Wit

Prof. dr. ir. H. Terryn

Samenstelling promotiecommissie:

Rector Magnificus	voorzitter
Prof. dr. J.H.W. de Wit	Technische Universiteit Delft, promotor
Prof. dr. ir. H. Terryn	Vrije Universiteit Brussel, promotor
Prof. dr. I.M. Richardson	Technische Universiteit Delft
Prof. dr. S.J. Picken	Technische Universiteit Delft
Prof. dr. J.H. van der Maas	Universiteit van Utrecht
Dr. ir. W.G. Sloof	Technische Universiteit Delft
Dr. F. Vangaever	Agfa-Gevaert NV, België

This research was carried out under the project number ME.97026B in the framework of the Strategic Research Program of the Netherlands Institute for Metals Research (NIMR) in The Netherlands.

Published by: Pasmans Offsetdrukkerij, Den Haag

ISBN 90-77172-10-6

Keywords: aluminium, polymers, adhesion

Copyright © 2004 by J. van den Brand

Printed in the Netherlands

Contents.

Chapter 1. Introduction

1.1. General introduction	1
1.2. Research Aim	1
1.3. Research approach	1

Chapter 2. Background

2.1. Bonding between metals and polymers	5
2.1.1. Acid-base interactions	5
2.1.2. Interactions between metals and polymers from a macroscopic point of view	6
2.2. X-ray photoelectron spectroscopy (XPS)	10
2.2.1. Introduction	10
2.2.2. Electronic structure of aluminium oxide	10
2.2.3. Theory of XPS	11
2.3. Optical spectroscopical techniques	13
2.3.1. Introduction	13
2.3.2. Absorption of light	13
2.3.3. Reflection and refraction of light	14
2.3.4. FTIR-RAS	17
2.3.5. FTIR-ATR	18
2.3.6. Spectroscopic ellipsometry	19

Chapter 3. Determination of the amount of hydroxyls on aluminium oxide surfaces

3.1. Introduction	22
3.2. Experimental	23
3.2.1. Oxide layers	23
3.2.2. Experimental details	25
3.2.3. Data evaluation	26
3.3. Results	32
3.3.1. O/Al atomic ratio of the oxide layers as determined from photoelectron intensities	32
3.3.2. Oxide layer hydroxyl fraction as determined by curve-fitting of the O 1s peak	33
3.4. Discussion	36
3.5. Conclusions	37

Chapter 4. Acid-base characterisation of aluminium oxide surfaces using XPS

4.1. Introduction	42
4.2. Interpretation of XPS core level binding energies	43
4.3. Experimental details and data evaluation	45
4.3.1. Oxide layers and experimental details	45
4.3.2. XPS Analysis and data evaluation	45
4.4. Results	46
4.4.1. Measured core level binding energies and Auger kinetic energies	46
4.4.2. Auger parameters	50

4.4.3. Initial state parameters	52
4.5. Discussion	54
4.6. Conclusions	56

Chapter 5. Interaction of anhydride and carboxylic acid functional groups with aluminium oxide surfaces studied using infrared reflection absorption spectroscopy

5.1. Introduction	60
5.1.1. Introduction	60
5.2. Experimental	62
5.2.1. Materials	62
5.2.2. Application method	63
5.2.3. Infrared analysis	63
5.2.4. Surface area determination	64
5.3. Results	64
5.3.1. XPS, FTIR and BET investigation of oxide surfaces	64
5.3.2. Succinic anhydride adsorption on the different aluminium substrates	68
5.3.3. Succinic acid adsorption on the different aluminium substrates	70
5.3.4. Myristic acid adsorption on the different aluminium substrates	74
5.3.5. Aqueous stability	76
5.4. Discussion	76
5.4.1. Hydrolysis of anhydride functionality and bonding mode with oxide surfaces	76
5.4.2. Orientation of groups	79
5.4.3. Reactivity of the different oxide layers	80
5.4.4. Aqueous stability	82
5.5. Conclusions	83

Chapter 6. Interaction of ester functional groups with aluminium oxide surfaces studied using infrared reflection absorption spectroscopy

6.1. Introduction	88
6.2. Experimental	90
6.2.1. Materials	90
6.2.2. Aluminium oxide layers, application method and infrared analysis	91
6.2.3. Determination of carbonyl peak contributions using curve-fitting	92
6.3. Results	92
6.3.1. FTIR, XPS and BET investigation of oxide surfaces	92
6.3.2. Glycol di-(monomethylsuccinic acid) ester adsorbed on the different aluminium oxide surfaces	94
6.3.3. Dimethyl adipate adsorption on the different oxide surfaces	96
6.3.4. Transmission spectra of molecules in different solvents	97
6.3.5. Stability of bonding	101
6.3.6. Reactivity of the different oxide surfaces	104
6.4. Discussion	105
6.4.1. Type of bonding with the oxide surfaces	105
6.4.2. Bonding stability and strength of the ester groups	108
6.5. Conclusions	109

Chapter 7. Ageing of aluminium oxide surfaces and their subsequent reactivity towards bonding with organic functional groups

7.1. Introduction	114
7.2. Experimental	115
7.2.1. Materials and experimental conditions	115

7.2.2. Substrate handling and ageing conditions	116
7.3. Results	117
7.3.1. Changes in surface chemistry due to ageing in ambient air	117
7.3.2. Changes in surface chemistry due to ageing in a clean and dry environment	121
7.3.3. Influence of cleaning	122
7.3.4. Influence of ageing on the adsorption of the model adhesive molecules	123
7.4. Discussion	125
7.4.1. Changes to the surface chemistry upon ageing	125
7.4.2. Influence of ageing on the bonding capacity	127
7.5. Conclusions	129

Chapter 8. Interaction of epoxy coatings with aluminium oxide surfaces

8.1. Introduction	132
8.2. Experimental	132
8.2.1. Choice of model compounds, application method, aluminium substrates and infrared analysis	132
8.3. Results	134
8.3.1. Infrared spectra of the compounds	134
8.3.2. Bonding and bonding stability of the N,N'-dimethylsuccinamide compound with the aluminium oxide surface	134
8.3.3. Bonding and bonding stability of N-methyldiethanolamine and 1,4-butanediol with the aluminium oxide surface	138
8.4. Discussion	140
8.5. Conclusion	142

Chapter 9. Changes in epoxy-coated aluminium due to exposure to water

9.1. Introduction	146
9.2. Experimental	147
9.2.1. Sample preparation	147
9.2.2. NMP adhesion testing and exposure conditions	148
9.2.3. Peel testing	149
9.2.4. Analysis methods	150
9.3. Results	152
9.3.1. Introduction	152
9.3.2. NMP adhesion tests	153
9.3.3. Peel testing	155
9.3.4. Investigation of the whole system	156
9.3.5. Investigation of the peeled-off coatings	160
9.3.6. Investigation of the aluminium substrates	164
9.3.7. Inhibition of hydration through the adsorption of NTMP	169
9.4. Discussion	170
9.4.1. First stage: the diffusion of water in the system and loss of adhesion	171
9.4.2. Second stage: the formation and growth of an aluminium oxyhydroxide layer	172
9.4.3. Third stage: the improvement of the adhesion of the coating	173
9.5. Conclusions	174

Chapter 10. Improving the adhesion between epoxy coatings and aluminium substrates by either using thin polymeric layers or by hydration of the aluminium

10.1. Introduction	178
10.2. Experimental	181

10.2.1. Thin polymeric interfacial layers	181
10.2.2. Coated substrate preparation	182
10.2.3. Adhesion testing	182
10.2.4. Analytical techniques	182
10.3. Results	183
10.3.1. Thin polymeric coatings	183
10.3.2. Visible spectroscopic ellipsometry	185
10.3.3. FTIR analysis of the system after coating	185
10.3.4. Pseudoboehmite layer	190
10.3.5. Adhesion testing	193
10.4. Discussion	197
10.5. Conclusions	199

Chapter 11. Photothermal imaging of localised delamination between organic coatings and metallic substrates using a scanning photopyroelectric (PPE) microscope

11.1. Introduction	204
11.2. Theoretical background	206
11.3. Experimental set-up	210
11.4. Results and discussion	211
11.4.1. Validation of finite element model	211
11.4.2. Mapping of artificial subsurface defects	214
11.4.3. Blisters and corrosion spots inside a drinking can	216
11.5. Conclusion	220
General overview and discussion	223
Summary	231
Samenvatting	233
Publications	235
Acknowledgements	237
Curriculum vitae	239

CHAPTER 1.

INTRODUCTION

1.1. General introduction

In practice, quite often bonds are made between metals and polymers. Examples of this are organic coatings that are applied onto metallic substrates for the purpose of corrosion protection and also structural adhesive bonds. When these bonds are exposed to aqueous environments, it is quite often observed that there is a deterioration of the bond between the metal and the polymer. A corrosion protective coating will then no longer be protective towards the underlying metallic substrate and for a structural adhesive bond this will result in failure of the structure.

Despite investigations over the past decades, there is still a lack of knowledge of how metals bond to polymers and why this bond deteriorates in presence of water. Moreover, it is also not well-understood which factors of both the polymer and the metal substrate have an influence on bonding and the stability of the bond in the presence of water. A significant part of this lack of knowledge is because the metal-polymer interface cannot be directly and non-destructively investigated using current measuring techniques.

1.2. Research Aim

The aim of this work is to obtain some basic knowledge on the type of bonds that are formed between typical polymers and aluminium oxide surfaces and to determine whether these bonds are stable in the presence of water. Moreover, the aim is to determine which factors of the aluminium oxide surface are of influence to this bonding. Ultimately, this knowledge is to be used to develop an aluminium-polymer system which is more durable in the presence of water.

1.3. Research approach

The different Chapters of this thesis are shown schematically in Fig. 1. The thesis can be considered to consist of two main parts.

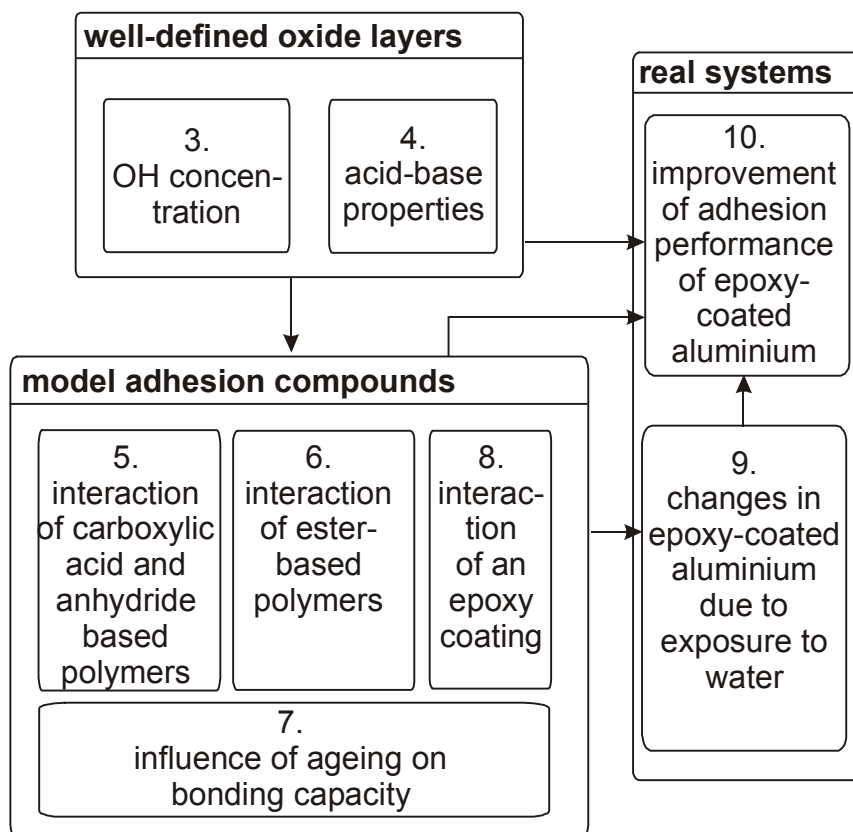


FIG. 1. Schematic of the structure of the thesis. The numbered boxes refer to the Chapter number in this thesis.

In the first part, a general investigation is performed of adhesion and loss of adhesion in ‘model’ systems. An investigation is performed of how typical organic functional groups bond to the aluminium oxide surface, how this is influenced by the chemistry of the aluminium oxide surface and whether these bonds are stable in the presence of water. A set of differently pretreated aluminium substrates is chosen and investigated using X-ray photoelectron spectroscopy (XPS) to determine the amounts of hydroxyls on their surfaces (Chapter 3) and their localised acid-base properties (Chapter 4). The aim of Chapters 5 and 6 is to study the bonding of polymers with the same set of pretreated aluminium substrates. To allow for a detailed investigation, a model adhesion compound approach is being followed. A given polymer is simplified to a small molecule, containing the same, for bonding relevant, functional groups. The compounds are adsorbed on the aluminium substrates as a thin layer. Subsequently, bonding of the compounds is being studied using infrared reflection absorption spectroscopy (FTIR-RAS). The bonding of two general, distinct classes of organic functional groups is investigated: functional groups capable of *chemisorption* with the oxide surface and functional groups capable of *physisorption*. From a macroscopic adhesion point of view, chemisorptive

bonding is preferred over physisorptive bonding because the bonding energy is roughly an order of magnitude larger. Model compounds based on carboxylic acids (Chapter 5) are chosen to represent functional groups capable of chemisorption and model compounds based on ester groups (Chapter 6) are chosen to represent functional groups capable of physisorption.

By combining the study of the bonding behaviour with the study of the oxide layer chemistry (Chapters 3 and 4) it can be determined how bonding of organic functional groups is influenced by the chemistry of the aluminium oxide surface.

Freshly prepared aluminium substrates are often exposed to the ambient for varying periods, prior to application of an organic overlayer like an organic coating. In Chapter 7, the changes that occur to the oxide surface and the resulting ‘capacity’ of the oxide surface towards bonding with organic functional groups is investigated.

In the original project plan of this PhD project, epoxy-coated aluminium is defined as the system to be investigated with respect to adhesion and loss of adhesion in presence of water. Therefore, in the second part of the thesis, adhesion and delamination in an epoxy-coated aluminium system is investigated. Epoxy-coated aluminium is a highly relevant system as it is widely used in the packaging, aerospace and automotive industries. In Chapter 8, bonding and bonding stability in the presence of water of a typical epoxy coating is investigated using appropriate model compounds. In Chapter 9, the adhesion and changes occurring at the interface for an epoxy-coated aluminium system exposed to water of different temperatures is investigated. Finally, in Chapter 10, the knowledge acquired throughout the thesis is used to give the same epoxy-coated aluminium system a larger initial adhesion strength and a better bonding stability in the presence of water. This is done by modifying the oxide layer or by adding a thin polymeric layer between the epoxy coating and the aluminium substrate. In Chapter 11, the scanning photopyroelectric microscope (SPPM) measuring technique is discussed. It is a new measuring technique which is highly suitable for studying macroscopic delamination below organic coatings at a high spatial resolution. Although the technique was not used in this thesis further, it is discussed here as the work was also performed within the scope of the PhD project and it is relevant for the subject of adhesion and delamination between organic coatings and metallic substrates in general.

CHAPTER 2.

BACKGROUND

Synopsis

In this chapter, some background on important topics of this thesis is given. A brief introduction will be given to the concept of acid-base interactions, which can be considered being the basis to adhesion between metals and polymers. Throughout this thesis, extensive use has been made of the X-ray photoelectron spectroscopy (XPS), infrared spectroscopy and spectroscopic ellipsometry. Some background on these measuring techniques is discussed.

2.1. Bonding between metals and polymers

2.1.1. Acid-base interactions

The acid-base interactions are considered to be the most important of the interactions that exist across the metal-polymer interface [1]. Following the Brönsted acid-base concept [2,3], acid-base interaction take place with the exchange of a proton:



where A is the Brönsted acid (proton donor), B⁻ the conjugated base (proton acceptor) and H⁺ the proton. An example of this is $HCl \leftrightarrow Cl^- + H^+$, with HCl the acid and Cl⁻ the conjugated base. In the Lewis acid-base concept, this is generalised in the sense that not necessarily a proton needs to be involved in the interaction [4,5]. A Lewis acid is an electron acceptor, capable of accepting electrons in its lowest energy unoccupied molecular orbital (LUMO) and a Lewis base is an electron donor, capable of sharing electrons from its highest energy occupied molecular orbital (HOMO):



with A the Lewis acid and B the Lewis base, having a pair of unshared electrons. The well-known hydrogen-bond is a sub-class (i.e. a special case) of the Lewis acid-base interactions. A hydrogen-bond can exist between two electronegative atoms or groups of which one has a hydrogen-atom covalently attached to it. A larger electronegativity of the attached atom results in more electronic charge withdrawn from the proton. As a result, the H is more positively charged and is capable of forming stronger hydrogen-bonds. Molecules that have a hydroxyl (OH) in it, can act both as a Lewis acid through the H and as a Lewis base through the O.

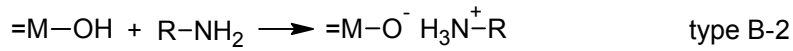
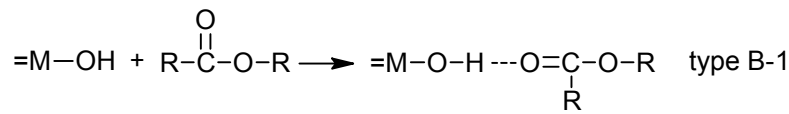
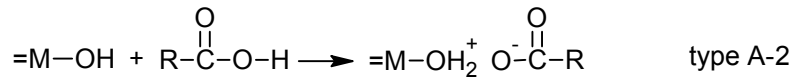
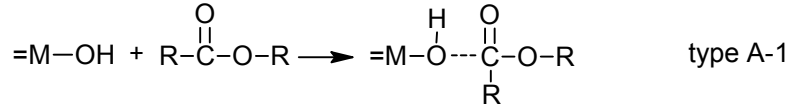
A metal oxide surface can be considered to be an ‘array’ of Lewis acid-base and Brønsted acid-base sites [6]. The O anions can act as electron-donating Lewis base sites, incompletely coordinated cations as (strong) electron-accepting Lewis acid sites and the OH anions can act either as Lewis acids/bases, but also as proton-exchanging Brønsted acids/bases [6-8].

Which of these sites are present on the surface, to which extent and their properties strongly depends on the type of metal oxide but also on the preparation conditions [1,6,9,10]. Probably the most important is the type of metal cation constituting the oxide lattice. Consider for example the differences between the SiO₂ and MgO oxides. Si in SiO₂ is a strong electron acceptor. As a result, it will comparably strongly withdraw electronic charge from the oxygen, leaving an O anion with a comparably low electronic charge, resulting in a comparably weak Lewis base site. Incompletely coordinated Si exposed on the oxide surface will be a comparably strong Lewis acid. For the OH on the oxide surface, the low negative charge on the oxygen will result in a comparably positively charged H. The OH will therefore be a strong Lewis acid (through H), a weak Lewis base (through O) and a strong Brønsted acid. For these reasons, the SiO₂ is considered an *acidic* oxide. Mg in MgO is a weak electron acceptor. As a result, less negative charge will be withdrawn from the O as compared to SiO₂. This results in a comparably strong Lewis base O site, an incompletely coordinated Mg site which is only a weak Lewis acid and an OH which is a comparably weak Lewis acid (through H), a comparably strong Lewis base (through O) and a comparably weak Brønsted acid. MgO can therefore be considered to be a *basic* oxide.

2.1.2. Interactions between metals and polymers from a macroscopic point of view

Bolger *et al* [9,10] developed a method of predicting which kinds of interactions can occur between a given polymer and metal oxide surface by considering macroscopic properties of the oxide surface and the polymer.

Although the theory is not further used in this thesis and in details is somewhat dated, it is very illustrative of metal-polymer bonding and the type of bonds that are typically formed. For this reason it is briefly outlined here. Four types of interactions are considered to be able to take place between polymers and oxides:



In these reactions it is thus assumed that bonding exclusively occurs with hydroxyls on the metal oxide surface and for example not with incompletely coordinated metal cations. For type-A interactions, the surface provides the *basic* hydroxyl that interacts with an organic *acid*. For type B interactions, the surface provides the *acidic* hydroxyl that interacts with an organic *base*. Reactions A-1 and B-1 are Lewis acid-base interactions and are denoted by Bolger as dipole-dipole interactions. Reactions A-2 and B-2 are Brönsted acid-base interactions and are denoted as ionic interactions. For a strong bonding between the oxide and the polymer, the ionic interactions are preferred as their bonding energy is roughly an order of magnitude larger than the A-1 and B-1 reactions. To determine the probability of the reactions, equilibrium constants for type A or type B interactions are derived [9,10]:

$$\Delta_A \equiv \log \kappa_A = \log \frac{[MOH_2^+][X^-]}{[MOH][HX]} = \text{IEPS} - \text{p}K_{A(A)} \quad (3)$$

$$\Delta_B \equiv \log \kappa_B = \log \frac{[MO^-][HX^+]}{[MOH][HX]} = \text{p}K_{A(B)} - \text{IEPS} \quad (4)$$

with $\text{p}K_{A(A)}$ and $\text{p}K_{A(B)}$ being acid-base ionisation constants, which are defined as $\text{p}K_{A(A)} \equiv -\log \frac{[H^+][X^-]}{[HX]}$ and $\text{p}K_{A(B)} \equiv -\log \frac{[X][H^+]}{[HX^+]}$. The IEPS is the iso-electric

TABLE 1. pK_A and resulting Δ_A and Δ_B values for different organic groups on three different oxides [9,10]. The pK_A values depend strongly on the molecular structure and the results in the table should be considered as a rough indication.

organic acid	$\text{pK}_{A(B)}$	$\text{pK}_{A(B)}$	Δ_A			Δ_B		
			SiO ₂	Al ₂ O ₃	MgO	SiO ₂	Al ₂ O ₃	MgO
			IEPS			IEPS		
			2	8	12	2	8	12
amines	20	10	-18	-12	-8	+8	+2	-2
carboxylic acid	4.5	-6	-2.5	+3.5	+7.5	-8	-14	-18
phosphonic acid	2.1		-0.1	+5.9	+9.9			
phenol	9.9	-6.7	-7.9	-1.9	+2.1	-8.7	-14.7	-18.7
water	15.7	-1.7	-13.7	-7.7	-3.7	-3.7	-9.7	-13.7
amide	15.1	-1	-13.1	-7.1	-3.1	-3	-9	-13
alcohol	15.5	-4.1	-13.5	-7.5	-3.5	-6.1	-12.1	-19.2

point of the oxide surface, which is a macroscopic measure for its acid-base characteristics. It is defined as the pH of the solution at which the surface has acquired an equal number of positive and negative charges. A high IEPS value indicates a basic surface and a low IEPS value an acidic surface.

Positive values for Δ_A or Δ_B indicate that the ionic interactions A-2 and B-2 dominate while negative values indicate that the dipole interactions A-1 and B-1 dominate. For very negative Δ_A and Δ_B , the ionic interactions are negligible and the dipole interactions are only weak. As an illustration, in Table 1, an overview is given of Δ_A and Δ_B values for typical functional groups found in polymers, for bonding to acidic SiO₂ (IEPS \sim 2), intermediate Al₂O₃ (IEPS \sim 8) and basic MgO (IEPS \sim 12) oxide surfaces. The values in the Table show that on the surface of an aluminium oxide, strong ionic bonds can only be formed with carboxylic acid, phosphonic acid (positive Δ_A , through reaction A-2) and amines (positive Δ_B , through reaction B-2). In Fig. 1, illustrations are shown for bonding of selected organic functional groups to hydroxyls on both SiO₂ and MgO, given in order of decreasing bonding strength.

The Δ_A and Δ_B values for water show that it is only capable of forming comparably weak dipole interactions with the oxide surface. Despite this, it is often observed that the bonds between organic overlayers and oxide surfaces are not stable in presence of water. According to Bolger *et al.*, the reason for this is that water additionally contains H⁺ and OH⁻ ions which can cause a change in

the acid-base equilibrium. Virtually every polar group is displaceable by water if the H^+ or OH^- activity is sufficiently high. Stability ranges can be derived to which strong dipole or ionic interactions are limited for both type A and type B interactions [9, 10]:

$$\text{type A : } pK_{A(A)} < pH < \text{IEPS} \quad (5)$$

$$\text{type B : } \text{IEPS} < pH < pK_{A(B)}. \quad (6)$$

A carboxylic acid on an aluminium oxide surface will for example show a stable bonding in the pH 4.5-8 range. Another characteristic of these ranges was also pointed out by Bolger *et al.* Although non-ionisable groups (alcohols, amides) bond less strongly than ionisable groups (carboxylic acids), they will show bonding stability to a higher pH. For example, an alcohol adsorbed on an aluminium oxide surface will show stable bonding in the pH range of 8-15.

Following this, bonding is however not expected to be stable in water, having a neutral pH. These stability ranges also have implications for corrosion occurring beneath organic coatings. Electrochemical reactions occurring below the coating can lead to a strong change of the local pH. Although the adhesion of the coating might be stable at neutral pH, progressing delamination of the

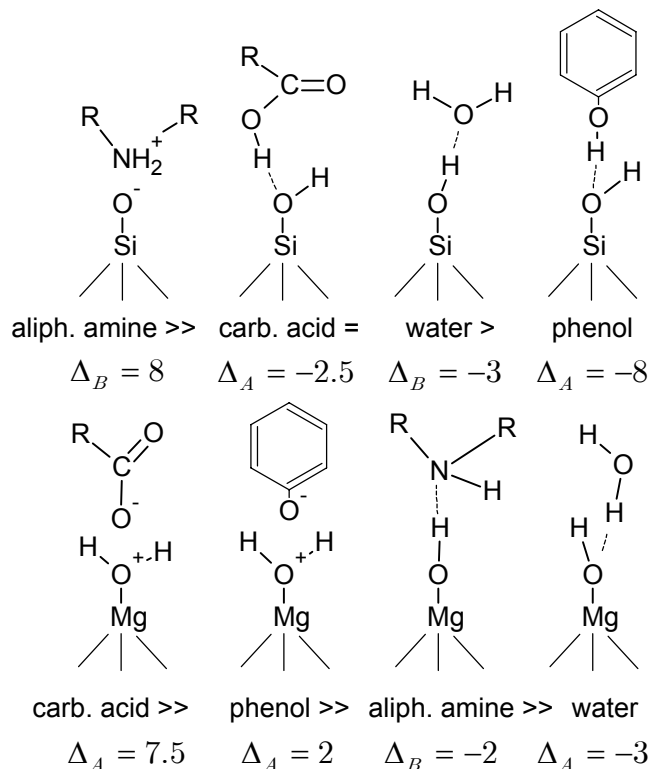


FIG. 1. Examples of bonds formed between typical organic groups and hydroxyls on a SiO_2 (top) or MgO (bottom) surface.

coating is caused due to the strong pH change, moving out of the bonding stability window given by Eqs. 5 and 6. An example of this is the well-known phenomenon of cathodic delamination, occurring on organic coated steel substrates.

2.2. X-ray photoelectron spectroscopy (XPS)

2.2.1. Introduction

The XPS analysis technique has been used in this thesis to study different aluminium oxide layers with respect to amounts of hydroxyls on their surfaces and localised acid-base properties. As an introduction to this, a brief overview will be given of the electronic structure of aluminium oxide, the XPS technique and core level binding energies.

2.2.2. Electronic structure of aluminium oxide

Each atom with atom number Z consists of a positively charged nucleus carrying a total net charge of $+Z$, surrounded by a number of electrons carrying a total net charge $-Z$. The electronic configuration of electrons in an atom is often described by the nl^a notation with n is the shell, l the orbital and a the number of electrons in the specific orbital. Using this notation, the Al atom with 13 electrons can be described by $1s^2 2s^2 2p^3 3s^2 3p^1$ and the O atom with 8 electrons by $1s^2 2s^2 2p^4$. The shells of an atom that are completely filled with electrons are called the *core shells* while the partially filled outer shells are called the *valence shells*. Furthermore, within one core shell, the different orbitals are called the *core levels*. The Al atom thus contains 2 core shells, $1s^2$ and $2s^2 2p^3$ respectively. The first core shell contains one core level ($1s^2$) and the second core shell contains two core levels ($2s^2$ and $2p^3$). The third level of Al is not completely filled and is thus called the valence shell, in this case containing 3 valence electrons.

When two atoms are brought to within bonding distance of each other, their valence electrons start to interact and their valence levels start to overlap, resulting in the formation of bonding and anti-bonding orbitals with associated discrete energy levels. If now an infinitely large amount of atoms are brought together, these bonding and anti-bonding energy levels become infinitely small spaced and energy *bands* are formed, which consist of a large number of energy levels from the separate atoms. These energy bands are called the *valence bands* and *conduction bands*. The valence band that is formed in an aluminium oxide

(Al_2O_3) consists of an upper valence band and a lower valence band (lower in energy). The valence bands in Al_2O_3 are fully occupied and the above-lying conduction band is empty and separated from the valence bands by a so-called interband gap E_g , which makes the solid an insulator. The Fermi-level E_f lies within this interband gap. In contrast to the valence bands, the core levels are not involved in bonding and therefore remain discrete energy levels.

2.2.3. Theory of XPS

In XPS analysis, the sample to be investigated is locally irradiated with photons of monoenergetic energy $h\nu$, originating from an X-ray source. Due to the irradiation, electrons are ejected from the sample with a kinetic energy E_k , which is given by [11]:

$$E_{\text{kin}} = h\nu - E_B - \phi_s \quad (5)$$

E_B is the binding energy of the ejected electron and Φ_s the sample work function, which is a potential barrier the electron has to pass when leaving the sample surface. The binding energies of the electrons are defined with respect to a reference level. In the investigation of solid samples, the Fermi level is mostly used as a reference. This is being provided by making electrical contact between the sample and the spectrometer. For metallic samples this will result in the Fermi-levels of the sample and spectrometer being aligned. As a result of this, the electrons feel an additional potential barrier equal to the difference between the sample Φ_s and spectrometer work functions Φ_{spec} (which has to be added on the right-hand side of Eq. 1). For non- or improperly conducting samples, this Fermi-edge level coupling does not properly occur. As a result, the sample surface will show the build-up of positive charges, due to the extraction of electrons in the XPS process, which are not replenished. This results in an additional potential barrier for the ejected electrons to pass. Due to this, the electrons will lose part of their kinetic energy, resulting in a higher binding energy to be measured, see Eq. 1, which is often denoted a charging shift. A correction for a charging shift is most often made by shifting all binding energies with respect to a known binding energy. Most often, the C-C/C-H core level peak is used for this purpose [12,13]. The C-C/C-H peak is considered to have a constant binding energy and is most often found on samples as a result of adventitious contamination.

After leaving the sample surface with a given kinetic energy, the electrons are detected by an electron energy analyser, coupled to an electron counter. The

XPS spectrum that ultimately results from this, is a plot of the measured intensity (i.e. number of electrons counted) versus their binding energy. This spectrum can be considered a direct measure of the density of electrons occupying the various bands (e.g. core and valence bands) in a material.

As it directly probes the electronic structure, XPS is highly suitable for and is also often used to study the chemical state of molecules and atoms (like type of bonding, ionicity and acid-base properties) [12,14]. From theory one would expect that it are mainly the *valence bands* that can provide the most valuable information in this respect, as they are directly involved in bonding between the constituents of the solid. This is indeed the case, but interpretation of these bands is difficult due to their complex nature. Siegbahn *et al* [15] demonstrated that the *core levels* are *also* influenced by a change in electronic environment, for example due to changes in ionicity of the oxide. As a result of this, the XPS core level peaks often show a so-called *chemical shift*. The core level peaks are easier to investigate than the valence bands as they are intense, sharp and well-defined and consequently can be measured with a high accuracy. According to the simple electrostatic potential model introduced by Siegbahn *et al.*, the core level binding energy $E_B(A)$ of a core level electron in an atom A which is part of a system X is equal to:

$$E_B(A) = \text{const} + kq_A + V_M - R \quad (6)$$

In this relation, q_A is the "effective charge" of A in the X system and the k term is related to interactions experienced by the *core level* due to changes in the *valence band* - the latter being actually involved in the bonding. The V_M term is the Madelung potential, which describes the interaction between all other atoms in the system X and the single A atom. This term is described by:

$$V_M = \sum_{B \neq A} \frac{q_B}{r_{A-B}} \quad (7)$$

in which it is assumed that the B atoms (all the atoms except A) can be represented as point charges and neglecting possible polarisation effects of the ions. In Eq. 7, q_B is the effective charge on the B atoms and r_{A-B} the interatomic distance between the various B atoms and the A atom. The final term of Eq. 6, R, is the relaxation energy. When a core electron is removed from a solid in the XPS photoionisation process, it will leave behind a core *hole*. The remaining electrons and atoms, surrounding the core hole will respond to this by locally rearranging. If this process occurs within the same timeframe as the core

electron removal, part of this relaxation energy is transferred to the outgoing electron, hence giving the term R . Now, for the binding energy *shift* $\Delta E_B(A)$ of an atom A in two different materials:

$$\Delta E_B(A) = k\Delta q_A + \Delta V_M - \Delta R^{ea} \quad (8)$$

With $k\Delta q_A$ the change in atomic charge, ΔV_M the change in Madelung potential and ΔR^{ea} the *extra-atomic* relaxation energy. This latter term differs from R in Eq. 1 by the *intra-atomic* relaxation energy, which corresponds to the internal relaxation of electrons within the A atom due to the core hole. As this term is approximately the same for A in both materials, it cancels out. The influence of the various components to the core level binding energies and how it influences interpretation is further considered in the chapter on the acid-base properties of aluminium oxides.

2.3. Optical spectroscopical techniques

2.3.1. Introduction

Throughout this thesis, extensive use is made of infrared spectroscopy and spectroscopic ellipsometry. A brief introduction is given to the interaction of light with matter, reflection of light on surfaces and finally some background on the different techniques is given.

2.3.2. Absorption of light

Molecules consist of atoms which have a certain mass and which can be considered to be connected by elastic bonds. As a result, they have vibrational degrees of freedom. Infrared light of a given angular frequency ω can interact with these vibrations. If absorption occurs, the vibration goes from its initial state n into an excited state m , having a higher energy. The molecule then absorbs a photon from the incident light of the given frequency and the light attenuates in intensity. By varying the frequency of the incident light, different vibrations are being excited and an infrared spectrum of the molecule can be obtained. Macroscopically, the interaction between the incident light and the molecule can be described by the optical constants of the absorbing medium.

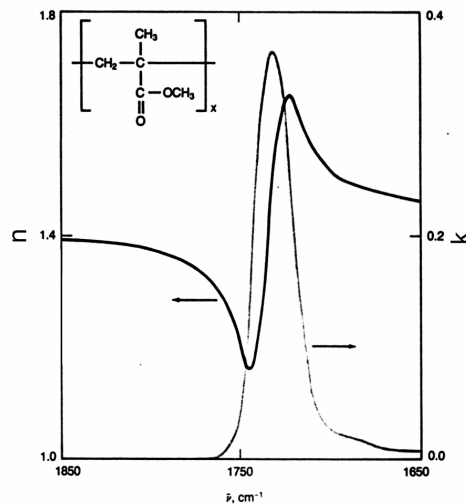


FIG. 2. Simulated k and n spectra for a carbonyl ($C=O$) carbonyl vibration in a PMMA polymer. Figure taken from Ref. [16].

The complex refractive index spectrum $\mathbf{n}(\omega)$ is defined as:

$$\mathbf{n}(\omega) = n(\omega) + ik(\omega) \quad (9)$$

with $n(\omega)$ being the real refractive index spectrum and $k(\omega)$ being the extinction coefficient spectrum. The absorption of light by a given molecular vibration can be visualized as an oscillator with a force constant, dampening constant and resonance frequency. For such an oscillator, an absorption index $k(\omega)$ and a refractive index $n(\omega)$ can be calculated. In Fig. 2, this is demonstrated for the $\nu(C=O)$ carbonyl stretching vibration of the ester group in poly(methyl methacrylate) (PMMA). The refractive index spectrum $n(\omega)$ appears like a derivative-like peak. The relevant information on the molecular absorptions is contained in the $k(\omega)$ spectrum, which is normally measured in infrared *transmission* spectroscopy.

2.3.3. Reflection and refraction of light

When light incidents on a perfectly flat interface between two media, it will be partially reflected and partially refracted (i.e. propagation with a different direction in the second medium). The angle of refraction is described by the well-known Snell's law of refraction [17]. Unpolarised incident light can be considered to consist of a p-component and an s-component, this is shown schematically in Fig. 3, where s stands for light polarised perpendicular to the

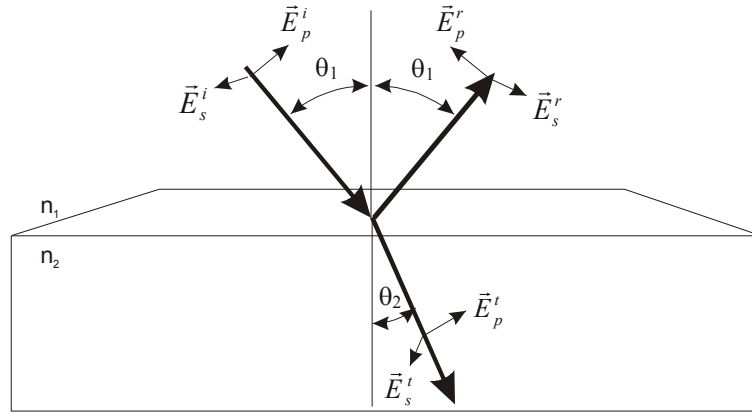


FIG 3. Reflection and refraction of light \vec{E} at the interface between two media of different refractive index with $n_2 > n_1$. \vec{E}^i is the incident light, \vec{E}^r is the reflected light and \vec{E}^t the refracted light. The light can be considered to consist of two polarisation states: an s-part (parallel to the plane of incidence) and a p-part (perpendicular to the plane of incidence).

plane of incidence and p for parallel to it. Both of the components interact independently with the surface.

The refracted and reflected light can be determined using the Fresnel equations [17-19]. As an example, in Fig. 4, calculated reflection data is shown for the reflection of light incident from a medium with a lower refractive index n_1 (vacuum) onto a medium having a high refractive index n_2 (aluminium). The left plot show the phase shift that occurs between the incident and reflected light for each of the polarisation states. The right plot shows the amplitude of the reflection coefficients r_p and r_s which are the ratios of the incident and

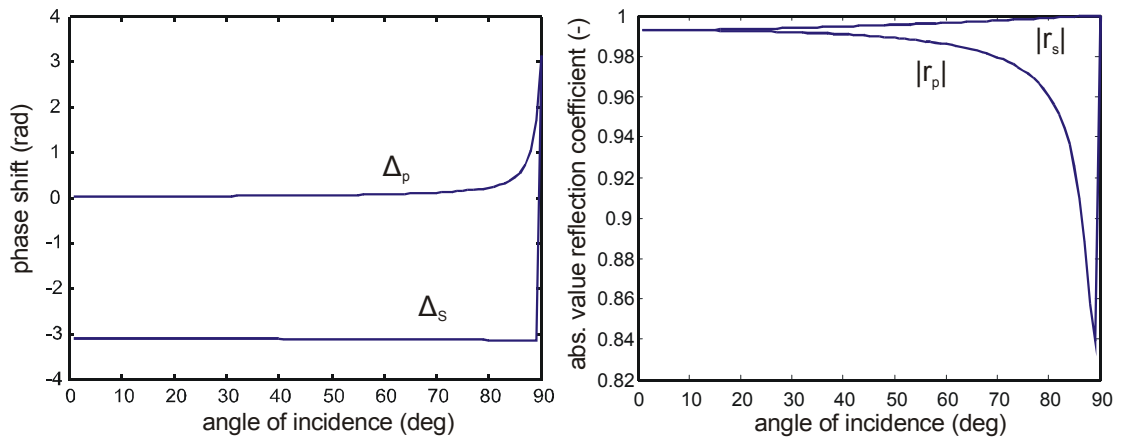


FIG 4. Reflection of p and s components of light on the interface vacuum/aluminium as a function of angle of incidence (with respect to the normal of the surface). Left plot shows the phase shift upon reflection and the right plot shows the reflection coefficient, which is the ratio of the incident and reflected amplitudes. (Plots are calculated with the Fresnel equations, using $n_1 = 1.0$, $k_1 = 0.0$ (vacuum), $n_2 = 8.67$, $k_2 = 48.6$ (aluminium), $\omega = 2000$ cm^{-1}).

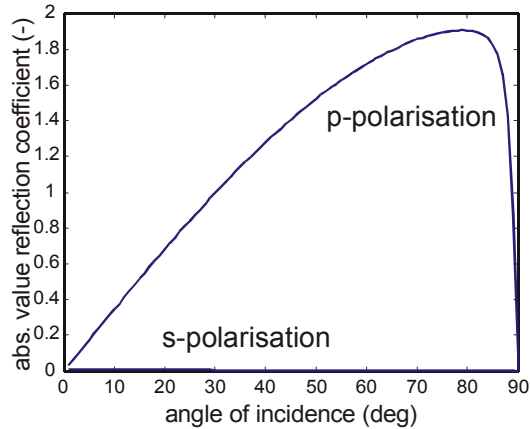


FIG 5. The p and s components of light, after interference at the vacuum/aluminium interface, as a function of angle of incidence (with respect to the normal of the surface).

reflected light. It can be seen that the p- and the s-components of the incident light have different reflection behaviour. The s-component shows an almost constant phase shift of about $-\pi$ up until 88 degrees, as compared to the incident light, while the p-component shows no phase shift. At higher angles of incidence, the phase shift for both the p and s components rapidly increases to $+\pi$. At the point of reflection on the surface, the incident and reflected light combines. In Fig. 5, the amplitudes of the reflection coefficients r_p and r_s after interference are plotted for the same situation as shown in Fig. 4. The amplitude of the s-component of light is practically zero, which is due to destructive interference as a result of the $-\pi$ phase difference between incident and reflected light (cf. Fig. 4). The p-component on the other hand shows constructive interference and the amplitude of the reflected light is enhanced as compared to the incident light.

This enhancement increases as a function of angle of incidence up to around 85 degrees and rapidly drops after this. The maximum enhancement is obtained for angles of incidence in the 80-85 degrees range.

For light travelling through a medium of high refractive index n_1 and incidenting on a medium with a lower refractive index n_2 (i.e. $n_1 > n_2$), the results are different. It can be derived using Snell's equation and the Fresnel equations that above a critical angle of incidence θ_c , so-called *total internal reflection* occurs and no component of the incident light is refracted into the second medium. This is shown in Fig. 6, where the amplitudes of the reflection coefficients r_p and r_s are plotted as a function of the angle of incidence for $n_1 > n_2$. However, at the point of reflection, a so-called evanescent electric field is generated, which extends a fraction of a wavelength into medium 2, having an intensity that decreases as a function of the distance from medium 1 [18]. The principle is shown schematically in Fig. 7. The penetration depth of the evanes-

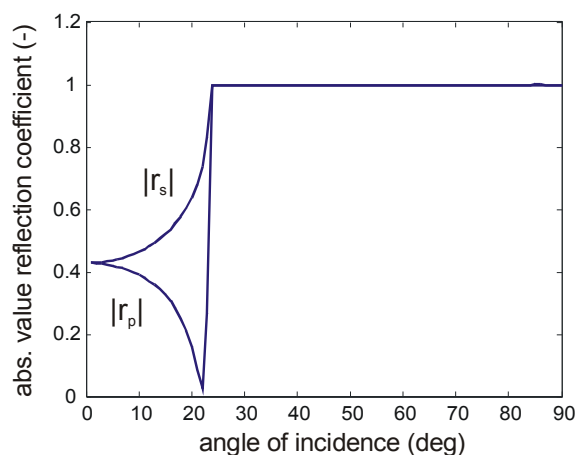


FIG. 6. Reflection coefficients for light reflection from a medium having a high refractive index n_1 onto a medium having a lower refractive index ($n_1 > n_2$). (Plots are calculated with the Fresnel equations using $n_1 = 2.5$, $k_1 = 0$, $n_2 = 1.0$, $k_2 = 0$).

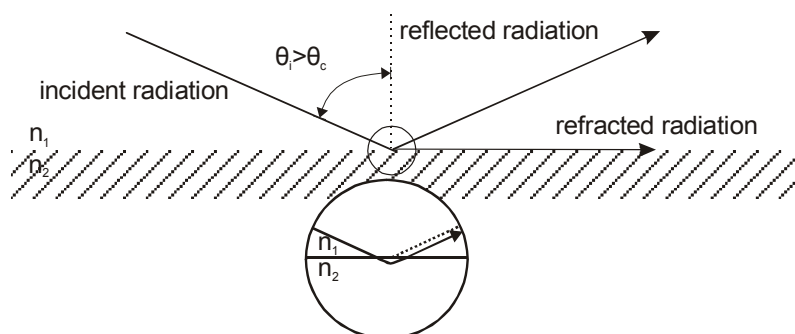


FIG. 7. Evanescent electric field generated into medium 2 as a result of total reflectance at the medium 1/medium 2 interface.

cent wave depends on the wavenumber of the light and on the optical properties of both medium 1 and 2. If medium 2 absorbs, the reflection is no longer without loss: the evanescent wave is weakened and the reflected wave cannot be reconstructed with full amplitude. As a consequence, the reflectance spectrum is modulated with an absorption spectrum of medium 2.

2.3.4. FTIR-RAS

In the infrared reflection absorption spectroscopy (FTIR-RAS) technique, infrared light is incident at an almost grazing angle (e.g. > 75 degrees with respect to the surface normal) on a reflective substrate, having a high refractive index [18,19]. As shown in Fig. 5, this causes enhancement of the p-component while the s-component is almost completely cancelled out due to destructive interference. The enhancement of the p-component makes it a very sensitive measuring technique.

Further advantages of having a high angle of incidence is an enhancement of the investigated area and a longer pathway of the infrared light through an absorbing overlayer on the reflecting metallic substrates. These advantages make the technique highly suitable for studying very thin layers applied on reflective substrates, for example monolayers of organic molecules adsorbed on metallic substrates. This was first demonstrated by Francis and Ellison [20] and Greenler [21] in the late 1950's, early 1960's.

As only the p component of the incident infrared light interacts with the metallic substrate, only vibrations perpendicular to the surface contribute to the resulting infrared spectrum. This phenomenon is being used to study orientation of adsorbed organic molecules [22,23].

A potential pitfall of FTIR-RAS is that the infrared spectrum may contain a contribution due to the refractive index part $n(\omega)$ of the absorption, causing distortion of infrared bands and shifts in their position. This effect is stronger for thicker layers, stronger absorptions and weakly reflecting surfaces. In Fig. 8, an illustration of the phenomenon is shown for different layer thicknesses of PMMA on glassy carbon. With an increasing layer thickness of the PMMA, a shoulder develops on the lower wavenumber side of the main PMMA band. Glassy carbon is a weakly reflecting surface and for this reason the effect is rather strong. For the highly reflective aluminium, studied in this thesis, a more limited effect is expected.

2.3.5. FTIR-ATR

The principle of total reflectance (cf. Fig. 6) is used as the basis for the FTIR attenuated total reflectance (ATR) measuring technique [19]. A

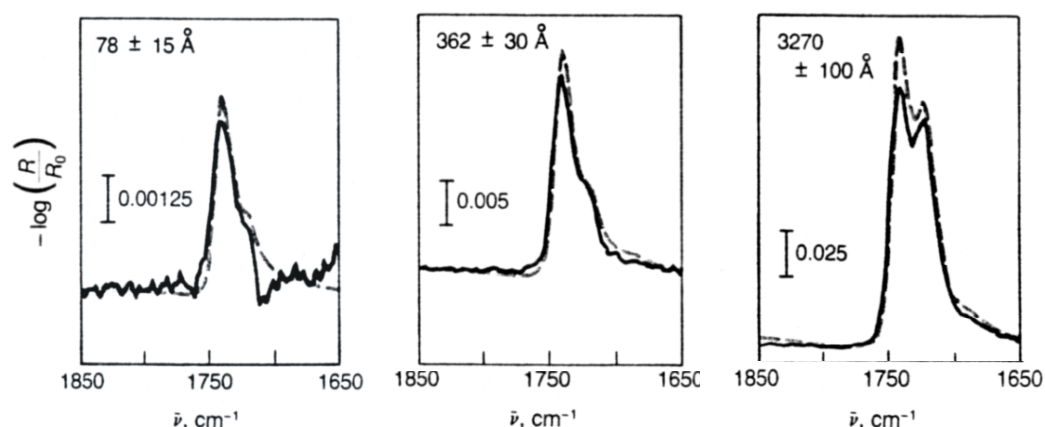


FIG. 8. Infrared reflection spectra showing the carbonyl band as obtained for different layer thicknesses of PMMA adsorbed on glassy carbon for p-polarised light. Solid lines show measured spectra and dotted lines show simulated spectra. Spectra taken from Ref. [16].

transparent optical element with a high refractive index ($n > 2.5$), like for example Ge, ZnSe or diamond is used as the incident medium. The sample – having a lower refractive index – is brought in direct contact with the surface of the optical element. The evanescent wave that is generated in the sample interacts with it and interferes with the reflected light. An infrared spectrum is obtained of the sample by detecting the reflected light. Advantages of the technique are that the investigated sample does not need to have good reflective properties, that the technique is also suitable for liquids and polymers and that only the surface region of the sample is being investigated.

2.3.6. Spectroscopic ellipsometry

Ellipsometry is widely used to accurately measure thicknesses of thin films in multilayered samples. With ellipsometry, the change in polarisation state after interaction of light with the sample is measured. The ratio ρ of the complex reflection coefficients \mathbf{r}_p and \mathbf{r}_s of the p and s polarised light after reflection is given by [24-27]:

$$\rho = \frac{\mathbf{r}_p}{\mathbf{r}_s} = \frac{|\mathbf{r}_p|}{|\mathbf{r}_s|} \exp[i(\delta_p - \delta_s)] = \tan(\Psi) \exp(i\Delta) \quad (10)$$

with $|\mathbf{r}_p|$ and $|\mathbf{r}_s|$ the amplitude change and δ_p and δ_s the phase change of the p and s components after reflection. This ratio is expressed as a function of the ellipsometric angles Ψ and Δ (in degrees). The azimuth Ψ is related to the ratio of amplitudes of reflection for the p and s components and the phase change Δ is the difference in phase between the components after reflection. Because the technique measures ratio's instead of absolute values, it is less sensitive to fluctuations in the optical set-up.

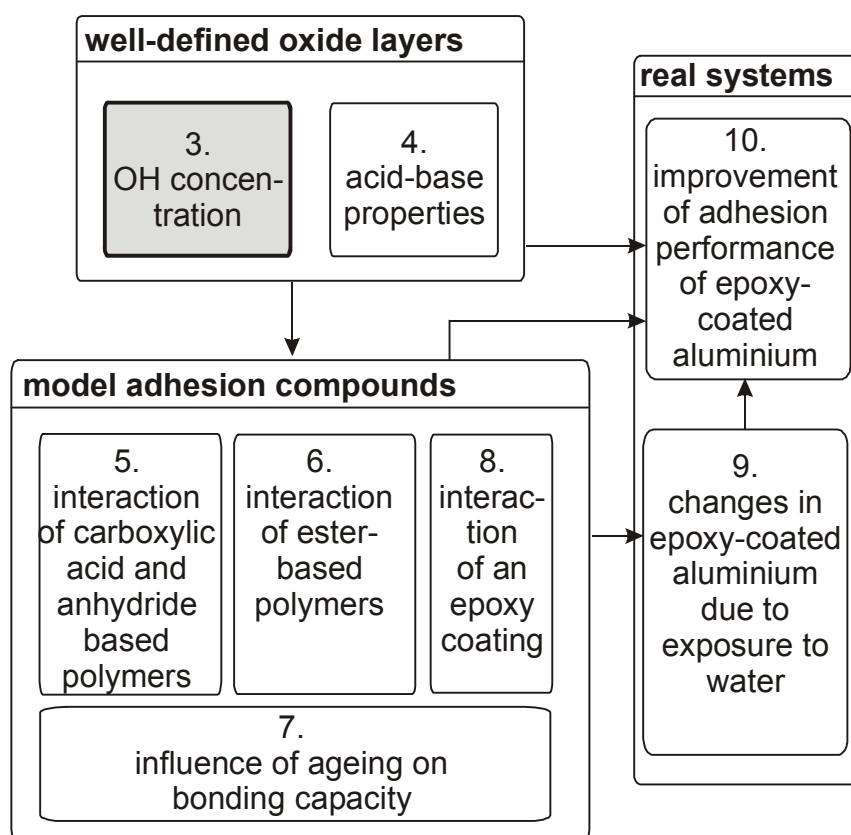
The Ψ and Δ versus wavelength spectra that result from a measurement are difficult to interpret directly. For this purpose, the generated Ψ and Δ of an optical model need to be fitted onto the measurement results. Consider for example a measurement performed to determine the oxide layer thickness on a metallic substrate, both having known optical properties. The optical model then consists of a thin layer with optical properties of the oxide layer on top of an infinitely thick substrate with optical properties of the metallic substrate. The optical model is then fitted onto the measurement data by variation of the oxide layer thickness until the best possible fit is obtained.

References

1. Lee, L. H. *Fundamentals of adhesion*; Plenum Press: New York, 1991.
2. Brönsted, J. N. *Recl.Trav.Chim.Pays-Bas* 1923, 42 718.
3. Lowry, T. *Chemical Industry* 1923, 42 274.
4. Lewis, G. N. *Valence and the structure of atoms and molecules*; The Chemical Catalog Co.: New York, 1923.
5. Lewis, G. N. *Journal of the Franklin Institute* 1938, 226 293-301.
6. Knözinger, H.; Ratnasamy, P. *Catalysis Reviews - Science and Engineering* 1978, 17(1), 31-69.
7. Peri, J. B.; Hannan, R. B. *Journal of Physical Chemistry* 1960, 64 1526-1530.
8. Davydov, A. A.; Rochester, C. H. *Infrared spectroscopy of adsorbed species on the surface of transition metal oxides*; Wiley: Chichester, 1990.
9. Bolger, J. C.; Michaels, A. S. *Interface conversion for polymer coatings*; Weiss, P.; Cheever, G. D., editors; Elsevier: New York, 1969.
10. Bolger, J. C.; Michaels, A. S. Molecular structure and electrostatic interaction at polymer-solid interfaces, in *Adhesion aspects of polymeric coatings*, Mittal, K. L., editor; Plenum Press: New York, 1983.
11. Feldman, L. C.; Mayer, J. W. *Fundamentals of surface and thin film analysis*; Prentice-Hall Inc: New Jersey, 1986.
12. Barr, T. L. *Modern ESCA*; CRC Press: Boca Raton, 1994.
13. Briggs, D.; Seah, M. P. *Practical surface analysis. Vol. 1. Auger and X-ray photoelectron spectroscopy*; 2nd ed.; Wiley: Chichester, 1990.
14. Moretti, G. *Journal of Electron Spectroscopy and Related Phenomena* 1998, 95(2-3), 95-144.
15. Siegbahn, K.; Nordling, C.; Fahlman, A. *Nova Acta Regiae Societate of Science* 1967, 4(20).
16. Porter, M. D. *Analytical Chemistry* 1988, 60(20), 1143-1155.
17. Born, M.; Wolf, E.; Bhatia, A. B. *Principles of optics : electromagnetic theory of propagation, interference and diffraction of light*; 7th ed.; Cambridge University Press: Cambridge, 1999.
18. Schrader, B. *Infrared and Raman spectroscopy; methods and applications*; VCH: Weinheim, 1995.
19. Ishida, H. *Rubber Chemistry and Technology* 1987, 60(3), 497-554.
20. Francis, S. A.; Ellison, A. H. *Journal of the Optical Society of America* 1959, 49(2), 131-138.
21. Greenler, R. G. *Journal of Chemical Physics* 1966, 44(1), 310.
22. Schlotter, N. E.; Porter, M. D.; Bright, T. B.; Allara, D. L.; . *Chemical Physics Letters* 1986, 132(1), 93-97.
23. Allara, D. L.; Nuzzo, R. G. *Langmuir* 1985, 1(1), 52-66.
24. van Gils, S. PhD thesis, Vrije Universiteit Brussel, 2004.
25. Vedam, K. *Thin Solid Films* 1998, 313 1-9.
26. Jenkins, T. E. *Journal of Physics: D Applied Physics* 1999, 32(9), 45-56.
27. Azzam, R. M. A.; Bashara, N. M. *Ellipsometry and polarised light*; Elsevier: Amsterdam, the Netherlands, 1987.

CHAPTER 3.

DETERMINATION OF THE AMOUNT OF HYDROXYLS ON ALUMINIUM OXIDE SURFACES ¹



¹ This chapter was published as a scientific paper in a slightly different form: J. van den Brand, W.G. Sloof, H. Terryn, J.H.W. de Wit, Surface and Interface Analysis, 36(1), 81-88, 2004

Synopsis

The hydroxyls on the oxide surface play an important role in bonding with a subsequently applied organic overlayer, as will be shown further on in this thesis. For this reason, correct and accurate knowledge of the amount of hydroxyls on the oxide surface is important. The X-ray photoelectron spectroscopy (XPS) measurement technique is highly suitable for providing this knowledge. In this chapter, XPS is used to determine the amount of hydroxyls on the surfaces of the oxide layers of a set of five differently prepared aluminium substrates. This same set of substrates is used throughout this thesis. Commonly, curve-fitting of the O 1s core level peak is employed to determine the amount of hydroxyls. This is also being done here. It is however not known whether this method gives accurate results. For this reason, in this chapter, an additional method is followed to obtain knowledge on the amount of hydroxyls and so to be able to validate the curve-fitting results. Both methods are found to give well-comparable results for the different substrates, giving confidence in the use of the curve-fitting method. The studied aluminium oxide layers are found to show significant variations in amount of hydroxyls on their surfaces and most layers are enriched in hydroxyls towards the surface region.

3.1. Introduction

It is widely recognized that the presence of hydroxyls on the surfaces of oxide layers plays an important role in the formation of chemical bonds with polymeric coatings and adhesives [1-3]. X-ray photoelectron spectroscopy (XPS) has been employed to obtain quantitative information on the amount of hydroxyls in oxide layers [2, 4-9]. The amount of hydroxyls is usually determined as a hydroxyl fraction by curve-fitting of the O 1s peak into single OH⁻, O²⁻ and possibly H₂O components [5, 9], but sometimes more types of OH⁻ components are being used [7, 8]. However, curve-fitting of the O 1s peak can be unreliable. It is commonly found that OH⁻ and O²⁻ components show a binding energy separation of only 1.2 - 1.4 eV and the peak does not show clear features to guide the fitting procedure. For these reasons, multiple solutions to the curve-fit can be obtained. To limit the number of possibilities, restrictions can be imposed on the used fitting procedure [5].

Confirmation of the curve-fitting procedure and results can be found by determining the O/Al atomic ratio of the oxide layer using the O 1s and oxidic Al 2p primary zero loss (PZL) photoelectron intensities. The hydroxyl fraction

is expected to be related to the O/Al atomic ratio. For a completely anhydrous amorphous oxide layer (Al_2O_3 with hydroxyl fraction is zero) the value for the O/Al atomic ratio corresponds to 1.5, while for crystalline AlOOH (with hydroxyl fraction is 0.5) this is 2.0. However, an accurate determination of the composition is complicated when contamination overlayers are present [10]. The magnitude of attenuation of the photoelectron signals, originating from below the contamination overlayer, depends exponentially on the inelastic mean free path (IMFP) of the photoelectrons in the overlayer. A method is presented to account for the attenuation of the photoelectron intensities by contamination overlayers. A set of coupled equations are given and used in which a correction for the contamination overlayer is incorporated. The relations allow a simultaneous determination of the composition of the oxide layer as well as the thicknesses of both the oxide and contamination overlayers.

The approach followed is similar to that followed by Evans *et al.* [10]. They derived equations and validated these using experiments for a two-layer system, consisting of a contamination overlayer on homogeneous samples with a well-defined composition. Here, this is extended to a three-layer system by the derivation of equations for a system consisting of a contamination overlayer on a thin aluminium oxide layer on a metallic substrate. This complements previous work, where a comparable approach was followed and equations were derived to determine the composition and thickness of thin aluminium oxide layers but without a contamination overlayer being present [11].

The correlation between the hydroxyl fraction as obtained by curve-fitting of the O *1s* peak and the O/Al atomic ratio as determined from the O *1s*, Al *2p* and C *1s* photoelectron intensities is verified for a set of five different aluminium oxide layers. The oxide layers were made by oxidising aluminium in vacuum, with an alkaline and acidic pretreatment and in boiling water. In addition, angle-resolved XPS measurements have been performed on the studied oxide layers to resolve the distribution of hydroxyls through the layer.

3.2. Experimental

3.2.1. Oxide layers

In this work, a set of five different types of aluminium oxides were investigated. All oxide layers were studied as freshly prepared and the time between preparation and introduction into the XPS apparatus was no more than 10 minutes.

Anhydrous, amorphous aluminium oxide

A disc-shaped specimen with a diameter of 10 mm of recrystallised aluminium was polished down to 0.05 μm . Then, the sample was chemically polished for 1.5 minutes in a solution consisting of 70 ml H_3PO_4 , 25 ml H_2SO_4 and 5 ml HNO_3 at a temperature of 85 $^\circ\text{C}$. Finally, the samples were rinsed using deionised water and blown dry using compressed nitrogen. The sample was subsequently mounted in the UHV preparation chamber (base pressure < $2 \cdot 10^{-8}$ Pa) which is directly coupled to the XPS instrument. First, the native oxide layer was sputtered away using a focussed Ar^+ beam. Next, the sample and sample holder were outgassed by repeated annealing for 4 hours at 773 K and subsequent cleaning with a focussed Ar^+ beam scanning the specimen surface area at room temperature. The procedure is discussed elsewhere in more detail [11, 12]. As a final step, the sample was oxidised by admitting pure oxygen (99.9998 vol.%) at room temperature to a pressure of $1.33 \cdot 10^{-4}$ Pa for 1 hour. Next, the sample was transferred into the XPS system for analysis without exposure to the ambient. Although the anhydrous amorphous aluminium oxide does not contain a contamination overlayer, it is included here as a reference oxide layer, free of hydroxyls and without a contamination overlayer.

Evaporated and oxidised aluminium

First, an approximately 100 nm thick aluminium layer was deposited onto a cleaned 12 x 12 x 1 mm glass slide (Agar Scientific) by evaporation of 99.998 wt.% pure aluminium at a base pressure of $3 \cdot 10^{-5}$ Pa, using a vacuum evaporation unit (Balzers BAE 250). Pure oxygen (99.998 vol.%) was subsequently admitted to a pressure of about $1 \cdot 10^{-2}$ Pa for 1 hour and finally the vacuum chamber was filled with pure oxygen to ambient pressure.

Acid pretreated aluminium

For this and the subsequent oxide types, an AA1050 aluminium alloy was used (99.5 wt.% Al, 0.04 wt.% Fe and 0.25 wt.% Si). First, the 12 x 12 x 1 mm samples were polished down in several subsequent steps. The final polishing step of 0.025 μm was done with a neutral aluminium oxide based polishing slurry (Struers). The samples were cleaned in hot chloroform (99+ vol.% pure). Thereafter, the substrates were immersed in a 30 vol.% HNO_3 solution

(chemically pure) in deionised water for 30 seconds. Finally, the substrates were thoroughly rinsed for at least 3 minutes using deionised water and blown dry using compressed clean air.

Alkaline pretreated aluminium

After polishing and cleaning, the samples were mildly etched in a $\text{pH} = 12.5$ solution made using NaOH (97+ vol.% pure) in deionised water for a period of 30 seconds. The substrates were then thoroughly rinsed for at least 3 minutes using deionised water and blown dry using compressed clean air.

Pseudoboehmite oxide

After polishing and cleaning, the samples were immersed in boiling deionised water for a period of 60 seconds which results in the formation of a thick pseudoboehmite (AlOOH) layer [13, 14]. The samples were then allowed to dry for a few minutes in an upright position.

3.2.2. Experimental details

XPS spectra of the Al $2p$, O $1s$ and C $1s$ photoelectron lines were recorded with a step size of 0.1 eV using a PHI 5400 ESCA instrument (base pressure $< 1 \cdot 10^{-8}$ Pa), set at a constant analyser pass energy of 35.75 eV and using unmonochromatised incident Mg X-ray radiation ($\text{Mg K}\alpha_{1,2} = 1253.6$ eV). The energy scale of the Spherical Capacitor Analyser (SCA) spectrometer was calibrated according to the procedure described in [15]. The samples were electrically grounded by mounting them in a stainless steel holder. For each oxide, 2 samples were investigated and for each sample, measurements were performed at take-off angles of 45 and 15 degrees with respect to the sample surface to study a possible enrichment of hydroxyls towards the outer most surface. The obtained spectra were corrected for the presence of X-ray satellites and also for the electron kinetic energy dependent transmission of the spectrometer by multiplying each spectral intensity with its corresponding kinetic energy [16]. For all samples studied, XPS survey spectra showed Al, O and C to be the main elements with other elements only appearing at trace levels. To correct for sample charging, the spectra were shifted to set the C-C/C-H components of the C $1s$ peak at a binding energy of 284.8 eV [17]. Only for the anhydrous, amorphous oxide this was not possible due to absence of a contamination overlayer and the same charging shift was applied as for the

evaporated and oxidised aluminium. Both types of oxidised aluminium samples showed the same initial Al $2p$ metal-Al $2p$ oxide shift of 2.8 eV which demonstrates that these oxides are comparable [18-20].

3.2.3. Data evaluation

Determination of the O/Al atomic ratio of the oxide layer

The measured photoelectron intensity I_A of photoelectrons, ejected with kinetic energy E from the n^{th} core level of an atom (or ion) A, situated in a solid at depth z below the surface of the solid can be written as [16]:

$$I_A = K\sigma_A \int_{z=0}^{\infty} C_A(z) \exp\left(-\int_{z=0}^z \frac{dz}{\lambda_A(z) \sin \theta}\right) dz \quad (1)$$

in which K is an instrumental factor depending on the area analysed, incident X-ray energy and intensity etc., σ_A the cross section for photoionisation, $\lambda_A(z')$ the depth z dependent inelastic mean free path (IMFP) of the photoelectrons with kinetic energy E in the solid s and θ the angle between the sample surface and the optical axes of the analyser input lenses.

Consider the layer/substrate system shown in Fig. 1, which consists of a metallic substrate of semi-infinite thickness (as compared to the IMFP of the photoelectrons) covered by an oxide layer of thickness d_{ox} and a contamination layer of thickness d_{cont} . It is assumed that the contamination and oxide layers are homogeneous in thickness and composition across the XPS analysis area, the surfaces are flat and that the effects of elastic electron scattering can be neglected. This latter assumption is allowed for the low atom number (and low elastic electron scattering) aluminium oxides and carbon layers for the measurements performed at a take-off angle of 45 degrees [21]. At the almost-grazing take-off angle of 15 degrees, the effect of elastic electron scattering becomes more important [16, 22-24] and also then the effects of surface roughness is likely to play a role for the samples studied here [25, 26]. To aid the analysis, the concentration of atoms C_A in the solid in Eq. 1 is rewritten as a molar fraction n_A . Then, it holds that, $\sum n_i = 1$ considering all elements that are present at significant concentrations. To compensate, the right side of Eq. 1 must then be multiplied by $\rho_s / \sum n_i A_i$, with ρ_s the density of the solid, n_i the molar fractions and A_i the relative atomic masses of all elements present in the solid at significant concentrations.

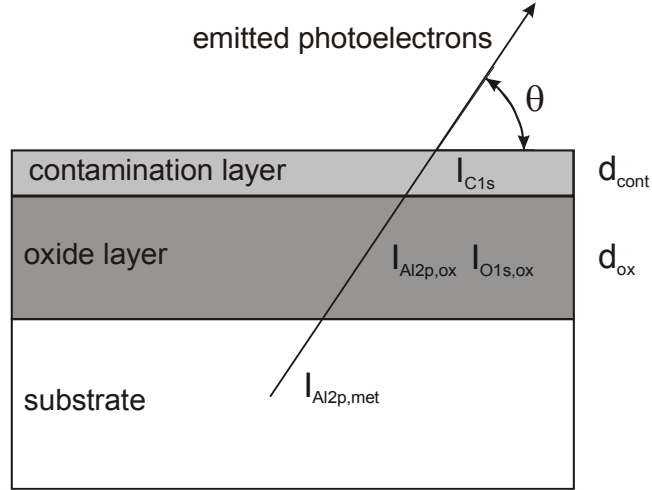


FIG. 1. Schematic representation of the sample system adopted for the simultaneous determination of the oxide composition and thicknesses of the contamination and oxide layers (see text for details).

In order to determine the O/Al atomic ratio of the oxide layer, the oxide and contamination layer thicknesses from the measured PZL photoelectron intensities for the considered system, the following set of equations has been derived using Eq. 1:

$$\left(\frac{I_{Al2p,met}}{I_{C1s}} \right) = \left(\frac{\rho_{Al} / A_{Al}}{\rho_C / A_C} \right) \frac{\sigma_{Al2p} \lambda_{Al2p,met}}{\sigma_{C1s} \lambda_{C1s}} \frac{\exp(t_1) \exp(t_2)}{[1 - \exp(t_3)]} \quad (2)$$

$$\left(\frac{I_{Al2p,ox}}{I_{O1s,ox}} \right) = n_1 F \frac{[1 - \exp(t_4)] \exp(t_5)}{[1 - \exp(t_6)] \exp(t_7)} \quad (3)$$

and

$$\left(\frac{I_{Al2p,met}}{I_{O1s,ox}} \right) = n_2 \left(\frac{\rho_{Al} / A_{Al}}{\rho_{ox}} \right) F \frac{\lambda_{Al2p,met}}{\lambda_{Al2p,ox}} \frac{\exp(t_1) \exp(t_2)}{[1 - \exp(t_6)] \exp(t_7)} \quad (4)$$

with

$$t_1 = -\frac{d_{ox}}{\lambda_{Al2p,met}^{ox} \sin \theta}, \quad t_2 = -\frac{d_{cont}}{\lambda_{Al2p,met}^{cont} \sin \theta}, \quad t_3 = -\frac{d_{cont}}{\lambda_{C1s}^{cont} \sin \theta}$$

$$t_4 = -\frac{d_{ox}}{\lambda_{Al2p,ox}^{ox} \sin \theta}, \quad t_5 = -\frac{d_{cont}}{\lambda_{Al2p,ox}^{cont} \sin \theta}, \quad t_6 = -\frac{d_{ox}}{\lambda_{O1s,ox}^{ox} \sin \theta}$$

and

$$t_7 = -\frac{d_{\text{cont}}}{\lambda_{\text{O}1s,\text{ox}}^{\text{cont}} \sin \theta}, \quad n_1 = \left(\frac{n_{\text{Al}}}{1 - n_{\text{Al}}} \right), \quad n_2 = \frac{n_{\text{Al}} A_{\text{Al}} + (1 - n_{\text{Al}}) A_{\text{O}}}{1 - n_{\text{Al}}}$$

In these Eqs., $I_{\text{Al}2p,\text{met}}$ is the PZL photoelectron intensity originating from Al ions in the metal substrate, $I_{\text{Al}2p,\text{ox}}$ from Al ions in the oxide layer, $I_{\text{O}1s,\text{ox}}$ from oxygen ions in the oxide layer and $I_{\text{C}1s}$ from carbon in the contamination overlayer (cf. Fig. 1). And, A_{Al} , A_{O} and A_{C} indicate respectively the relative atomic masses (units mass per mole) of aluminium, oxygen and carbon, and ρ_{Al} , ρ_{ox} and ρ_{c} the densities (units mass per volume) of respectively the aluminium substrate, oxide layer and contamination overlayer. Further, $\sigma_{\text{Al}2p}$ and $\sigma_{\text{C}1s}$ are the cross sections for photoionisation (units surface area) for respectively the Al $2p$ and C $1s$ electron emissions, n_{Al} is the molar fraction of aluminium in the oxide layer, with $n_{\text{O}} = (1 - n_{\text{Al}})$, assuming no other elements present at significant concentrations. And, d_{cont} and d_{ox} are the thickness of the contamination and oxide layers (cf. Fig. 1) respectively, whereas $\lambda_{\text{A}}^{\text{B}}$ denotes the IMFP of the photoelectrons A which are travelling through B. The term F is obtained from of a clean $\alpha\text{-Al}_2\text{O}_3$ reference (Goodfellow) of known composition, by using:

$$F = \frac{\sigma_{\text{Al}2p} \lambda_{\text{Al}2p,\text{ox}}}{\sigma_{\text{O}1s} \lambda_{\text{O}1s,\text{ox}}} = \frac{3}{2} \left(\frac{I_{\text{Al}2p,\text{ox}}^{\text{ref}}}{I_{\text{O}1s,\text{ox}}^{\text{ref}}} \right) \quad (5)$$

with $I_{\text{Al}2p,\text{ox}}^{\text{ref}}$ and $I_{\text{O}1s,\text{ox}}^{\text{ref}}$ the photoelectron intensities obtained from the reference sample, measured under the same experimental conditions as for the oxide layer samples. An iterative procedure is used to solve Eqs. 2-4. First, an initial estimate of the contamination overlayer thickness d_{cont} is made and an oxide layer thickness d_{ox} is calculated using the measured $(I_{\text{Al}2p,\text{met}} / I_{\text{C}1s})$ PZL intensity ratio (Eq. 2). Next, a value for the molar fraction n_{Al} is calculated, using the measured $(I_{\text{Al}2p,\text{ox}} / I_{\text{O}1s})$ ratio (Eq. 3). Finally, the $(I_{\text{Al}2p,\text{met}} / I_{\text{O}1s,\text{ox}})$ PZL intensity ratio is calculated using Eq. 4. If this calculated ratio deviates from the measured $(I_{\text{Al}2p,\text{met}} / I_{\text{O}1s,\text{ox}})$ PZL intensity ratio, the value for d_{cont} is adapted. This procedure is repeated till the measured and calculated $(I_{\text{Al}2p,\text{met}} / I_{\text{O}1s,\text{ox}})$ ratios are the same within a predefined error. Then, values for n_{Al} , d_{cont} and d_{ox} are obtained that satisfy all three relations to within this error.

For thick oxide layers, (i.e. $d_{\text{ox}} \gg \lambda_{\text{Al}2p,\text{met}}^{\text{ox}}$) as evidenced by the absence of an Al $2p$ metal peak, the set of Eqs. 2-4 cannot be used. In this case, Eq. 3 reduces to:

$$\left(\frac{I_{\text{Al}2p,\text{ox}}}{I_{\text{O}1s,\text{ox}}} \right) = n_1 F \frac{\exp(t_5)}{\exp(t_7)} \quad (6)$$

and the PZL intensity ratio between $I_{\text{Al}2p,\text{ox}}$ and $I_{\text{C}1s}$ is now considered. Then, it follows that:

$$\left(\frac{I_{\text{Al}2p,\text{ox}}}{I_{\text{C}1s}} \right) = n_3 \left(\frac{\rho_{\text{ox}}}{\rho_{\text{C}} / A_{\text{C}}} \right) \frac{\sigma_{\text{Al}2p} \lambda_{\text{Al}2p,\text{ox}}}{\sigma_{\text{C}1s} \lambda_{\text{C}1s}} \frac{\exp(t_5)}{[1 - \exp(t_3)]} \quad (7)$$

with

$$n_3 = \frac{n_{\text{Al}}}{(n_{\text{Al}} A_{\text{Al}} + (1 - n_{\text{Al}}) A_{\text{O}})}$$

Also here a similar iterative procedure is followed to obtain a solution (see above).

Determination of the hydroxyl fraction using curve-fitting

Curve-fitting of the O *1s* photoelectron peak to determine the fraction of hydroxyls was performed using a constrained fitting procedure in which the widths and shapes (mixed Gauss-Lorentz) for the different fit components in the peak were allowed to change but the change was restricted to be the same for the different components. No restrictions were imposed on the peak positions of the different components. The fitting of the O *1s* photoelectron peak was performed in the 526-538 eV binding energy region, after subtraction of a simple Shirley-type background.

Calculation procedure details

For the determination of the composition (cf. Eqs. 2-7), the Al *2p* peak was resolved into an oxidic and a metallic component in the 68-78 eV binding energy region, using a procedure in which the metallic peak (obtained from a clean aluminium sample without an oxide layer) plus its associated Tougaard background and including the tail towards higher binding energies (constructed using a Doniach-Sunjic lineshape) is reconstructed in the measured spectrum of the oxidised sample. The details of this procedure are discussed elsewhere [27, 28]. As an example, the Al *2p* spectrum of the evaporated and oxidised

aluminium type of oxide with the resolved oxidic and metallic components is shown in Fig. 2. The total *metallic* Al $2p$ PZL (primary zero loss) intensity was determined by integration of the intensity of this reconstructed metallic peak in the binding energy range from 68 – 78 eV and the total *oxidic* Al $2p$ (PZL) peak intensity was determined by integration in the 68 – 78 eV binding energy region of the oxidic rest spectrum, remaining after subtraction of the reconstructed metallic main peak and a universal Tougaard background. For the O $1s$ and C $1s$ peaks, the (PZL) peak intensities were determined by integration, after subtraction of a simple Shirley-type background. Since the O $1s$ and C $1s$ spectra only contain a small contribution of inelastically scattered electrons, they were found to be insensitive to the type of background subtraction [27].

For the composition determination, the contamination overlayer was assumed to consist of graphite [10]. For the cross sections σ_i , the theoretical values of Scofield were used [29] and for the IMFP's, the TPP-2M algorithm was used [30, 31]. The IMFP's and densities are summarized in Table 1. The calculations were started with an (arbitrary low) value of 0.01 nm for the contamination overlayer thickness and the iteration was stopped when the calculated intensity ratios (Eqs. 4 and 7) differed from the experimental by less than $1 \cdot 10^{-8}$.

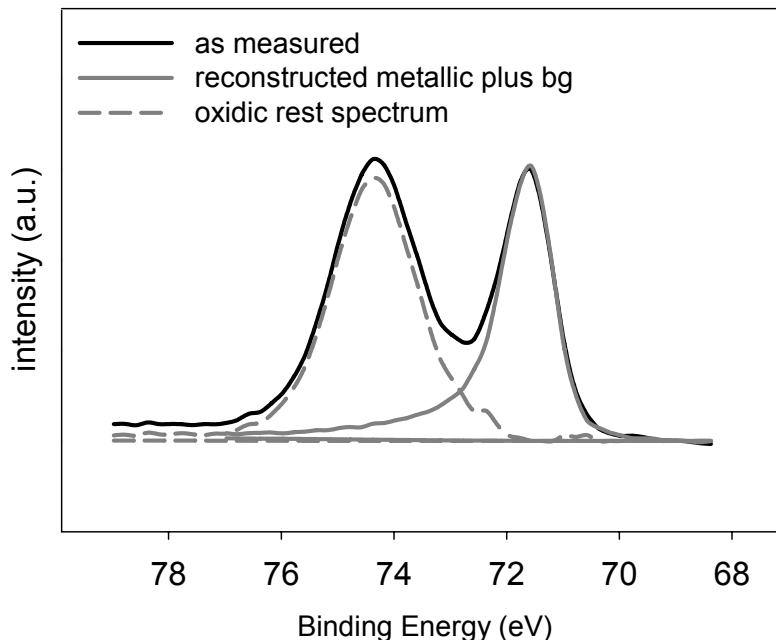


FIG. 2. Al $2p$ spectrum, resolved into a metallic and oxidic component for the evaporated and oxidised aluminium. In the spectrum of the oxidised sample, the metallic main peak (measured from a clean reference) is reconstructed plus its associated background and high binding energy tail (constructed using a Doniach-Sunjic lineshape) (see also [27, 28]).

TABLE 1. Densities and inelastic mean free paths (IMFP's) used in the determination of the oxide composition and thicknesses of the oxide and contamination layers. Densities have been taken from [37] and IMFP have been calculated using the TPP-2M algorithm [30, 31]

material	density (g/cm ³)	IMFP	
		symbol	value (nm)
contamination	2.23	$\lambda_{\text{C1s}}^{\text{cont}}$	2.30
		$\lambda_{\text{Al2p,met}}^{\text{cont}}$	2.69
		$\lambda_{\text{Al2p,ox}}^{\text{cont}}$	2.69
aluminium oxide	3.50	$\lambda_{\text{O1s,ox}}^{\text{cont}}$	1.83
		$\lambda_{\text{Al2p,met}}^{\text{ox}}$	2.76
		$\lambda_{\text{Al2p,ox}}$	2.75
aluminium	2.70	$\lambda_{\text{O1s,ox}}^{\text{ox}}$	1.91
		$\lambda_{\text{Al2p,met}}$	2.22

Oxygen-functionalised contamination correction

The contamination overlayer on top of the oxide layer often also contains oxygen and hydroxyl-functionalized carbon molecules (e.g. alcohols, carboxyls, esters and carbonates). These species will also give a contribution to the O *1s* peak intensity. Neglecting this contribution may lead to significant errors when determining the oxide layer composition and its fraction of hydroxyls. The C *1s* peak was resolved into three components, characteristic of C-O, O-C=O and C-C/C-H species [4, 16, 32]. In Fig. 3, an example of a C *1s* peak and the resolved components is shown. The intensity contribution to the O *1s* peak of these resolved C-O and O-C=O components was then determined using the intensity yield ratio between carbon and oxygen which is 2.5 [4, 32]. For the *curve-fitting* of the O *1s* peak, the contributing intensity was subtracted from the resolved OH component, which approximately has the same binding energy as the oxygen and hydroxyl-functionalized carbon molecules [2, 4, 16, 32]. For the *O/Al atomic ratio determination*, the contributing intensity was subtracted from the integrated O *1s* photoelectron intensity. The maximum correction that had to be applied to the O *1s* peak intensity for the (freshly prepared) oxide layers studied was low and around 5%.

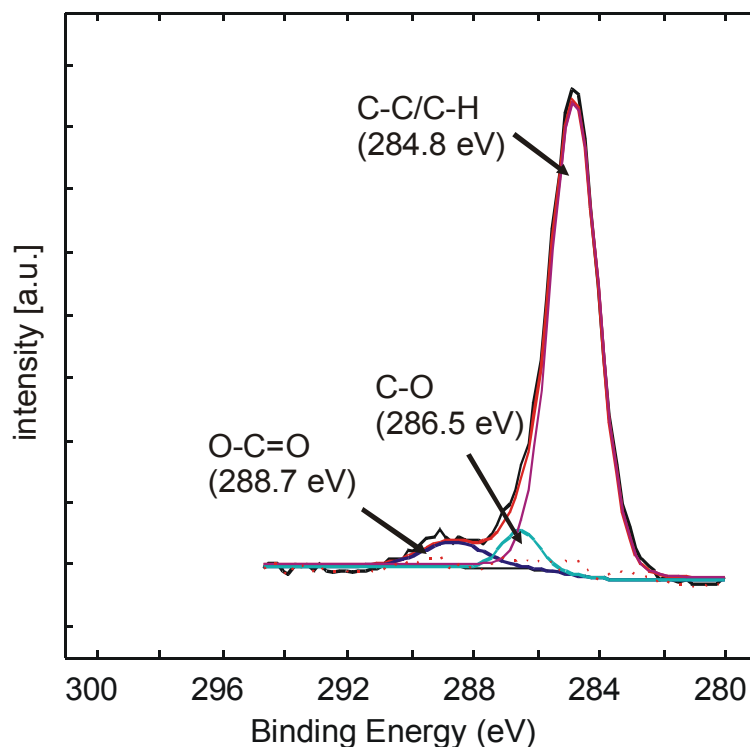


FIG. 3. C $1s$ photoelectron peak as measured on a vacuum evaporated and oxidised type of aluminium at a detection angle of 15 degrees. The constituting components in the peak were resolved by curve-fitting.

3.3. Results

3.3.1. O/Al atomic ratio of the oxide layers as determined from photoelectron intensities

The composition, oxide and contamination layer thicknesses of the individual oxide layers were determined using the procedure discussed in Section 2. The results are summarized in Table 2. The composition of the oxide layers are given in terms of an O/Al atomic ratio, obtained from $O/Al = (1-n_{Al})/n_{Al}$.

For the evaporated, acid and alkaline pretreated aluminium type of oxide layers, the calculations were performed using Eqs. 2, 3 and 4. The pseudoboehmite oxide has a relatively thick oxide layer and thus no detectable Al $2p$ metal component was observed. To determine the O/Al atomic ratio for this oxide, Eqs. 6 and 7 were used. For the anhydrous amorphous aluminium oxide, which does not contain a contamination overlayer, the O/Al atomic ratio was determined using only Eqs. 3 and 4, while setting d_{cont} to zero.

All types of oxides, except the anhydrous aluminium oxide, showed oxidic rest spectra (i.e. spectrum obtained after subtraction of the reconstructed metallic peak) with a single symmetrical Al $2p$ oxidic peak. Also the FWHM's

(full widths at half maxima) which were in the 1.70-1.90 eV range does not suggest the presence of several components [33, 34]. Only for the pseudoboehmite oxide a larger peak width was observed, probably due to charging effects. For the anhydrous amorphous oxide, an additional component was however present, which is due to a minor amount of an aluminium-enriched surface oxide. This is discussed in detail in another work [11, 12]. Both oxidic components were included in the determination of the O/Al atomic ratio for this oxide.

3.3.2. Oxide layer hydroxyl fraction as determined by curve-fitting of the O 1s peak

The fraction of hydroxyls for the individual oxide layers as determined by curve-fitting of the O 1s peak using the constrained procedure (cf. Section 2) are summarized in Table 3. The O 1s peak of the anhydrous, amorphous aluminium oxide could be described accurately using only one component, corresponding to O²⁻. The O 1s peaks of all ambient-exposed oxide layers could be described accurately using two components, corresponding to OH⁻ and O²⁻ respectively. Only for the pseudoboehmite oxide, a small third peak was required, which corresponds to H₂O. An example of the resolved OH⁻ and O²⁻ contributions to the measured O 1s peak is shown in Fig. 4, for an evaporated and oxidised

TABLE 2. O/Al atomic ratio, contamination layer and oxide layer thickness of the studied oxide layers as determined from the resolved Al 2p, O 1s and C 1s photoelectron intensities. The results are obtained from spectra measured at the 45 degrees take-off angle with respect to the sample surface.

type of oxide	contamination layer thickness (nm)	oxide layer thickness (nm)	O/Al atomic ratio (-)
anhydrous am. aluminium oxide	-	0.72	1.53
evaporated and oxidised aluminium	0.14	1.60	1.62
acid pretreated aluminium	0.34	2.39	1.70
alkaline pretreated aluminium	0.41	5.03	1.77
pseudoboehmite	0.22	> 9	2.27
estimated error	± 0.02	± 0.02	± 0.02

aluminium type of oxide at both take-off angles. The Gauss-Lorentz ratio of the fitted components was in the 0.85 - 0.95 range and the FWHM's in the 2.0 - 2.3 eV range with the pseudoboehmite oxide showing the largest values, which is probably due to charging effects. The spread in the determined hydroxyl fractions for different samples of a certain type of oxide was determined to be around 0.02. All ambient-exposed oxide layers contain hydroxyls to different extents with the surface regions being more enriched with hydroxyls than the bulk, as evidenced from the angle-resolved measurements; see Table 3.

At the 15 degrees take-off angle, more of the surface region of the oxide layer is being probed as compared to the 45 degrees take-off angle. This agrees well with results found by others using other measuring techniques [35]. For pseudoboehmite such an enrichment is not observed, because this oxide is known to have a homogenous AlOOH composition throughout the thickness [13, 14]. The binding energies corresponding to the resolved O^{2-} , OH^- and H_2O components are also listed in Table 3. The binding energies of the O^{2-} component are found within a narrow range of 530.9 – 531.1 eV and for the OH^-

TABLE 3. Hydroxyl fraction and binding energies corresponding to O^{2-} and OH^- components of the aluminium oxide layers as obtained from curve-fitting of the O 1s peaks (see text for details).

type of oxide	take-off angle (deg)	OH^- fraction (-)	O^{2-} BE (eV)	OH^- BE (eV)
anhydrous am. aluminium oxide	45	0.00	530.9	-
evaporated and oxidised	45	0.10	531.0	532.4
	15	0.21	531.1	532.4
acid pretreated aluminium	45	0.21	531.0	532.4
	15	0.35	531.0	532.4
alkaline pretreated aluminium	45	0.30	531.0	532.4
	15	0.43	530.9	532.3
pseudoboehmite	45	0.49	530.5	532.0
		0.01 H_2O		533.5
	15	0.47	530.4	531.8
		0.04 H_2O		533.7
estimated error		± 0.01	± 0.05	± 0.05

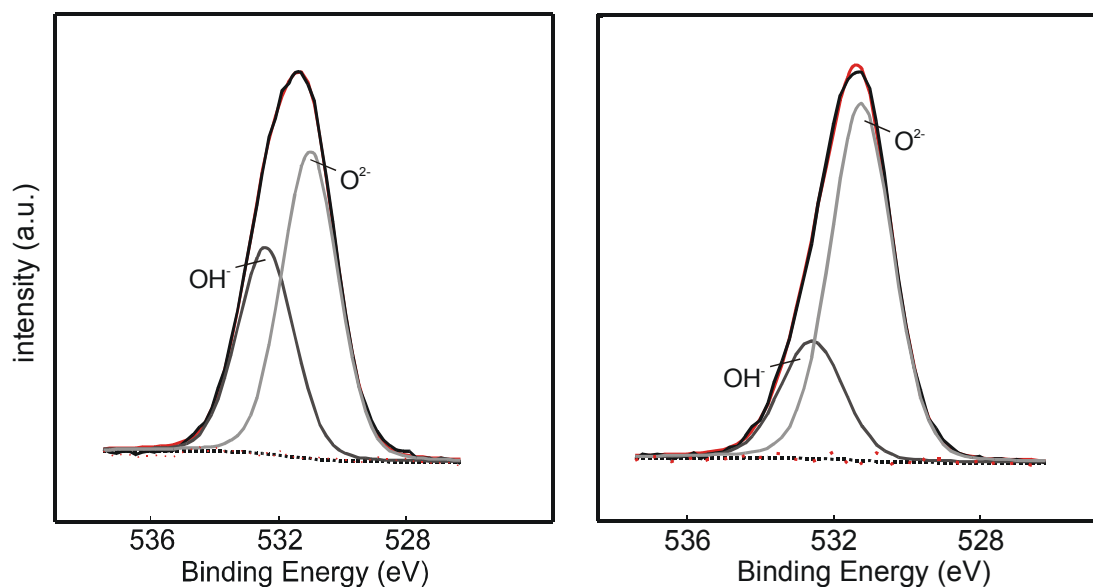


FIG. 4. Resolving the O $1s$ peaks into an O^{2-} and OH^- component by linear least square (LLS) curve-fitting using Gauss-Lorentz shape functions after subtraction of a Shirley-type background. Spectra were obtained for the acid pretreated aluminium at 15 degrees (left) and 45 degrees (right) take-off angles with respect to the sample surface.

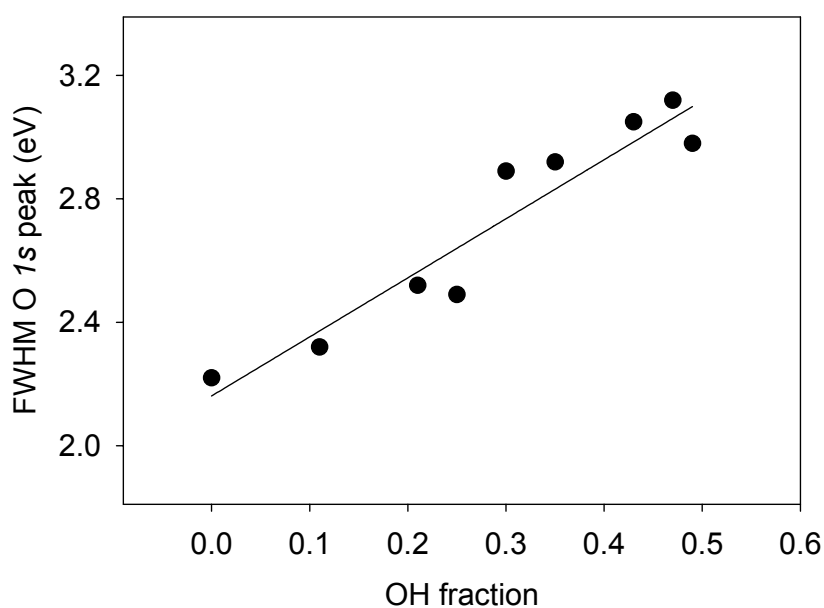


FIG. 5. O $1s$ peakwidth (FWHM) plotted versus the hydroxyl fraction as determined from curve-fitting of the O $1s$ spectra, measured for the different types of aluminium oxides.

within a narrow range of 532.3 – 532.4 eV. However, only the binding energies of the O^{2-} and OH^- components for the pseudoboehmite type of oxide are lower: 530.5 and 531.9 eV respectively. The difference between the OH^- and O^{2-} components binding energies lies for all oxides within a small range of 1.3-1.4 eV. The values for the peak component separations and positions are well in

agreement with the results found by others [2, 5, 6, 36]. For the oxides studied, the trend of the hydroxyl fraction determined from curve-fitting was found to correlate with the O *1s* peakwidth.

This is shown in Fig. 5, in which the FWHM of the O *1s* peak is plotted versus the hydroxyl fraction as determined from curve-fitting of the O *1s* peak, for all oxides at both take-off angles. An alternate explanation for the observed peak broadening can also be charging [16, 17], but the applied charging shifts were comparable for the different oxides and only the pseudoboehmite oxide required a larger value. These results suggest that the O *1s* peakwidth can serve as a first assessment of the amount of hydroxyls.

3.4. Discussion

The composition of the various aluminium oxide layers has been determined in terms of an O/Al atomic ratio and a hydroxyl fraction. The O/Al atomic ratio is determined from the resolved photoelectron intensities using Eqs. 2-7 while the hydroxyl fraction is determined from curve-fitting; see Tables 2 and 3 respectively.

Although the O/Al atomic ratio and hydroxyl fraction are related to each other, their values have been obtained from independent methods. A linear relation however exists between the hydroxyl fraction and the O/Al atomic ratio. The hydroxyl fraction of an anhydrous aluminium oxide (Al_2O_3) is zero and it has an O/Al atomic ratio of 1.5 while the hydroxyl fraction of crystalline boehmite (AlOOH) is 0.5 and it has an O/Al atomic ratio of 2.0. This linear relationship allows a direct comparison between the results as obtained in this study. In Fig. 6, the experimentally determined O/Al atomic ratio is plotted versus hydroxyl fraction for the different studied oxide layers, together with a line corresponding to the linear relationship between the two parameters. An excellent correlation is evident between the O/Al atomic ratio and hydroxyl fraction as obtained with the two different methods. Only for the pseudoboehmite oxide the determined O/Al atomic ratio and the hydroxyl fraction do not match (cf. Fig. 6). This discrepancy can be explained from the fact that the pseudoboehmite oxide is porous and the surface of the layer is rough [13, 14], which is not the case for the other types of oxides studied. Due to this, the pseudoboehmite oxide does not satisfy the conditions for determining the O/Al atomic ratio using Eqs. 2-7, (i.e. a flat and homogeneous oxide layer). This likely results in an incorrectly determined O/Al atomic ratio.

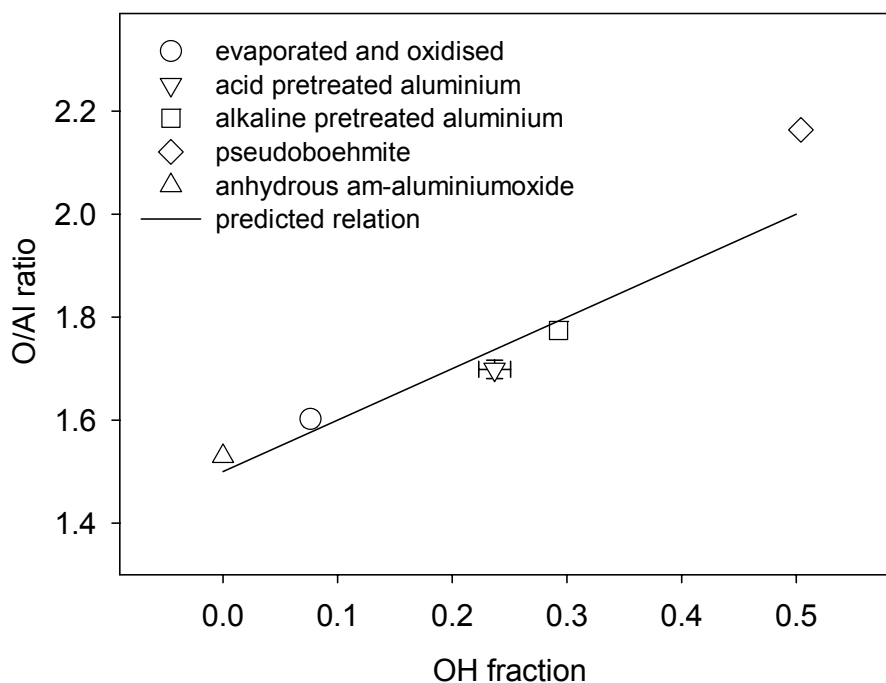


FIG. 6. Comparison between O/Al atomic ratios as determined from photoelectron intensities and hydroxyl fractions from curve fitting of the photoelectron spectra as measured for the different types of aluminium oxide layers. The solid line represents the relation predicted between the O/Al atomic ratio and hydroxyl fraction for different samples of the same oxide. The error margin, corresponding to the spread of the values as determined for different samples of the same type of oxide, is for most oxides smaller than the symbol size.

3.5. Conclusions

The O/Al atomic ratios, oxide and contamination film thicknesses were determined simultaneously from measured PZL photoelectron intensities for the differently prepared aluminium oxide layers. The composition of the oxide layer prepared and analysed in vacuum corresponds to stoichiometric aluminium oxide, i.e. the O/Al atomic ratio equals about 1.5. The O/Al atomic ratio is higher for ambient exposed aluminium and those pretreated in acidic or alkaline solutions. The highest O/Al atomic ratio (about 2.3) is observed for a pseudoboehmite oxide layer, produced by immersion of aluminium in boiling water. The values for the O/Al atomic ratio are consistent with the hydroxyl fractions as determined from curve-fitting of the O $1s$ peak. A linear relation exists between O/Al ratio and the hydroxyl fractions of the studied oxide layers. Also, a linear relation is observed between the hydroxyl fraction and the

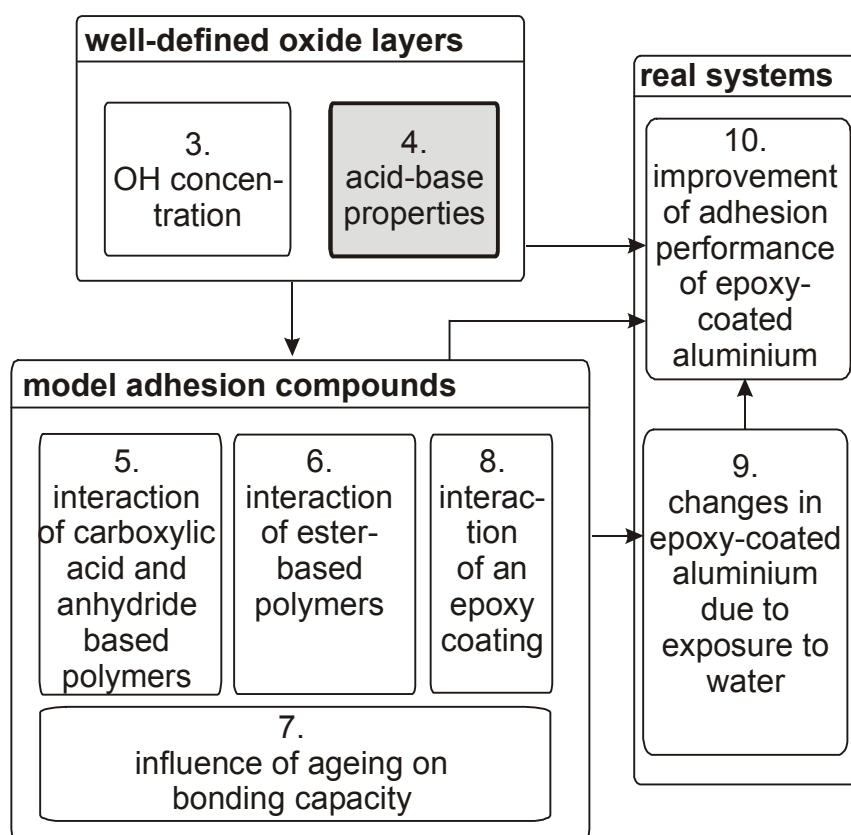
O *1s* peakwidth. The O *1s* binding energies of the O²⁻ and OH⁻ components in the O *1s* peak for the oxide layer prepared by oxidising aluminium in vacuum, acid or alkaline solutions are found in the relatively narrow ranges of 530.9 – 531.1 eV and 532.3 – 532.4 eV respectively. Compared with these values, the pseudoboehmite type of oxide shows about 0.5 eV lower binding energies. From angle-resolved measurements it could be derived that most of the oxides are more enriched in hydroxyls towards the surface region.

References

1. Bolger, J.C.; Michaels, A.S. *Interface conversion coatings for polymeric coatings* Elsevier: New York, 1967.
2. McCafferty, E.; Wightman, J.P. *Surface and Interface Analysis* 1998, *26*(8), 549—564
3. Barthes-Labrousse, M.G., *Vacuum* 2002, *67*(3-4), 385-392
4. Olefjord, I.; Nylund, A. *Surface and Interface Analysis* 1994, *21*(5), 290—297
5. Alexander, M.R.; Thompson, G.E.; Beamson, G. *Surface and Interface Analysis* 2000, *29*(7), 468—477
6. Nylund, A.; Olefjord, I. *Surface and Interface Analysis* 1994, *21*(5), 283—289
7. Cordier, F.; Ollivier, E. *Surface and Interface Analysis* 1995, *23*(9), 601—608
8. Lopez, S.; Petit, J.P.; Dunlop, H.M.; Butruille, J.R.; Tourillon, G. *Journal of the Electrochemical Society* 1998, *145*(3), 829—834
9. McCafferty, E.; Wightman, J.P.; Cromer, T.F. *Journal of the Electrochemical Society*, 1999, *146*(8), 2849—2853
10. Evans, S. *Surface and Interface Analysis* 1997, *25*(12), 924—930
11. Jeurgens, L.P.H.; Sloof, W.G.; Tichelaar, F.D.; Mittemeijer, E.J. *Surface Science* 2002, *506*(3), 313—332
12. Jeurgens, L.P.H.; Sloof, W.G., Tichelaar, F.D.; Mittemeijer, E.J. *Thin Solid Films* 2002, *418*(2), 89—101
13. Alwitt, R.S. *The aluminium-water system*. Dekker: New York, 1976.
14. Wefers, K.; Misra, C. *Oxides and hydroxides of aluminium*. Alcoa Technical Paper no. 19, 1987
15. American Society for Testing and Materials. *Surface and Interface Analysis* 1991, 17, 889
16. Seah, M.P.; Briggs, M.D. (eds). *Practical surface analysis*. vol. 1., 2nd edition, Wiley New York, 1990.
17. Barr TL. *Thin Solid Films* 1994, *253*(1-2), 277—284
18. Barrie A. *Chemical Physics Letters* 1973, *19*(1), 109—113
19. Eberhardt, W.; Kunz, C. *Surface Science* 1978, *75*, 709—720
20. Bianconi, A. *Physical Review B* 1979, *19*(6), 2837—2843
21. Zemek, J.; Hucek, S.; Jablonski, A.; Tilinin, I.S. *Journal of Electron Spectroscopy* 1995, *76*, 443—447
22. Powell, C.J.; Jablonski, A.; Tilinin, I.S.; Tanuma, S.; Penn, DR. *Journal of Electron Spectroscopy* 1999, *99*, 1—15
23. Powell, C.J.; Jablonski, A. *Journal of Vacuum Science and Technoly A* 2001, *19*(5), 2604-2611
24. Powell, C.J.; Jablonski, A. *Journal of Electron Spectroscopy*, 2001, *114*, 1139-1143
25. Werner, W.S.M. *Surface and Interface Analysis*, 1995, *23*(10), 696
26. Gunter, P.L.J.; Niemantsverdriet, J.W. *Applied Surface Science* 1995, *89*(1), 69—76
27. Jeurgens, L.P.H.; Sloof, W.G.; Tichelaar, F.D.; Borsboom, C.G.; Mittemeijer, E.J. *Applied Surface Science* 1999, *144-145*, 11-15
28. Jeurgens, L.P.H.; Sloof, W.G.; Borsboom C.G.; Tichelaar, F.D., Mittemeijer E.J. *Applied Surface Science* 2000, *161*(1-2), 139-148
29. Scofield, J.C. *Journal of Electron Spectroscopy* 1976, *8*, 129—137
30. Tanuma, S.; Powell, C.J.; Penn, D.R. *Surface and Interface Analysis* 1993, *21*(3), 165—176
31. Tanuma, S.; Powell, C.J.; Penn, D.R. *Surface and Interface Analysis* 1988, *11*(11), 577—589
32. Beamson, G.; Briggs, M.D. *High resolution XPS spectra of organic polymers* Wiley New York, 1992.
33. Ebina, T.; Iwasaki, T.; Chatterjee, A.; Katagiri, M.; Stucky, G.D. *Journal of Physical Chemistry B* 1997, *101*(7), 1125—1129
34. Barr, T.L. *Journal of the Chemical Society: Faraday Transactions* 1997, *93*(1), 181—186
35. Aexander, M.R.; Beamson, G.; Bailey, P.; Noakes, T.C.Q.; Skeldon, P.; Thompson, G.E.; Beamson, G. *Surface and Interface Analysis* 2003, *14*(3), 408-412
36. Strohmeier, B.R. *Surface and Interface Analysis* 1990, *15*, 51—56
37. CRC Handbook of Chemistry and Physics, 81st edition. CRC Press Cleveland

CHAPTER 4.

ACID-BASE CHARACTERISATION OF ALUMINIUM OXIDE SURFACES USING XPS ¹



¹ This chapter was published as a scientific paper:
J. van den Brand, P.C. Snijders, W.G. Sloof, H. Terryn, J.H.W. de Wit,
Journal of Physical Chemistry B, 108(22), 6017-6024, 2004

Synopsis

The localised acid-base properties of the aluminium oxide surface play an important role in determining which types of interactions can occur with functional groups of the organic overlayer. As the X-ray photoelectron spectroscopy (XPS) technique directly probes the electronic structure of a material, it is highly suitable for studying the localised acid-base properties of the oxide layer. In this chapter, the localised acid-base properties of the O, OH and Al sites on the surfaces of the oxide layers of 5 differently prepared aluminium substrates are studied using XPS. This same set of substrates is used throughout this thesis and was in Chapter 3 studied with respect to the amount of hydroxyls. To determine the localised acid-base properties, Al 2p and O 1s electron core-level binding energy shifts are evaluated while taking into consideration the factors that contribute to these shifts. It is found that for structurally comparable oxides, the core level binding energy shifts can be directly evaluated to study changes in acid-base properties. Although different methods are followed to prepare the substrates, their oxide layers in fact have the same localised acid-base properties. Only the pseudoboehmite layer, made by boiling of aluminium in water, shows more basic OH, O and Al sites. This can be ascribed to a fundamentally different structure for this oxide as compared to the other oxides.

4.1. Introduction

The acid-base properties of an oxide surface play a major role in interfacial reactions and are therefore important in fields like catalysis, adhesion, corrosion and wetting [1-4]. This macroscopic property is on the atomic scale determined by a large number of different reactive sites, which each have their own acid-base properties. The oxide surface can be considered to consist of three different types of sites. The O anions can act as electron-donating Lewis base sites, incompletely coordinated cations as electron-accepting Lewis acid sites and the OH anion can act either as a Lewis acid or base, but also as proton-exchanging Brønsted acid-base sites [4]. For a localised description of the acid-base events that can occur on the oxide surface, an understanding of the acid-base properties of these separate sites is required. The X-ray photoelectron spectroscopy (XPS) analysis technique enables the study of these acid-base properties. It probes the electronic structure of a material and specifically enables to distinguish separate sites related to the elemental constituents. XPS

is widely used to determine valence state of ions [5], nature of bonding (e.g. ionicity/covalency) [6-8] and acid-base properties of oxides [3, 9-10].

In this work, the localised acid-base properties are investigated of the oxide layers on a set of five differently pretreated aluminium substrates. These layers were also investigated in Chapter 3 and represent typical layers that can develop on aluminium surfaces. They are frequently encountered in fields like adhesion, lithographic plates [11-13] and as models to investigate alumina-based catalysts [14]. The oxide layers studied were produced by oxidising of aluminium in vacuum, with an alkaline and acidic pretreatment, and in boiling water. To evaluate the localised acid-base properties of their Al, O and OH sites, the Al $2p$ and O $1s$ electron core-level binding energies are evaluated, while taking into consideration the initial and final state effects in the photoelectron emission process and the O $1s$ peak is resolved into the constituting OH and O components. To study the oxide layer and chemistry at the surface and the interior of the layers, angle-resolved XPS was performed. To our knowledge, such a detailed analysis of the correctness of the use of binding energies for evaluating the acid-base properties of the Al, O and OH sites has not been performed before.

4.2. Interpretation of XPS core level binding energies

According to the simple electrostatic potential model introduced by Siegbahn *et al* [15], the binding energy shift $\Delta E_B(A)$, observed for the core level of an atom A in two different materials can be described with [5, 15-16]:

$$\Delta E_B(A) = k\Delta q + \Delta V_M - \Delta R^{ea} \quad (1)$$

In this equation, Δq is the change in effective electronic charge on the A atom with k being a constant. The ΔV_M term is the change in the Madelung potential, which describes the electrostatic interaction between the single atom A and charges on the other atoms grouped in the lattice around A . The term ΔR^{ea} arises from the extra-atomic charge rearrangement or relaxation that occurs in response to the core hole created in the photoelectron process. Eq. 1 can be divided into two parts. The first part ($k\Delta q + \Delta V_M$) represents the *initial state* chemistry of the photoionised atoms/ions and is the important parameter for the localised acid-base properties considered here. The second part, ΔR^{ea} , represents the *final state* contribution to the binding energy due to the photoionisation process in the measuring technique. The final state and Madelung potential contributions to the binding energies are often neglected

and k is assumed to be constant in XPS analysis of oxides [5, 9]. A direct relation between the change in electronic charge on the ions or atoms and measured binding energy shift is then obtained, i.e. $\Delta E_B(A) = k\Delta q$. For a cation ($q > 0$) a more positive charge will then result in an higher binding energy, while for an anion ($q < 0$), a more negative charge will result in a lower binding energy. This approach often leads to correct results [17, 18], but in some cases it was found that either the Madelung potential or extra-atomic relaxation showed a dominant contribution to the binding energy shifts [16, 19-20].

Using the Auger-parameter concept introduced by Wagner [21], the contribution of the final state effects to the binding energy can be evaluated. The Auger-parameter is defined as $\alpha' = E_k(C^*C^*C^{**}) + E_B(C)$ [16, 22] with $E_k(C^*C^*C^{**})$ being the kinetic energy of an Auger transition involving the C^* , C^* and C^{**} core electron levels. For a shift in this Auger-parameter $\Delta\alpha'$ [23]:

$$\Delta\alpha' = 2\Delta R^{ea} \quad (2)$$

which can therefore be used to evaluate the effect of changes in extra-atomic relaxation. The Auger-parameter is insensitive to charging effects and Fermi level changes because the effects cancel out in the calculation [16]. The Auger-parameter is considered to be a sensitive indicator to study changes in local environment of the core ionised atom [22, 24-27]. In addition to the Auger-parameter, also a parameter can be derived which corresponds to the initial state part of the binding energy (cf. Eq. 1). This initial state parameter, denoted as β , is defined as $[E_k(C^*C^*C^{**}) + 3E_B(C)]$ and a shift in this parameter corresponds to [16]:

$$\Delta\beta = 2\Delta[V_M + kq] \quad (3)$$

and can therefore be used to evaluate the effect of changes in the initial state chemistry. In contrast with the Auger-parameter, this initial state parameter is sensitive to errors in charging corrections and work function changes and an error in one of these will result in a twice as large error in the calculated values. The Madelung potential contribution to the initial state parameter can be calculated if detailed structural knowledge of the atomic arrangement of the considered oxide is available [10, 16, 20, 24]. A direct separation of the contributing terms to the initial state parameter is then possible. For most amorphous aluminium oxides – as studied in this work – such detailed structural information is not available. However, an alternative approach can be followed which allows a direct evaluation of the electronic charge q on the O

anion in the oxide. Using an electrostatic model, Ascarelli *et al.* [28] demonstrated that the Auger peak separation $E_k(\text{O } KL_{23}L_{23}) - E_k(\text{O } KL_1L_{23})$ is a direct measure of this electronic charge, independent of Madelung potential and relaxation effects. Increases in this peak separation indicate an increasing electronic charge on the O anion. For a large set of different aluminium oxides it was found that this peak distance indeed correctly described trends in ionicities [29]. Similar approaches were followed by others [30,31]. Since the Fermi-level is used as a reference for the energy of the emitted photoelectrons in XPS, a change of the Fermi-level will cause a homogeneous binding energy shift of the core electron peaks [5, 32-33]. This Fermi-level shift is not included in Eq. 1. Such a Fermi-level shift can be caused by impurities, defects or a non-stoichiometric composition in non-conductive materials; which all introduce states in the band gap.

4.3. Experimental details and data evaluation

4.3.1. Oxide layers and experimental details

In this work, the same set of five differently prepared aluminium substrates were investigated as in Chapter 3. The preparation procedure for the substrates is given in paragraph 3.2.1, page 23. The experimental details of the XPS measurements are given paragraph 3.2.2, page 25.

4.3.2. XPS Analysis and data evaluation

Data evaluation

For the determination of the oxidic Al $2p$ core level binding energies and Al $KL_{23}L_{23}$ kinetic energies, the measured spectra were resolved into an oxidic and a metallic component in their respective binding energy regions. A procedure was used in which the metallic peak (obtained from a clean aluminium sample without an oxide layer) plus its associated Tougaard background and including the tail towards higher binding energies is reconstructed in the measured spectrum of the oxidised sample. This procedure is discussed in detail in paragraph 3.2.3 and also elsewhere [34, 35]. For the O $1s$, O KLL and C $1s$ peaks, the binding energy positions were determined after subtraction of a simple Shirley-type background. Since the spectra only contain a small contribution of inelastically scattered electrons as compared to the intensity of the main peak, the result was found to be insensitive to the choice of type of

background subtraction [34]. The various binding and kinetic energy positions were determined accurately by fitting of a third degree polynomial function through the top of the respective peaks. Curve-fitting of the O *1s* photoelectron peak to determine the fraction of hydroxyls was performed in the 526-538 eV binding energy region, using a constrained fitting procedure in which the widths and shapes (mixed Gauss-Lorentz function) for the different fit components in the peak were allowed to change. However, the change was restricted to be the same for all components. No restrictions were imposed on the binding energy positions of the components. The procedure is discussed in detail in the previous chapter. In the previous chapter, an analysis was performed of the layer thicknesses of the studied oxides. All thicknesses were found to be close to or much larger than 1 nm. For this reason, a contribution to the binding energies due to polarization of the underlying metal is not expected [28]. For both Al and O, Auger-parameters α'_{Al} and α'_{O} have been calculated where α'_{Al} has been calculated as $[E_{\text{k}}(\text{Al } KL_{23}L_{23}) + E_{\text{B}}(\text{Al } 2p)]$ and α'_{O} as $[E_{\text{k}}(\text{O } KL_{23}L_{23}) + E_{\text{B}}(\text{O } 1s)]$. The initial state parameters β_{Al} and β_{O} have been respectively calculated as $[E_{\text{k}}(\text{Al } KL_{23}L_{23}) + 3 E_{\text{B}}(\text{Al } 2p)]$ and $[E_{\text{k}}(\text{O } KL_{23}L_{23}) + 3 E_{\text{B}}(\text{O } 1s)]$.

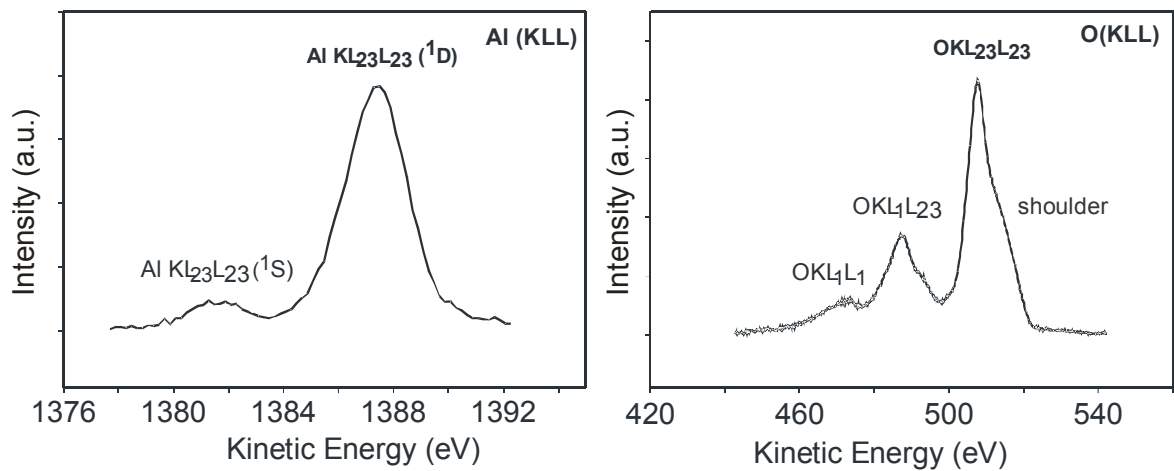
4.4. Results

4.4.1. Measured core level binding energies and Auger kinetic energies

The measured O *1s*, Al *2p* binding energies and O *KL₂₃L₂₃*, Al *KL₂₃L₂₃* kinetic energies of the 5 different types of studied oxides at the two different take-off angles are summarized in Table 1. The binding energy positions of both the O *1s* and Al *2p* peaks correspond well to values reported for comparable types of amorphous aluminium oxides [36-41]. A typical example of the Al *KLL* and O *KLL* Auger electron transition spectra is shown in Fig. 1 with the associated peak designations. In Table 1 also the full-width at half maxima (FWHM) of the O *1s* and Al *2p* peaks are listed. The different oxides clearly show variations in FWHM of the O *1s* peak, but not in the Al *2p* peak. The higher Al *2p* peakwidth for the anhydrous amorphous oxide is due to a surface oxide component at a lower binding energy, as discussed in detail elsewhere [26]. For the pseudoboehmite oxide, the increase in Al *2p* binding energy is likely due to charging effects. The increase in O *1s* peakwidth can be ascribed entirely to the increase of the hydroxyl concentrations in the oxides, see the previous chapter. The different components constituting the O *1s* peak, corresponding to O, OH and for pseudoboehmite also H₂O, were resolved by curve-fitting.

TABLE 1. Measured O $1s$, Al $2p$ core level binding energies and O $KL_{23}L_{23}$ and Al $KL_{23}L_{23}$ kinetic energies of the various aluminium oxides

type of oxide layer	angle (deg)	O $1s$ BE (FWHM) (eV)	Al $2p$ BE (FWHM) (eV)	E(Al-O) (eV)	O $KL_{23}L_{23}$ KE (eV)	Al $KL_{23}L_{23}$ KE (eV)
anhydrous amorphous oxide	45	531.0 (2.2)	74.3 (2.1)	456.7	509.0 (6.5)	1387.6 (2.2)
	15	531.1 (2.5)	74.3 (1.8)	456.8	508.5 (6.8)	1387.6 (2.1)
evaporated and oxidised	45	531.2 (2.3)	74.4 (1.8)	456.8	508.5 (6.8)	1387.6 (2.1)
	15	531.1 (2.5)	74.3 (1.8)	456.8	508.5 (7.0)	1387.6 (2.2)
acid pretreated	45	531.4 (2.5)	74.6 (1.9)	456.9	508.3 (6.9)	1387.2 (2.3)
	15	531.4 (2.9)	74.4 (1.9)	457.0	508.5 (8.0)	1387.3 (2.2)
alkaline pretreated	45	531.5 (2.9)	74.7 (1.9)	456.8	508.3 (7.4)	1386.9 (2.2)
	15	531.6 (3.1)	74.6 (1.9)	457.1	508.3 (8.4)	1387.0 (2.1)
pseudoboemite (boiled)	45	531.2 (3.0)	73.9 (2.2)	457.3	508.0 (8.5)	1387.6 (2.6)
	15	531.2 (3.1)	73.9 (2.2)	457.3	507.9 (9.0)	1387.5 (2.6)
estimated error	\pm	0.05	0.05	0.1	0.1	0.1

FIG. 1. Al KLL and O KLL Auger-electron spectra and designations for a pseudoboemite oxide (Shirley-type background subtracted).

The results of this were already discussed in Chapter 3 but for completeness are repeated here. The values of the binding energies of these components and their relative fractions are reported in Table 2.

It was observed that with changing hydroxyl concentration, the intensity of a shoulder on the high kinetic energy side of the O $KL_{23}L_{23}$ transition in the O KLL spectrum also changed. This is illustrated in Fig. 2, where the O KLL spectra are shown for the anhydrous amorphous aluminium, alkaline pretreated aluminium and pseudoboehmite types of oxides. Such a shoulder is more often reported in the literature and has been ascribed to a $KL_{23}m$ transition [42, 43], in which a L_{23} hole on the central O anion is filled by an electron from a metal-like orbital. Other authors, however, associate this phenomenon with hydroxyls in a hydroxide [44], or hydrogen bonding between different hydroxyls [45]. The shoulder has the effect of broadening of the O $KL_{23}L_{23}$ peak. In Fig. 3, the O $KL_{23}L_{23}$ FWHM's are plotted versus the corresponding hydroxyl fractions. The relation between the O $KL_{23}L_{23}$ FWHM and the OH fraction was confirmed by an additional experiment in which a pseudoboehmite oxide was dehydrated in-situ in vacuum at a temperature of 300 °C. The *removal* of the hydroxyls from the oxide (as evidenced by a decreasing OH component in the O $1s$ core level peak) resulted in a significant *reduction* of the shoulder.

TABLE 2. Resolved components in the O $1s$ core level peak by curve-fitting of the various aluminium oxides.

type of oxide layer	angle (deg)	OH fraction (-)	O BE (eV)	OH BE (eV)
anhydrous amorphous oxide	45	0.00	530.9	-
evaporated and oxidised	45	0.11	531.0	532.4
	15	0.21	531.1	532.4
acid pretreated	45	0.25	531.1	532.4
	15	0.35	531.0	532.4
alkaline pretreated	45	0.30	531.0	532.4
	15	0.43	530.9	532.3
pseudoboehmite (boiled)	45	0.49	530.5	532.0
		0.01 H ₂ O		533.5
	15	0.47	530.4	531.8
		0.04 H ₂ O		533.7
estimated error	±	0.05	0.05	0.05

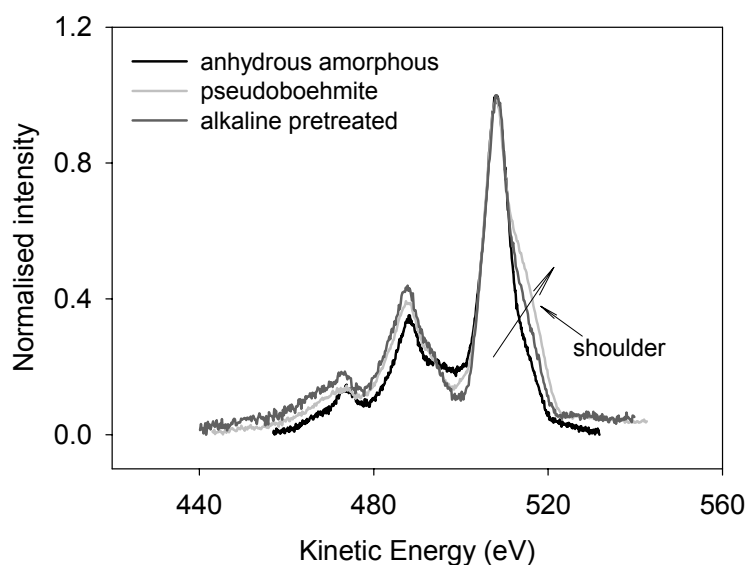


FIG. 2. Measured $OKLL$ spectra for anhydrous, alkaline pretreated and pseudoboehmite oxides after subtraction of a Shirley-type background. (Spectra are shifted to give the same $O KL_{23} L_{23}$ kinetic energy).

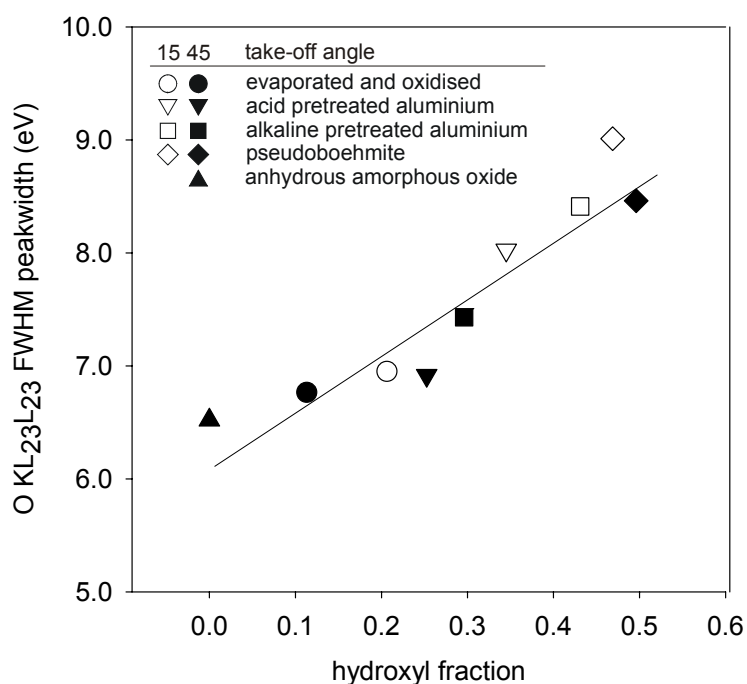


FIG. 3. Full-width at half maximum (FWHM) of $O KL_{23}L_{23}$ peak versus hydroxyl fraction as determined from curve-fitting of the $O 1s$ core level for the various aluminium oxides, at 15 and 45 degrees take-off angle.

As a clear correlation is observed between the hydroxyl fractions and the $O KL_{23}L_{23}$ peakwidth, the major part of this shoulder is not associated with a $KL_{23}m$ transition, but is related to the hydroxyls in the oxide layer.

TABLE 3. Al and O Auger-parameters for the various aluminium oxides. The corresponding core level binding energies are listed in Table 1.

type of oxide layer	angle (deg)	α'_{Al} (eV)	α'_{O} (eV)
anhydrous amorphous oxide evaporated and oxidised	45	1461.9	1039.9
	15	1461.9	1039.7
acid pretreated	45	1461.8	1039.7
	15	1461.7	1039.9
alkaline pretreated	45	1461.5	1039.7
	15	1461.4	1039.8
pseudoboehmite (boiled)	45	1461.5	1039.2
	15	1461.4	1039.1
estimated error	\pm	0.1	0.1

4.4.2. Auger parameters

The Auger-parameters α'_{O} and α'_{Al} are considered to evaluate the contribution of the extra-atomic relaxation to the measured core level binding energies (cf. Eq. 2). The Auger-parameters as determined for all oxides at both take-off angles are summarized in Table 3. The various oxides exhibit an almost constant α'_{O} in the narrow 1039.7-1039.9 eV range. The pseudoboehmite oxide shows a significantly lower value of 1039.1-1039.2 eV. These α'_{O} values also do not change significantly when going from the bulk of the oxide layer (45 degrees take-off angle) to more towards the surface region (15 degrees take-off angle). The α'_{O} values must be considered as an average of the chemical environments of the OH and O ions in the oxide layers, because it was not possible to resolve the contribution of these constituents to the O *KLL* peak, see also Ref. [43]. The α'_{O} values for the *amorphous* oxides studied here are not comparable to literature values given for *crystalline* oxides with a similar composition [22]. This is at least in part due to structural differences between the amorphous and crystalline oxides: a gradual transition from amorphous Al_2O_3 to crystalline $\gamma\text{-Al}_2\text{O}_3$ results in a gradual change in the α'_{O} from 1039.9 to 1038.9 eV [27].

The α'_{Al} values of the studied oxides are in the range of 1461.4 - 1461.9 eV. These values also do not change significantly when going from the bulk towards the surface region of the oxide layer. The α'_{Al} value of pseudoboehmite (1461.5 eV) is lower than the value given by Wagner for crystalline boehmite (1461.8

eV) [22] and the values for the other oxides are higher than the value for crystalline γ -Al₂O₃ (1461.8 eV). The α'_{Al} values, however, do correspond well to structurally more comparable amorphous oxide layers. For anhydrous amorphous aluminium oxides, values of 1461.9 eV have recently been obtained [27, 46] and about 0.4 eV lower values have been found for hydroxyl containing oxide layers obtained by oxidation in H₂O/O₂ gas mixtures [42] and ambient-exposed native oxide layers, likely also containing hydroxyls [47]. It appears that there is a trend in which the α'_{Al} values decrease with an increase in hydroxyl concentration in the oxide layers. This can have the effect of lowering the α'_{Al} directly, due to the lower polarisability of the OH as compared to the O anion [48]. However, this conclusion does not appear to be fully justified. Upon removal of hydroxyls from a pseudoboehmite oxide through dehydroxylation by heating at 300 °C in vacuum, see above, the Auger-parameter did not show a significant increase again. Shifts of the α'_{Al} are often explained as changes in coordination number of the Al cations [22]. The presence of different coordination states is expected to show up as a broadening of the Al $KL_{23}L_{23}$ and Al $2p$ peaks [10, 17, 49]. Sometimes curve-fitting of the Al $KL_{23}L_{23}$ peak or Al $2p$ peak is performed to distinguish states with a different coordination [10, 17, 49]. However, such an effect was not observed and all oxides showed an Al $KL_{23}L_{23}$ FWHM in the 2.1-2.3 eV and the Al $2p$ peak in the 1.8-1.9 eV range, with only the pseudoboehmite oxide showing significantly higher values due to charging. The presence of different aluminium coordination states in the oxides can therefore be excluded as a possible explanation for the α'_{Al} shifts. The absence of different coordination states also suggests that the hydroxyls in the alkaline pretreated, acid pretreated and evaporated and oxidised types of oxides are not present in separate Al(OH)₃ or AlOOH units in an 'Al₂O₃ matrix' [40, 50] but rather obtain isolated positions [41] as otherwise mixtures of different coordination states are expected to show up in the Al $2p$ and Al KLL peaks.

The much lower value of the α'_o for the pseudoboehmite oxide, see Table 3, indicates that the local environment around the O anion deviates significantly from the other oxides. In the crystalline boehmite, the Al cations reside in distorted octahedra of O ions. These octahedra are joined to form an interlocking double layer in which the oxygen anions are in a cubic-closed packing but the whole structure is not close-packed [13, 51]. The double layers are linked by hydrogen bonds between hydroxyl ions in neighbouring planes. As compared to the crystalline boehmite, the pseudoboehmite is structurally less well defined and further it has interlamellar water in its structure. As shown in Ref. [27], in the anhydrous amorphous oxide, the short range ordering around

the Al ions is the same as that in crystalline γ -Al₂O₃; i.e. both tetrahedrally and octahedrally coordinated Al ions exist in the same ratio as in the well defined crystalline γ -Al₂O₃. These tetrahedral and octahedral units are stacked without long range order with some excess free volume located in between the units. The local order in the other oxides studied here, most likely resembles that from the anhydrous oxide as indicated by the similar α'_O . Therefore, the deviating pseudoboehmite Auger-parameters are likely caused by the fundamentally different local structure of pseudoboehmite as compared to the other oxides in this study. For this reason, the results of pseudoboehmite will in the following be considered separately from the other oxides.

4.4.3. Initial state parameters

The shifts observed in the measured O *1s* binding energies of the various oxides are fully dominated by initial state effects, because the practically constant O Auger-parameter α'_O (Table 3) implies that the contribution of final state effects (ΔR^{ea} , Table 3 and Eq. 2) is negligible. The total Al *2p* binding energy shift observed is 0.5 eV (Table 1), while the extra-atomic relaxation changes over 0.25 eV but in the opposite direction (Table 3 and Eqs. 1 and 2). This then implies that the shifts observed in the Al *2p* core level binding energies will to some extent also be influenced by final state effects.

The initial state parameters β_{Al} and β_O for respectively Al and O have been determined using the measured electron core level binding energies and Auger electron transition kinetic energies (cf. Eq. 3 and Table 1). In Fig. 4, the measured electron core level binding energies are plotted versus initial state parameters. For both Al and O, the initial state parameter increases with increasing core level binding energies and a linear relationship is observed for both β_O vs. O *1s* and β_{Al} vs. Al *2p*. The initial state parameters of Al and O are composed of a contribution due to the charge q and Madelung potential, cf. Eq. 3. For the O anion, a direct evaluation can be made of the charge q present by considering the $E_k(O KL_{23}L_{23}) - E_k(O KL_L L_{23})$ peak separation [28]. This peak separation increases linearly with the O *1s* core level binding energy for the studied oxides, see Fig. 5. Thus, the O *1s* binding energies are directly related with the surface-averaged charge q present on the anions. According to the work of Ascarelli *et al* [28], the peak separation range $E_k(O KL_{23}L_{23}) - E_k(O KL_L L_{23})$ of 19.7 – 21.0 eV (see Fig. 5) corresponds to a surface-averaged charge q on the anions between about -1.2e for the alkaline pretreated to about -1.7e for the anhydrous amorphous aluminium oxide.

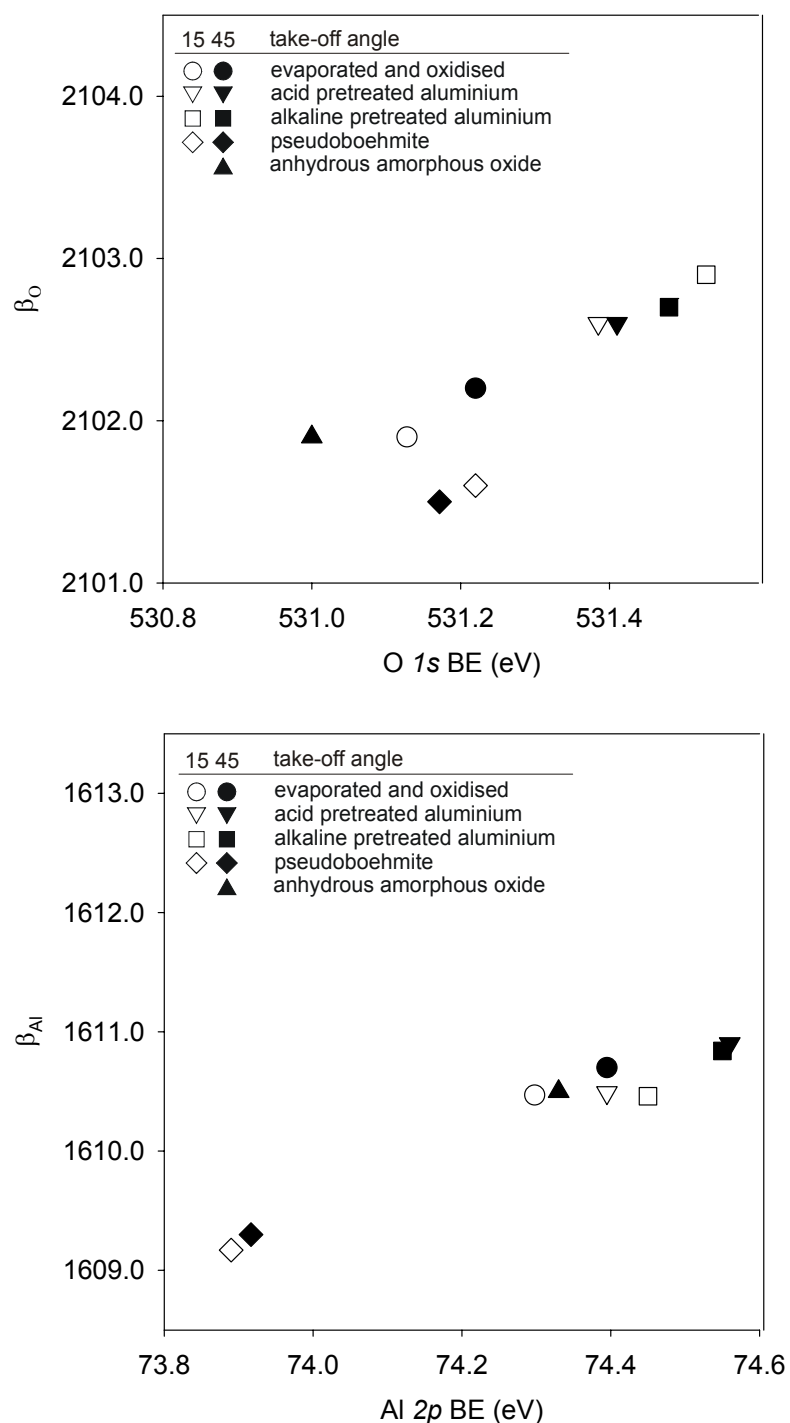


FIG 4. The initial state parameters versus their corresponding core level binding energies for oxygen (top) and aluminium (bottom) for the various aluminium oxides.

In this context, it is noted that the binding energy shifts are not due to changes in Fermi level, as then a change in binding energy would not be reflected in a change in $E_{\text{k}}(\text{O } KL_{23}L_{23}) - E_{\text{k}}(\text{O } KL_1L_{23})$ peak separation and thereby in q . Moreover, the $E(\text{Al } 2p - \text{O } 1s)$ peak separations, often used to

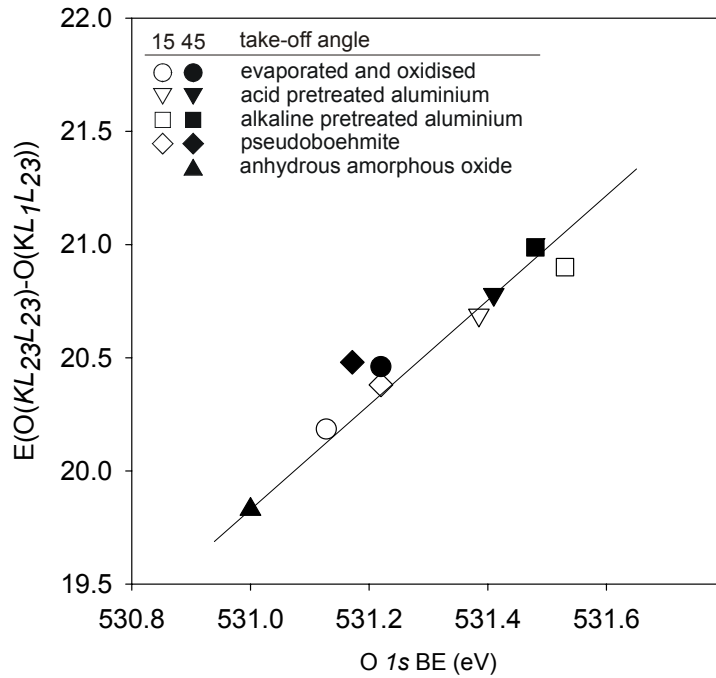


FIG. 5. The distance between the O $KL_{23}L_{23}$ and the O KL_1L_{23} lines versus the O $1s$ core level binding energy for various aluminium oxide layers.

separate Fermi-level shifts from chemical shifts [32, 33], does not show a constant value for the studied oxides, see Table 2. The pseudoboehmite, being structurally different, shows deviating behaviour from the other oxides. It has a much lower α'_O and therefore a lower extra-atomic relaxation contribution to the O $1s$ binding energy, cf. Eq. 2. Also the initial state parameter β_O of the pseudoboehmite oxide is significantly lower than those of the other types of oxides; see Fig. 4. However, the $E_k(O KL_{23}L_{23}) - E_k(O KL_1L_{23})$ versus O $1s$ binding energy values of all oxides, including pseudoboehmite, fall on a straight line, see Fig. 5. Thus, the O $1s$ binding energy also for pseudoboehmite represents the charge q on the oxygen-containing anions (see above). Then, as compared to the other oxides (according to Eq. 1), the lower extra-atomic relaxation contribution must be compensated for by a lower Madelung potential contribution ΔV_M to the O $1s$ binding energy for pseudoboehmite.

4.5. Discussion

Evaluation of the measured core level binding energies (O $1s$ and Al $2p$) and Auger-electron kinetic energies (O KLL and Al KLL) for various aluminium oxides in terms of their initial state (β_{Al} and β_O) and final state (α'_{Al} and α'_O)

parameters was performed. This analysis showed that for the *structurally comparable oxides* as evidenced from the similar value of their Auger-parameter, see Table 3, the O *1s* core level binding shifts *directly* represent changes in the initial state chemistry of the system and do not suffer from final state effects, cf. Fig. 3 and Table 3. Moreover, it was shown that the O *1s* core level binding energy shifts directly represent changes of the surface-averaged charge q present on the O anions and do not suffer from changes of the Madelung potential. The minor Al *2p* core level binding energy shifts also corresponds with changes in the initial state chemistry, cf. Fig. 4, but these binding energy shifts do have a contribution from final state effects, cf. Table 3. It has been demonstrated that the core level binding energy shifts are not due to differences in the Fermi-level of these oxides.

The O *1s* binding energy increases in the order anhydrous oxide < evaporated and oxidised < acid pretreated < alkaline pretreated aluminium, for both take-off angles, see Table 2. This implies that the surface-averaged electronic charge on the anions increases in the same order. The observed increases in O *1s* binding energy can, however, be attributed solely to the increase of the OH component to O *1s* peak, which is present at a 1.3-1.4 eV higher binding energy, see paragraph 4.4.1 and Table 3. The binding energies of the separate components do not vary significantly for the oxides, see Table 2. Further, there are no differences observed in binding energy of the resolved components for the surface region (15 degrees take-off angle) and for the more bulk region of the oxide layer (45 degrees take-off angle). This indicates the absence of a surface oxide with a different chemistry for the ambient-exposed oxides. The chemical behaviour of the separate hydroxyls (when present, see Table 2) and also oxygens is thus constant among the oxides. Therefore, the OH's will all have the same Brönsted/Lewis acid-base properties and the O's all the same Lewis base properties for all these oxides.

The Al *2p* binding energy increases in the order anhydrous oxide < evaporated and oxidised < acid pretreated < alkaline pretreated aluminium, see Table 1. The increase of the Al *2p* binding energy is small as compared to the shift observed for the O *1s* peak, see Table 1. It has been demonstrated that there is a significant contribution of changes in extra-atomic relaxation to Al *2p* core level binding energy shifts. This implies that there are only minor changes in chemical behaviour for the Al cations for these oxides. There are no clear differences observed in binding energy for the surface region and for the more bulk region of the oxide layer, which indicates the absence of surface oxide, having a different chemistry. Thus, the Al sites for the different oxides are expected to have very similar Lewis acid properties.

The pseudoboehmite oxide shows significantly lower binding energies for its constituents as compared to the other oxides studied, see Table 2. However, the shift in binding energy can not be used to directly ascribe this to changes in its initial state chemistry, see Fig. 4, as the pseudoboehmite oxide is structurally different from the other oxides as evidenced from the Auger-parameters, see Table 3. As discussed above, this results in different contributions to the core level binding energy as compared to the other oxides, see Fig. 4. This signifies that a *direct* comparison of binding energy shifts to compare acid-base properties is only possible for structurally similar oxides. The position of pseudoboehmite in the initial state plots, see Fig. 4, and $E_k(\text{O } KL_{23}L_{23}) - E_k(\text{O } KL_1L_{23})$ versus O *1s* plot, Fig. 5, indicates that this oxide has OH, O and also Al sites on its surface that are considerably more basic as compared to the other studied oxides.

It can be concluded that the oxides have very similar acid-base properties of their O, OH and Al sites, with only the pseudoboehmite oxide showing a more basic sites. However, the different oxides do show differences with respect to the *number* of hydroxyls present on their surfaces, cf. Table 2. These hydroxyls are for most organic functional groups directly involved in chemical bonding mechanism [1, 2]. Thus, an increase in the amount of hydroxyls will lead to a larger number of sites being available for interactions with organic molecules.

4.6. Conclusions

Structurally similar oxide layers are formed when producing oxide layers with an alkaline or acidic pretreatment and by oxidising of aluminium in vacuum, despite the different preparation procedures. The oxides exhibit OH sites with the same Brönsted/Lewis acid-base properties, O sites with the same Lewis base properties and Al sites with very similar Lewis acid properties. Moreover, the oxides do not show a different chemistry on their surfaces as compared to the interior of the layers. The oxides do however differ in the amounts of hydroxyls that are present on their surfaces. After boiling of aluminium in water, a pseudoboehmite oxide is formed, which is structurally different from the other oxides. This oxide has more basic O, OH and Al sites.

XPS analysis evidenced that the values of the O *1s* binding energies for the structurally similar oxides directly reflect the initial state chemistry of the anions. The oxides show shifts in their O *1s* binding energy, but these are entirely due to changes in the amounts of hydroxyls in the oxide layer. The structurally different pseudoboehmite oxide has a lower extra-atomic relaxation and Madelung potential contribution to the binding energies. The O *1s* binding

energy is directly related to the surface-averaged charge present on the O-anions. This charge varies between about $-1.2e$ for the oxide formed after an alkaline pretreatment to about $-1.7e$ for the anhydrous amorphous aluminium oxide. A correlation between the Al $2p$ core level binding energy shift and the changes of the initial state chemistry of the oxides exists, but this Al $2p$ binding energy shift is also partially caused by changes in extra-atomic relaxation.

References

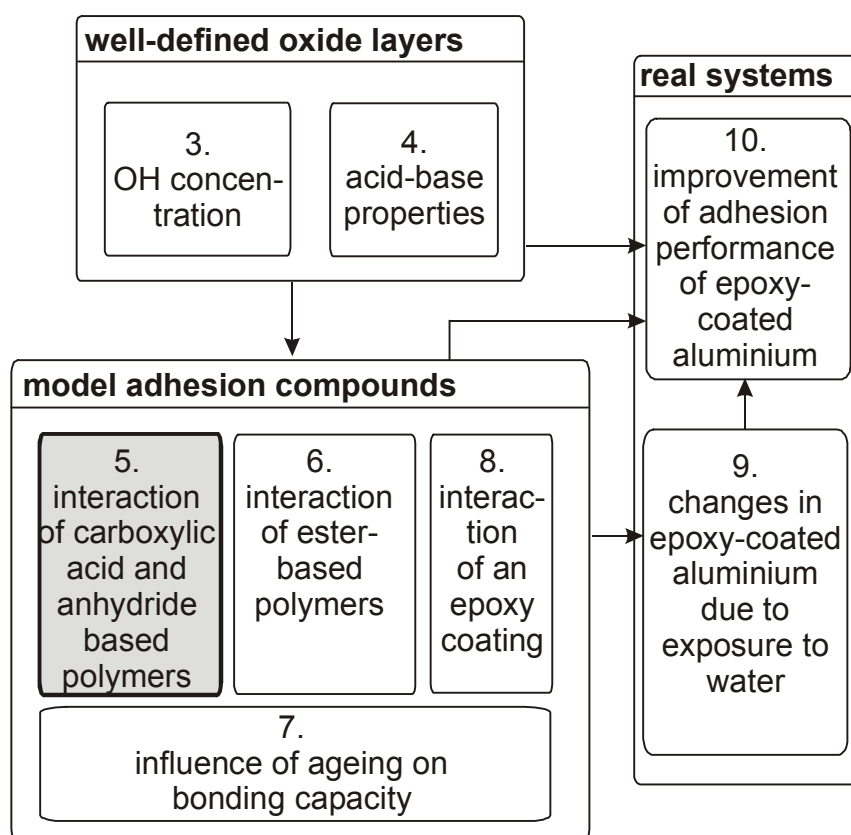
1. Fowkes, F.M. *Journal of Adhesion Science and Technology* 1990, *4*(8), 669-691
2. Fowkes, F.M. *Advanced Chemistry Series no. 43*, American Chemical Society: Washington DC, 1964, 99
3. Barthes-Labrousse, M.G. *Vacuum* 2002, *67*,385-392
4. Davydov, A.A.; Rochester, C.H., *Infrared spectroscopy of adsorbed species on the surface of transition metal oxides*, Wiley:Chichester, 1990
5. Barr, T.L. *Modern ESCA: The principles and practice of X-ray photoelectron spectroscopy*, CRC Press: Boca Raton, 1994
6. Barr, T.L.; Brundle, C.R. *Physical Review B* 1992, *45*,9199-9204
7. Barr, T.L. *Journal of Vacuum Science and Technology A* 1991, *9*(3),1793-1805
8. Guittet, M.J.; Crocombette, J.P. *Physical Review B* 2001, *63*,125117
9. Bosman, H.J.M.; Pijpers, A.P. *Journal of Catalysis* 1996, *161*,551-559
10. Grunert, W.; Muhler, M. *Journal of Physical Chemistry* 1994, *98*,10920-10929
11. Strålin, A.; Hjertberg, T., *Journal of Applied Polymer Science* 1993, *49*(3),511-520
12. Wernick, S.; Pinner, R.; Sheasby, P.G., *The surface treatment and finishing of aluminium and its alloys vol. 1, 5th edition*, Teddington, 1987
13. Wefers, K.; Misra, C. *Oxides and hydroxides of aluminium. Alcoa Technical Paper no. 19*, 1987
14. Cocke, D.L., *Catalysis Reviews* 1984, *26*(2),163-231
15. Siegbahn, K.; Nordling, C. *Nova Acta Regiae Society of Science* 1967, *4*,20
16. Moretti, G. *Journal of Electron Spectroscopy* 1998, *95*,95-144
17. Barr, T.L.; Seal, S. *Journal of the Chemical Society: Faraday Transactions* 1997, *93*(1),181-186
18. Bagus, P.S.; Illas, F. *Journal of Electron Spectroscopy* 1999, *100*(1-3),215-236
19. Pacchioni, G.; Bagus, P.S. *Physical Review B* 1994, *50*,2576-2581
20. Vasquez, R.P., *Journal of Electron Spectroscopy* 1991, *56*,217-240
21. Wagner, C.D. *Analytical Chemistry* 1972, *44*,967-973
22. Wagner, C.D. *Journal of Electron Spectroscopy* 1988, *47*,283-313
23. Wagner, C.D. *Faraday Discussions* 1975, *60*,291-300
24. Moretti, G.; Filippone, F. *Surface and Interface Analysis* 2001, *31*,249-254
25. Moretti, G. *J Electron Spectroscopy* 1992, *58*,105-118
26. Jeurgens, L.P.H.; Sloof, W.G. *Journal of Applied Physics* 2002, *92*(3):1649-1656
27. Snijders, P.C.; Jeurgens, L.P.H.; Sloof, W.G., to be published
28. Ascarelli P.; Moreti, G. *Surface and Interface Analysis* 1985, *7*(1),8-12
29. Ealet, B.; Elyakhloufi, E. *Thin Solid Films* 1994, *250*,92-100
30. Weismann, R. *Solid State Communications* 1979, *31*,347-349
31. Teterin, Y.A.; Ivanov KE. *Journal of Electron Spectroscopy* 1999, *103*,401-405
32. Mullins, W.M.; Averbach, B.L. *Surface Science* 1988, *206*(1-2),29-40
33. Mullins, W.M.; Averbach, B.L., *Surface Science* 1988, *206*(1-2),52-60
34. Jeurgens, L.P.H.; Sloof, W.G., *Applied Surface Science*, 1999, *144-145*,11-15
35. Jeurgens, L.P.H., Sloof, W.G., *Applied Surface Science*, 2000, *161*,139-148
36. Barr, T.L. *Thin Solid Films* 1994, *253*,277-284
37. Barr, T.L. *Journal of Physical Chemistry* 1978, *82*(16),1801-1810
38. Olefjord, I. *Surface and Interface Analysis* 1990, *15*,681-692
39. Rotole, J.A.; Sherwood, P.M.A. *Journal of Vac Science and Techn A* 1999, *17*(4),1091-1096
40. Cordier, F.; Ollivier, E. *Surface and Interface Analysis* 1995, *23*,601-608
41. Alexander, M.R.; Thompson, G.E. *Surface and Interface Analysis* 2000, *29*,468—477
42. Frederick, B.G.; Apai, G. *Surface Science* 1991, *244*,67-80
43. Fuggle, J.C. *Journal of Electron Spectroscopy* 1982, *26*,111-132
44. Wagner, C.D.; Zatko, D.A. *Analytical Chemistry* 1980, *52*(9),1445-1451
45. Rye, R.R.; Madey, T.E. *Journal of Physical Chem Chemical Physics* 1978, *68*(4),1504-1512
46. Jeurgens, L.P.H.; Sloof, W.G. *Surface Science* 2002, *506*(3),313—332
47. Wagner, C.D. *Journal of Vacuum Science and Technoly* 1982, *21*(4),933-944
48. Tessman, J.R.; Kahn, A.H. *Physical Review* 1953, *92*(4),890-895
49. Remy, M.J.; Genet, G.J. *Journal of Physical Chemistry* 1992, *96*(6),2614-2617
50. Scotto-Sheriff, S.; Darque-Ceretti, E. *Journal of Materials Science* 1999, *34*,5081-5088
51. Alwitt, R.S. *Oxides and oxide films vol. 4*, Dekker: New York, 1976.

CHAPTER 5.

INTERACTION OF ANHYDRIDE AND CARBOXYLIC ACID

FUNCTIONAL GROUPS WITH ALUMINIUM OXIDE SURFACES STUDIED

USING INFRARED REFLECTION ABSORPTION SPECTROSCOPY ¹



¹ This chapter was published as a scientific paper:
J. van den Brand, O. Blajiev, P.C.J. Beentjes, H. Terryn, J.H.W. de Wit
Langmuir, 20(15), 6308-6317, 2004

Synopsis

Carboxylic acid and anhydride functional groups are present in many commonly used adhesives and organic coatings and carboxylic acid end-groups are also used in many self-assembling monolayers (SAM's). A good understanding of how these groups interact with the oxide surface and how this is influenced by the composition and chemistry of the oxide layer is important. Moreover, it is also important to know their bonding stability in the presence of water. For polymeric coatings, a study of bonding with the metal substrate is not possible due to the buried interface. To allow for such an investigation anyhow, a model compound approach is followed in this Chapter. The polymer is simplified to a small molecule – a model compound – that is adsorbed as a thin layer on the aluminium oxide surface. The bonding with the oxide surface is subsequently studied using infrared reflection absorption spectroscopy. Two of the model compounds are chosen to represent a maleic anhydride grafted or co-polymerised polyolefin polymer. The third model compound is an aliphatic monofunctional carboxylic acid. The bonding of the model compounds is studied to the same set of five differently pretreated aluminium substrates as were studied in Chapters 3 and 4 using XPS. This allows determining the relation between composition and chemistry of the oxide layer and the subsequent interaction of the carboxylic acid and anhydride based compounds. It is found that on all oxide surfaces, the anhydride hydrolyses, thereby forming two carboxylic acid groups. Subsequently, the carboxylic acid groups interact with the oxide surface to form a chemisorbed (i.e. strongly bonded) carboxylate species. This reaction proceeds through the hydroxyls on the oxide surface. The substrates with more hydroxyls on their surfaces are found to be capable of bonding more carboxylic acid groups. The bonding stability in the presence of water is found to be not very good for a monocarboxylic acid but very good for a dicarboxylic acid.

5.1. Introduction

5.1.1. Introduction

Carboxylic acid and anhydride functional groups are present in many commonly used adhesives and organic coatings [1-3] and carboxylic acid end groups are also found in many self-assembling monolayers (SAM) [4,5]. The

groups have the capability of coordinative bonding to the aluminium oxide surface [4-6]. An aluminium substrate is often given a surface treatment prior to applying a self-assembling monolayer or a polymeric overlayer. The surface treatment changes the chemistry and composition of the oxide layer, which is thereby expected to also influence the bonding behaviour of the organic overlayer that is subsequently applied [7]. Because of the widespread usage of polymer and SAM coated aluminium, knowledge of the interaction of anhydride and carboxylic acid functional groups with the aluminium oxide surface is important. Moreover, it is important to understand how this is influenced by the oxide layer chemistry and composition and to know the stability of bonding in an aqueous environment. Such knowledge would ultimately allow tailoring of the aluminium oxide surface to obtain a specific bonding with an organic overlayer.

For polymeric overlayers, such a study is however experimentally difficult, because of the buried interface. The polymeric overlayer can then be simplified to model compounds that model the bonding functionality of the polymer. The compounds are applied as a very thin layer on the oxide surface and the interaction is studied using for example X-ray photoelectron spectroscopy (XPS) [8-10], infrared reflection absorption spectroscopy (FTIR-RAS) [11,12], or time-of-flight secondary ion mass spectroscopy (TOF-SIMS) [13].

In this work, the interaction of three different carboxylic acid and anhydride based model compounds with a set of five differently prepared aluminium substrates has been investigated using FTIR-RAS. Two of the model compounds were chosen to represent a maleic anhydride grafted or copolymerised polyolefin polymer. Maleic anhydride is added into the polyolefin backbone of an apolar polyolefin polymer to improve its adhesion [1,2]. As the third compound, an aliphatic monofunctional carboxylic acid, often used for SAM's was investigated [4,5]. Additionally, the bonding stability of the compounds with the oxide surface in the presence of water is investigated.

The various oxide layers to which the bonding was investigated were made by giving different, relatively simple, but typical surface treatments to the aluminium substrate. These surface treatments were an alkaline and an acidic pretreatment, oxidising of aluminium in vacuum, dehydroxylation of aluminium in air at 275 °C and boiling in water, resulting in the formation of a pseudoboehmite oxyhydroxide layer. The same set of differently prepared aluminium substrates was investigated in Chapters 3 and 4, to determine their composition and localised acid-base properties. The results are summarised and used in this Chapter because they are important to determine the relation

between composition and chemistry of the oxide layer and the subsequent interaction of the carboxylic acid and anhydride based compounds.

5.2. Experimental

5.2.1. Materials

To model an anhydride grafted or copolymerised polyolefin polymer, two model compounds, namely succinic anhydride and succinic acid are used. Their molecular structure is shown in Fig. 1. The third model compound is myristic acid, an aliphatic monofunctional carboxylic acid; $\text{CH}_3(\text{CH}_2)_{12}\text{COOH}$, and is also shown in Fig. 1. Succinic anhydride, acid and myristic acid were obtained from Sigma-Aldrich as 99.5+% purity and were used without further purification. The deuterated equivalent of succinic acid (d_4 , $(\text{CD}_2)\text{COOH}$)₂) was obtained from Cambridge Isotopes Labs as >97% purity.

The differently prepared aluminium substrates were the same as studied in Chapters 3 and 4. The samples in this Chapter however had a deviating size of 80 x 25 mm. The preparation procedure was discussed in paragraph 3.2.1, page 23. Instead of the anhydrous, amorphous oxide layer, a dehydroxylated aluminium was studied. The aluminium substrate was first polished and cleaned, following the procedure also used for the other substrates. Then, the

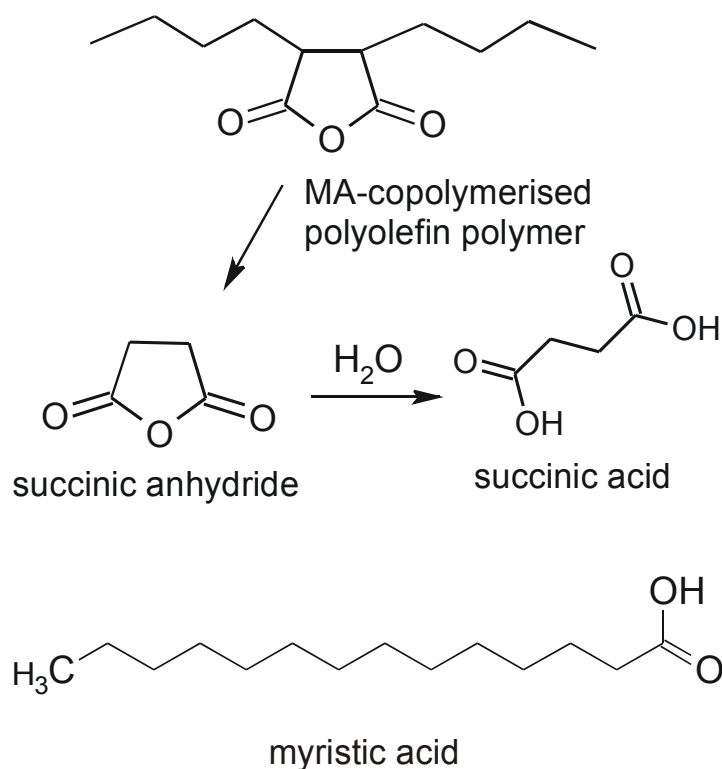


FIG. 1. Molecular structure of the studied model compounds.

sample was heated in air for 24 hrs at a temperature of 275 °C. This procedure causes removal of hydroxyls through condensation and the subsequent desorption of water molecules

5.2.2. Application method

The used glassware was cleaned by first rinsing using hot HNO₃ (35 vol.%), then a hot NaOH solution (20 mass%), then in deionised water and finally rinsed dry using hot chloroform (99.9% purity). The model compounds were dissolved in a solvent at a concentration of 0.02 g/l. For myristic acid, chloroform (99.9% purity) was used. Succinic acid and succinic anhydride were found not to be well-dissolvable in chloroform and for this reason THF (tetrahydrofuran, 99.9% purity) was used.

After preparation of the substrates, a background infrared spectrum was recorded and immediately after this the substrates were immersed in the solvent/model compound mixture and allowed to react for a period of 30 minutes. Longer immersion times (as tested up until 3 hours) were found not to have a significant effect on the results. The substrates were then withdrawn from the solvent mixture and rinsed using clean solvent. The samples were then directly transferred into the infrared apparatus.

5.2.3. Infrared analysis

A Thermo-Nicolet Nexus FTIR apparatus was used, which was equipped with a liquid-nitrogen cooled MCT-A (mercury-cadmium-tellurium) detector and a nitrogen-purged measurement chamber. The measurements were performed using a Specac variable angle reflection accessory set at a near-grazing incident angle of 82 degrees with respect to the normal of the surface. The infrared radiation was p-polarized by employing a Specac grid-wire polarizer. For the spectra of the adsorbed molecules, an infrared background was obtained of the freshly prepared aluminium substrate prior to application of the molecules. The final measurements were ratioed versus this background. The spectra of the oxide layers were ratioed against a clean gold substrate. Approximately 128 scans with a resolution of 2 cm⁻¹ were co-added to obtain the final spectrum.

5.2.4. Surface area determination

The specific surface area of the oxide layers was determined with the Brunauer Emmett and Teller (BET) method, see also Ref. [14]. Krypton was used as the adsorption gas, because of the low surface area of the samples. Aluminium substrates were polished on both sides and then given the surface treatment, described above. A minimum of 150 cm² of geometric area was prepared for a single measurement to obtain accurate results. The set-up was tested and calibrated using material with a known surface area in this regime. After drying in vacuum, the krypton adsorption isotherm was measured at 77K on a Micrometrics ASAP 2010.

5.3. Results

5.3.1. XPS, FTIR and BET investigation of oxide surfaces

The composition, acid-base properties, amounts of adventitious contamination and effective surface areas of the oxide layers on the differently prepared substrates have been investigated using FTIR-RAS, XPS and BET. The XPS measurements were performed at a detection angle of 15 degrees with respect to the sample surface to obtain maximum surface sensitivity. The results and the experimental procedure are discussed in detail in Chapters 3 and 4 and a summary of them is given in Table 1.

The oxide layers on the different prepared aluminium substrates show differences in the amounts of hydroxyls on their surfaces, as determined from curve-fitting of the XPS O *1s* core level peak. The obtained values are reported in column 2 of Table 1, as a fraction of the total O *1s* core level peak intensity. For pseudoboehmite, an additional component due to water was found to be present in the O *1s* peak, which is due to interlamellar water that is present inside the oxide layer [15].

The acid-base properties of the Al cations and O and OH anions are important as they determine the reactions that are subsequently possible with organic functional groups [16,17]. The core level binding energies can be used to directly evaluate the acid-base properties for structurally comparable oxides. The obtained values are reported in columns 3-5 of Table 1. Despite that quite different methods are used to prepare the oxide layers, significant differences in the core level binding energies are not observed and therefore the respective Al, O and OH sites have the same acid-base properties on the different oxide surfaces.

Table 1. Chemistry and composition of the different oxide layers as determined from XPS measurements. See Chapters 3 and 4 for more details.

type of oxide layer	OH fraction	Al BE	O BE	OH BE	α'_{Al} Auger-parameter	cont. layer thickness
	(-)	(eV)	(eV)	(eV)	(eV)	(nm)
pseudoboehmite	0.47 0.04 H ₂ O	73.9	530.4	531.8 533.7 H ₂ O	1461.4	0.2
alkaline pretreated aluminium	0.43	74.5	530.9	532.3	1461.4	0.4
acid pretreated aluminium	0.35	74.4	531.0	532.4	1461.7	0.3
evaporated and oxidised aluminium	0.21	74.3	531.1	532.4	1461.9	0.1
dehydroxylated aluminium	0.09	74.3	531.1	532.4	1461.6	0.1
estimated error \pm	0.01	0.05	0.05	0.05	0.1	0.02

The structurally different pseudoboehmite oxide deviates, having more basic Al, O and OH sites, see also furtheron.

The so-called Auger-parameter α' is a sensitive measure for the electronic polarisability of the environment around the considered anion or cation in presence of a core hole that is generated in the photoelectron process [18-20]. It is calculated from a XPS core level binding energy and the XPS kinetic energy of an Auger transition [19,20]. The Auger-parameters α'_{Al} for the Al cations in the different oxide layers, calculated from the Al $2p$ and Al KLL energies, show that there are clear differences [19] in the electronic polarisability of the environment of the Al ions in the different oxide layers, see column 6 of Table 1.

Ambient-exposed oxide layers are inevitably contaminated by an adventitious carbon overlayer. The amount of contamination for the studied oxide layers is reported in column 7 of Table 1, as an equivalent carbon layer thickness. The layer thickness is determined from the intensity of the XPS C $1s$ core level peak, see Chapter 3, for details on the used procedure. The obtained values indicate that the contamination levels are comparably low [21,22]. Resolving the XPS C $1s$ peak into its constituting components showed that the contamination layers are composed almost exclusively of unreactive C-C/C-H components (>95%), see Chapter 3. The contamination overlayers are therefore

only loosely bound and can be readily displaced by more reactive functional groups (i.e. the solvent or the model compounds).

In Fig. 2, the infrared spectra are shown for the different types of oxide layers in the 1300-900 cm^{-1} and 3700-1400 cm^{-1} regions. In the 1300-900 cm^{-1} region, pseudoboehmite shows its the main bands at 1080 and 860 cm^{-1} , which are respectively the $\delta(\text{OH})$ hydroxyl bending and the $\nu(\text{Al-O})$ stretching vibrations [23]. The other four oxide layers show the main band at around 950 cm^{-1} , which is due to the $\nu(\text{Al-O})$ stretching vibration. For crystalline, well-defined aluminium oxides, free, terminal hydroxyls are often observed as a set of well-resolved sharp bands in the 3800-3700 cm^{-1} region, due to the $\nu(\text{OH})$ hydroxyl stretching vibrations [16,24-27]. Bridging hydroxyls and hydroxyls experiencing hydrogen-bonding are observed at lower wavenumber [26-29]. The 3800-2600 cm^{-1} region for pseudoboehmite consists of a broad band with a

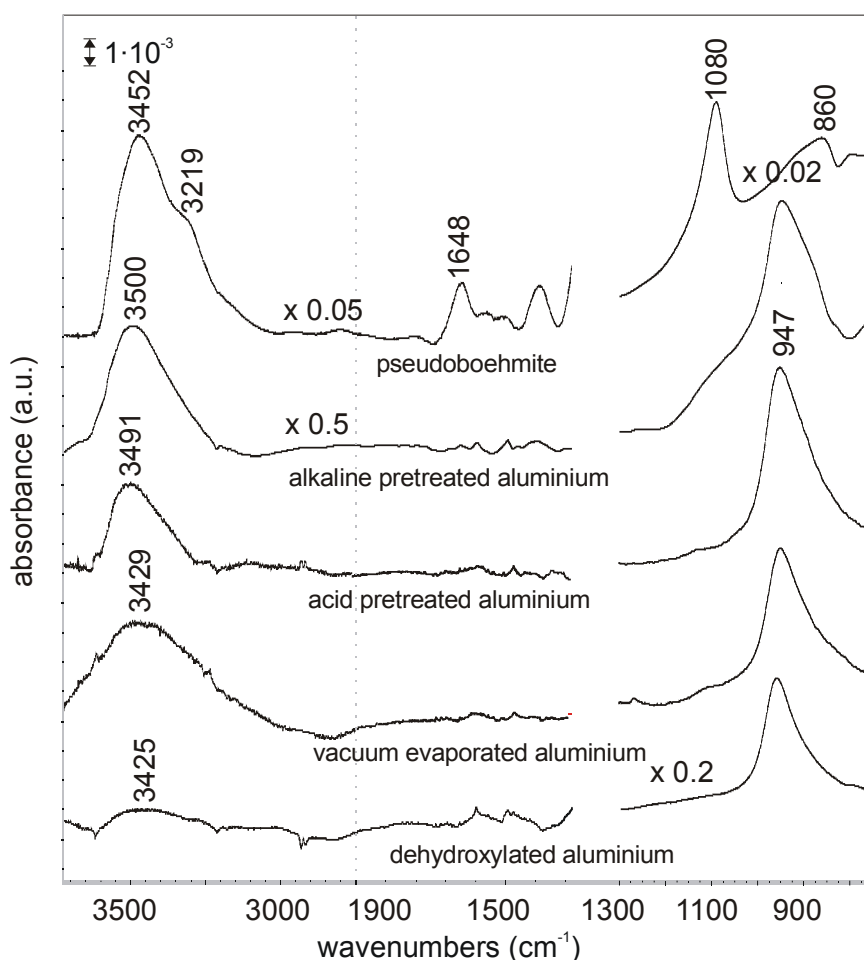


FIG. 2. FTIR-RAS spectra of the differentially prepared aluminium substrates, obtained with respect to a clean gold substrate. For clarity, some spectra are shown with a different vertical scaling above 1400 and below 1300 cm^{-1} which is indicated by the multiplication factors.

maximum at 3452 cm^{-1} and a shoulder at 3219 cm^{-1} , see Fig. 2. The band at 3452 cm^{-1} is due to stretching vibrations of interlamellar water in the oxide structure, as also found from the XPS measurements, see Table 1. The shoulder at 3219 cm^{-1} is due to the $\nu(\text{OH})$ vibration of hydroxyls in the pseudoboehmite layer [15]. The other four oxides show a similar, asymmetrically shaped band, having its maximum in the $3500\text{-}3425\text{ cm}^{-1}$ region, see Fig. 2. The stretching vibration of water molecules at around 3450 cm^{-1} have an associated bending vibration $\delta(\text{H}_2\text{O})$ at around 1650 cm^{-1} [30], with a fixed and known integrated peak intensity ratio of 1:6 [31,32]. This is observed for pseudoboehmite, while the other oxides show only minor and not well-resolved H_2O -related bands. From the XPS measurements water was not detected for the other four oxides, see Table 1, but physisorbed water is likely to become desorbed in the ultra-high vacuum environment. This indicates that for the other four oxides, the largest part of the asymmetrically shaped band in the $3500\text{-}3425\text{ cm}^{-1}$ region is due to the $\nu(\text{OH})$ of the hydroxyls, while for pseudoboehmite this band is found at 3219 cm^{-1} , see above.

Pseudoboehmite thus deviates from the other four oxides, having both a lower $\nu(\text{OH})$ wavenumber and lower XPS OH binding energies. This indicates differences in the hydroxyl chemistry as compared to the other oxides. As discussed in Chapter 4, this is due to a different local environment around the O and OH anions in pseudoboehmite.

The comparably low wavenumber position of the hydroxyl stretching vibrations of 3219 cm^{-1} for pseudoboehmite and $3500\text{-}3425\text{ cm}^{-1}$ for the other oxides indicates significant hydrogen-bonding of the hydroxyls in the oxide layers, for example between neighbouring hydroxyls. Moreover, the broadness of the bands indicates inhomogeneity and the presence of a broad distribution of different hydroxyls.

The specific surface areas of the different oxide layers, as determined using the BET method are given in Table 2. The values are reported as a multiplication factor with respect to the geometric area put in the sample cell. For practical reasons, BET measurements were not performed on the evaporated and oxidised aluminium. The surfaces show on average an about 1.5 times increase as compared to the geometric surface area. The alkaline and acidic etching pretreatments do not give significantly higher surface areas. Although these surface treatments are known to cause enhancement of surface area [33], the pretreatment times were deliberately kept short, see the Experimental section, to limit the effect of this. The BET measurements thus show that the surfaces are well-comparable with respect to their surface areas.

TABLE 2. Increase in surface area as compared to the geometric area put in the sample cell as determined using the BET technique for the different oxides

pretreatment	geometric area increase factor
pseudoboehmite	14.6
alkaline pretreated aluminium	1.6
acid pretreated aluminium	1.4
dehydroxylated aluminium	1.3
estimated error	± 0.1

Only pseudoboehmite shows a significant increase in surface area, which is due to the rough and porous nature of this layer [15,31,39].

5.3.2. Succinic anhydride adsorption on the different aluminium substrates

Succinic anhydride was adsorbed to study the interaction with the differently prepared aluminium substrates. In Fig. 3 an infrared spectrum is shown of a multilayer of succinic anhydride, applied on the alkaline pretreated aluminium, using dip-coating from a 0.05 g/l chloroform solution. In Table 3, the relevant peak assignments for succinic anhydride are reported, obtained from a transmission measurement of the solid. The strongest band in the spectrum is observed at 1790 cm^{-1} , and can be ascribed to the symmetric carbonyl stretching vibration $\nu(\text{C=O})_s$ of the anhydride ring. The corresponding asymmetric stretching $\nu(\text{C=O})_a$ vibration is observed as a comparably minor band at 1861 cm^{-1} . The other infrared bands are also from succinic anhydride, except for the small bands at 1724 cm^{-1} and 1598 cm^{-1} . The nature of the band at 1598 cm^{-1} will be discussed furtheron. The band at 1724 cm^{-1} can be ascribed to the $\nu(\text{C=O})$ carbonyl stretching vibration of a carboxylic acid (COOH) group [35], indicating hydrolysis (resulting in ring opening) has occurred. Hydrolysis was found not to occur in the chloroform solvent from which the layer was applied. Layers of different thickness were applied by varying the concentration in solution. The amount of hydrolysed succinic anhydride, as evidenced from the $\nu(\text{C=O})$ carbonyl stretching vibration peak intensity at 1724 cm^{-1} , was found to be independent on the adsorbed amount. Therefore, hydrolysis likely does not occur throughout the layer, but close to the oxide surface.

TABLE 3. FTIR peak positions (cm^{-1}) as measured from infrared transmission measurements of the solids and their corresponding peak assignments for succinic anhydride [34,35], succinic acid [36], succinic acid-d4 [36] and myristic acid [4,5,35,37,38].

succinic anhydride	succinic acid	succinic acid-d4	myristic acid	assignment
			2953 (m)	$\nu_{\text{as}}(\text{CH}_3)$ [asym stretch]
			2914 (s)	$\nu_{\text{as}}(\text{CH}_2)$ [asym stretch]
			2871 (m)	$\nu_{\text{s}}(\text{CH}_3)$ [sym stretch]
	2930		2848 (s)	$\nu_{\text{s}}(\text{CH}_2)$ [sym stretch]
	2500-3100(b)	2500-3100 (b)	2500-3100	ν_{OH} [OH stretch]
	2536 / 2631(m)	2570 / 2679 (m)		overtones C-O
1861 (w)				$\nu_{\text{as}}(\text{C=O})$ [asym stretch anhydride ring]
1790 (s)				$\nu_{\text{s}}(\text{C=O})$ [sym stretch anhydride ring]
	1681(s)	1680(s)	1697 (s)	$\nu(\text{C=O})$ [C=O stretching]
1420 (m)			1471 (m)	$\delta(\text{CH}_2)$ [CH_2 deform]
			1463 (m)	
	1410(s)	1406(s)	1430 (m)	$\delta\text{OH}\dots\text{O}$ [OH bend, coupled]
	1306(s)	1279(s)	1306 (m)	$\nu(\text{C-O})$ [CO stretch, coupled]
1299 (m)				$\nu(\text{C-O})$ [CO stretch, ring]?
1279 / 1240 (m)	1197(s)		1350-1190(m)	$\omega(\text{CH}_2)$ [CH_2 wagging]
1212 (m)	1176(s)			$\gamma(\text{CH}_2)$ [CH_2 twisting]
1064 (s)		1055(s)		$\nu_{\text{s}}(\text{COC})$ [ring stretch]
		1012(s)		$\text{s}(\text{CD}_2)$ [CD_2 scissoring]
		947(s)		$\omega(\text{CD}_2)$ [CD_2 wagging]
				$\text{t}(\text{CD}_2)$ [CD_2 twisting]
921 (s)				ring vibration?
	908 (m)	899 (m)	939 (m)	$\pi\text{OH} - \text{OH}$ out of plane bending

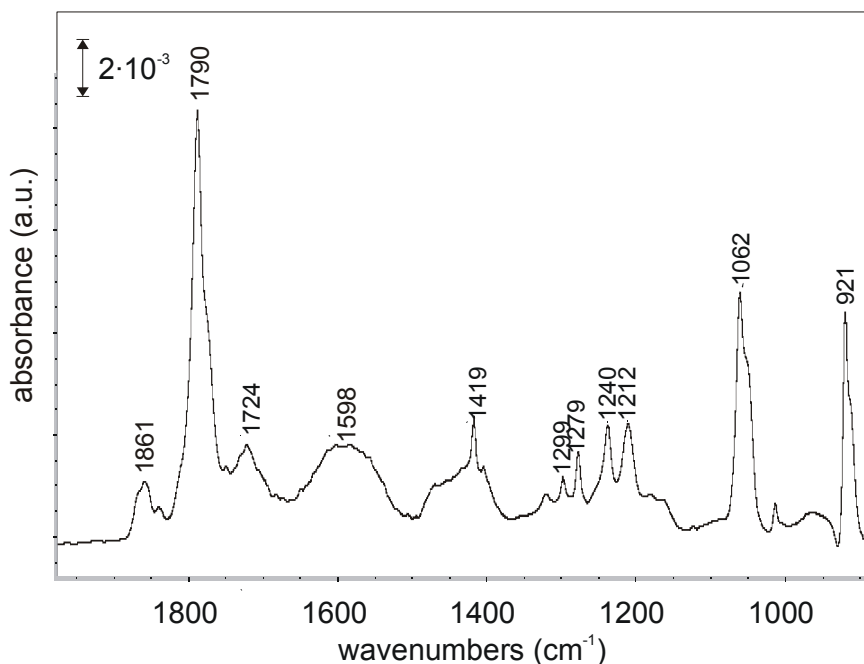


FIG. 3. FTIR-RAS spectrum obtained from a multilayer of succinic anhydride, applied from a 0.05 g/l solution in chloroform on the alkaline pretreated aluminium.

The hydrolysis reaction can proceed with either physisorbed water or hydroxyls on the oxide surface [11,12,40]. The $\nu(\text{C}=\text{O})$ carbonyl stretching vibration at 1724 cm^{-1} showed up as a comparably intense bands for all oxides and its intensity did not show a relation with the amount of hydroxyls present on the oxide surface. It is therefore concluded that hydrolysis primarily proceeds through physisorbed water, which is in agreement with results found by others [11,40]. The hydrolysis of succinic anhydride due to water then results in the formation of succinic acid, having two carboxylic acid groups, see Fig. 1.

5.3.3. Succinic acid adsorption on the different aluminium substrates

The carboxylic acid groups which are formed by hydrolysis of the anhydride group, see Fig. 1, are capable of subsequent bonding with the oxide surface through physisorption with hydroxyls or chemisorption with the formation of a coordinatively bonded carboxylate. To study this, the succinic *acid* model compound was adsorbed on the differently prepared aluminium substrates. In Fig. 4, the infrared spectra are shown for succinic acid on the differently prepared aluminium substrates. The infrared bands and their assignment for bulk succinic acid are given in Table 3, obtained from a transmission measurement of the solid. The main bands in the spectra are a broad band around 1600 cm^{-1} and an asymmetrically shaped band in the $1500\text{--}1400\text{ cm}^{-1}$ region. The band at around 1600 cm^{-1} is not due to succinic acid, see Table 3.

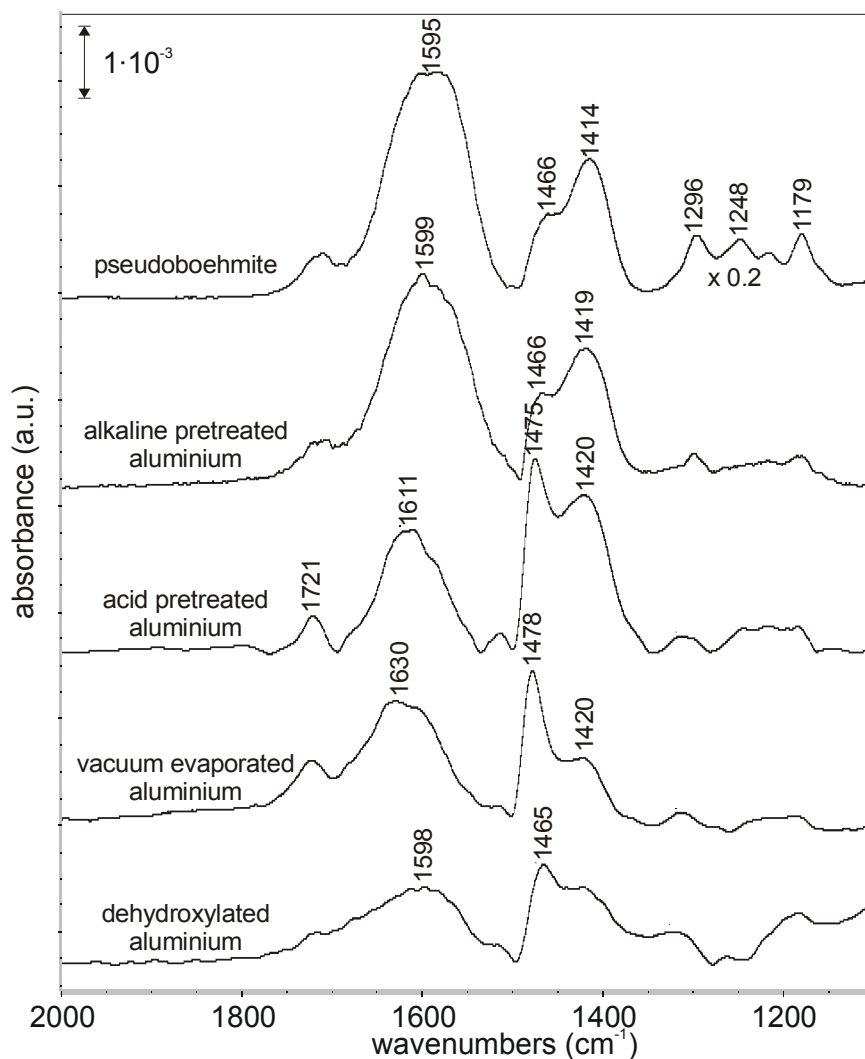


FIG. 4. FTIR-RAS spectra of succinic acid on the differently prepared aluminium substrates.

It indicates that the carboxylic acid groups have been deprotonated to form a coordinatively bonded carboxylate species. The band is then assigned to the asymmetric carboxylate stretching vibration $\nu_{as}(\text{COO}^-)$. [4,34,41,42]. A band at this position is also observed in the spectrum of adsorbed succinic *anhydride*, see Fig. 3, indicating that also there eventually a chemisorbed carboxylate is formed after hydrolysis.

The asymmetrically shaped band in the 1500-1400 cm^{-1} region can be the corresponding symmetric carboxylate stretching vibration $\nu_s(\text{COO}^-)$. There is however some discussion in the literature [41,43,44] regarding the detailed assignment of bands in the 1500-1400 cm^{-1} region for coordinatively bonded aliphatic carboxylic acids, as the region also contains CH_2 and CH_3 deformation bands and a coupled $\delta\text{OH}\dots\text{O}$ bending band due to hydrogen-bonded carboxylic acid groups [35]. A significant contribution to the band of the coupled $\delta\text{OH}\dots\text{O}$ bend at 1410 cm^{-1} (see Table 3) is not expected, because of the relatively low

number of unreacted carboxylic acid groups, see Fig. 4. For succinic acid, the $\nu_s(\text{COO}^-)$ band can contain a contribution due to the CH_2 deformation vibration $\delta(\text{CH}_2)$, which is located around this position [36], see Table 3. To evaluate this, the deuterated succinic acid-d4 (CD_2COOH)₂ was adsorbed on the differently prepared aluminium substrates. In Fig. 5, the obtained infrared spectra are shown.

The spectra resemble those of succinic acid on the different prepared aluminium substrates, having a broad band located at around 1600 cm^{-1} and an asymmetrically shaped band in the $1500\text{--}1400\text{ cm}^{-1}$ region. The similarity between the results for succinic acid and succinic acid-d4 implies that the asymmetrically shaped band in the $1500\text{--}1400\text{ cm}^{-1}$ region can be assigned fully to the symmetric carboxylate stretching vibration $\nu_s(\text{COO}^-)$. The $\nu_{\text{as}}(\text{COO}^-)$ and $\nu_s(\text{COO}^-)$ peak positions for both adsorbed succinic acid and succinic acid-d4, as

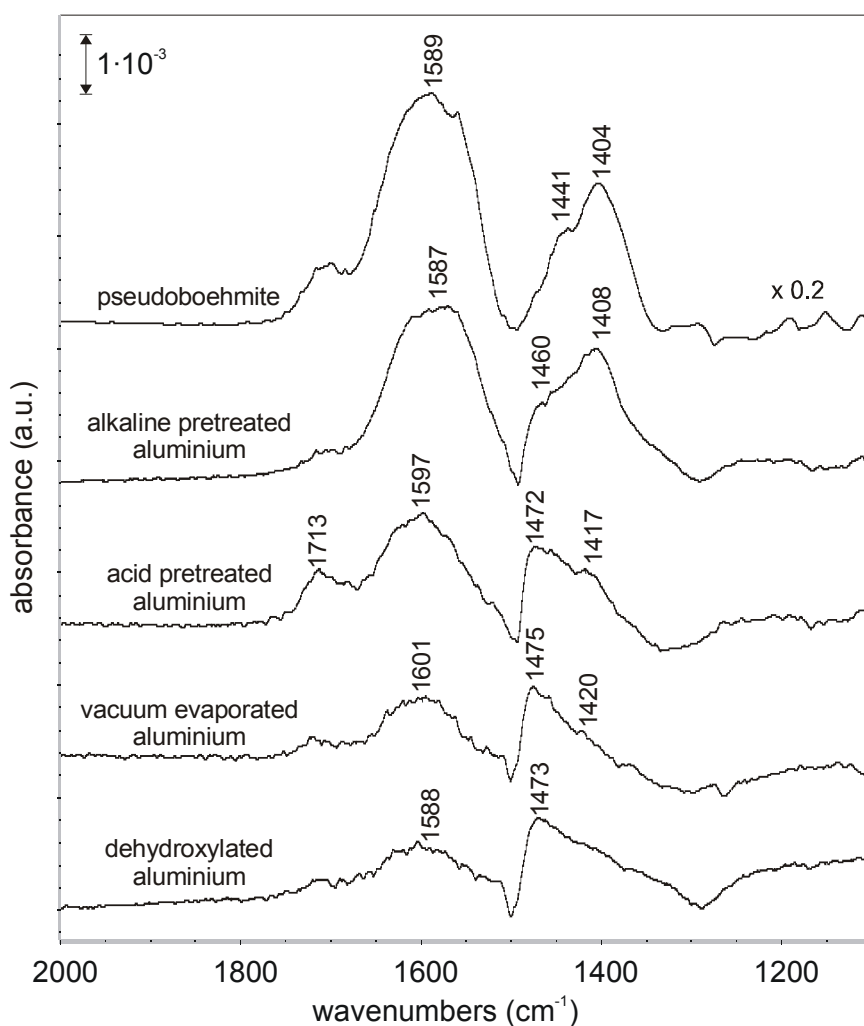


FIG. 5. FTIR-RAS spectra of succinic acid d4 on the differently prepared aluminium substrates.

obtained for the differently prepared aluminium substrates, are summarized in Table 4.

In the spectra of adsorbed succinic acid and succinic acid-d4, a minor band due to a carbonyl stretching vibration $\nu(\text{C}=\text{O})$ is observed, having a position around 1720 cm^{-1} for succinic acid, and about 10 cm^{-1} lower values for succinic acid-d4. It indicates the presence of a minor amount of undissociated carboxylic acid groups. As the band remains present after the solvent-rinse, it originates from species that are strongly bonded to the oxide surface. The peak position is too low to be due to a non-hydrogen bonded carboxylic acid group [45,46], but much higher than acid groups in the succinic acid bulk layer, see Table 3, implying involvement in not very strong hydrogen bonding [47]. It is tentatively assumed that the bands are due to a minor amount of succinic acid molecules, having one end chemisorbed as a coordinatively bonded carboxylate, while the other group is undissociated, but involved in hydrogen-bonding.

In the $3000\text{-}2800\text{ cm}^{-1}$ region, minor negative bands were observed after

TABLE 4. $\nu_{\text{as}}(\text{COO}^-)$ and $\nu_{\text{s}}(\text{COO}^-)$ carboxylate stretching vibration peak position for the different compounds on the differently prepared aluminium substrates For the $\nu_{\text{s}}(\text{COO}^-)$, two components are observed, (m) indicates the peak position of the minor component, which is in some cases not well-resolved.

pseudoboehmite	alkaline pretreated aluminium	acid pretreated aluminium	evaporated and oxidised aluminium	dehydroxylated aluminium	assignment
succinic acid					
1595	1599	1611	1630	1598	$\nu_{\text{as}}(\text{COO}^-)$
1414	1419	1475	1478	1465	$\nu_{\text{s}}(\text{COO}^-)$
1466(m)	1466(m)	1420(m)	1420(m)	1420(m)	
181	180	136	152	133	$\nu_{\text{as}}-\nu_{\text{s}}$
succinic acid – d4					
1589	1587	1597	1601	1588	$\nu_{\text{as}}(\text{COO}^-)$
1404	1408	1472	1475	1473	$\nu_{\text{s}}(\text{COO}^-)$
1441(m)	1460(m)	1417(m)	1420(m)	1420(m)	
185	179	125	126	115	$\nu_{\text{as}}-\nu_{\text{s}}$
myristic acid					
1574	1591	1587	1588	1569	$\nu_{\text{as}}(\text{COO}^-)$
1411	1417	1470	1474	1466	$\nu_{\text{s}}(\text{COO}^-)$
1468(m)	1463(m)	1417(m)	1417(m)	1415(m)	
163	174	117	114	103	$\nu_{\text{as}}-\nu_{\text{s}}$

adsorption of the compounds (not shown). Succinic acid and succinic acid-d4 do not have infrared vibrations with a significant intensity in this region, see Table 3. The negative bands therefore indicate the displacement of the adventitious carbon overlayer, see Table 1, from the oxide surface upon adsorption of the compounds. In the 1350-1100 cm^{-1} region, only for pseudoboehmite well-resolved, succinic acid related, bands are observed, while the other oxides only show weak and unresolved bands, see Figs. 4 and 5.

5.3.4. Myristic acid adsorption on the different aluminium substrates

The third model compound is myristic acid. The infrared spectra obtained for adsorption of myristic acid on the differently prepared aluminium substrates are shown in Fig. 6. In Table 3, infrared peak assignments are given for bulk myristic acid are given, as obtained from a transmission measurement of the

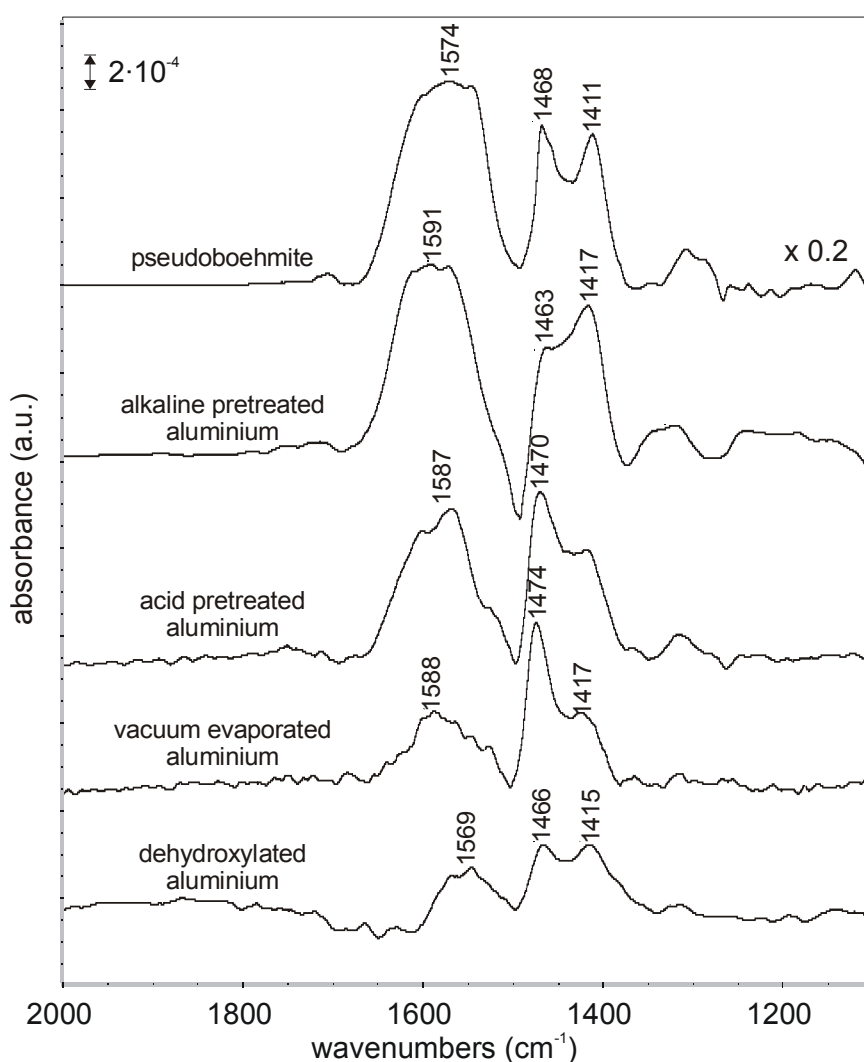


FIG. 6. FTIR-RAS spectra of myristic acid on the differently prepared aluminium substrates.

solid. The spectra show a broad band at around 1600 cm^{-1} and an asymmetrically shaped band in the $1500\text{-}1400\text{ cm}^{-1}$ region. Given the similarity with the results obtained for succinic acid, see above, the bands can be ascribed to respectively the asymmetric carboxylate stretching vibration $\nu_{\text{as}}(\text{COO}^-)$ and the symmetric carboxylate stretching vibration $\nu_{\text{s}}(\text{COO}^-)$. The peak positions as obtained for the differently prepared aluminium substrates are summarized in Table 4. The shape of the $\nu_{\text{s}}(\text{COO}^-)$ band for adsorbed myristic acid is slightly different than for succinic acid, compare Figs. 4 and 6, which is due to a contribution of the CH_2 deformation vibration $\delta(\text{CH}_2)$ of the aliphatic chain, appearing around this wavenumber, see Table 3.

In the $3000\text{-}2800\text{ cm}^{-1}$ region, myristic acid shows well-resolved CH_2 and CH_3 stretching vibrations. As an example, in Fig. 7, the $3000\text{-}2600\text{ cm}^{-1}$ region for myristic acid, on the alkaline pretreated aluminium is shown. In the lower wavenumber region (Fig. 7), a broad band around $1320\text{-}1310\text{ cm}^{-1}$ is observed for all oxide layers. Following Tao [5], this band is ascribed to the CH_2 wagging and twisting series of vibrations.

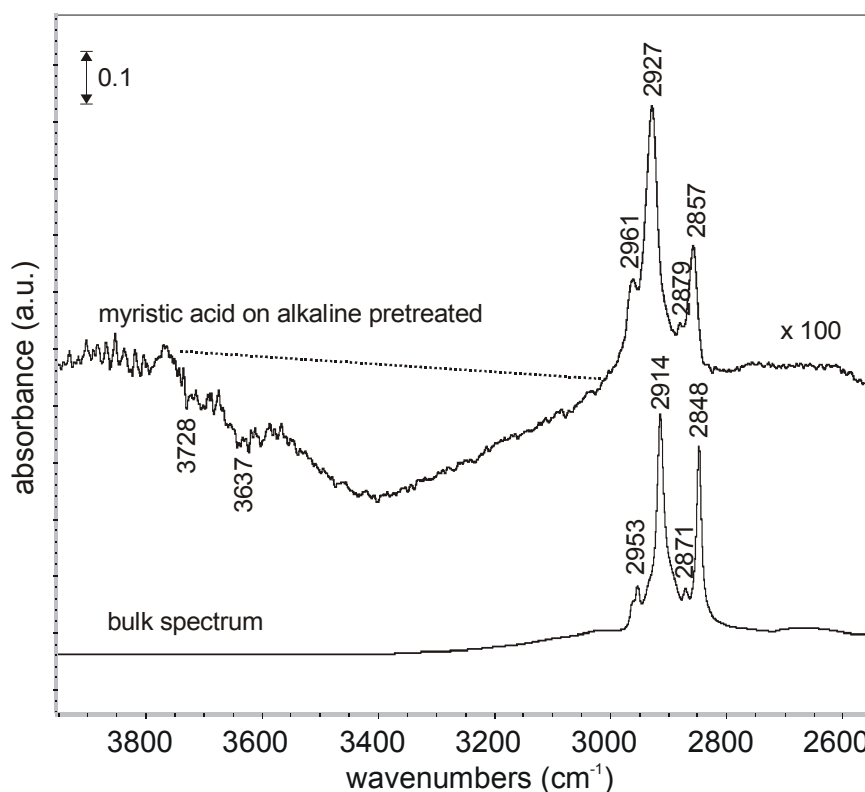


FIG. 7. FTIR-RAS spectrum of hydroxyl stretching region for myristic acid on the alkaline pretreated aluminium. Bottom spectrum shows the infrared transmission spectrum obtained for bulk, solid myristic acid. The bands observed at 3728 cm^{-1} and 3637 cm^{-1} are an experimental artefact and are due to water in the beam path in the infrared compartment [48].

5.3.5. Aqueous stability

To evaluate the bonding stability of chemisorbed myristic and succinic acid, immersion of the substrates was performed in room temperature triple deionised water for a period of up to 60 minutes. No differences in bonding stability were observed among the differently prepared aluminium substrates. In Fig. 8, infrared spectra obtained initially and after 15 and 60 minutes of immersion are shown for both myristic and succinic acid on the alkaline pretreated aluminium.

Succinic acid was found to remain adsorbed for a period of 60 minutes, showing only small modifications, see Fig. 8. In contrast, myristic acid was found to become rapidly and completely desorbed from the oxide surface. The CH_2/CH_3 stretching vibrations of the aliphatic chain of myristic acid (not shown) and the $\nu_{\text{as}}(\text{COO}^-)$ stretching vibration band at 1598 cm^{-1} are absent after immersion. The bands are replaced by broad bands at 1555 cm^{-1} and 1416 cm^{-1} , see Fig. 8, corresponding to water molecules, adsorbed on the oxide surface [30]. The growth of the 950 cm^{-1} band and the upward bending of the infrared spectrum is observed, after the displacement of myristic acid. This is due to the development of broad shoulders around the main Al-O band at 950 cm^{-1} band, corresponding to hydroxyl bending vibrations [23,31,32]. It indicates that growth and through-film hydroxylation of the oxide layer occurs, due to a direct contact of the oxide surface with water. As it does not occur for succinic acid, it apparently only occurs after displacement of the chemisorbed molecules from the aluminium substrate.

5.4. Discussion

5.4.1. Hydrolysis of anhydride functionality and bonding mode with oxide surfaces

The anhydride functional group in succinic anhydride is hydrolysed upon adsorption, see Fig. 3. This occurs for all the differently prepared aluminium substrates. The reaction proceeds through physisorbed water on the oxide surface. As a result, succinic acid, having two carboxylic acid functional groups, is formed, see Fig. 1. Both of the carboxylic acid groups are subsequently deprotonated on the oxide surface to form a coordinatively bonded carboxylate. More anhydride groups are being hydrolysed than are subsequently being chemisorbed as a carboxylate on the oxide surface, as evidenced from the clear presence of a remaining $\nu(\text{C}=\text{O})$ carbonyl stretching vibration at 1724 cm^{-1} , see Fig. 3. For myristic acid, deprotonation of the carboxylic acid group also occurs upon adsorption on the differently prepared aluminium substrates.

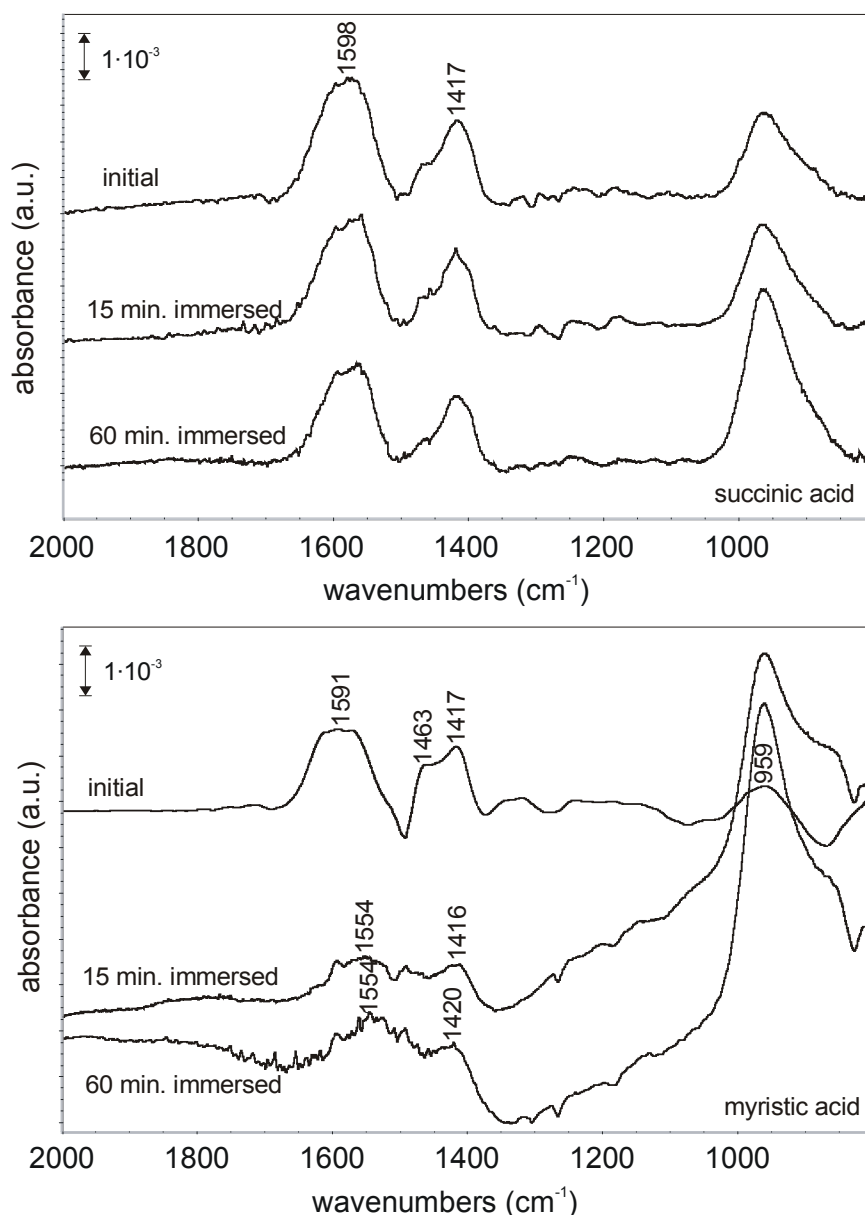


FIG. 8. FTIR-RAS spectra for succinic acid (top) and myristic acid (bottom) on the alkaline pretreated aluminium after immersion in triple deionised water for the indicated period.

The spectra of both chemisorbed succinic acid and myristic acid on the differently prepared aluminium substrates consist of two main infrared bands. A broad band in the 1600 cm⁻¹ region is assigned to the asymmetric carboxylate stretching vibration $\nu_{as}(\text{COO}^-)$ and an asymmetrically shaped band in the 1500-1400 cm⁻¹ region to the symmetric carboxylate stretching vibration $\nu_s(\text{COO}^-)$. The peak separation $\Delta = \nu_a(\text{COO}^-) - \nu_s(\text{COO}^-)$ can be used to determine the coordination type of the carboxylate [49-53]. Three different main types of coordination are distinguished: bridging bidentate, chelating bidentate and unidentate, which each give a characteristic peak separation [49-53]. Values ranging from 114 to 185 cm⁻¹ are obtained, see Table 4. Myristic acid, adsorbed

on the dehydroxylated aluminium is slightly outside of this range, but this is likely due to the comparably low spectral quality. The values indicate a bridging bidentate coordination for the compounds and oxide layers studied. The two C-O bonds of the carboxylate COO^- become equivalent (the double bond is lost) and the carboxylate is coordinated to two aluminium cations on the oxide layer surface [49-53]. This assignment is in agreement with that of others, studying the chemisorption of carboxylic acids on aluminium oxide surfaces [4,5,41,42,54].

The symmetric carboxylate stretching vibration band shows clear asymmetry, see Figs. 4-6. The band appears to consist of two bands, located roughly at positions of around 1420 cm^{-1} and 1470 cm^{-1} . The contributing intensity of these two bands changes across the oxides. Berada *et al.* [34] and Allara *et al.* [4] have also observed spectra with a main $\nu_s(\text{COO}^-)$ band at around 1470 cm^{-1} and a shoulder at around 1420 cm^{-1} for n-alkanoic acids adsorbed on an aluminium oxide. Their substrates were very similar to the evaporated and oxidised aluminium. The shoulder was ascribed to a second type of coordinatively bonded carboxylate, showing differences in the coordination to the oxide surface [4,34]. The presence of a second type of coordinatively bonded carboxylate is expected to also result in a second asymmetric $\nu_{as}(\text{COO}^-)$ band [53,55,56]. This is not observed, see Fig. 4-6, but the $\nu_{as}(\text{COO}^-)$ band has a relatively large peakwidth, with FWHM's (full width at half maximum) values of around 100 cm^{-1} . For solid sodium succinate, a much lower value of 50 cm^{-1} was obtained, corresponding to values reported in the literature for ordered systems [57]. The broad band can therefore hide the unresolved presence of different types of coordinatively bonded carboxylates.

The infrared band positions, resulting from the coordinatively bonded carboxylates are known to depend on many factors like the type of cation, CO bond lengths, angle etc. [47,49,52,53,56]. Tao [5] observed a relation between the acidity/basicity of the cations and the carboxylate peak positions for n-alkanoic carboxylic acids, adsorbed on different types of metal oxides. This is not observed here, compare Table 2 and Figs. 4-6. Pseudoboehmite has considerably more basic cations and anions than the other oxide layers, but the spectra for the adsorbed compounds are similar. Instead, we note a relation between the shape of the $\nu_{as}(\text{COO}^-)$ band and the Auger-parameter α'_{Al} , being a measure for polarisability of the local electronic environment around Al cation, see Tables 1 and 4. The relative contribution of the 1420 cm^{-1} band – indicating a change in bonding of the carboxylate species – is observed to increase in the order evaporated and oxidised < dehydroxylated \approx acid pretreated < alkaline pretreated \approx pseudoboehmite. In the same order, there is an increase in the

Auger-parameter, indicating a change in the electronic polarisability of the environment around the Al cations. It is noted that in the same order also the peak maximum of the asymmetric carboxylate stretching vibration shifts to lower wavenumber. It is therefore suggested that the positions of the carboxylate stretching vibrations and thus coordination mode are strongly influenced by the electronic polarisability of the local environment around the Al cation and not by the acidity/basicity of the Al cations. Although the infrared results indicate two discrete types of coordinatively bonded carboxylates, from the XPS analysis, no discrete types of environment around aluminium cations could be resolved, see also Chapter 4.

5.4.2. Orientation of groups

Infrared reflection absorption spectroscopy can be used to determine the orientation of molecules with respect to the metallic surface plane. Infrared vibrations with a dipole component *perpendicular* to the surface plane will be observed while vibrations with a dipole component *parallel* to the surface plane will not be observed [4,54]. For flat surfaces, this allows determining the orientation of molecules with respect to the surface plane. For this reason, for pseudoboehmite, information on the orientation cannot be derived, because of its macroscopic roughness. The orientation information is then lost because the infrared spectrum is a statistical average of the different orientations of the molecules with respect to the *metallic* surface plane.

The CH_2/CH_3 stretching vibrations can be used to determine the orientation of the aliphatic chain of n-alkanoic carboxylic acids with respect to the metallic surface plane [4-6,38,45,46,58]. The CH_2 transition dipole moment is perpendicular to the molecular axis. Therefore, with an increasing net orientation of the chains perpendicular to the metallic surface plane, the $\nu_a(\text{CH}_2)/\nu_a(\text{CH}_3)$ intensity ratio decreases [59]. In Fig. 7, the CH_2/CH_3 stretching vibration region is shown for myristic acid, adsorbed on the alkaline pretreated aluminium, together with the infrared transmission spectrum for the bulk myristic acid. A $\nu_a(\text{CH}_2)/\nu_a(\text{CH}_3)$ intensity ratio of 2.5 was obtained for myristic acid adsorbed on the differently prepared substrates, while a ratio of 5 was obtained for the bulk spectrum. This suggests some perpendicular orientation of myristic acid on the differently prepared substrates, but the value is comparably low as compared to literature values given for highly organised SAM-layers [59]. Additionally, the $\nu_a(\text{CH}_2)$ peak position can be used to evaluate the organisation of the layer, with lower values indicating more ordering [60]. All the different oxide layers gave a $\nu_a(\text{CH}_2)$ peak position of 2927 cm^{-1} , which also indicates that

a well-organised, ordered layer is not formed. As shown by Allara *et al.* [60] better organised layers are expected to be formed only for molecules have a longer aliphatic chain than myristic acid.

The carboxylate species is generally considered to have C_{2v} point group symmetry [4,5]. The $\nu_{as}(\text{COO}^-)$ vibration then has its dipole moment *perpendicular* and the $\nu_s(\text{COO}^-)$ vibration *parallel* to the molecular axis. The spectra obtained, see Figs. 4-6, show the presence of both symmetric and asymmetric carboxylate stretching modes, having roughly an equal intensity. Therefore, for both myristic and succinic acid, the carboxylate has a tipped geometry in which the oxygens are at an unequal distance from the oxide surface [4,5].

5.4.3. Reactivity of the different oxide layers

The oxide layers exhibited clear differences in the infrared peak intensities of the chemisorbed molecules, see Figs. 4-6. For the oxide layers with a constant surface area, see Table 2, and comparing the same molecules, this indicates differences in chemisorptive capacity, because an increase in the molecular coverage results in more intense bands [61-63]. To evaluate the chemisorptive capacity of the differently prepared aluminium substrates, the total integrated infrared peak intensities in the $3000\text{-}2800\text{ cm}^{-1}$ (CH_2/CH_3 stretching vibrations) were determined for adsorbed myristic acid. The bands were chosen because they show the same shape for the different oxide layers and because of their comparably strong intensity, see Fig. 7. Absolute quantitative information, in terms of the amount of molecules per unit of surface area was not obtained. Despite this, a comparison among the different oxides is possible, which is considered to be the most important for the current work. Because of its large surface area and macroscopic roughness, the pseudoboehmite oxide is not included in this analysis.

The chemisorptive capacity of the oxide layers was found to be not determined by the contamination levels. The alkaline pretreated aluminium has the largest amount of contamination, but showed the most intense bands after adsorption, indicating the largest amount of chemisorbed molecules. This is because the non-functional contamination present on the oxides can be readily displaced, see Chapter 3.

A clear correlation was however found with the amount of hydroxyls on the oxide surfaces. This is shown in Fig. 9 in which the total integrated CH_2/CH_3 intensity is plotted versus the amount of hydroxyls, as found from the XPS measurements, see Table 1. It can be seen that with a larger amount of

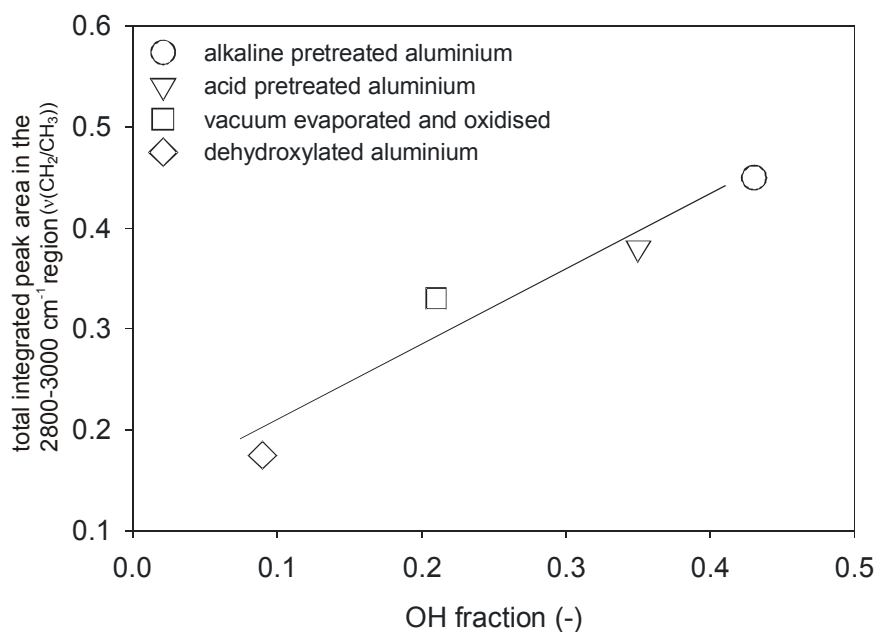


FIG. 9. Total integrated infrared peak area in the 3000-2800 cm^{-1} region ($\nu(\text{CH}_2/\text{CH}_3)$ vibrations) for myristic acid adsorbed on the differently prepared aluminium substrates as a function of the OH fraction on their surfaces.

hydroxyls on the oxide surface, also more carboxylic acid molecules are being chemisorbed. In an additional experiment, this correlation was further confirmed. A freshly evaporated and oxidised aluminium was heated in air at a temperature of 275 °C for 24 hours, resulting in the removal of hydroxyls [24,25,64]. The amount of subsequently chemisorbed myristic acid molecules dropped to that for the dehydroxylated aluminium.

It has been suggested before in the literature that the deprotonation of carboxylic acid groups proceeds through hydroxyls on the oxide surface, see Refs. [41,42,65-67] but as far as known, a direct relation has not been observed yet. It should be noted that multiple other factors however likely also play a role in determining the amount of chemisorbed molecules, like steric hindrance of the organic molecules and also intramolecular interactions [5]. Further, at an XPS detection angle of 15 degrees, still around five Al-O layers are being investigated [68] and so not all hydroxyls being detected, necessarily have to be accessible to the adsorbed molecules. In this context, it is also noted that the slope of the linear relation between the amount of hydroxyls and the peak intensity is smaller than unity.

In Fig. 7, the hydroxyl stretching region is shown for the alkaline pretreated aluminium, after the adsorption of myristic acid. The consumption of hydroxyls through deprotonation showed up in the hydroxyl stretching region as a broad negative band, centred at around 3420 cm^{-1} . This indicates consumption of

hydroxyls and also displacement of water from the oxide surface. The intensity of this band was observed to scale with the intensity of the CH_2/CH_3 stretching vibrations. The negative band was the most clearly visible for the hydroxyl-rich alkaline pretreated aluminium and pseudoboehmite. In Fig. 10, an illustration is shown of how a succinic acid molecule can become chemisorbed as a carboxylate with both of its ends through consumption of hydroxyls and displacement of water from the oxide surface [37,66,69,70]. The water molecule, generated in the process, is generally considered to become desorbed from the surface. See also Refs. [69,70] for a more detailed discussion.

5.4.4. Aqueous stability

Bolger *et al.* [17] suggested that the coordinative bonding between an aluminium oxide surface and a carboxylate is thermodynamically stable in aqueous environments. This is however not observed: an adsorbed layer of the monofunctional myristic acid becomes rapidly and fully displaced from the oxide

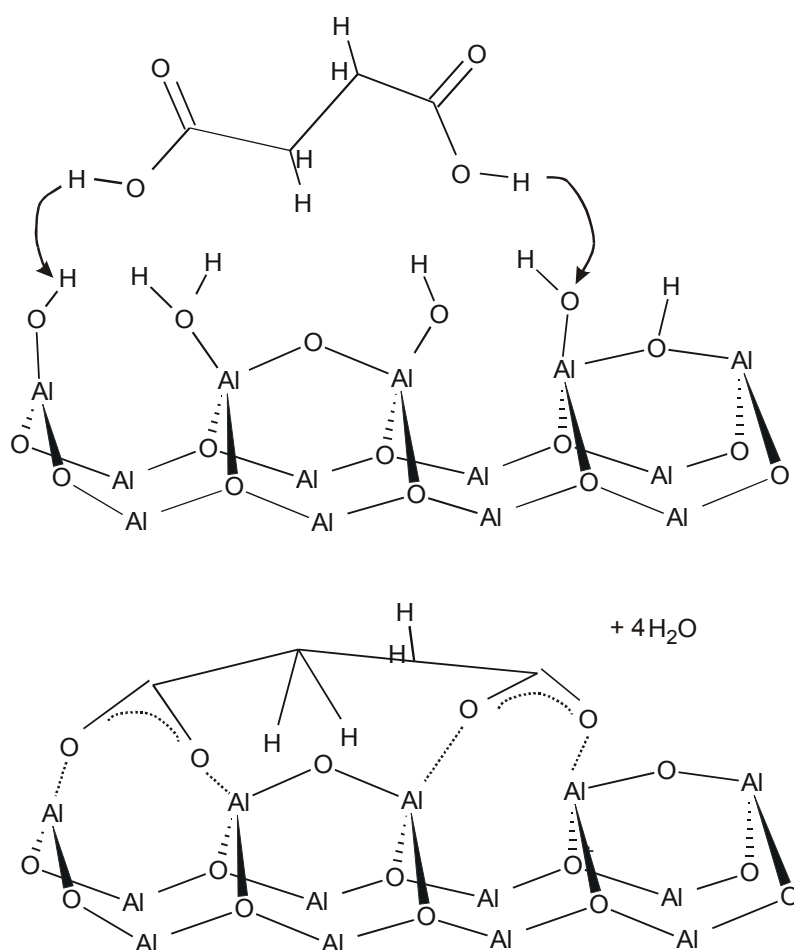


FIG. 10. Illustration of chemisorption of succinic acid on an aluminium oxide surface through the consumption of hydroxyls on the oxide surface.

surface when immersed in water, see Fig. 8. Allara *et al.* demonstrated that exchange with other species is still possible for coordinatively bonded n-alkanoic carboxylates. Moreover, Schneider *et al* [69,70] used cluster model and thermodynamics calculations to demonstrate that a chemisorbed carboxylate can be replaced by water. In contrast, the bifunctional succinic acid molecules remains chemisorbed to the surface for a prolonged period upon exposure to water. Similar differences for monofunctional and bifunctional carboxylic acids were also found by Dobson *et al* [71]. The difference in stability between the two compounds is likely a kinetic effect, due to the number of carboxylic acid groups per molecule. For succinic acid, two bonds need to be replaced by water simultaneously, before the whole molecule can be displaced from the surface and dissolved in water.

5.5. Conclusions

The chemical bonding of three different anhydride and carboxylic acid based model compounds with a set of differently prepared aluminium substrates has been investigated using infrared reflection absorption spectroscopy. All oxide layers are capable of hydrolysis of the anhydride group in succinic anhydride through physisorbed water on the oxide surface, resulting in the formation of succinic acid, having two carboxylic acid groups. Both of the carboxylic acid groups are deprotonated to form a coordinatively bonded carboxylate. The monofunctional myristic acid is also deprotonated on the oxide surface. The carboxylate species are found to coordinate to two aluminium cations in the oxide layer in a bridging bidentate conformation. The different oxide layers show minor differences in the bonding of the carboxylate, as evidenced from changes in carboxylate infrared peak positions. The differences are due to coordination to aluminium cations having a different electronic polarisability of their environment. The oxides show clear differences in the amount of chemisorbed molecules and a relation is established with the amounts of hydroxyls on the oxide surfaces. The coordinative bonding of a monofunctional carboxylic acid group on the oxide surface is not stable in an aqueous environment, while a bifunctional carboxylic acid group can resist water for a prolonged period of time.

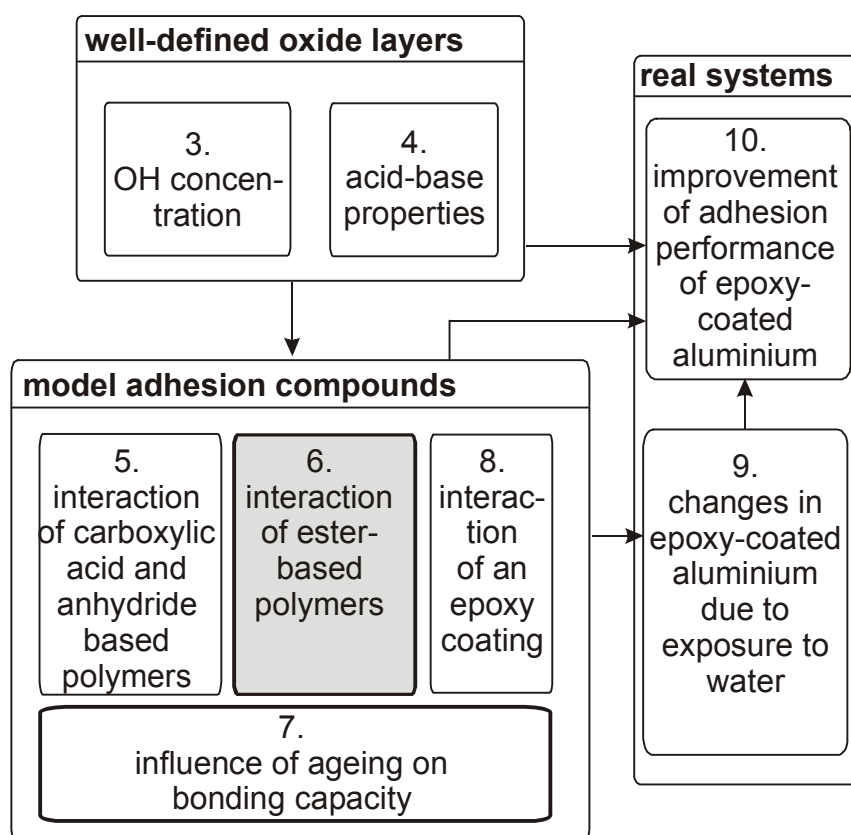
References

1. Lin, C. W.; Lee, W. L. *Journal of Applied Polymer Science* 1998, *70*(2), 383-387.
2. Roy, D.; Simon, G. P. *Polymer International* 2001, *50*(10), 1115-1123.
3. Roy, D.; Simon, G. P. *International Journal of Adhesion and Adhesives* 2002, *22*(5), 395-403.
4. Allara, D. L.; Nuzzo, R. G. *Langmuir* 1985, *1*(1), 52-66.
5. Tao, Y. T. *Journal of the American Chemical Society* 1993, *115*(110), 4350-4358.
6. Allara, D. L.; Nuzzo, R. G. *Langmuir* 1985, *1*(1), 45-52.
7. Strålin, A.; Hjertberg, T. *Journal of Adhesion Science and Technology* 1992, *6*(11), 1233-1250.
8. Alexander, M. R.; Beamson, G.; Blomfield, C. J.; Legget, G.; Duc, T. M. *Journal of Electron Spectroscopy and Related Phenomena* 2001, *121*(1-3), 19-32.
9. Marsh, J.; Minel, L.; Barthes-Labrousse, M.; Gorse, D. *Applied Surface Science* 1996, *99*(4), 335-343.
10. Marsh, J.; Minel, L.; Barthes-Labrousse, M.; Gorse, D. *Applied Surface Science* 1998, *133*(4), 270-286.
11. They, S.; Jacquet, D.; Mantel, M. *Journal of Adhesion* 1996, *56*(1-4), 1-13.
12. Szumilo, C.; Dubot, P.; Verchere, D.; Hocquaux, H.; Vilar, M.; Rei Dumas, P. *Journal of Adhesion Science and Technology* 1997, *11*(4), 553-572.
13. Abel, M. L.; Rattana, A.; Watts, J. F. *Journal of Adhesion* 2000, *73*(2-3), 313-340.
14. Terryn, H.; Vereecken, J.; de Jaeger, N. *Colloids and Surfaces A: Physicochemical and Engineering Aspects* 1993, *80*(2-3), 171-179.
15. Alwitt, R. S. The aluminium-water system, in *Oxides and oxide films vol. 4*, Diggle, J. W., editor; Dekker: New York, 1976; Chapter 3, pp. 169-250.
16. Knözinger, H.; Ratnasamy, P. *Catalysis Reviews - Science and Engineering* 1978, *17*(1), 31-70.
17. Bolger, J. C.; Michaels, A. S. *Interface conversion for polymer coatings*; Weiss, P.; Cheever, G. D., editors; Elsevier: New York, 1969; pp. 2-60.
18. Moretti, G.; Filippone, F.; Satta, M. *Surface and Interface Analysis* 2001, *31*(4), 249-254.
19. Wagner, C. D.; Joshi, A. *Journal of Electron Spectroscopy and Related Phenomena* 1988, *47* 283-313.
20. Moretti, G. *Journal of Electron Spectroscopy and Related Phenomena* 1998, *95*(2-3), 95-144.
21. McCafferty, E.; Wightman, J. *Journal of Colloid and Interface Science* 1997, *194*(2), 344-355.
22. Dartevelle, C.; McAlpine, E.; Thompson, G. E.; Alexander, M. R. *Surface and Coatings Technology* 2003, *173*(2-3), 249-258.
23. Kiss, A. B.; Kerezturny, G.; Farkas, L. *Spectrochimica Acta Part A* 1980, *36*(7), 653-658.
24. Peri, J. B.; Hamman, R. B. *Journal of Physical Chemistry* 1960, *64*(10), 1526-1530.
25. Peri, J. B. *Journal of Physical Chemistry* 1965, *69*(1), 211-219.
26. Hass, K. C.; Schneider, W. F.; Curioni, A.; Andreoni, W. *Journal of Physical Chemistry Part B* 2000, *104*(23), 5527-5540.
27. Busca, G. *Physical Chemistry Chemical Physics* 1999, *1*(5), 723-736.
28. Digne, M.; Sautet, P.; Raybaud, P.; Euzen, P.; Toulhoat, H. *Journal of Catalysis* 2002, *211*(1), 1-5.
29. Raybaud, P.; Digne, M.; Iftimie, M.; Wellens, M.; Euzen, P.; Toulhoat, H. *Journal of Catalysis* 2001, *201*(2), 236-246.
30. Vlaev, L.; Damyanov, D.; Mohamed, M. M. *Colloids and Surfaces* 1989, *36*(4), 427-437.
31. van Gils, S.; Melendres, C. A.; Terryn, H. *Surface and Interface Analysis* 2003, *35*(4), 387-394.
32. Melendres, C. A.; van Gils, S.; Terryn, H. *Electrochemistry Communications* 2001, *3*(12), 737-741.
33. Wernick, S.; Pinner, R.; Sheasby, P. G. *The surface treatment and finishing of aluminium and its alloys*; 5 ed.; Teddington: 1987; Vol. 1.
34. Berrada, K.; Dumas, P. *Journal of Electron Spectroscopy and Related Phenomena* 1990, *54* 1153-1162.
35. Roeges, N. P. G. *A guide to the complete interpretation of infrared spectra of organic structures*; Wiley: Chichester, 1994.
36. Suzuki, M.; Shimanouchi, T. *Journal of Molecular Spectroscopy* 1968, *28*(3), 394-410.

37. Hill, I. R.; Levin, I. W. *Journal of Chemical Physics* 1979, *70*(2), 842-851.
38. Schlotter, N. E.; Porter, M. D.; Bright, T. B.; Allara, D. L.; . *Chemical Physics Letters* 1986, *132*(1), 93-98.
39. Sivel, V. G. M.; van den Brand, J.; Wang, W. R.; Mohdadi, H.; Tichelaar, F. D.; Alkemade, P. F. A.; Zandbergen, H. W. *Journal of Microscopy* 2003, *accepted*.
40. Do, N. T.; Baerns, M. *Applied Catalysis* 1988, *45*(1), 9-26.
41. Evans, H. E.; Weinberg, W. H. *Journal of Chemical Physics* 1979, *71*(12), 4789-4798.
42. Hall, J. T.; Hansma, P. K. *Surface Science* 1978, *77*(1), 61-76.
43. Alexander, M. R.; Payan, S. *Surface and Interface Analysis* 1998, *26*(13), 961-973.
44. Hu, H.; Saniger, G.; Garciaalejandro, J.; Castano, V. M. *Materials Letters* 1991, *12*(4), 281-285.
45. Martin, D. S.; Cole, R. J.; Haq, S. *Surface Science* 2003, *539*(1-3), 171-181.
46. Martin, D. S.; Cole, R. J.; Haq, S. *Physical Review B* 2002, *66*(15), 155427.
47. Bellamy, L. J. *The infrared spectra of complex molecules. Vol. 1*; 3rd ed.; Chapman and Hall: New York, 1978.
48. Yao, H. L.; Yeh, H. H. *Langmuir* 1996, *12*(12), 2981-2988.
49. Nara, M.; Torii, H.; Tasumi, M. *Journal of Physical Chemistry* 1996, *100*(51), 19812-19817.
50. Alcock, N. W.; Tracy, V. M. *Journal of the Chemical Society: Dalton Transactions I* 1976, *21* 2243-2249.
51. Davydov, A. A.; Rochester, C. H. *Infrared spectroscopy of adsorbed species on the surface of transition metal oxides*; Wiley: Chichester, 1990.
52. Deacon, G. B.; Phillips, R. J. *Coordination Chemistry Reviews* 1980, *33*(3), 227-250.
53. Ohe, C.; Ando, N.; Sato, Y.; Urai, M.; Yamamoto, M.; Itoh, K. *Journal of Physical Chemistry Part B* 1999, *103*(3), 435-444.
54. Boerio, F. J.; Boerio, J. P.; Bozian, R. C. *Applied Surface Science* 1988, *31*(1), 42-58.
55. Gericke, A.; Huhnerfuss, H. *Thin Solid Films* 1994, *245*(1-2), 74-82.
56. Simon-Kutscher, J.; Gericke, A.; Huhnerfuss, H. *Langmuir* 1996, *12*(4), 1027-1034.
57. Cameron, D. G.; Umemura, J.; Wong, P. T. T.; Mantsch, H. H. *Colloids and Surfaces* 1982, *4*(2), 131-145.
58. Brunner, H.; Mayer, U.; Hoffmann, H. *Applied Spectroscopy* 1997, *51*(2), 209-217.
59. Liakos, I. L.; Newman, R. C.; McAlpine, E.; Alexander, M. R. *Surface and Interface Analysis* 2004, *36* 347-354.
60. Allara, D. L.; Parikh, A. N.; Judge, E. *Journal of Chemical Physics* 1994, *100*(2), 1761-1764.
61. Zhuang, G.; Chottiner, G. *Review of Scientific Instruments* 1994, *65*(8), 2494-2499.
62. Wang, X. D.; Tysoe, W. T.; Greenler, R. G.; Truszkowska, K. *Surface Science* 1991, *258*(1-3), 335-345.
63. Hayden, B. E.; Prince, K.; Woodruff, D. P.; Bradshaw, A. M. *Surface Science* 1983, *133*(2-3), 589-604.
64. Alexander, M. R.; Thompson, G. E.; Beamson, G. *Surface and Interface Analysis* 2000, *29*(7), 468-477.
65. Kiselev, A. V.; Uvarov, A. V. *Surface Science* 1967, *6*(4), 399-421.
66. Buckland, A. D.; Rochester, C. H.; Topham, S. A. *Journal of the Chemical Society: Faraday Transactions I* 1980, *76* 302-313.
67. Karaman, M. E.; Antelmi, D. A.; Pashley, R. M. *Colloids and Surfaces* 2001, *182*(1-3), 285-298.
68. Jeurgens, L. P. H.; Sloof, W. G.; Tichelaar, F. D.; Mittemeijer, E. J. *Physical Review B* 2000, *62*(7), 4707-4719.
69. Schneider, B. PhD thesis University of Saarland, 2001.
70. Schneider, B.; Possart, W. *Journal of Adhesion* 2004, (to be published).
71. Dobson, K.; McQuillan, A. J. *Spectrochimica Acta Part A* 1999, *55*(7-8), 1395-1405.

CHAPTER 6.

INTERACTION OF ESTER FUNCTIONAL GROUPS WITH ALUMINIUM OXIDE SURFACES STUDIED USING INFRARED REFLECTION ABSORPTION SPECTROSCOPY ¹



¹ This chapter was published as a scientific paper:
J. van den Brand, O. Blajiev, P.C.J. Beentjes, H. Terryn, J.H.W. de Wit
Langmuir, 20(15), 6318-6326, 2004

Synopsis

Ester functional groups can be found in many different polymers like PMMA, polyester and PET, which are frequently applied onto aluminium surfaces. A good understanding of how these groups bond to the oxide surface and how this is influenced by the composition and chemistry of the oxide layer is important. Moreover, it is also important to know their bonding stability in the presence of water. In this chapter, the interaction of ester functional groups with the aluminium oxide surface is studied following the model adhesion compound approach also used in Chapter 5. The model compounds are chosen to represent different, commonly used ester-based polymers. The interaction of the model compounds is studied with the same set of five differently prepared aluminium substrates as were studied in Chapters 3 and 4 using XPS. This allows determining the relation between composition and chemistry of the oxide layer and the subsequent interaction with the ester functional groups. It is found that bonding of the ester functional groups is the same for all substrates and occurs exclusively through hydrogen-bonding with hydroxyls on the oxide surface. For this reason, more ester model compound molecules are found to bond to the more hydroxyl-rich oxide surfaces. The bonding stability in the presence of water is found to be not very good.

6.1. Introduction

Ester functional groups ($\text{C}(=\text{O})\text{O}$) can be found in many different polymers like PMMA, polyester and PET, which are frequently applied onto aluminium surfaces. The carbonyl ($\text{C}=\text{O}$) of the ester has the capability of Lewis acid-base bonding, relatively weakly to hydroxyls [1,2] or more strongly to incompletely coordinated cations on the oxide surface [3]. Some authors also find that the ester functional group is saponified on the oxide surface [4,5]. A carboxylate is then formed, which chemisorbs on the oxide surface. The aluminium substrate is often given a surface treatment prior to application of an organic overlayer like a coating or an adhesive. The surface treatment leads to changes in the oxide chemistry and composition, which will have a direct influence on the subsequent bonding behaviour with the organic functional groups [6,7]. Strålin *et al.* for example found that the ester groups of an EVA polymer showed a stronger bonding to a pseudoboehmite aluminium oxyhydroxide than to a dehydroxylated aluminium oxide [7].

Because of the widespread use of polymer-coated aluminium, knowledge of the nature of the ester-oxide bond is important. Also, it is important to understand the way it is influenced by the oxide layer chemistry and composition and to know the stability of this bond in an aqueous environment. Such knowledge would ultimately allow tailoring of the aluminium oxide surface to obtain a specific bonding with an organic overlayer.

For polymeric coatings and adhesives, the study of the chemical bonding with the oxide surface is experimentally difficult because of the buried oxide/polymer interface. To allow for such a study, the polymer can be either applied as a very thin layer [1] or it can be simplified to model compounds that represent the bonding functionality. The compounds are applied as a thin layer on the oxide surface and the interaction is studied by various methods for example X-ray photoelectron spectroscopy (XPS) [8-10], time-of-flight secondary ion mass spectroscopy (TOF-SIMS) [11] or infrared reflection absorption spectroscopy (FTIR-RAS) [12,13]. The model compound approach has the advantage that the bonding can be studied accurately and the obtained spectra do not have contributions due to the bulk of the layer.

In this Chapter, the bonding of two ester-based model compounds to a set of five different aluminium oxide layers has been investigated using FTIR-RAS. The technique is highly suitable for this purpose. Upon interaction with the oxide surface, the carbonyl of the ester group is expected to either partially donate to or accept electrons from sites on the oxide surface [2]. This results in a modification of the force constant of the (C=O) carbonyl stretching vibration and therefore in an infrared peak shift [14]. Moreover, saponification of the ester group and the formation of a carboxylate can be readily identified [5].

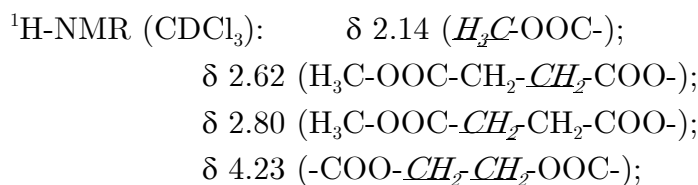
The bonding-stability of the two ester-based compounds on the oxide surface, in an aqueous environment and in presence of a compound which is capable of chemisorption to the aluminium oxide surface has been evaluated.

The various oxide layers to which the bonding was investigated were made by giving different, relatively simple, but typical surface treatments to the aluminium substrate. The same set of oxide layers has been investigated in Chapters 3 and 4 using XPS to determine their composition and localised acid-base properties. These results are briefly summarised here as they are relevant for the current work to evaluate the relation between the composition and chemistry of the oxide and the bonding behaviour of the ester groups.

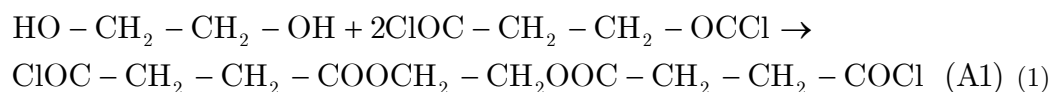
6.2. Experimental

6.2.1. Materials

Two different ester-based model compounds were studied. The first one of them, glycol di-(monomethylsuccinic acid) ester contains four ester groups and was chosen to model a polyester polymer². Its structure is shown in Fig. 1. The compound was prepared by adding glycol to an excess of succinyl chloride, thereby producing the intermediate product A1, reaction 1. The excess succinyl chloride was removed by vacuum distillation. An excess of dry methanol was added to the intermediate product A1, dissolved in dry CH₂Cl₂ and 1 ml dry methanol was added, reaction 2. The mixture was stirred for 2 hours at room temperature and the solvent was evaporated. Recrystallisation was performed using CH₂Cl₂/hexane. The yield was 42% and the reaction product was identified by using ¹H-NMR, resulting in:



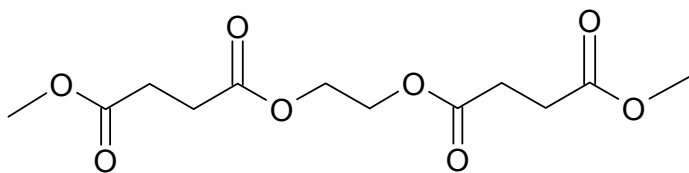
(δ being the ¹H-NMR chemical shift relative to the tetra methyl silane standard).



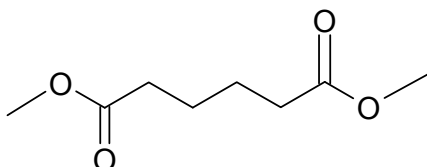
The second compound studied, dimethyl adipate, has two ester groups, see Fig. 1. It was obtained from Sigma-Aldrich as a 99+% purity and was used without further purification.

Succinic acid (HOOC-CH₂CH₂-COOH) was obtained from Sigma-Aldrich as a 99.5+% purity and used without further purification. Chloroform, 2 chloromethane, THF and ethanol were obtained from Sigma-Aldrich, 2 chloroethanol was obtained from Riedel de Haen and 2,2,2 trichloroethanol was obtained from Fluka. All solvents used were obtained as a >99 vol.% purity.

² The preparation route for glycol di-(monomethylsuccinic acid) ester was derived by Peter Beentjes, Corus RD&T. The preparation of the compound was done by Polymer Service Centre Groningen.



glycol di-(monomethylsuccinic acid) ester



dimethyl adipate

FIG. 1 Molecular structure of the two studied ester-based compounds.

6.2.2. Aluminium oxide layers, application method and infrared analysis

The differently prepared aluminium substrates were the same as studied in Chapters 3, 4 and 5. See paragraph 3.2.1 on page 23 and paragraph 5.2.1 on page 62 for their preparation procedure.

The compounds were dissolved in chloroform. For glycol di-(monomethylsuccinic acid) ester, the concentration in solution was modified so saturation coverage of the oxide layer was obtained and excess, non-bonding molecules were not present, see furtheron. For dimethyl adipate, a concentration of ~0.01 g/l was used. The concentration was found to be not very important for this compound since excess molecules sublimed from the surface.

After preparation of the substrates, a background infrared spectrum was recorded. Immediately after this the substrates were immersed in the compound mixture, allowed to react for a period of 15 minutes and then slowly withdrawn at a constant and uniform speed. Longer immersion times (tested up to 1 hour) did not have a significant effect on the obtained results. The substrates were directly transferred from the solvent mixture into the infrared apparatus. The infrared measurements were performed following the same procedure as in Chapter 5. See paragraph 5.2.4 on page 63 for more details.

6.2.3. Determination of carbonyl peak contributions using curve-fitting

Curve-fitting of the main carbonyl peak was performed to determine the constituting components. Gauss-Lorentz peak shapes were used and the widths and shapes for the different fit components in the peak were allowed to change during the fit. No restrictions were imposed on the peak positions of the different components. The fitting was performed in the 1850-1650 cm^{-1} region, after subtraction of a linear background.

6.3. Results

6.3.1. FTIR, XPS and BET investigation of oxide surfaces

The different oxide layers have been investigated in Chapters 3 and 4 using X-ray photoelectron spectroscopy (XPS) and the Brunauer Emmett and Teller (BET) method, see Chapter 5, to obtain information on their composition, acid-base properties, amounts of adventitious contamination and effective surface areas. The obtained results are discussed in detail in the previous Chapters and a summary of them is given in Table 1.

TABLE 1. Summary of results obtained from XPS and BET measurements performed on the different oxide layers. The results are discussed in more detail in the previous Chapters.

type of oxide	OH fraction (-)	O BE (eV)	OH BE (eV)	contamin ation layer thickness (nm)	geometric area increase factor (-)
dehydroxylated aluminium	0.09	531.1	532.4	0.1	1.3
evaporated and oxidised aluminium	0.21	531.1	532.4	0.1	-
acid pretreated aluminium	0.35	531.0	532.4	0.3	1.4
alkaline pretreated aluminium	0.43	530.9	532.3	0.4	1.6
pseudoboehmite	0.47	530.4	531.8	0.2	14.6
	0.04 H ₂ O		533.7		

The XPS measurements were performed at a detection angle of 15 degrees with respect to the sample surface to obtain maximum surface sensitivity. The oxides have different amounts of hydroxyls on their surfaces, which was determined by curve-fitting of the O *1s* core level peak, see Chapter 3. The obtained values are reported in the first column of Table 1, as a fraction of the total O *1s* peak intensity. For pseudoboehmite, an additional component due to water was found to be present in the O *1s* peak, which is due to interlamellar water that is present inside the oxide layer [15].

The core level binding energies can be used to evaluate the acid-base properties of the ions on the oxide surface, provided that the oxides are structurally comparable, see Chapter 4. The binding energies of the O and OH components, resolved from the O *1s* peak using curve-fitting, are reported in columns 2-3 of Table 1. Despite the fact that quite different methods are used to prepare the layers, significant differences in core level binding energies are not observed. The oxides therefore have the same acid-base properties for the respective O and OH sites on their surfaces. The structurally different pseudoboehmite oxide deviates, having a much lower binding energy and therefore more basic O and OH sites, see Chapter 4.

Ambient-exposed oxide layers are inevitably contaminated by adventitious carbon overlayers. The amount of contamination on the oxides is reported in column 4 of Table 1, as an equivalent carbon layer thickness. They were determined from the intensities of the XPS C *1s* core level peak, see Chapter 3. The obtained values indicate that the contamination levels are relatively low for the studied oxides [16,17]. Analysis of the XPS C *1s* peak showed that the contamination layer is composed almost exclusively of unreactive C-C/C-H components (>95%), see Chapter 3. The contamination overlayers are therefore only loosely bound and can be readily displaced by more reactive functional groups (i.e. the solvent or the model compounds).

The specific surface areas of the oxide layers were determined using the BET method, see Chapter 5. This technique is considered to be the most suitable for the current work because it directly measures the real physical magnitude of the surface area of the oxide surfaces. Krypton was used as the adsorption gas, because of the low surface area of the samples. For practical reasons, BET measurements were not performed on the evaporated and oxidised aluminium. The values are reported as a multiplication factor with respect to the geometric area that was put in the sample cell in the last column in Table 1. The surfaces show on average an about 1.5 times increase as compared to the geometric surface area. The alkaline and acidic etching pretreatments do not give significantly higher surface areas. Although these surface treatments are known

to cause enhancement of surface area, the pretreatment times were deliberately kept short, see the Experimental section, to limit the effect of this. The BET measurements thus show that the surfaces are well-comparable with respect to their surface areas. Only pseudoboehmite shows a significant increase in surface area, which is due to the rough and porous nature of this layer [15,18,19].

6.3.2. Glycol di-(monomethylsuccinic acid) ester adsorbed on the different aluminium oxide surfaces

In Fig. 2, the 1850-1650 cm^{-1} carbonyl region is shown for glycol di-(monomethylsuccinic acid) ester on the alkaline pretreated type of oxide layer, applied using dip-coating from different concentrations of the compound in

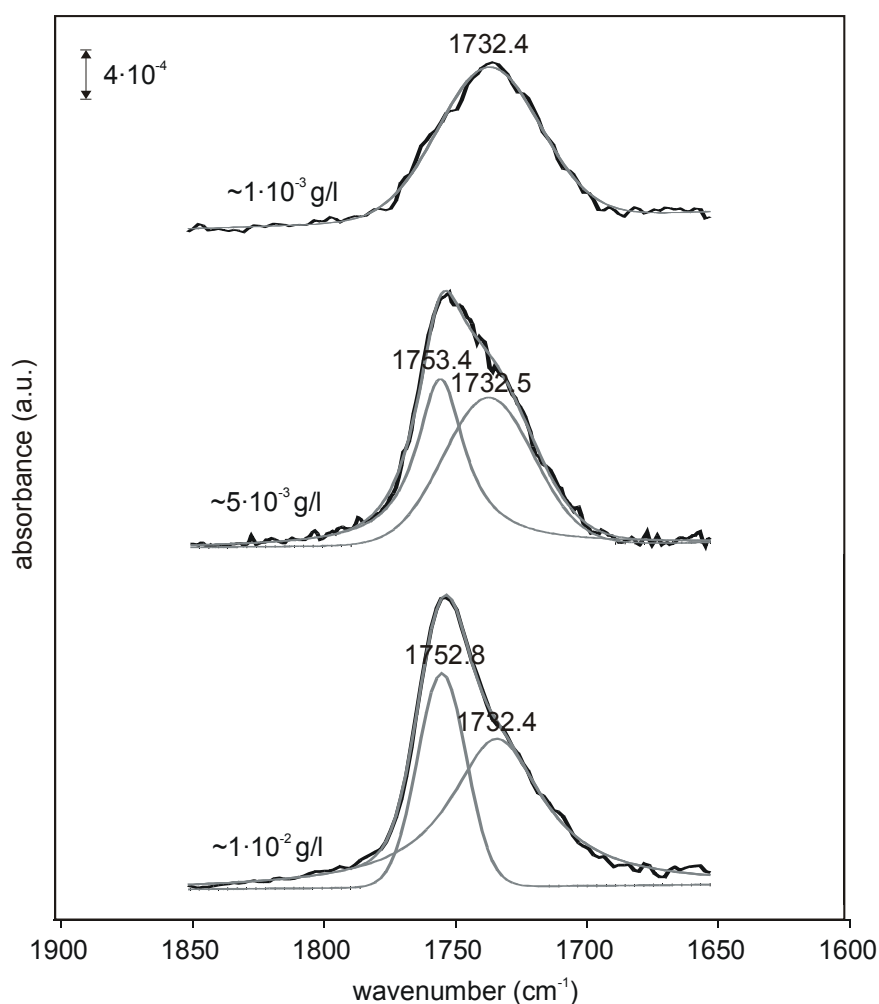


FIG. 2. FTIR-RAS spectra of glycol di-(monomethylsuccinic acid) ester on the alkaline pretreated type of aluminium as applied from three different concentrations (indicated) in chloroform using dip-coating. The experiments were performed on different samples. The fits had an r^2 goodness of fit of respectively 0.998, 0.995 and 0.997, from top to bottom.

chloroform ($\sim 1 \cdot 10^{-3}$, $5 \cdot 10^{-3}$ and $1 \cdot 10^{-2}$ g/l). At the highest concentration of $\sim 1 \cdot 10^{-2}$ g/l, the $\nu(\text{C}=\text{O})$ carbonyl band has a clear asymmetric shape, while at the lowest concentration of $\sim 1 \cdot 10^{-3}$ g/l, the carbonyl band has a symmetric shape. Peak distortion due to a contribution of the refractive index $n(\nu)$, as a result of optical effects in reflection measurements, is not a reason for the asymmetrically shaped peaks. The studied layers are very thin (estimated to be a few monolayers, with consequently not very intense peaks) and therefore the contribution of the refractive index $n(\nu)$ to the measured spectrum is limited [20]. Indeed, based on a limited investigation using Fresnel equations, the effect was found to be limited for the studied compounds and range of thicknesses.

Using curve-fitting, the asymmetric bands were found to be composed of two peaks, located at around 1753 and around 1732 cm^{-1} . The curve-fitting results showed that with an increasing lower concentration of the molecules in the solvent, the peak at 1753 cm^{-1} reduces in intensity, while the peak at 1732 cm^{-1} has a constant intensity. The peak at 1753 cm^{-1} corresponds to free carbonyls that are not involved in an interaction with the oxide surface and correspond to excess, non-bonding molecules. At a lower concentration of the molecules in solution, less free carbonyls are present, as evidenced from the decreasing 1753 cm^{-1} peak. The peak at 1732 cm^{-1} is due to molecules that are involved in bonding with the oxide surface and its intensity is expected and observed not to change with the concentration in solution for the considered range. The band obtained for the lowest concentration of $\sim 1 \cdot 10^{-3}$ g/l, see Fig. 2, can be described using a single, symmetrically shaped peak. The infrared spectrum therefore fully corresponds to molecules that are involved in bonding with the oxide surface. The absence of a carbonyl peak due to free carbonyls also indicates that the adsorbed glycol di-(monomethylsuccinic acid) ester molecules are bonded with all of their four ester groups to the oxide surface.

In Fig. 3, infrared spectra are provided as obtained for glycol di-(monomethylsuccinic acid) ester on the different oxide surfaces. For each oxide, the concentration was modified so no excess, non-bonding molecules were present anymore, see Fig. 2. The used concentration varied from $\sim 1 \cdot 10^{-3}$ g/l for the alkaline pretreated, see Fig. 2, to $\sim 5 \cdot 10^{-4}$ g/l for the dehydroxylated type of oxide.

For all oxides, the spectra show a broad $\nu(\text{C}=\text{O})$ carbonyl stretching vibration band, located at 1732 cm^{-1} . The FWHM (full width at half maximum) of the peak is roughly constant for the different oxides, having a value of 41 cm^{-1} . This is considerably larger than the peak width for free carbonyls, see Fig. 2, which have FWHM peak width of around 23 cm^{-1} . Besides the carbonyl

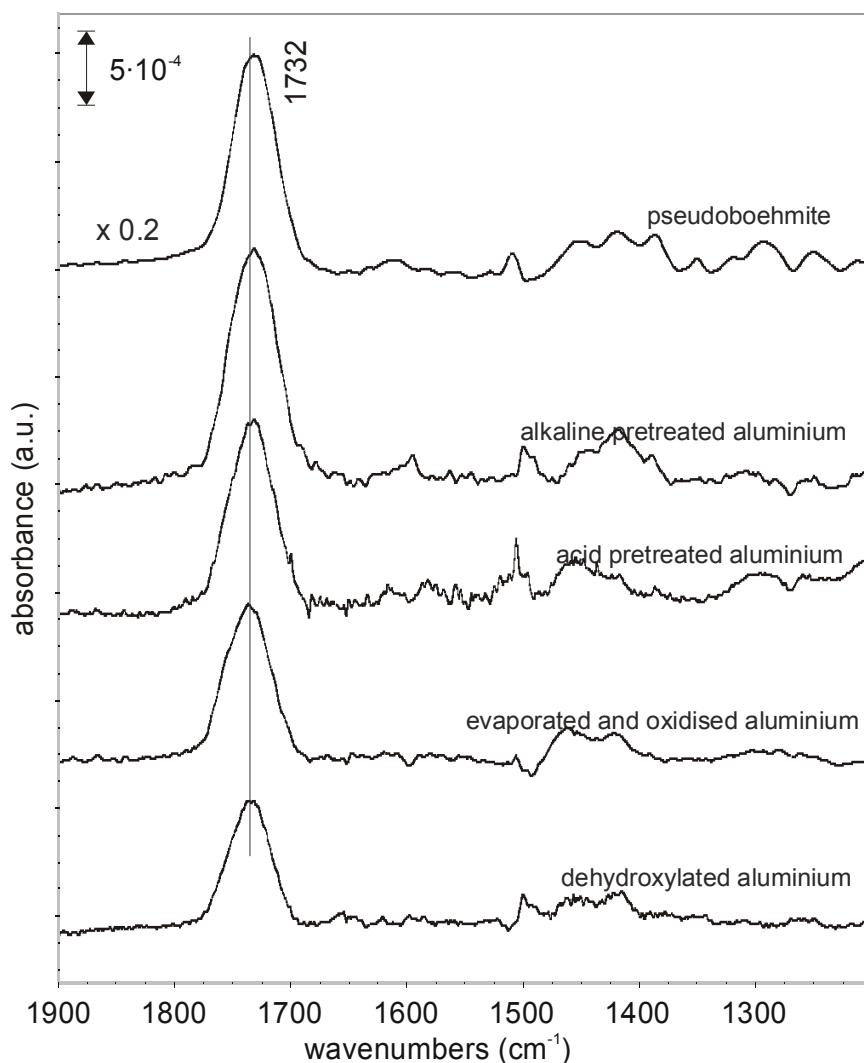


FIG. 3. FTIR-RAS spectra of glycol di-(monomethylsuccinic acid) ester on the different aluminium oxide surfaces.

stretching vibrations, the spectra only show minor, broad and unresolved peaks in the 1500-1400 cm⁻¹ region, which are due to CH₂ and CH₃ vibrations [21].

6.3.3. Dimethyl adipate adsorption on the different oxide surfaces

In Fig. 4, infrared spectra are shown of a multilayer of dimethyl adipate on the pseudoboehmite type of oxide, obtained respectively 5 and 10 minutes after the adsorption of a multilayer. The $\nu(\text{C}=\text{O})$ carbonyl stretching vibration band can be described using two peaks, the first one representing the free carbonyls at 1746 cm⁻¹ and the second at a lower wavenumber of 1720 cm⁻¹ representing carbonyls that are bonded to the oxide surface.

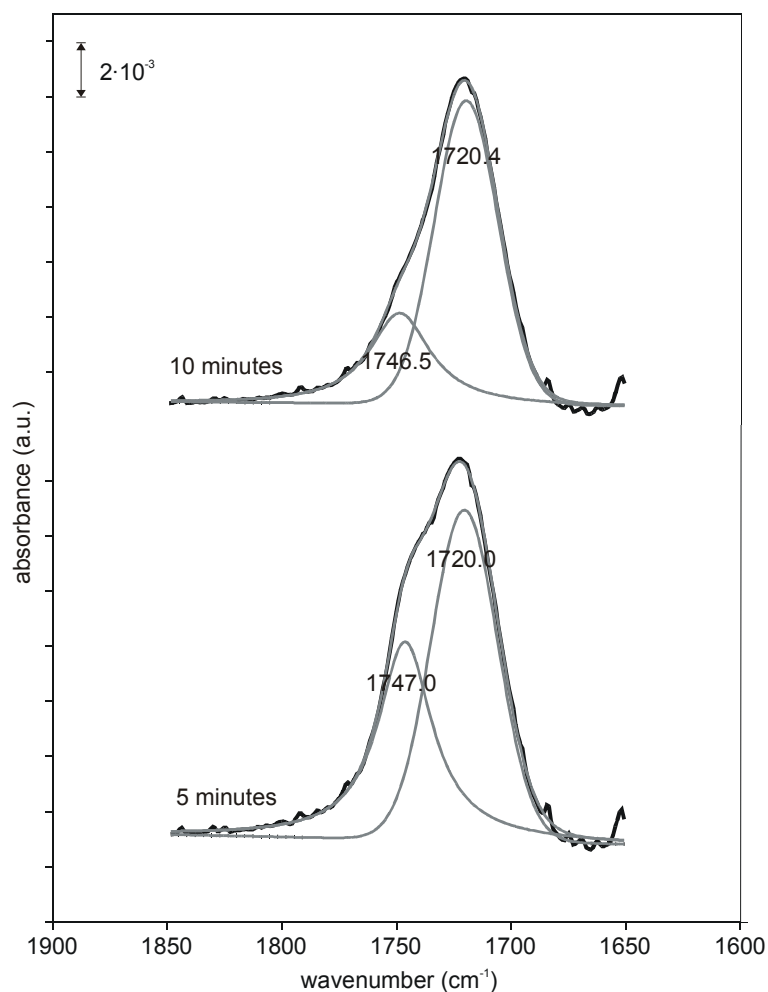


FIG. 4. FTIR-RAS spectra of dimethyl adipate on the pseudoboehmite type of oxide. Spectra obtained 5 (bottom) and 10 (top) minutes after adsorption of a multilayer. The fits had an r^2 goodness of fit of respectively 0.995 and 0.997, from top to bottom

The dimethyl adipate molecules not bonded to the oxide surface were found to sublime from the surface and therefore the intensity of the peak at 1746 cm⁻¹ decreases with time, while the peak at 1720 cm⁻¹ has a constant intensity, see Fig. 4. Eventually, the 1746 cm⁻¹ peak completely disappears due to sublimation and only the bonded molecules remain adsorbed. In Fig. 5, spectra are shown for adsorption on three of the studied oxides. For the different oxides, the $\nu(\text{C}=\text{O})$ carbonyl stretching vibration was found to have a constant value of 1720 cm⁻¹. The FWHM peak width of the carbonyl stretching vibration is roughly constant for the different oxides, having an average FWHM peak width of 34 cm⁻¹. This value is larger than the value obtained for the free carbonyls in the bulk of the layer, which shows a FWHM peak width of 25 cm⁻¹.

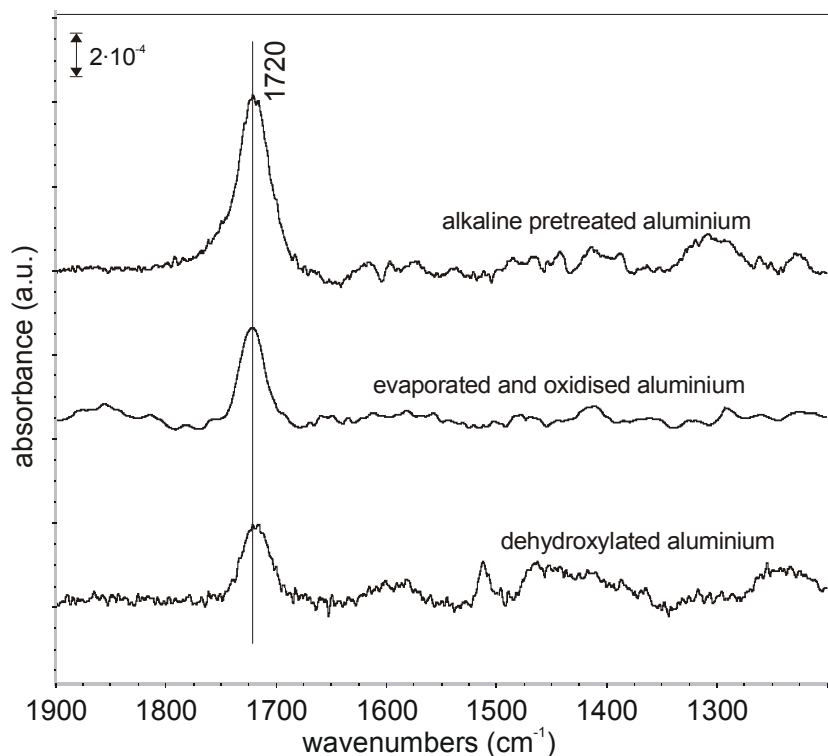


FIG. 5. FTIR-RAS spectra of the dimethyl adipate compound, adsorbed on three of the different aluminium oxide surfaces.

6.3.4. Transmission spectra of molecules in different solvents

The carbonyl of the ester has the capability of Lewis acid-base bonding, to hydroxyls or to incompletely coordinated cations on the oxide surface. Moreover, saponification of the ester groups may take place on the oxide surface and a carboxylate is then formed. Because of the strong electron-accepting nature of incompletely coordinated metal cations on the oxide surfaces, bonding to these sites is expected to result in significantly larger wavenumber shifts than for bonding to hydroxyls [22,23]. Kiselev *et al.* [3] studied the adsorption of acetone on aluminium oxides in an ultrahigh vacuum environment.

The free $\nu(\text{C}=\text{O})$ carbonyl stretching vibration peak was found at 1720 cm⁻¹. When adsorbed on the oxide surface, they observed peaks at 1692 cm⁻¹, 1625 cm⁻¹ and 1600 cm⁻¹. The 1692 cm⁻¹ was ascribed to the acetone molecules which were hydrogen-bonded to hydroxyls, while the other two peaks at 1625 and 1605 cm⁻¹ were ascribed to acetone, bonded to incompletely coordinated aluminium cations. Peaks at or close to these positions are not observed for the oxides studied, see Fig. 3 and 5. For the studied *ambient-exposed* oxide surfaces, incompletely coordinated cations are therefore likely not exposed at the surface, because the strong acidic centres readily react away with oxygen and water

from the ambient. This is confirmed by work of Ma *et al.* [24]. They found incompletely coordinated metal cations to be present on oxide surfaces, when dehydroxylated in an ultra-high vacuum environment, but absent on surfaces that were exposed to the ambient environment. Some authors have shown that aluminium oxide surfaces are capable of saponification of the ester group, which then forms a carboxylate anion that subsequently reacts with the oxide surface to form a chemisorbed carboxylate [5]. While a wide variety of differently prepared aluminium oxides was investigated in this work, none of them were however capable of saponification, as evidenced by the absence of infrared peaks, representing carboxylate species. This does correspond well to results found by other authors [1,1,2,6]. Strålin *et al.* [7] showed that saponification of the ester group only occurs at high temperatures.

Excluding these two bonding mechanisms, leaves bonding to hydroxyls as an explanation for the results obtained upon adsorption of the compounds on the oxide surfaces.

Infrared transmission measurements were performed of glycol di-(monomethylsuccinic acid) ester and dimethyl adipate in a range of solvents with different electrophilicities [14] and with and without hydroxyl functionality. This gives information on the $\nu(\text{C}=\text{O})$ carbonyl stretching peak shifts that the two compounds show when electrons are withdrawn from the carbonyl oxygen of their ester groups and on the peak shifts that occur when the ester groups are involved in hydrogen-bonding. With an increasing electrophilicity of the solvent, to an increasingly larger extent negative charge is withdrawn from the carbonyl oxygen, resulting in an increasing downward shift of the $\nu(\text{C}=\text{O})$ carbonyl stretching band. In Table 2, the obtained $\nu(\text{C}=\text{O})$ carbonyl stretching vibration peak positions and the associated FWHM peak widths are summarized. In Fig. 6, as an example, the $\nu(\text{C}=\text{O})$ carbonyl stretching region is shown for the compounds in respectively chloroform and 2-chloroethanol.

The components present in the $\nu(\text{C}=\text{O})$ carbonyl stretching bands were resolved by curve-fitting. In the aprotic solvents, the band can be described by a single, symmetrically shaped peak. For the protic solvents, the carbonyl stretching band consists of an additional peak, due to intermolecular hydrogen bonding of the carbonyl to the labile proton [25,26]. Overall, the compounds show comparable shifts in the different solvents, with the $\nu(\text{C}=\text{O})$ carbonyl stretching peak positions of glycol di-(monomethylsuccinic acid) ester being always higher by 3-5 cm^{-1} than for dimethyl adipate, see Table 2. The two compounds show comparable FWHM peak widths of the carbonyl bands in the different solvents. The higher $\nu(\text{C}=\text{O})$ for glycol di-(monomethylsuccinic acid)

ester indicates that the carbonyls are slightly more acidic than in dimethyl adipate [26]. The acidity of the solvent hydroxyls increases in the order methanol < 2 chloroethanol < 2,2,2 trichloroethanol. The strong electron-withdrawing nature of the chlorine atoms leads to less negative charge on the oxygen of the hydroxyl, thereby leaving a more positively charged and so more acidic proton. The more acidic proton is then a stronger electron acceptor towards the lone pair electrons on the carbonyls. Hydrogen-bonding to increasingly more acidic protons results in an increasing downward shift of the

$\nu(\text{C}=\text{O})$ carbonyl stretching band. Generally, the peak separation between the main carbonyl vibration peak (highest wavenumber) and the peak representing intermolecular hydrogen bonding (lowest wavenumber) is considered as a measure for the relative strength of the hydrogen bond that the carbonyl is involved in [26]. This separation increases in the order in which the acidity of the solvent protons increases, see Table 2.

TABLE 2. $\nu(\text{C}=\text{O})$ carbonyl stretching vibration peak positions and corresponding FWHM peak widths for the compounds in different solvents as measured from FTIR-transmission measurements. The peak positions were resolved using curve-fitting.

solvent	glycol di- (monomethylsuccinic acid)		dimethyl adipate	
	$\nu(\text{C}=\text{O})$ (FWHM) (cm^{-1})	$\nu(\text{C}=\text{O}:\text{HO})$ (FWHM) (cm^{-1})	$\nu(\text{C}=\text{O})$ (FWHM) (cm^{-1})	$\nu(\text{C}=\text{O}:\text{HO})$ (FWHM) (cm^{-1})
chloroform	1736.6 (25)		1731.9 (28)	
dichloromethane	1737.2 (23)		1733.6 (22)	
ethanol	1743.5 (16)	1726.8 (15)	1740.7 (15)	1723.2 (18)
2 chloroethanol	1739.9 (22)	1722.0 (24)	1736.6 (18)	1717.3 (27)
2,2,2 trichloroethanol	1742.4 (23)	1721.2 (23)		1714.2 (26)
tetrahydrofuran	1744.4 (17)		1741.1 (15)	
free carbonyls in bulk layer	1753.2 (23)		1746.8 (25)	

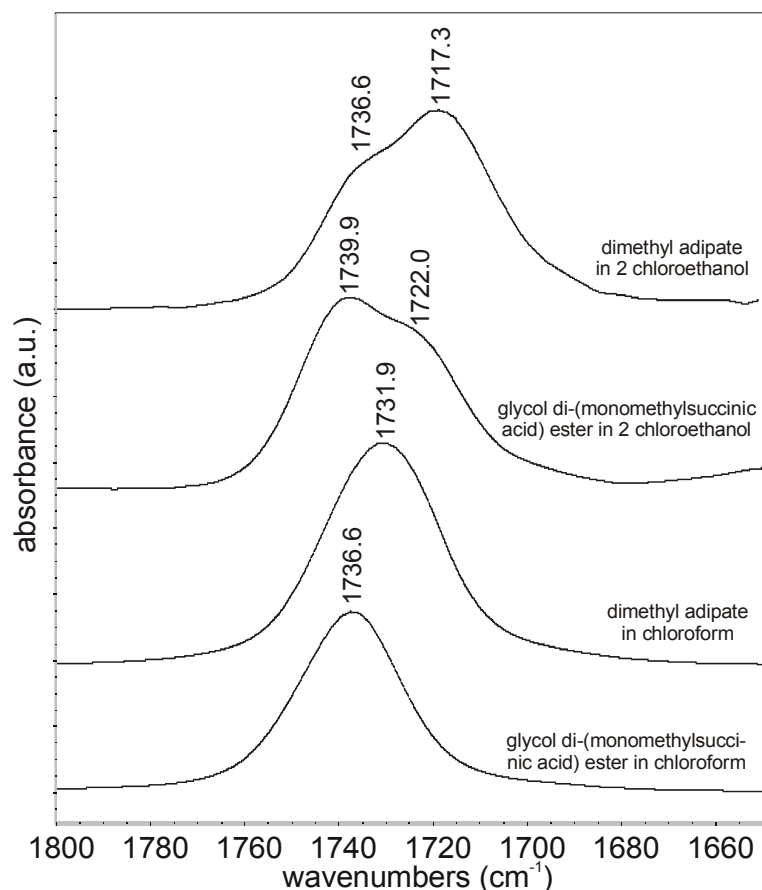


FIG. 6. FTIR-Transmission spectra of the carbonyl stretching vibration region of the two studied compounds in two different solvents. The peak positions were resolved using curve-fitting.

6.3.5. Stability of bonding

To evaluate the stability of the bonds in water, immersion experiments in triple deionised water were performed at room temperature of the oxide layers with adsorbed molecules. The dimethyl adipate compound does not show a stable bond. Already after 1 minute of immersion, all molecules have become desorbed, as evidenced by absence of the $\nu(\text{C}=\text{O})$ carbonyl stretching vibration. The glycol di-(monomethylsuccinic acid) ester shows a more stable adsorption. In Fig. 7, infrared spectra are shown obtained initially and after 1, 5 and 10 minutes of immersion in water for the evaporated and oxidised aluminium. After 1 minute, a significant part of the molecules have become desorbed and the $\nu(\text{C}=\text{O})$ carbonyl peak is shifted to lower wavenumber. For longer immersion times, more molecules become desorbed and the $\nu(\text{C}=\text{O})$ carbonyl peak shifts further to lower wavenumber. Broad bands develop in the spectrum around 1590 cm⁻¹ and around 1430 cm⁻¹.

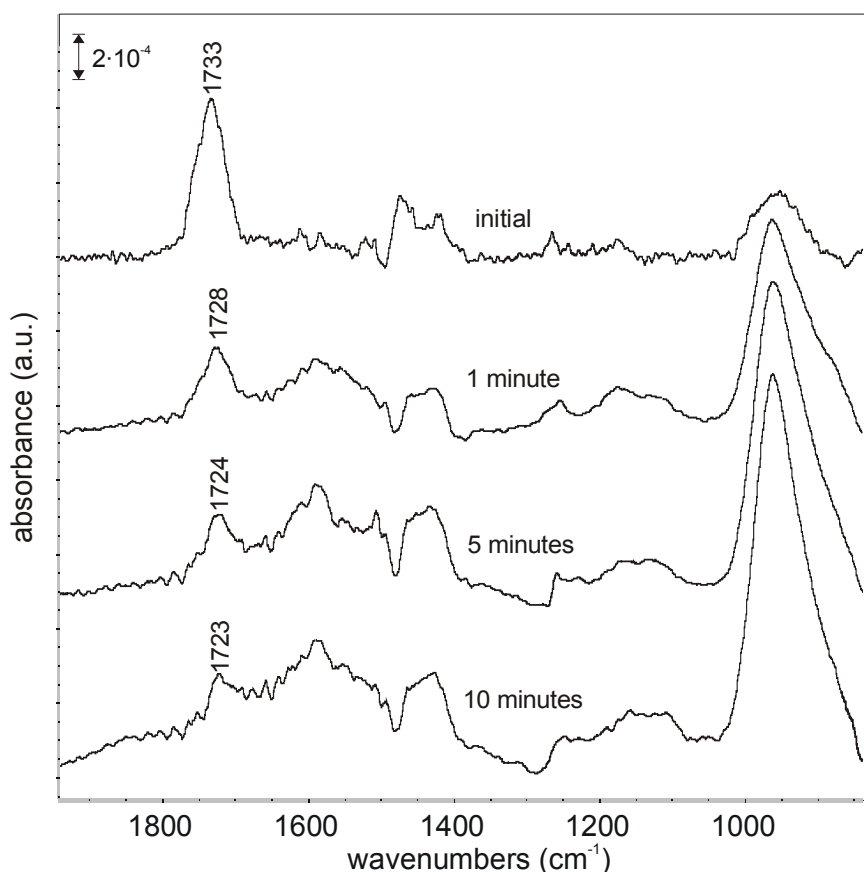


FIG. 7. FTIR-RAS spectra of glycol di-(monomethylsuccinic acid) ester molecules on the evaporated and oxidised type of aluminium, after different immersion times in room temperature deionised water.

These are due to water molecules, adsorbed on the oxide surface [27]. Moreover, the growth of the main Al-O peak at 950 cm⁻¹ is observed, which is due to the development of broad shoulders, corresponding to hydroxyl bending vibrations [18,28,29]. It indicates growth and through-film hydroxylation of the oxide layer, due to a direct contact of the oxide surface with water.

The stability of the bonding of the ester compounds has also been evaluated as compared to a compound capable of chemisorption to the oxide surface. The (dicarboxylic acid) succinic acid (COOH-CH₂-CH₂-COOH) molecule was chosen for this purpose. The compound has been studied in Chapter 5 with respect to its capability of bonding with aluminium oxide surfaces. Both carboxylic acid groups were found to react with the oxide surface to form a chemisorbed carboxylate, coordinating to two aluminium cations on the oxide surface. In Fig. 8, infrared spectra are shown for an alkaline pretreated aluminium oxide surface, with the adsorbed glycol di-(monomethylsuccinic acid) ester molecules,

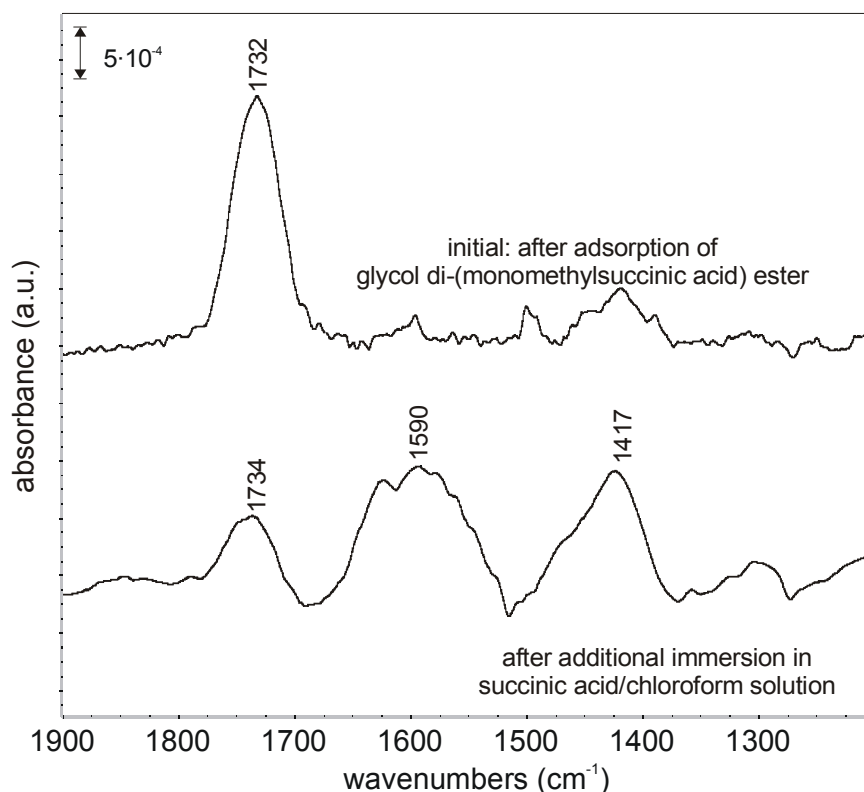


FIG. 8. FTIR-RAS spectra of glycol di-(monomethylsuccinic acid) on the alkaline pretreated aluminium initially (top) and after immersion in a diluted solution of succinic acid in chloroform for 5 minutes (bottom).

before and after immersion for 5 minutes in a diluted solution of succinic acid in chloroform at room temperature. After immersion, additional peaks develop at 1590 and 1417 cm^{-1} , which are respectively the $\nu_{\text{as}}(\text{COO}^-)$ asymmetric and $\nu_{\text{s}}(\text{COO}^-)$ symmetric carboxylate stretching vibrations, see Chapter 5. The peak of the carbonyl stretching vibration of the glycol di-(monomethylsuccinic acid) ester has decreased significantly in intensity after immersion.

Given the results obtained in Chapter 5, this carbonyl peak is expected to also contain a contribution due to unreacted carboxylic acid groups of succinic acid. Immersion of the samples with adsorbed molecules in chloroform without succinic acid did not lead to an appreciable decrease in the $\nu(\text{C}=\text{O})$ carbonyl stretching band, indicating displacement does not occur by the chloroform itself. It is evident that the glycol di-(monomethylsuccinic acid) ester molecules are largely displaced by succinic acid, which is chemisorbed on the oxide surface as a carboxylate. For dimethyl adipate, similar results were obtained.

6.3.6. Reactivity of the different oxide surfaces

The oxides exhibit differences in carbonyl infrared peak intensities, representing the adsorbed molecules, see Figs. 3 and 5. For the oxides, having constant surface areas and flat surfaces, this indicates differences in the amounts of bonded molecules [30-32]. To evaluate the amount of bonded molecules, the total integrated infrared peak intensities of the $\nu(\text{C}=\text{O})$ carbonyl stretching vibration was determined. A similar approach was used by others, evaluating the amount of bonded ester groups for thin polymeric layers on aluminium [1,2]. Absolute quantitative information, in terms of the amount of molecules per unit of surface area was not obtained. Despite this, a comparison among the different oxides is possible, which is considered to be the most important for the current work. Because of its large surface area and macroscopic roughness, the pseudoboehmite oxide is not included in this analysis.

The amount of bonded molecules was not influenced by the adventitious contamination levels. The alkaline pretreated aluminium has the largest amount of adventitious contamination, see Table 1, but shows the most intense $\nu(\text{C}=\text{O})$ carbonyl stretching vibration peaks after adsorption, indicating the largest amount of bonded molecules. This is because the non-functional contamination, see above, for the oxides studied is readily displaced by either the solvent or the adsorbed molecules, see Chapter 3.

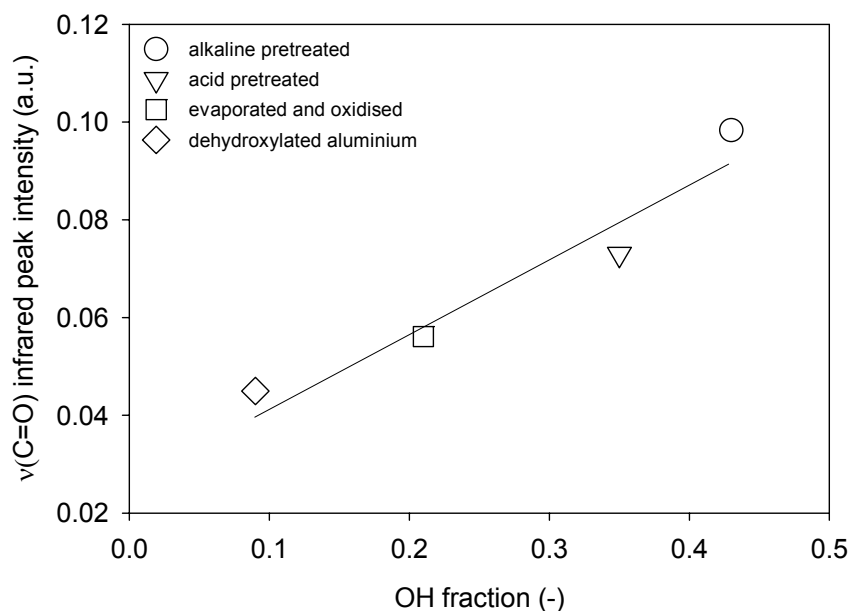


FIG. 9. Relation between the $\nu(\text{C}=\text{O})$ carbonyl stretching vibration peak area of glycol di-(monomethylsuccinic acid) ester molecules at saturation coverage on the different aluminium oxides versus their hydroxyl fraction as determined from the XPS measurements.

A correlation was found with the hydroxyl concentration on the oxide surfaces. This is shown in Fig. 9, in which the $\nu(\text{C}=\text{O})$ carbonyl stretching vibration peak intensity of the bonded glycol di-(monomethylsuccinic acid) ester molecules is plotted with respect to the hydroxyl concentration, as determined from the XPS measurements, see Table 1. Each point corresponds to the average of 2-3 samples. Thus, with a higher hydroxyl concentration, also more glycol di-(monomethylsuccinic acid) ester molecules bond to the oxide surface. Further confirmation of this relation was obtained by performing an additional measurement. An alkaline pretreated substrate was dehydroxylated for 24 hours at a temperature of 275 °C, following the same procedure as for the dehydroxylated type of aluminium oxide. Subsequently, glycol di-(monomethylsuccinic acid) ester was adsorbed on the oxide surface. It was found that the amount of bonded molecules dropped to that obtained for the dehydroxylated type of aluminium. Multiple other factors like steric hindrance of the organic molecules and also intramolecular interactions [33] may also play a role in determining the concentration of bonded molecules. Further, at an XPS detection angle of 15 degrees, still around five Al-O layers are being probed [34] and so not all hydroxyls being detected, necessarily have to be accessible to the adsorbed molecules. In this context, it is also noted that the slope of the linear relation between the amount of hydroxyls and the peak intensity is smaller than unity.

6.4. Discussion

6.4.1. Type of bonding with the oxide surfaces

Upon adsorption of both ester compounds on the studied oxide surfaces, the $\nu(\text{C}=\text{O})$ carbonyl stretching band of the ester shows a peak shift to lower wavenumber, as compared to the free carbonyl values, see Figs. 2 and 4. For glycol di-(monomethylsuccinic acid) ester, the $\nu(\text{C}=\text{O})$ carbonyl stretching band of the excess molecules, representing free ester groups, is observed at 1753 cm^{-1} . For the bonded ester groups, it is found at 1732 cm^{-1} . For dimethyl adipate, the $\nu(\text{C}=\text{O})$ carbonyl stretching band for the excess molecules is found at 1746 cm^{-1} , and the peak for the bonded ester groups at 1720 cm^{-1} . The infrared peak positions and the free to bonded $\nu(\text{C}=\text{O})$ carbonyl infrared peak shift correspond to values obtained for carbonyls involved in hydrogen-bonding, see Table 2. Moreover, the involvement in hydrogen-bonding is also evident from the relation between the amount of hydroxyls and the intensity of the $\nu(\text{C}=\text{O})$ carbonyl stretching vibration peak of the hydrogen-bonded esters, see Fig. 9.

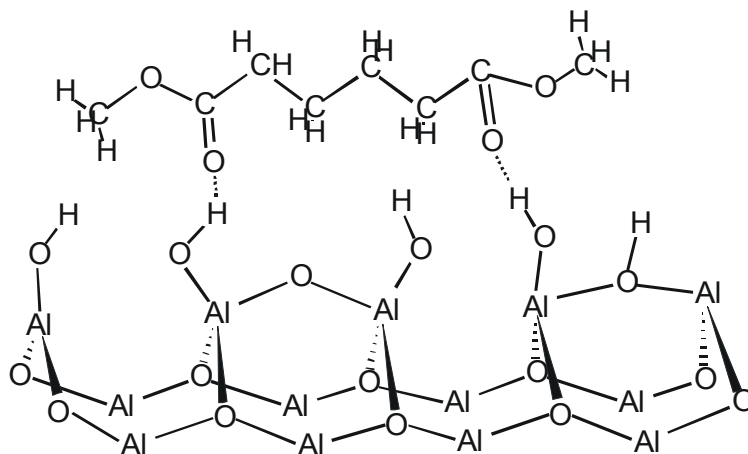


FIG. 10. Illustration of bonding of dimethyl adipate with hydroxyls on an aluminium oxide surface.

The downward infrared peak shift from the free to the bonded carbonyl indicates that the carbonyl oxygen acts as the Lewis base (electron donor) and the proton of the hydroxyl group as the Lewis acid (electron acceptor) [2]. This is shown schematically in Fig. 10, in which the bonding of dimethyl adipate with hydroxyls on the oxide surface is shown.

As discussed above, the shift upon adsorption of the $\nu(\text{C}=\text{O})$ peak strongly depends on the extent of lone pair electron transfer. With increasingly more acidic hydroxyls, increasingly more negative charge is withdrawn from the carbonyl oxygen lone pair electrons, resulting in a lower $\nu(\text{C}=\text{O})$ and therefore an increase in the free to bonded infrared peak shift [2], see Table 2.

Despite the fact that a wide range of different preparation methods are used for the aluminium surfaces, the ester groups show very similar adsorption behaviour on the different oxides, as evidenced from the constant $\nu(\text{C}=\text{O})$ carbonyl stretching band positions. The XPS analysis shows that the hydroxyls on the different oxide surfaces do not have differences in their acid-base properties, as evidenced by their very similar hydroxyl binding energies. A constant $\nu(\text{C}=\text{O})$ carbonyl stretching band position of the bonded ester groups is therefore also expected. The XPS analysis shows however that pseudoboehmite has more basic hydroxyls. This will result in less lone pair electron transfer from the carbonyl oxygen and as a consequence, a higher $\nu(\text{C}=\text{O})$ peak position and therefore a smaller free to bonded $\nu(\text{C}=\text{O})$ infrared peak shift is expected. However, the same $\nu(\text{C}=\text{O})$ carbonyl stretching vibration position as for the other oxides is observed. This is not well understood. The bonding of glycol di-(monomethylsuccinic acid) ester was also studied on freshly prepared steel substrates, which are known to have an oxide layer, with more basic hydroxyls than for aluminium [35-37]. The details on this will be discussed

in a future work [38]. On the steel surface, the compound showed a peak position of 1738 cm^{-1} for the bonded molecules, in correspondence with their hydroxyls being more basic. A possible explanation might be found in the fact that XPS was used as the analysis technique to determine the acid-base properties of the oxide layer surfaces. Despite the analysis angle of 15 degrees, used for the experiments, it can be estimated that still roughly the outer 5 Al-O layers are being probed in the analysis [34]. The XPS signal therefore has to be considered as a weighed average of these outer layers. The properties of the hydroxyls present on the outer surface can deviate from the interior of the oxide layer. Raybaud *et al.* [39] performed a density functional simulation study of the aluminium oxyhydroxide boehmite, which is structurally similar to the pseudoboehmite studied in this work [15,40]. While the hydroxyls in the interior of the oxides deviated and showed considerable internal hydrogen-bonding, the hydroxyls on the surface were more or less comparable to those found on $\gamma\text{-Al}_2\text{O}_3$ [39].

The two compounds show differences in the amount of free to bonded infrared peak shift and also in their FWHM peak widths. Glycol di-(monomethylsuccinic acid) ester showed a peak width of 41 cm^{-1} and a free to bonded infrared peak shift of 20 cm^{-1} while the dimethyl adipate shows a FWHM peak width of 34 cm^{-1} and a peak shift of 26 cm^{-1} . Because the compounds showed similar peak shifts and peak widths in the different solvents, see Table 2, these difference are due to differences in bonding behaviour.

An explanation for the differences in peak width and peak shift between adsorbed glycol di-(monomethylsuccinic acid) ester and dimethyl adipate can lie in differences in structural flexibility of the molecules. Dimethyl adipate is more flexible than glycol di-(monomethylsuccinic acid) ester, because it only has two ester groups and because of its aliphatic centre part. It is therefore likely better capable of optimising its interaction with hydroxyls on the oxide surface, resulting in stronger hydrogen-bonds and thereby resulting in a larger $\nu(\text{C}=\text{O})$ infrared peak shift. The glycol di-(mono-methylsuccinic acid) ester is less flexible, having four ester groups, and is therefore likely less capable of optimising all four hydrogen bond distances. Part of the ester-oxide hydrogen-bonds will then be weaker, resulting in a carbonyl peak that is extended to the high-wavenumber side as compared to adsorbed dimethyl adipate. This then results in broader peak and a smaller infrared peak shift as compared to adsorbed dimethyl adipate.

It is also noted that the dimethyl adipate compound shows significantly less intense carbonyl stretching vibration peaks as compared to the glycol di-(monomethylsuccinic acid) ester compound, when adsorbed on the oxide

surface, compare Figs. 3 and 5. This might indicate less molecules being bonded to the surface, for example because of the aliphatic centre part of dimethyl adipate blocking hydroxyls that are then no longer available for bonding. A straightforward comparison of intensities is however likely not possible due to differences in molar absorption coefficients [1,41].

6.4.2. Bonding stability and strength of the ester groups

Fowkes *et al.* established a relationship between the carbonyl infrared peak shift $\Delta\nu^{AB}$ and the enthalpy of the bond ΔH_{ads} [14]:

$$\Delta H_{\text{ads}} = -k^{AB} \Delta\nu^{AB}, \quad (1)$$

with k^{AB} having a value of 0.99 kJ/mol/cm⁻¹. With an infrared peak shift of 20 cm⁻¹, a value of 19.8 kJ/mol is obtained for glycol di-(monomethylsuccinic acid) ester bonded on the oxide surfaces. For dimethyl adipate, which shows an infrared peak shift of 26 cm⁻¹, a value of 25.8 kJ/mol is then obtained. These values are an order of magnitude smaller than the value of about 200 kJ/mol reported for chemisorbed carboxylates [23]. The enthalpy of the total (macroscopic) bond between the organic layer and the metal substrate also depends on the number of bonds, see Eq. 1. The oxides studied differ in the amounts of hydroxyls that are present on their surfaces, see Table 1. With an increasing amount of hydroxyls, more ester groups can bond to the oxide surface, see Fig. 9. As a result, the total macroscopic bond enthalpy will be the largest for the most hydroxyl-rich oxides, resulting in an increased macroscopic bonding strength.

On the microscopic scale, the bonds between the carbonyls of the ester groups and the oxide surface are shown to be not very stable in an aqueous environment or in presence of another functional group that is capable of forming a stronger bond with the oxide surface. Dimethyl adipate, having two ester groups, is displaced almost instantly in an aqueous environment. Glycol di-(monomethylsuccinic acid) ester is displaced to the largest extent in around 10 minutes, see Fig. 7, notwithstanding that the compound is bonded with four ester groups to the oxide surface. The carbonyl stretching peak of the molecules remaining after immersion, shifts to lower wavenumber and shows a lower peak width. The shift is likely because the least strongly bonded ester groups (with a corresponding higher wavenumber, as a result of less electron transfer) are more likely to be displaced from the oxide surface, while the more strongly bonded ester groups (with a corresponding higher wavenumber) remain adsorbed for a

longer period. The differences in aqueous stability between adsorbed dimethyl adipate and glycol di-(monomethylsuccinic acid) ester are likely a kinetic effect, due to the number of ester groups per molecule. For dimethyl adipate, only two bonds need to be displaced before the whole molecule is desorbed from the surface.

The compounds can also be readily displaced by molecules containing carboxylic acid groups, which are capable of chemisorbing to the oxide surface, see Fig. 8. This likely also plays an important role in the relatively bad performance of ester group containing polymers in acetic acid, citric acid etc. [42,43] environments. Small carboxylic acid based molecules can readily penetrate the polymer and after having arrived at the polymer-oxide interface, they are capable of displacing the ester groups from the oxide surface.

The low value of the bond enthalpy, the aqueous environment performance, the relatively easy displacement in the presence of carboxylic acid groups demonstrates that the bond between ester groups and the aluminium oxide surface is not very strong. The results emphasize that for a more durable bond, one should preferably have functional groups that are chemisorbed to the oxide surface, for example carboxylic acids.

6.5. Conclusions

The bonding of the two compounds containing ester groups with a set of different aluminium oxide layers has been investigated using infrared reflection absorption spectroscopy. Bonding of the ester groups to the different aluminium oxide surfaces occurs through Lewis acid-base bonding in which the carbonyl of the ester is the Lewis base and the proton of the oxide hydroxyl the Lewis acid. Not much difference in bonding was observed among the different oxides, despite the use of different methods to prepare the layers. Differences between the two compounds were observed in the strength of the hydrogen-bond with the oxide surface. The oxides showed clear differences in the amount of molecules being bonded to the oxide surface and a clear relation was observed with the amounts of hydroxyls present on the oxide surface, as determined from XPS measurements. The bonding of the ester groups with the oxide surfaces was found to be not stable in presence of water and also not in the presence of a compound which can chemisorb to the aluminium oxide surface.

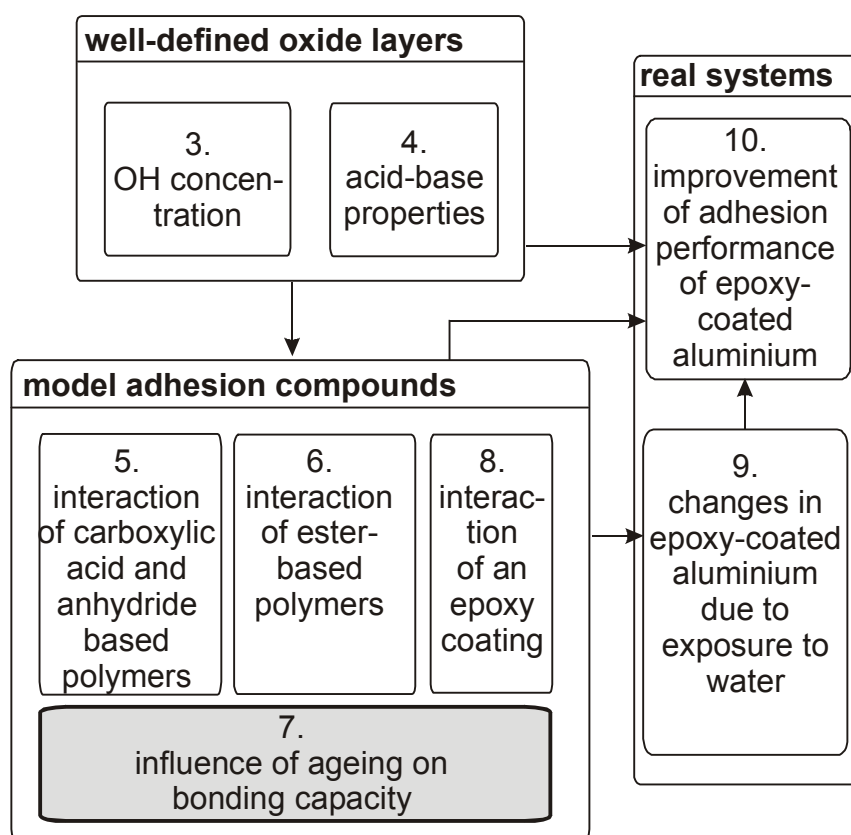
References

1. Brogly, M.; Grohens, H.; Labbe, C.; Schultz, J. *International Journal of Adhesion and Adhesives* 1997, *17*(3), 257-261.
2. Brogly, M.; Nardin, M.; Schultz, J. *Journal of Adhesion* 1996, *58*(3-4), 263-279.
3. Kiselev, A. V.; Uvarov, A. V. *Surface Science* 1967, *6*(4), 399-421.
4. Tannenbaum, R.; Hakanson, C.; Zeno, A.; Tirrell, M. *Langmuir* 2002, *18*(14), 5592-5599.
5. Öberg, K.; Persson, P.; Shchukarev, A.; Eliasson, B. *Thin Solid Films* 2001, *397*(1-2), 102-108.
6. Strålin, A.; Hjertberg, T. *Journal of Adhesion Science and Technology* 1992, *6*(11), 1233-1250.
7. Strålin, A.; Hjertberg, T. *Journal of Applied Polymer Science* 1993, *49*(3), 511-521.
8. Alexander, M. R.; Beamson, G.; Blomfield, C. J.; Legget, G.; Duc, T. M. *Journal of Electron Spectroscopy and Related Phenomena* 2001, *121*(1-3), 19-32.
9. Marsh, J.; Minel, L.; Barthes-Labrousse, M.; Gorse, D. *Applied Surface Science* 1996, *99*(4), 335-343.
10. Marsh, J.; Minel, L.; Barthes-Labrousse, M.; Gorse, D. *Applied Surface Science* 1998, *133*(4), 270-286.
11. Abel, M. L.; Rattana, A.; Watts, J. F. *Journal of Adhesion* 2000, *73*(2-3), 313-340.
12. Thery, S.; Jacquet, D.; Mantel, M. *Journal of Adhesion* 1996, *56*(1-4), 1-13.
13. Szumilo, C.; Dubot, P.; Verchere, D.; Hocquaux, H.; Vilar, M.; Rei Dumas, P. *Journal of Adhesion Science and Technology* 1997, *11*(4), 553-572.
14. Fowkes, F. M.; Tischler, D. O.; Wolfe, J. A.; Lannigan, L. A.; Ademu-John, C. M. *Journal of Polymer Science A - Polymer Chemistry* 1984, *22* (3), 547-566.
15. Alwitt, R. S. The aluminium-water system, in *Oxides and oxide films vol. 4*, Diggle, J. W., editor; Dekker: New York, 1976; Chapter 3, pp. 169-250.
16. McCafferty, E.; Wightman, J. *Journal of Colloid and Interface Science* 1997, *194*(2), 344-355.
17. Dartevelle, C.; McAlpine, E.; Thompson, G. E.; Alexander, M. R. *Surface and Coatings Technology* 2003, *173*(2-3), 249-258.
18. van Gils, S.; Melendres, C. A.; Terry, H. *Surface and Interface Analysis* 2003, *35*(4), 387-394.
19. Sivel, V. G. M.; van den Brand, J.; Wang, W. R.; Mohdadi, H.; Tichelaar, F. D.; Alkemade, P. F. A.; Zandbergen, H. W. *Journal of Microscopy* 2003, *accepted*.
20. Röseler, A. *Infrared spectroscopic ellipsometry*; Akademie Verlag: Berlin, 1990.
21. Bellamy, L. J. *The infrared spectra of complex molecules. Vol. 1*; 3rd ed.; Chapman and Hall: New York, 1978.
22. Knözinger, H.; Ratnasamy, P. *Catalysis Reviews - Science and Engineering* 1978, *17*(1), 31-70.
23. Davydov, A. A.; Rochester, C. H. *Infrared spectroscopy of adsorbed species on the surface of transition metal oxides*; Wiley: Chichester, 1990.
24. Ma, H.; Berthier, Y.; Marcus, P. *Corrosion Science* 2002, *44*(1), 171-178.
25. Nyquist, R. A.; Fiedler, R. S. *Vibrational Spectroscopy* 1994, *6*(3), 285-291.
26. Nyquist, R. A. *Vibrational Spectroscopy* 1991, *2*(4), 221-226.
27. Vlaev, L.; Damyanov, D.; Mohamed, M. M. *Colloids and Surfaces* 1989, *36*(4), 427-437.
28. Melendres, C. A.; van Gils, S.; Terry, H. *Electrochemistry Communications* 2001, *3*(12), 737-741.
29. Kiss, A. B.; Kerezury, G.; Farkas, L. *Spectrochimica Acta Part A* 1980, *36*(7), 653-658.
30. Zhuang, G.; Chottiner, G. *Review of Scientific Instruments* 1994, *65*(8), 2494-2499.
31. Wang, X. D.; Tysoe, W. T.; Greenler, R. G.; Truszkowska, K. *Surface Science* 1991, *258*(1-3), 335-345.
32. Hayden, B. E.; Prince, K.; Woodruff, D. P.; Bradshaw, A. M. *Surface Science* 1983, *133*(2-3), 589-604.
33. Tao, Y. T. *Journal of the American Chemical Society* 1993, *115*(110), 4350-4358.
34. Jeurgens, L. P. H.; Sloof, W. G.; Tichelaar, F. D.; Mittemeijer, E. J. *Physical Review B* 2000, *62*(7), 4707-4719.
35. Bolger, J. C.; Michaels, A. S. *Interface conversion for polymer coatings*; Weiss, P.; Cheever, G. D., editors; Elsevier: New York, 1969; pp. 2-60.
36. McCafferty, E.; Wightman, J. *Surface and Interface Analysis* 1998, *26*(8), 549-564.

37. Horner, M. F.; Boerio, F. J.; Clearfield, H. M. *Journal of Adhesion Science and Technology* 1992, 6(1), 1-22.
38. Beentjes, P. C. J.; van den Brand, J.; de Wit, J. H. W. *Applied Surface Science* 2003, *to be published*.
39. Raybaud, P.; Digne, M.; Iftimie, M.; Wellens, M.; Euzen, P.; Toulhoat, H. *Journal of Catalysis* 2001, 201(2), 236-246.
40. Wefers, K.; Misra, C. *Oxides and hydroxides of aluminium*; Alcoa Cooperation of America: 1987.
41. Allara, D. L.; Wang, Z.; Pantano, C. G. *Journal of non-crystalline solids* 1990, 120(1-3), 93-101.
42. Olafsson, G.; Jagerstad, M.; Oste, R.; Wesslen, B.; Hjertberg, T. *Food Chemistry* 1993, 47(3), 227-233.
43. Strålin, A.; Hjertberg, T. *Journal of Adhesion Science and Technology* 1993, 7(11), 1211-1229.

CHAPTER 7.

AGEING OF ALUMINIUM OXIDE SURFACES AND THEIR SUBSEQUENT REACTIVITY TOWARDS BONDING WITH ORGANIC FUNCTIONAL GROUPS ¹



¹ This chapter was published as a scientific paper:
J. van den Brand, S. van Gils, P.C.J. Beentjes, H. Terryn, J.H.W. de Wit
Applied Surface Science, 2004, accepted for publication

Synopsis

In previous chapters, the interaction of different organic functional groups with differently prepared, fresh aluminium substrates has been investigated. In practice, freshly prepared metallic substrates are often left in the ambient for varying periods before an organic overlayer like a coating is applied. This ageing of the substrate can be expected to also influence the bonding of the subsequently applied organic overlayer. In this chapter, the changes occurring to an aluminium oxide layer as a function of ageing time in both ambient air and in a clean nitrogen environment are investigated. Moreover, the bonding capacity of the oxide surface towards organic functional groups as a function of ageing time is evaluated for these environments. It is found that contaminants like water and air-borne carboxylic acids are rapidly adsorbed on the oxide surface when the substrate is aged in ambient air. As a result of this, the bonding capacity of the oxide surface towards organic functional groups very rapidly decreases with ageing time. Within 24 hours of ageing, the oxide surface irreversibly loses 60% of its initial reactivity. This occurs to a considerably lesser extent for ageing in a clean, nitrogen environment.

7.1. Introduction

Aluminium substrates are often given a surface treatment prior to application of an organic overlayer like a coating, a self-assembling monolayer or an adhesive [1]. The surface treatment results in a fresh, clean and reactive aluminium oxide surface, which shows its maximum bonding capacity towards the organic overlayer. Quite often, however, the surfaces are exposed to ambient air for periods varying from hours until even several days prior to applying the overlayer. Ambient air contains water and several organic and inorganic species. Water adsorbs on the oxide surface and causes hydroxylation (i.e. the incorporation of hydroxyls) of the aluminium oxide layer [2,3]. This can be considered a positive change because bonding of organic functional groups primarily proceeds through the hydroxyls, see Chapters 5 and 6. The adsorbed water however also blocks surface sites, which are then no longer available for the organic functional groups, resulting in a decrease of the bonding capacity of the surface, meaning the amount of bonds that the oxide surface is capable of forming with organic functional groups. For much longer ageing times (in the order of months), water causes the formation of aluminium hydroxide and

oxyhydroxide particles on the oxide surface [4-6]. These are only loosely bound and are therefore detrimental for formation of strong adhesive bonds. Besides water, several air-borne organic and inorganic contaminants can also adsorb on the oxide surface [7]. These generally bond strongly to the oxide surface, resulting also in a decrease of the bonding capacity of the surface [8-11].

For these reasons, it is important to know which changes to the oxide surface occur upon ageing in the ambient as a function of time and to which extent this influences the bonding capacity of the oxide surface.

In this work, the changes that occur to a freshly prepared amorphous aluminium oxide layer, upon ageing in ambient air and upon ageing in a clean and dry environment have been investigated in detail. The bonding capacity of the substrate towards bonding with organic functional groups has been evaluated as a function of prior ageing time of the aluminium substrate. This was done by evaluation of the amount of chemisorbed monofunctional aliphatic carboxylic acid molecules. The investigation was carried out using infrared reflection absorption spectroscopy (FTIR-RAS). The technique is highly suitable for this purpose, because it is non-destructive, does not require a vacuum environment and allows identification of adsorbed species and changes to the aluminium oxide layer.

This Chapter complements the work discussed in Chapters 5 and 6, in which bonding of carboxylic acid and anhydride functionalised and ester functionalised organic compounds was investigated to a set of differently pretreated but *freshly prepared* aluminium substrates.

7.2. Experimental

7.2.1. Materials and experimental conditions

The capacity of the oxide surfaces towards bonding with organic functional groups was studied using myristic acid, $\text{CH}_3(\text{CH}_2)_{12}\text{COOH}$, often used for self-assembling monolayers [12,13]. Myristic acid was obtained from Sigma-Aldrich as 99.5+% purity and was used without further purification. Myristic acid was applied on the aluminium substrates, following the same experimental procedure as used in Chapter 5, see paragraph 5.2.2 on page 63.

As the aluminium substrate, the vacuum evaporated and oxidised aluminium substrate was chosen. Its preparation procedure is discussed paragraph 3.2.1 on page 23. The infrared measurements were performed according to the same procedure as discussed in paragraph 5.2.3 on page 63.

7.2.2. Substrate handling and ageing conditions

In Fig. 1, a scheme shows the way in which the substrates are handled during the ageing experiments. Immediately after preparation of the aluminium substrate, an infrared background spectrum was obtained. The substrate was then aged for a given period. For ageing in ambient air, a climatized room was chosen, having a constant temperature of 21 °C and a relative humidity of 30%. For ageing in a dry and clean environment, the substrate was stored in the infrared compartment at 21 °C. The compartment is continuously flushed with a flow of dry and clean pure nitrogen (99.998 vol.% purity, flow approximately 400 l/hr), obtained from the overpressure of a liquid nitrogen vessel. The humidity in the infrared compartment was determined to be smaller than 1%. Then, an infrared spectrum of the substrate was obtained with respect to the background obtained prior to ageing. The infrared spectrum then shows changes that have occurred during ageing and does not have contributions due to the initial state of the substrate, making interpretation easier. After this, the substrates were cleaned using clean, hot THF (tetrahydrofuran, 99+% purity) and clean, hot chloroform (99+% purity). Finally, a new background spectrum was obtained, myristic acid was adsorbed and an infrared spectrum was obtained with respect to the background obtained prior to adsorption. The final infrared spectrum then shows only the changes that have occurred upon adsorption of myristic acid.

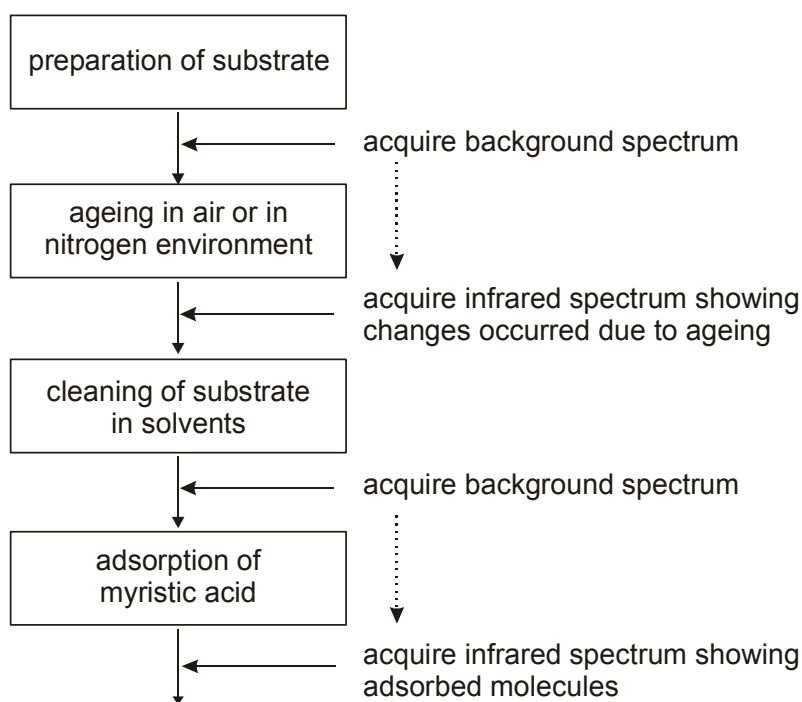


FIG. 1. Schematic overview of substrate handling for the ageing experiments.

7.3. Results

7.3.1. Changes in surface chemistry due to ageing in ambient air

In Fig. 2, infrared spectra are shown for aluminium substrates, aged for 1, 4, 16 and 67 hours in ambient air. The spectra show only the changes that have occurred during the ageing period, see Experimental section.

A summary of the bands observed in the spectra upon ageing of the substrates and their assignment is given in Table 1. Below 1300 cm^{-1} there is the growth of a band at 960 cm^{-1} and the upward bending of the infrared spectrum with increasing ageing time. The band at around 960 cm^{-1} is the Al-O stretching vibration due to the aluminium oxide layer [14,15]. An increase in intensity of

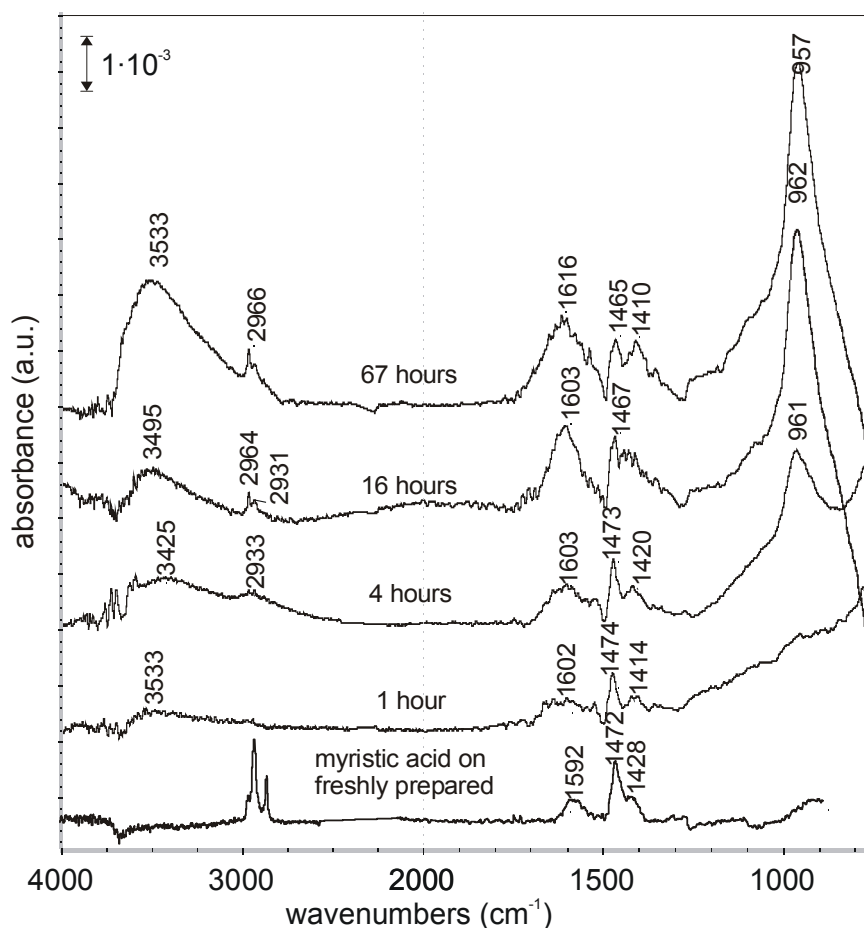


FIG. 2. FTIR-RAS spectra from aluminium substrates after ageing in ambient air for indicated periods. Spectra are shown with respect to a background prior to ageing and therefore only show the changes that have occurred in the ageing process. The sharp bands at around 3700 cm^{-1} are experimental artefacts and are due to water in the infrared compartment [3]

the band indicates growth of the oxide layer as a function of ageing time. Around this band, there is the development of unresolved shoulders, having estimated positions around 1100 cm^{-1} and 800 cm^{-1} , resulting in the observed upward bending of the spectra. The development of these bands indicates that hydroxylation of part of the oxide layer occurs. The bands are respectively $\delta(\text{OH})$ bending and $\gamma(\text{OH})$ twisting vibrations and their positions and broadness have the characteristics of an amorphous, pseudoboehmite-type aluminium oxyhydroxide [16-21]. A similar conclusion was also reached by others studying ageing of aluminium surfaces in ambient air by XPS [2,22]. The presence of hydroxyls is also evidenced from the development of the broad, asymmetric band at around 3500 cm^{-1} which is partially due to the corresponding stretching vibrations $\nu(\text{OH})$ of the hydroxyls and partially due to the $\nu(\text{OH})$ of water molecules, see furtheron [23].

In the $1800\text{-}1300\text{ cm}^{-1}$ region, already after 1 hour of ageing, a clear change is visible. A broad band at 1602 cm^{-1} and a more intense sharp, band at around 1474 cm^{-1} , having a shoulder at 1414 cm^{-1} appear. Very similar bands are observed when a carboxylic acid-based compound is deliberately adsorbed on this type of aluminium oxide. The bottom spectrum shows the results obtained for myristic acid, adsorbed on a freshly evaporated and oxidised aluminium substrate. Just as for the 1 hour aged substrate, the spectrum shows a broad band at around 1600 cm^{-1} and a band at around 1470 cm^{-1} , having a shoulder at around 1410 cm^{-1} . When adsorbed, the carboxylic acid group is deprotonated by

TABLE 1. Infrared peak positions and assignments for the various infrared peaks observed for ageing of an aluminium substrate in ambient air.

approximate infrared band position (cm^{-1})	assignment
800	$\delta(\text{OH})$ bend, aluminium oxyhydroxide region
960	$\nu(\text{Al-O})$ stretch, aluminium oxide
1100	$\gamma(\text{OH})$ twist, aluminium oxyhydroxide region
1349	$\delta(\text{CH}_3)$ deformation, adsorbed contamination
1410	adsorbed water
1472	$\nu_s(\text{COO}^-)$ carboxylate stretch, adsorbed contamination
1610	composite: adsorbed water and $\nu_{\text{as}}(\text{COO}^-)$ carboxylate stretch, adsorbed contamination
2920, 2850	CH_2/CH_3 stretch, adsorbed contamination
3500	$\nu(\text{OH})$ hydroxyl stretch, adsorbed water and aluminium oxyhydroxide region

hydroxyls on the oxide surface, see Chapter 5. A carboxylate results which is coordinatively bonded to aluminium cations on the oxide surface. The broad band at around 1600 cm^{-1} is due to the asymmetric carboxylate stretching vibration $\nu_{\text{as}}(\text{COO}^-)$ and the band at around 1470 cm^{-1} including the shoulder at around 1410 cm^{-1} due to the symmetric carboxylate stretching vibration $\nu_{\text{s}}(\text{COO}^-)$. The similarity with the spectra for adsorbed myristic acid indicates that chemisorbed carboxylates are present on the 1 hour aged substrate. The slight differences in carboxylate stretching peak positions as compared to chemisorbed myristic acid are likely due to differences in groups to which the carboxylate group is attached [24].

With increasing ageing time, there is a growth of several bands in the $1800\text{--}1300\text{ cm}^{-1}$ region. To study this in detail, the constituting components were resolved using curve-fitting. In Fig. 3, an example is shown of the region with the resolved components for a substrate aged in ambient air for 60 hours. The region could be adequately described using four components, having positions at around 1610 , 1472 , 1410 and 1349 cm^{-1} . The resolved components only varied significantly in intensity and no variation in peak position was observed during the ageing period. In Fig. 4, the peak areas of the four resolved components are plotted as a function of ageing time for all substrates studied, with each point obtained on a different substrate. The intensity of the bands at around 1610 and 1410 cm^{-1} both increase significantly by a factor of around three during the

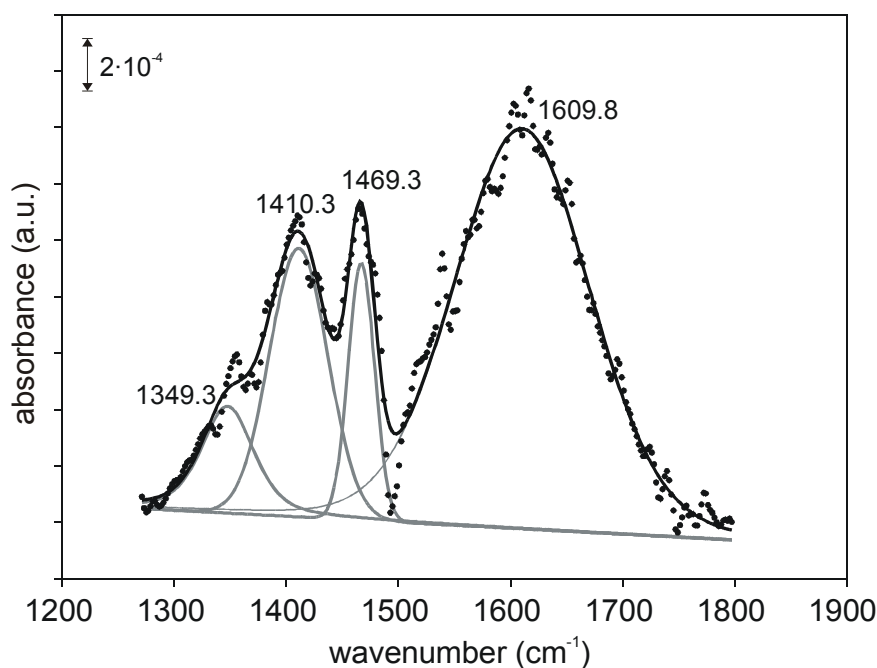


FIG. 3. Components resolved in the $1800\text{--}1300\text{ cm}^{-1}$ infrared region using curve-fitting, for an aluminium substrate that was aged in ambient air for 60 hours. The fit had an r^2 goodness of fit of 0.961.

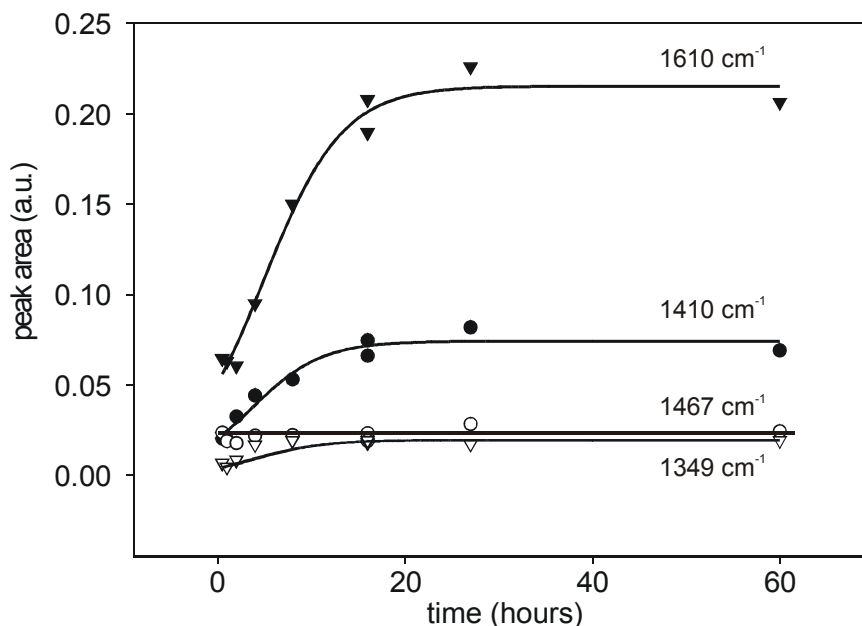


FIG. 4. Infrared peak areas of peaks resolved in the 1800-1300 cm^{-1} infrared region, see Fig. 3, of the aluminium substrates aged in air as a function ageing time.

first 20 hours of ageing, see Fig. 4. Interpretation of bands at these positions is complicated. The broad band at around 1600 cm^{-1} was already ascribed to the asymmetric $\nu_{\text{as}}(\text{COO}^-)$ carboxylate stretching vibration due to adsorbed carboxylates, see above, with the asymmetrically shaped band at around 1470 cm^{-1} being the corresponding symmetric $\nu_{\text{s}}(\text{COO}^-)$ carboxylate stretching vibration. The further growth of the band at 1610 cm^{-1} would then imply the adsorption of additional carboxylates. However, the 1472 cm^{-1} band does clearly not increase in intensity anymore after around 1 hour of ageing, see Fig. 4. As shown by Vlaev *et al.* [23], bands at around 1610 and 1410 cm^{-1} can be ascribed to the bending vibrations of water molecules, being adsorbed on the aluminium oxide surface. Indeed, simultaneous to the growth of the bands at around 1610 and 1410 cm^{-1} , there is also the growth of a broad, asymmetric band around 3500 cm^{-1} in the infrared spectra, see Fig. 2, which is partially also due to water, see above [23]. Moreover, hydroxylation of the oxide layer is observed to occur, see above, through water layers adsorbed on the oxide surface [16,21].

For these reasons, the bands at around 1610 cm^{-1} and 1410 cm^{-1} are ascribed to water. The 1610 cm^{-1} is then a composite band, which is partially due to adsorbed water and partially due to the $\nu_{\text{as}}(\text{COO}^-)$ carboxylate stretching vibration of chemisorbed carboxylates.

In the 3000-2800 cm^{-1} region, the growth of peaks owing to CH_2/CH_3 stretching vibrations is observed [24,25]. This indicates the presence of short-chained aliphatic contamination on the oxide surface. The amount increases

with ageing time, indicating the continuing adsorption of contamination on the surface, despite that the amount of chemisorbed carboxylates does not increase anymore. Related to this is the growth of the band at around 1349 cm^{-1} , see Fig. 4, which is likely a $\delta(\text{CH}_3)$ deformation vibration of the adsorbed organic contamination [24,26].

7.3.2. Changes in surface chemistry due to ageing in a clean and dry environment

In Fig. 5, infrared spectra are shown for substrates aged for different periods in a clean, dry nitrogen environment. The spectra show only the differences that have occurred due to the ageing, see experimental section. Comparing the results with ageing in ambient air shows that ageing in a clean, dry environment results in much less changes, see Fig. 2.

Small CH_2/CH_3 peaks are observed in the $3000\text{-}2800\text{ cm}^{-1}$ and also in the $1800\text{-}1300\text{ cm}^{-1}$ region several not well-resolved bands are present, indicating the adsorption of some organic contamination. There is no adsorption of water as bands at around 1610 , 1410 and 3500 cm^{-1} are not formed. As then expected, also hydroxylation of the oxide layer does not occur and no $\delta(\text{OH})$ bending and $\gamma(\text{OH})$ twisting vibration shoulders develop around the main Al-O band

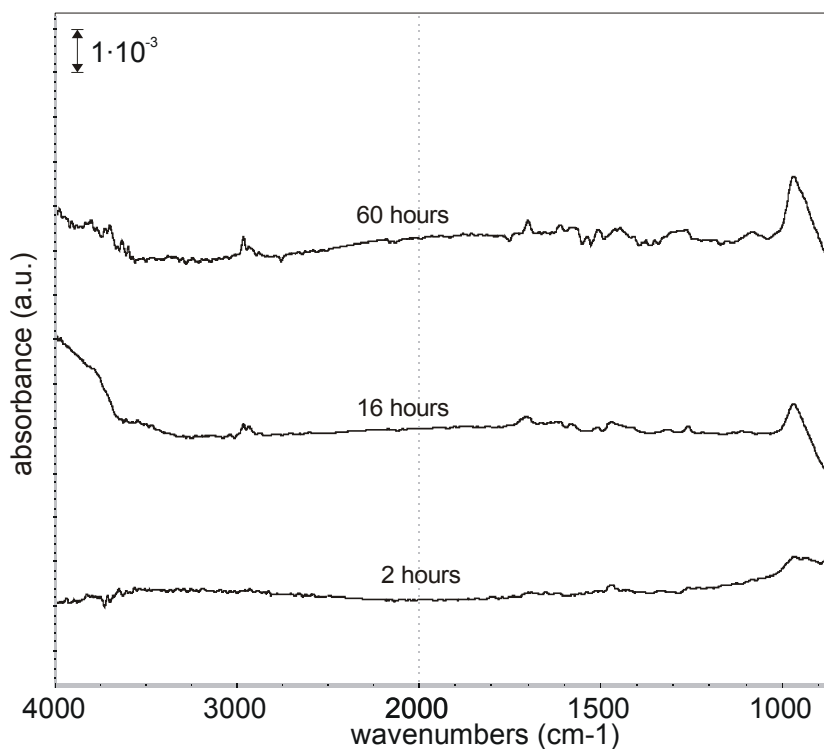


FIG. 5. FTIR-RAS spectra of aluminium substrates aged in a clean, dry nitrogen environment. Spectra are shown with respect to a background prior to ageing and therefore only show the changes that have occurred in the ageing process.

(compare Figs. 2 and 5). Some growth of the oxide layer occurs, as there is a slight growth of the Al-O band at around 950 cm^{-1} .

7.3.3. Influence of cleaning

The substrates aged in ambient air show adsorption of organic contaminants and water. The substrates were subsequently cleaned using solvent to investigate the extent to which the adsorbed species can be removed. For the cleaning, repeated alternating rinsing was performed in hot, clean THF and hot, clean chloroform for a period of around 5 minutes. In Fig. 6, infrared spectra are shown for a substrate that was aged in ambient air for 60 hours and then cleaned according to this procedure. The spectra show only the changes that have occurred during the ageing, see experimental section.

The bottom spectrum shows the difference of the spectra obtained before and after cleaning. In the CH_2/CH_3 -stretching region ($3000\text{-}2800\text{ cm}^{-1}$) and C-OH region (1250 cm^{-1}) [24,25], minor negative bands are observed, indicating

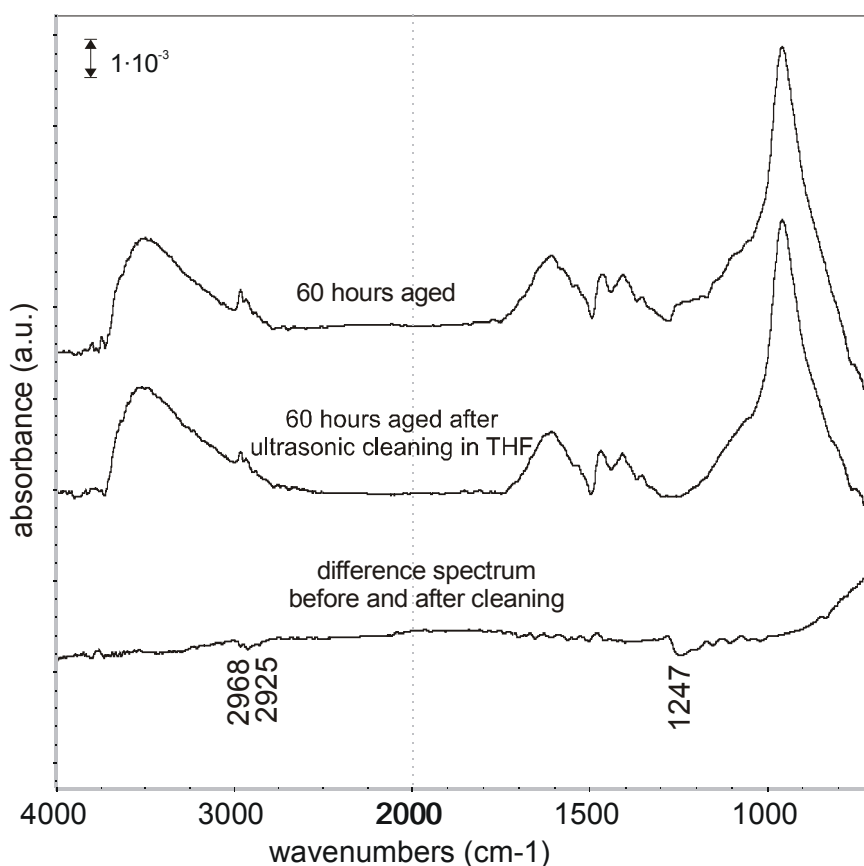


FIG. 6. FTIR-RAS spectra showing the influence of solvent cleaning of an aged aluminium oxide surface. Spectra are shown with respect to a background prior to ageing and therefore show the changes that have occurred in the ageing process.

part of the (likely less strongly bonded) contamination is removed from the substrate.

7.3.4. Influence of ageing on the adsorption of the model adhesive molecules

It is expected that the presence of organic contaminants and water on the oxide surface will modify its bonding capacity towards organic overlayers. To investigate the extent of this, the aged aluminium substrates were cleaned following the procedure discussed above and a new background spectrum was obtained, see experimental section. Subsequently, to evaluate the bonding capacity of the oxide surfaces towards bonding with organic functional groups, myristic acid was adsorbed. In Fig. 7, selected infrared spectra are shown, obtained after adsorption of myristic acid for different ageing times of the substrates prior to the adsorption. The spectra show only changes that have occurred during adsorption, see Experimental section.

For comparison, in Fig. 2, the spectrum is shown of myristic acid adsorbed on a freshly prepared aluminium substrate. For the aged substrates, positive bands are observed in the CH_2/CH_3 stretching region ($3000\text{--}2800\text{ cm}^{-1}$),

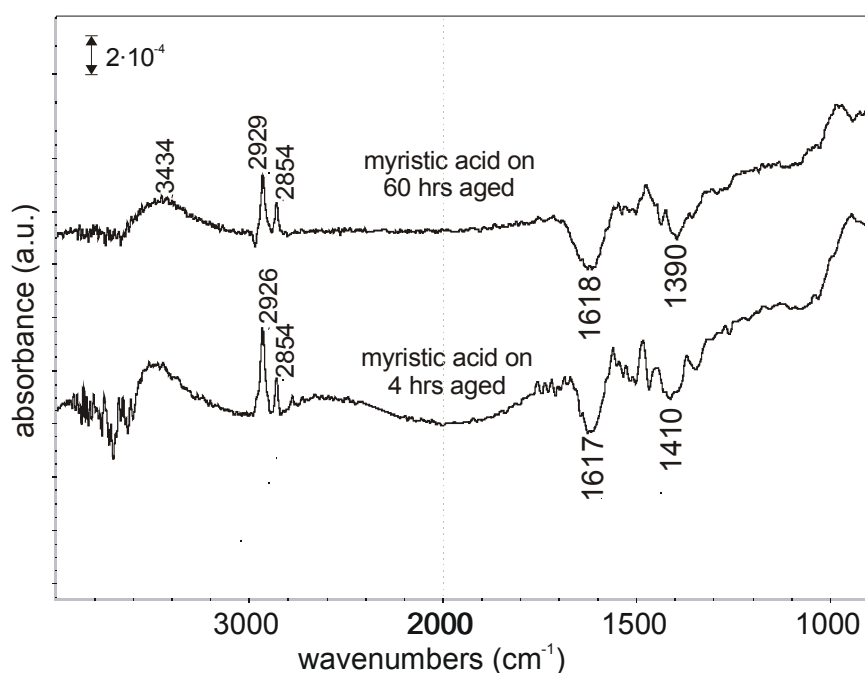


FIG. 7. FTIR-RAS spectra obtained after the adsorption of myristic acid on a substrate aged in ambient air for 60 hours (top) and 4 hours (middle). Spectra are shown with respect to a background prior to ageing and therefore only show the changes that have occurred in the ageing process. The sharp bands at around 3700 cm^{-1} are an experimental artefact and are due to water in the infrared compartment [3].

indicating the presence of myristic acid. Due to negative (downward) bands at around 1610 cm^{-1} and 1410 cm^{-1} , it is not possible to determine the type of bonding of myristic acid. However, rinsing of the substrates using chloroform did not result in decrease of the peaks in the CH_2 and CH_3 stretching region, indicating chemisorption as a carboxylate. As discussed, the bands at 1610 cm^{-1} and 1410 cm^{-1} are due to water on the oxide surface. As negative bands are observed after adsorption, it can be derived that myristic acid causes displacement of water from the surface. Negative bands are then also expected to show up around 3500 cm^{-1} , as there the hydroxyl stretching vibrations of water are located, see above. Additionally, chemisorption as a carboxylate causes dehydroxylation of the oxide surface, see Chapter 5, also resulting in negative bands in the 3500 cm^{-1} region, see Fig. 2, bottom spectrum.

Despite this, however, even slightly positive bands at around 3500 cm^{-1} are observed after myristic acid adsorption on the aged substrates. This might be due to hydroxyls, previously involved in hydrogen-bonding with water molecules, showing an infrared peak shift upon desorption of the adsorbed water. In this context it was also noted that the infrared spectrum were somewhat distorted in the hydroxyl stretching region ($3700\text{-}2900\text{ cm}^{-1}$), most clearly visible for the 4 hours aged samples.

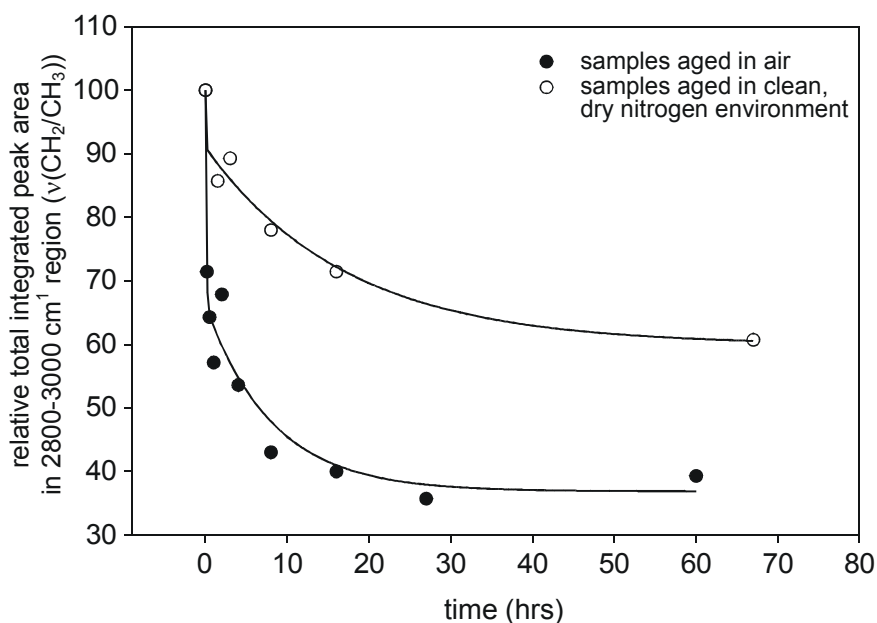


FIG. 8. Bonding capacity of the aluminium oxide surfaces towards chemisorption of carboxylic acid based molecule as a function of ageing time of the aluminium substrate in ambient air and in a clean, dry nitrogen environment. The bonding capacity is evaluated by determining the total integrated peak intensity in the $3000\text{-}2800\text{ cm}^{-1}$ region of infrared spectra obtained after adsorption of myristic acid. Results are given relative to myristic acid adsorbed on a clean substrate.

The amount of chemisorbed myristic molecules, being a measure for the bonding capacity of the oxide surface, can be evaluated from the total integrated peak intensity in the 3000-2800 cm^{-1} region, where the CH_2 and CH_3 stretching vibrations are located, with more adsorbed molecules also resulting in more intense peaks [27,28]. The total integrated peak intensities were determined after subtraction of a linear background and are plotted in Fig. 8 as a function of ageing time. The results are given relative to results obtained for a freshly prepared substrate. Absolute information on the coverage, i.e. the amount of adsorbed molecules per unit of surface area was not obtained. For the current discussion, the relative decrease is however considered to be most important.

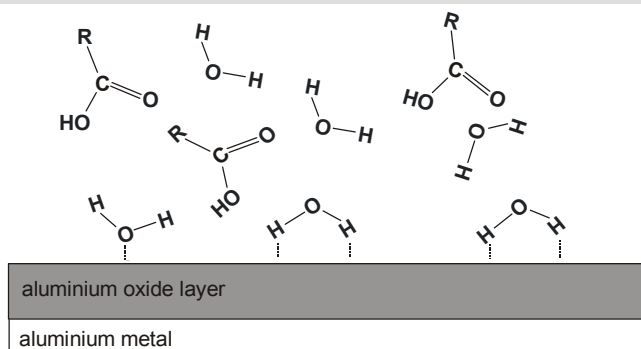
The results have to be treated with some caution. During adsorption of myristic acid, some loosely bound contamination is likely also desorbed from the substrate. For the used procedure, this results in 'negative' CH_2/CH_3 stretching vibration bands onto which the CH_2/CH_3 bands of myristic acid are superimposed, resulting in slightly less intense peaks. The effect of this is however probably limited because of the minor CH_2/CH_3 peaks observed after ageing, see Fig. 2.

7.4. Discussion

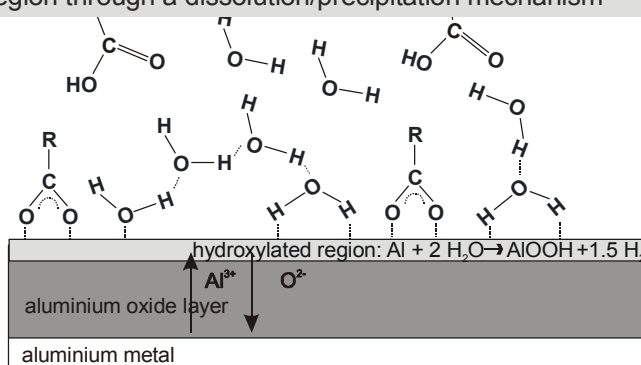
Based upon the discussed results, a model can be developed, schematically showing the changes to the surface, the oxide layer and the influence this has on the subsequent adsorption of myristic acid. This model is shown schematically in Fig. 9.

7.4.1. Changes to the surface chemistry upon ageing

Upon ageing in ambient air, quite rapidly an initially more or less clean oxide surface is contaminated. After an hour of ageing in ambient air, carboxylates chemisorb on the oxide surface, see Figs. 2 and 4. The chemisorbed carboxylates on the aged substrates are relatively short-chained as the spectra only show minor CH_2/CH_3 stretching vibrations (3000-2800 cm^{-1}), which is in sharp contrast with the well-resolved bands for myristic acid, see Fig. 2. This indicates that small air-borne contaminants like acetic acid and formic acid (which are present in ambient air [7]) have reacted with the oxide surface to form chemisorbed carboxylates. The symmetric $\nu_s(\text{COO}^-)$ carboxylate stretching vibration at 1472 cm^{-1} shows a constant intensity after 1 hour of ageing, see Fig. 4.

1. initial state**2. until about 20 hours of ageing**

adsorption of small carboxylic acid-based contamination and water on the oxide surface. growth of the oxide layer at the metal/oxide interface. formation of a hydroxylated region through a dissolution/precipitation mechanism

**3. after adsorption of myristic acid**

upon myristic acid adsorption, part of adsorbed water is desorbed. myristic acid not capable of displacing all adsorbed species from the surface resulting in decrease of the bonding capacity.

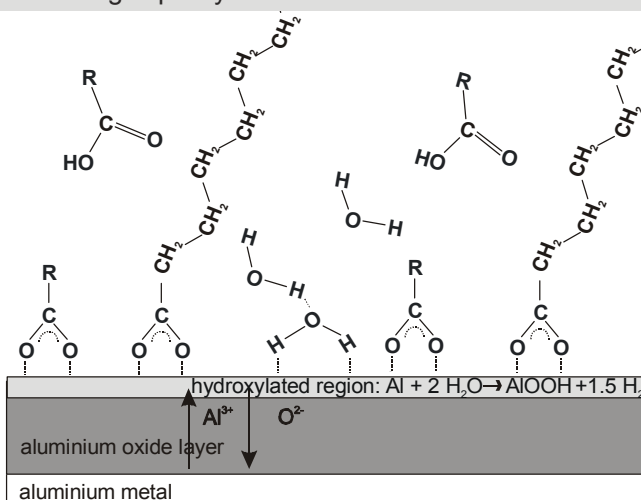


FIG. 9. Schematic of the processes occurring during ageing of an aluminium oxide layer in ambient air and the subsequent influence on the reactivity towards chemisorption of a carboxylic acid based molecule.

Upon continued ageing, the amount of chemisorbed carboxylates therefore does not further increase. Additional, short-chained organic contamination is however still adsorbed as the peaks in the CH_2/CH_3 stretching region continue to increase in intensity, see Fig. 2. The functionality of this contamination is difficult to determine because of a dominant contribution to the infrared spectra of bands due to adsorbed water and hydroxylation of the oxide layer.

The infrared spectra show the increase of bands at 1610 cm^{-1} , 1410 cm^{-1} and 3500 cm^{-1} as a function of ageing time, see Figs. 2 and 4, which increase in intensity until around 20 hours of ageing. The growth of the bands indicates the continuing adsorption of water on the oxide surface. The adsorbed water layer causes hydroxylation of the oxide layer, which is observed in the infrared spectrum as the formation of broad unresolved $\delta(\text{OH})$ bending and $\gamma(\text{OH})$ twisting bands around the main Al-O peak. Water layers, adsorbed on the oxide surface, cause Al-O bond breaking and localised dissolution of the layer [16,29]. This preferentially occurs at sites where there are defects in the oxide layer like close to impurities and at grain boundaries [16,29]. The dissolution allows passage of ions through the locally dissolved oxide layer, e.g. hydroxyls and oxygen inwards and aluminium ions outwards. Hydroxylation of the outer region of the oxide layer [2,22] is considered to occur through a dissolution-precipitation mechanism, occurring through a reaction between water and aluminium ions [22,30]. With this reaction, an amorphous aluminium oxyhydroxide region is formed. The passage of oxygen and aluminium ions through the oxide layer also allows further growth of the oxide layer at the oxide/metal interface [22], as evidenced from the growth of the main Al-O band. The amount of hydroxylation in ambient air is limited as compared to for example hydroxylation upon immersion of aluminium substrates in water [29] and only minor hydroxyl-related bands are observed. This was also noted by Vedder *et al* [16], comparing immersion of aluminium substrates in water with exposure to a humid atmosphere.

For ageing in the dry nitrogen environment, having a relative humidity of smaller than 1%, adsorbed water layers are not present and therefore dissolution of the oxide layer, growth of the oxide layer and the formation of a hydroxylated region does not occur, see Fig. 5.

7.4.2. Influence of ageing on the bonding capacity

The chemisorbed carboxylates and water adsorbed on the oxide surface cannot be removed by cleaning in solvent as evidenced by absence of negative bands upon cleaning, see Fig. 6. Therefore, the adsorbed organic contaminants

and water on the oxide surfaces have serious implications for the bonding capacity of the substrates.

Because of the very similar type of bonding, myristic acid is expected to be incapable of displacing the chemisorbed carboxylates from the oxide surface. The influence of other functionalised contamination, which is also adsorbed on the oxide surface, see above, could not be distinguished. Work performed by others [31] however indicates that part of this will also remain adsorbed upon adsorption of carboxylic acids. Myristic acid is capable of displacing some adsorbed water from the oxide surface, as evidenced by negative water bands, see Fig. 7. Despite this, the adsorbed water *does* appear to significantly influence the bonding capacity of the oxide surfaces. During the first 20 hours of ageing in ambient air, the largest changes in the infrared spectra of the oxides are observed, see Fig. 4, due to the adsorption of water on the oxide surface. In the same period, the surface shows a significant drop in its bonding capacity, see Fig. 8.

All these adsorbed species cause a significant reduction of the bonding capacity of the oxide surface. Within 20 hours of ageing in ambient air, the substrate is observed to lose 60% of its initial bonding capacity. Although this was studied using myristic acid, for bonding with other organic functional groups, a similar influence is expected as bonding proceeds through similar sites on the oxide surface [32].

Ageing of the substrates in a clean and dry nitrogen environment results in less decrease in bonding capacity of the surfaces. Some organic contaminants are adsorbed, see Fig. 5, but chemisorbed carboxylates appear not to be present. Also, no water is adsorbed on the substrates, because of the low humidity of this atmosphere. As a result of this, more reactive sites on the oxide surfaces remain available for the chemisorption of myristic acid. Consequently, the substrate loses only around 35% of its initial bonding capacity during the first 20 hours of ageing, see Fig. 8, which is low, compared to the 60% for ageing in air.

The results clearly demonstrate that it is of great importance that a metallic substrate should be covered with the organic overlayer (i.e. organic coating, adhesive or self-assembling overlayer) as soon as possible after the substrate surface treatment and should not be left in the ambient. Otherwise, the organic functional groups are capable of displacing part of the adsorbed species, but not all of them and therefore a significant number of sites are not available anymore for bonding. Consequently, the interfacial region will then be a patched region of sites where contaminants are adsorbed and sites where there is bonding between the organic overlayer and the oxide surface.

7.5. Conclusions

An investigation was made of the changes that occur to the aluminium oxide layer and to the bonding capacity of the surface upon ageing in ambient air and in a dry and clean environment. Ageing in air results in the adsorption of airborne organic contaminants and water on the oxide surface, which cannot be removed using common solvents. The water adsorbed on the oxide surface causes growth and hydroxylation of the oxide layer. As a result of the adsorbed species, it was found that the bonding capacity of the oxide surface rapidly decreases as a function of ageing time. During the first 20 hours, the substrate loses 60% of its initial bonding capacity.

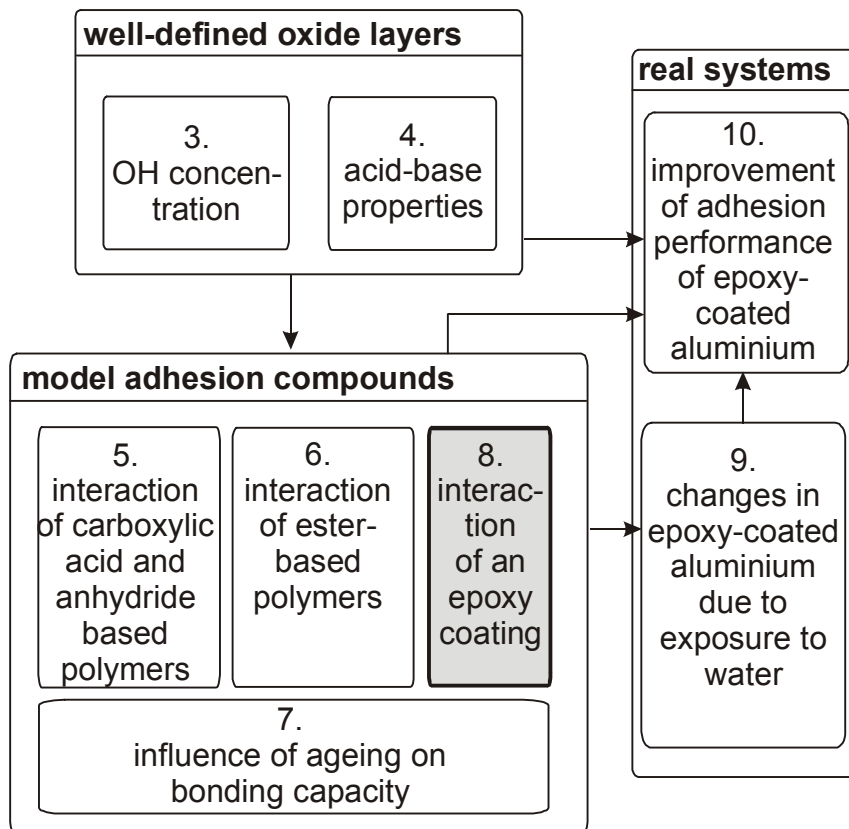
Ageing in a clean and dry nitrogen environment results also in the adsorption of some organic contaminants but the adsorption of water does not occur. Consequently, only a slight growth of the oxide layer and no hydroxylation is observed to occur. Also here, there is a decrease in the bonding capacity, but not as severe as for ageing in ambient air. During the first 20 hours of ageing, the substrate loses around 35% of initial bonding capacity.

References

1. Wernick, S.; Pinner, R.; Sheasby, P. G. *The surface treatment and finishing of aluminium and its alloys*; 5 ed.; Teddington: 1987; Vol. 1.
2. Alexander, M. R.; Thompson, G. E.; Beamson, G. *Surface and Interface Analysis* 2000, *29*(7), 468-477.
3. Hass, K. C.; Schneider, W. F.; Curioni, A.; Andreoni, W. *Journal of Physical Chemistry Part B* 2000, *104*(23), 5527-5540.
4. Davis, G. D. *Surface and Interface Analysis* 1991, *17*(7), 439-447.
5. Nylund, A.; Olefjord, I. *Surface and Interface Analysis* 1994, *21*(5), 283-289.
6. Thorne, N. A. *Surface and Interface Analysis* 1990, *16* 236-240.
7. Wattson, A. Y.; Bates, R. R.; Kennedy, D. *Air Pollution, the Automobile, and Public Health*; National Academies Press: Washington DC, 1988.
8. Sondag, A. H. M.; Raas, M. C.; van Velzen, P. N. T. *Chemical Physics Letters* 1989, *155*(4-5), 503-510.
9. Rider, A. N.; Arnot, D. R.; Wilson, A. R.; Vargas, O. *Materials Science Forum* 1995, *189* 235-240.
10. OlssonJacques, J. R.; Wilson, A. R.; Rider, A. N.; Arnot, D. R. *Surface and Interface Analysis* 1996, *24*(9), 569-577.
11. Davis, G. D. *Surface and Interface Analysis* 1993, *20*(5), 368-372.
12. Tao, Y. T. *Journal of the American Chemical Society* 1993, *115*(110), 4350-4358.
13. Allara, D. L.; Nuzzo, R. G. *Langmuir* 1985, *1*(1), 52-66.
14. van Gils, S.; Melendres, C. A.; Terryn, H. *Surface and Interface Analysis* 2003, *35*(4), 387-394.
15. Melendres, C. A.; van Gils, S.; Terryn, H. *Electrochemistry Communications* 2001, *3*(12), 737-741.
16. Vedder, W.; Vermilyea, D. A. *Transactions of the Faraday Society* 1969, *65* 561-584.
17. Kiss, A. B.; Kerezury, G.; Farkas, L. *Spectrochimica Acta Part A* 1980, *36*(7), 653-658.
18. Frost, R. L.; Kloprogge, J. T.; Russell, S. C.; Szetu, J. *Applied Spectroscopy* 1999, *53*(7), 829-835.
19. Kloprogge, J. T.; Ruan, H. D.; Frost, R. L. *Journal of Materials Science* 2002, *37* 1121-1129.
20. Music, S.; Dragevic, D.; Popovic, S. *Materials Letters* 1999, *40* 269-274.
21. Wefers, K.; Misra, C. *Oxides and hydroxides of aluminium*; Alcoa Cooperation of America: 1987.
22. Alexander, M. R.; Thompson, G. E.; Beamson, G. *ATB Metallurgy* 2000, (3-4), 133-141.
23. Vlaev, L.; Damyanov, D.; Mohamed, M. M. *Colloids and Surfaces* 1989, *36*(4), 427-437.
24. Bellamy, L. J. *The infrared spectra of complex molecules. Vol. 1*; 3rd ed.; Chapman and Hall: New York, 1978.
25. Roeges, N. P. G. *A guide to the complete interpretation of infrared spectra of organic Structures*; Wiley: Chichester, 1994.
26. Evans, H. E.; Weinberg, W. H. *Journal of Chemical Physics* 1979, *71*(12), 4789-4798.
27. Hayden, B. E.; Prince, K.; Woodruff, D. P.; Bradshaw, A. M. *Surface Science* 1983, *133*(2-3), 589-604.
28. Zhuang, G.; Chottiner, G. *Review of Scientific Instruments* 1994, *65*(8), 2494-2499.
29. Alwitt, R. S. The aluminium-water system, in *Oxides and oxide films vol. 4*, Diggle, J. W., editor; Dekker: New York, 1976; Chapter 3, pp. 169-250.
30. van Gils, S.; Terryn, H.; Stijns, E.; Thompson, G. E.; Alexander, M. R. *ATB Metallurgy* 2003, *43*(1-2), 358.
31. Liakos, I. L.; Newman, R. C.; McAlpine, E.; Alexander, M. R. *Surface and Interface Analysis* 2004, *36* 347-354.
32. Fowkes, F. M. *Physicochemical aspects of polymer surfaces*; Plenum Press: New York, 1983; Vol. 2.

CHAPTER 8.

INTERACTION OF EPOXY COATINGS WITH ALUMINIUM OXIDE SURFACES



Synopsis

In the next chapter, the changes occurring in a typical epoxy-coated aluminium system due to exposure to water are investigated. As an introduction, in this chapter, an investigation is performed of the interaction of this epoxy coating with the aluminium oxide surface. Just as in the previous chapters, this is done by choosing appropriate model adhesion compounds to represent the functional groups in the epoxy coating. These are adsorbed on the oxide surface and their interaction is studied using infrared reflection absorption spectroscopy. Moreover, the stability of bonding of these compounds in the presence of water is being evaluated. It is found that all model adhesion compounds (and thus also the epoxy coating) bond through hydrogen-bonding with the aluminium oxide surface and their bonding is not stable in the presence of water.

8.1. Introduction

In previous chapters, already a quite extensive investigation was performed of how various model adhesion compounds bond to the aluminium oxide surface and how this is influenced by the chemistry of the aluminium oxide surface. For this reason, the current investigation is kept limited and the bonding of the epoxy model adhesion compounds is only considered for one type of aluminium oxide. The alkaline pretreated type of aluminium oxide is chosen for this as it likely most closely resembles the oxide layer onto which the epoxy coating is applied in Chapters 9 and 10.

8.2. Experimental

8.2.1. Choice of model compounds, application method, aluminium substrates and infrared analysis

The epoxy coating that is studied in the next chapter is a quite commonly used type, based on a DGEBA (diglycidyl ether of bisphenol-A) (Epikote 1001) and which is cured using a poly(amide) based curing agent (Versamid 115). Poly(amide)-based curing agent are formed by the reaction between dimerised or polymerised fatty acids and the higher homologues of ethylene amines [1]. The curing reaction with the epoxy proceeds through the amines present in the poly(amide) curing agent [1].

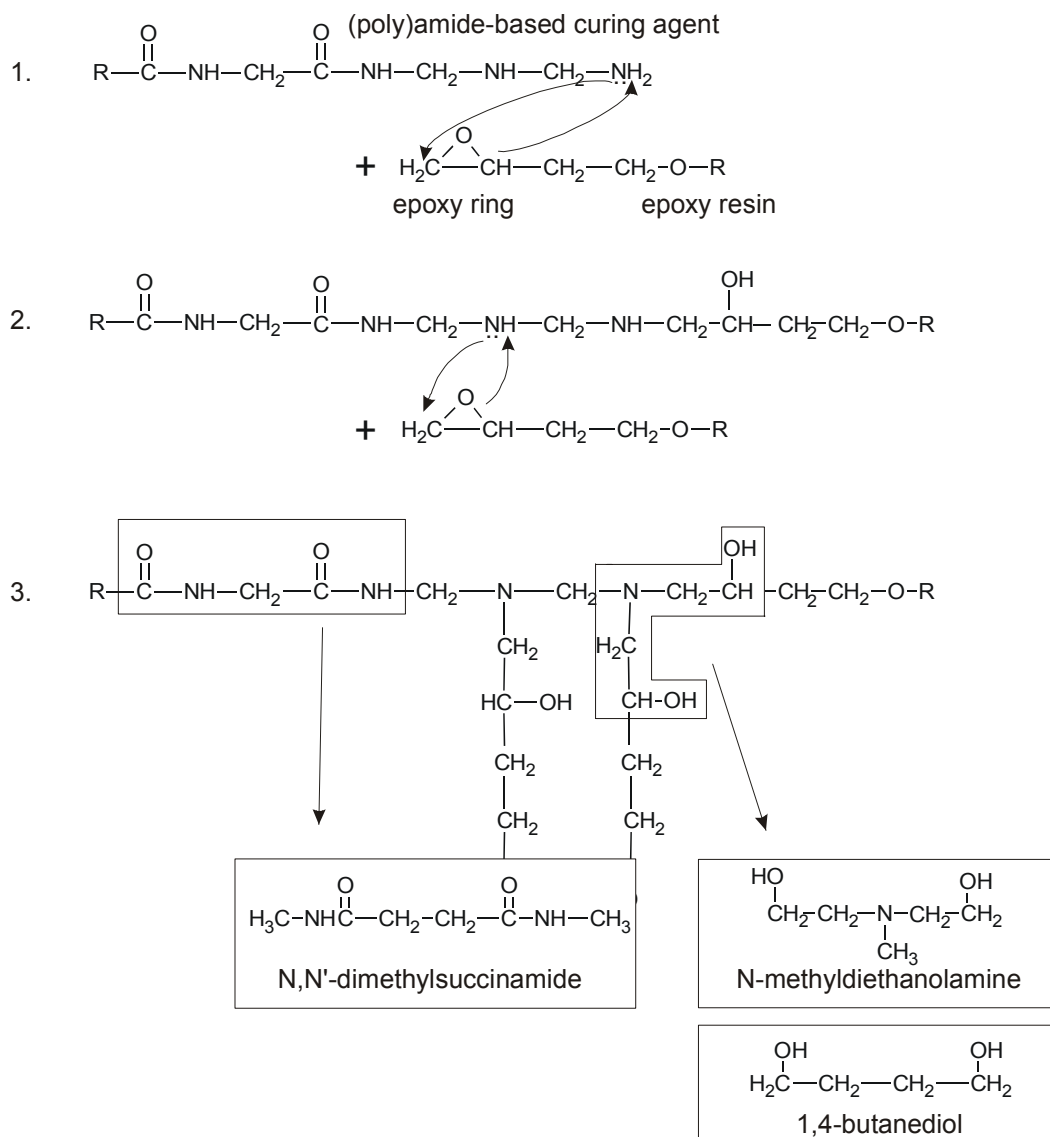


FIG. 1. Schematic showing the curing of an epoxy resin in presence of a poly(amide) based curing agent and the epoxy model adhesion compounds derived from this for the purpose of studying bonding with the aluminium oxide surface.

In Fig. 1, the curing reaction of this epoxy resin in presence of a poly(amide)-based curing agent is shown schematically. In step 1, the primary amine (NH_2) endgroups of the curing agent cause epoxy ring opening and chain extension occurs. In step 2, network formation occurs through reaction with a secondary amine (NH). From the final cured coating, three model adhesion compounds were derived. Their derivation is shown as step 3 in Fig. 1. The N,N' dimethylsuccinamide compound was chosen to model the amide functional groups in the cured coating and the N-methyldiethanolamine compound was chosen to model the hydroxyl and amine functional groups in the cured coating. As infrared bands due to tertiary amines (N) are very weak [2,3], the 1,4-

butanediol compound was studied additionally. If bonding to the oxide surface only occurs through the amine functional group and not or only very weakly through the hydroxyl groups, then 1,4-butanediol will not bond to the oxide surface. All compounds were obtained from Sigma-Aldrich as a >98% purity and were used without further purification.

The preparation procedure of the alkaline pretreated aluminium substrates is discussed in paragraph 3.2.1 on page 23. The molecules were applied onto the substrates by dipcoating from a mixture in chloroform. For N,N'-dimethylsuccinamide, the concentration in solution was modified so saturation coverage of the oxide surface was obtained and excess, non-bonding molecules were not present anymore. For the N-methyldiethanolamine and 1,4-butanediol compounds this was not necessary as excess, non-bonding molecules were found to sublime again from the substrates. Bonding of the molecules with the substrates was investigated using FTIR-RAS, following the same experimental procedure as used in previous chapters, see paragraph 5.2.3 on page 63.

8.3. Results

8.3.1. Infrared spectra of the compounds

In Fig. 2, infrared bulk spectra are shown for the three compounds and in Table 1 assignments of the infrared bands are given. The top spectrum shows the spectrum for N,N' dimethylsuccinamide. The most important bands in the spectrum are at 1649 and 1563 cm^{-1} and are respectively due to the C=O stretching and the N-H bending/C-N stretching vibration. These bands are generally respectively denoted as the amide I and amide II bands [2-5]. The spectrum for N-methyldiethanol amine shows the most important band at 1030 cm^{-1} , which is due to the $\nu(\text{C-OH})$ stretching vibration of the hydroxyl groups [6,7]. Bands due to the amine are not present, as they are very weak for tertiary amines [2,3]. Finally, the 1,4-butanediol spectrum shows the most important band at 1049 cm^{-1} , which is also due to the $\nu(\text{C-OH})$ of the hydroxyl groups.

8.3.2. Bonding and bonding stability of the N,N'-dimethylsuccinamide compound with the aluminium oxide surface

Amides can bond through Lewis acid-base interactions with either their carbonyl (C=O) or their amine (N-H) functionality [4,5,8]. Both will result in *downward* shifting of the amide I band (1653 cm^{-1}) but in *upward* shifting of the

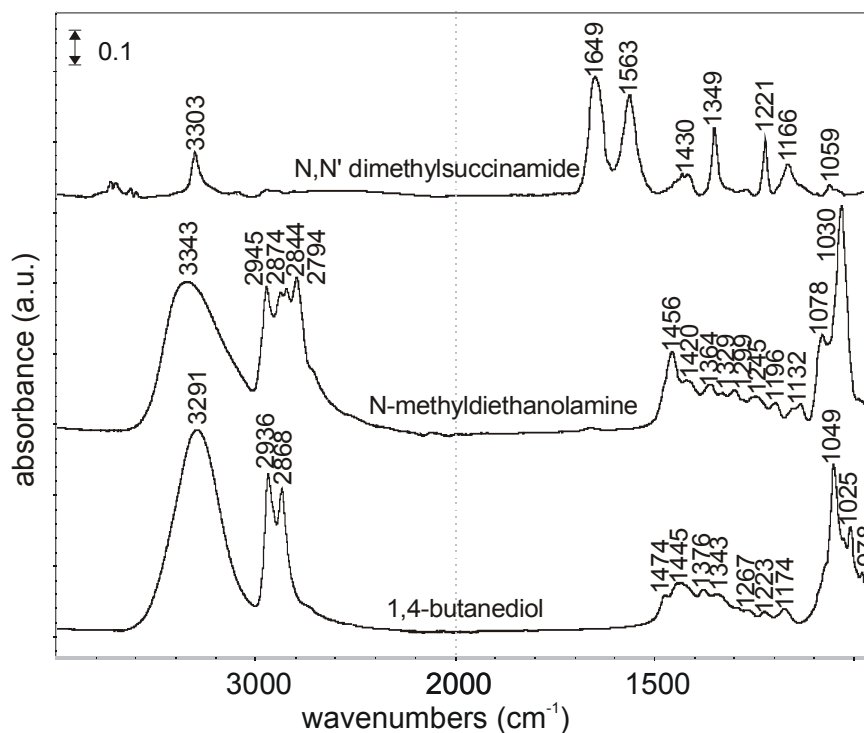


FIG. 2. Bulk FTIR spectra of the three epoxy model adhesion compounds.

amide II band (1563 cm^{-1}), with stronger electron-exchange resulting in larger shifts [4,5,8].

In Fig. 3, FTIR-RAS spectra are shown in the $1700\text{--}1525\text{ cm}^{-1}$ (amide I/II) region, as obtained for adsorption from two different concentration of N,N'-dimethylsuccinamide in chloroform on the aluminium substrates. At the higher concentration, the band clearly consists of two separate bands, while at the lower concentration an asymmetrically shaped band is present. The components present in the region were resolved by curve-fitting. The results are shown in Fig. 3. For the layer applied from the highest concentration, four components were necessary to accurately describe the region. The components found at 1653 and 1562 cm^{-1} are close to the positions observed for the amide I (C=O stretch) and amide II (N-H bend/C-N stretch) for bulk N,N'-dimethyl succinamide, see Table 1, and are therefore due to molecules not involved in bonding to the oxide surface. At the lower concentration in solution, the region could be accurately described using 2 components, having positions of 1632 and 1573 cm^{-1} , see Fig. 3. No components were present in the spectrum anymore due to molecules which are not involved in bonding with the oxide surface and consequently, the spectrum fully corresponds to bonded molecules.

TABLE 1. FTIR peak assignments for the bulk spectra of the epoxy coating model compounds [2-7].

N,N' dimethyl succinamide (cm^{-1})	N-methyl diethanolamine (cm^{-1})	1,4-butanediol (cm^{-1})	assignment
3303			ν_{NH} [NH stretch]
	3343	3291	ν_{OH} [OH stretch]
	2945	2936	$\nu_{\text{as}}(\text{CH}_2)$ [asym stretch]
	2874	2868	$\nu_{\text{s}}(\text{CH}_2)$ [sym stretch]
	2844 / 2794		$\nu(\text{CH}_3)$ next to amine
1649			amide I [C=O stretch]
1563			amide II [N-H bend / C-N stretch]
		1474	$\delta(\text{CH}_2)$ [CH ₂ bend]
	1456		δCH_3 [CH ₃ bend]
1430	1420	1445	$\delta(\text{CH}_2)$ [CH ₂ bend]
	1356		CH ₃ [CH ₃ def]
1349	1346	1376	$\delta(\text{CH}_2)?$ [CH ₂ bend]
	1329	1343	$\delta(\text{C-OH})$ [bend]
	1298	1292	$\omega(\text{CH}_2)$ [CH ₂ wagging]
	1245	1267	$\delta(\text{CH}_2)$ [CH ₂ bend]
1221			amide III
	1196	1174	$\tau(\text{CH}_2)$ [CH ₂ twisting]
1166	1132		$\rho(\text{CH}_3)$ [CH ₃ rock]
	1078		$\rho(\text{CH}_2)$ [CH ₂ rock]
	1030	1049	$\nu(\text{CO})$ [C-OH stretch]

The bulk spectrum shows approximately equal intensity of the amide I and II bands, see Fig. 2. The infrared spectrum of the bonded molecules, see Fig. 3, however show an amide I band at 1632 cm^{-1} which is much stronger than the amide II band at 1573 cm^{-1} . This is likely the result of the surface selection rule in FTIR-RAS, which causes infrared vibrations perpendicular to the metallic surface plane appearing much stronger than infrared vibrations parallel to the metallic surface plane. The stronger amide I band, which is due to the C=O stretch, then indicates that there is a net alignment of the C=O group perpendicular to the metallic surface plane and a more parallel alignment of the C-N/N-H group (amide II band) [9,10].

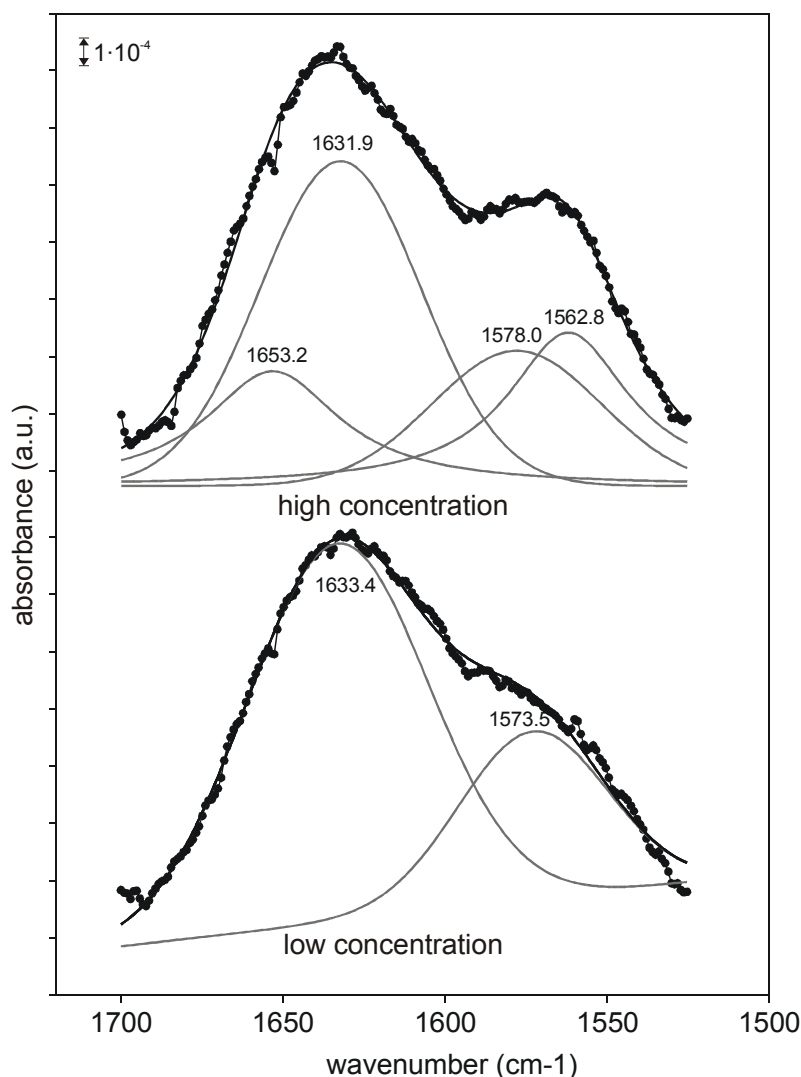


FIG. 3. FTIR-RAS spectra of the amide I/II region obtained for N,N'-dimethylsuccinamide molecules, adsorbed on the alkaline pretreated aluminium oxide surface from two concentrations in chloroform. The fits had an r^2 goodness of fit of respectively 0.995 and 0.996, from top to bottom.

In Fig. 4, the full FTIR-RAS spectrum is shown as obtained for N,N'-dimethylsuccinamide molecules bonded to the aluminium oxide surface. The $\nu(\text{OH})$ hydroxyl stretching is distorted, showing a negative band at around 3600 cm^{-1} and a positive band at around 3500 cm^{-1} . The sharp, downward band at 3734 cm^{-1} is an artefact and is due to water in the infrared compartment, as discussed in previous chapters. In the $\nu(\text{CH}_2/\text{CH}_3)$ stretching region, slightly negative bands are observed. N,N'-dimethylsuccinamide does not have infrared bands in this region and the presence of negative bands therefore indicates that displacement of adventitious contamination from the oxide surface occurs. Besides the asymmetrically shaped amide I and II bands at 1629 cm^{-1} , the spectrum shows relatively intense bands at around 1418, 1298, 1251 and 1184

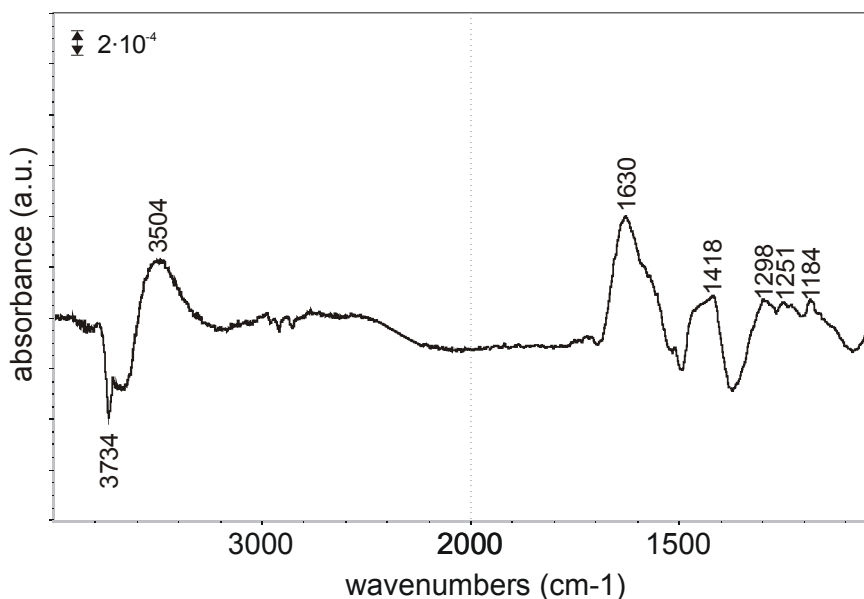


FIG. 4. FTIR-RAS spectrum of the N,N'-dimethylsuccinamide molecules, adsorbed on the alkaline pretreated aluminium oxide surface.

cm⁻¹. The band at 1251 cm⁻¹ is likely the amide III band, see Table 1, shifted to higher wavenumbers due bonding of the amide group with the oxide surface [8]. The bands at 1298 and 1184 cm⁻¹ are likely due to shifted CH₂/CH₃ related vibrations, see Table 1. The presence of the intense, asymmetrically shaped band at 1418 cm⁻¹ is not understood, as the peak is observed to be only weak in the bulk spectrum.

The bonding stability of the N,N'-dimethylsuccinamide compound with the oxide surface was evaluated by immersion of the substrates with the bonded molecules in water. This was found to lead to removal of all molecules from the substrate within 5 minutes, indicating that the bonding of the molecules to the oxide surface is not stable in the presence of water.

8.3.3. Bonding and bonding stability of N-methyldiethanolamine and 1,4-butanediol with the aluminium oxide surface

Alcohol groups bond intact through hydrogen-bonding or dissociatively with deprotonation and the formation of a coordinatively bonded alkoxide [11-14]. For hydrogen-bonding, the hydroxyl can either act as a base (through its oxygen) or as an acid (through its proton). For dissociative adsorption, the proton from the alcohol combines with either an oxygen or hydroxyl on the oxide surface to respectively form a hydroxyl or a water molecule. In Fig. 5, infrared spectra are shown for both N-methyldiethanolamine and 1,4-butanediol, adsorbed on the aluminium oxide surface. For both of these compounds it was

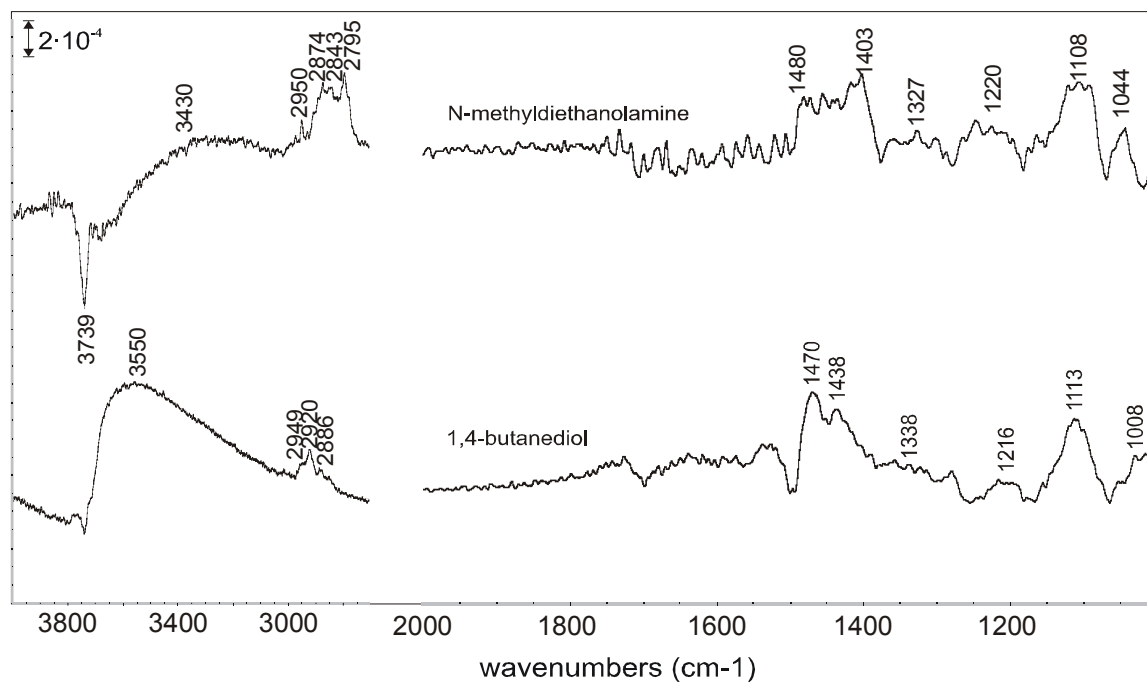


FIG. 5. FTIR-RAS spectra of a N-methyldiethanolamine and 1,4-butanediol molecules, adsorbed on the alkaline pretreated aluminium oxide surface.

found to be not necessary to modify the concentration in solution to obtain a layer of only bonded molecules because excess, non-bonded molecules were found to sublime from the substrate. The spectra for both adsorbed compounds are very similar to each other. In the $\nu(\text{CH}_2/\text{CH}_3)$ region ($3000\text{--}2800\text{ cm}^{-1}$), clear bands are present, indicating the presence of the compounds on the oxide surface. Positive, slightly distorted bands are observed in the $\nu(\text{OH})$ stretching vibration regions. For the N-methyldiethanolamine a strong negative, water-related band is observed at 3739 cm^{-1} . In the $1500\text{--}1400$ and $1250\text{--}1200\text{ cm}^{-1}$ region, both compounds show broad, unresolved peaks due to CH_2/CH_3 related vibrations.

The presence of a $\delta(\text{COH})$ hydroxyl bending vibration infrared band allows to determine whether the alcohol groups bond intact or whether dissociative adsorption occurs, as for dissociative adsorption, the band is expected to be absent [11-14]. For the bulk spectra, the band due to the $\delta(\text{COH})$ vibration is found at $1329/1343\text{ cm}^{-1}$, see Table 1. For the adsorbed compounds, a peak around the position of the $\delta(\text{COH})$ band appears to be present, although the region is not very well-resolved.

Both adsorbed compounds give a broad band at around 1110 cm^{-1} . This is likely the $\nu(\text{CO})$ stretching band, which for the bulk spectra is found as an intense band at around 1050 cm^{-1} , see Table 1 and Fig. 2. For the adsorbed compounds, the peak is thus shifted over roughly 50 cm^{-1} to higher

wavenumbers. This comparably large shift is not well-understood as it is significantly larger than the 30 cm^{-1} on average reported for an alcohol being involved in hydrogen-bonding with an oxide surface [11,12,15,16].

The bonding of the amine functional group in N-methyl diethanolamine with the oxide surface cannot be determined because of absence of infrared vibrations related to this group and because both compounds show a stable bonding, see the Experimental section.

The bonding stability of the N-methyldiethanolamine compound with the oxide surface was tested in water. Immersion in water was found to lead to rapid detachment of all molecules from the substrates within 5 minutes, comparable with the results obtained for the amide functional group bonding stability.

8.4. Discussion

The epoxy coating that is studied in chapters 9 and 10 was studied with respect to its bonding capacity with the oxide surface, using 3 different model adhesion compounds.

The N,N' dimethylsuccinamide compound was chosen to study the amide functional groups in the cured coating. The infrared spectra for the N,N' dimethylsuccinamide molecules bonded to the oxide surface show an amide I band shift of 22 cm^{-1} and an amide II band shift of -11 cm^{-1} as compared to their bulk values. The amount of shift corresponds well to bonding of amides to protic solvents, reported in the literature [5,8,17,18]. Moreover, the $\nu(\text{OH})$ hydroxyl stretching region shows up distorted in the spectrum, likely due to perturbation of the hydroxyls on the oxide surface (resulting in an infrared peak shift) as a result of their interaction with the amide functional groups.

It is therefore likely that interaction of the amide groups in N,N' dimethylsuccinamide occurs through hydroxyls on the surface, similar to the ester and carboxylic acid functional groups, studied in Chapters 5 and 6.

The differences in amide I and II peak intensities indicate that bonding occurs through the carboxyl $\text{C}=\text{O}$ group as it is oriented towards the surface. The carbonyl then acts as base, by donating negative charge through its oxygen lone pair electrons to hydroxyls on the oxide surface, which act as the acid.

The bonding stability of the compounds in the presence of water is found to be not stable. This compares well with the results for the ester groups, discussed in chapter 6, which also showed hydrogen-bonding to hydroxyls on the oxide surface, but the bond was found to be not stable in the presence of water.

In Fig. 6a, a schematic is shown of the bonding of the N,N' dimethylsuccinamide compound with the oxide surface. The figure only serves as an illustration for the type of bonding and for example the orientation of the groups with respect to the surface plane is not taken well into account.

For the N-methyldiethanolamine and 1,4-butanediol compounds, representing the alcohol and amine functionality of the cured coating, assignment of bonding is more difficult. As discussed, alcohols can either adsorb intact through hydrogen-bonding or dissociatively with the formation of an alkoxide species. The spectra likely show the presence of a $\delta(\text{COH})$ band, although not well-resolved, indicating dissociative adsorption does not occur. However, the $\nu(\text{CO})$ band shows a comparably large upward shift as compared

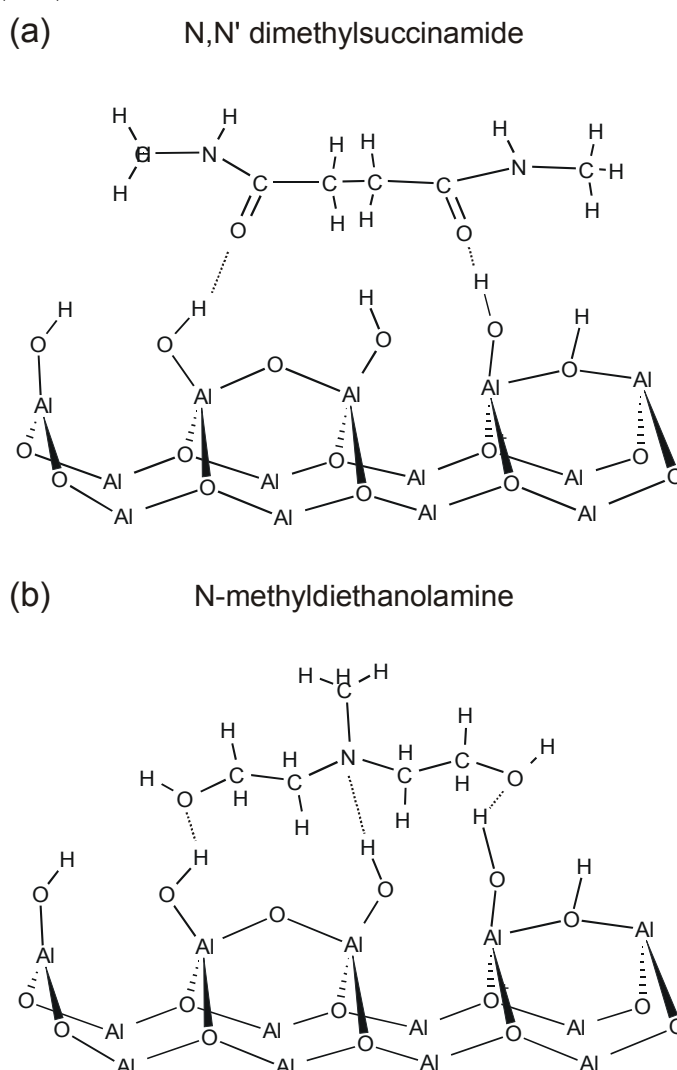


FIG. 6. Schematic of the bonding of the (a) N,N' dimethylsuccinamide and (b) N-methyldiethanolamine compounds with an aluminium oxide surface. Figures only serves as an illustration for the type of bonding and for example the orientation of the groups with respect to the surface plane is not considered.

to literature data for hydrogen-bonded alcohols. But, the compound does not show a very stable bonding with the oxide surface in presence of water, despite being bonded by two groups, making dissociative adsorption and bonding as a coordinatively bonded alkoxy species unlikely. For these reasons, bonding of the alcohol groups is tentatively assumed to be through hydrogen-bonding. This corresponds with results obtained by Marsh *et al* [19], also studying the bonding of N-methyldiethanolamine with an aluminium oxide surface but using XPS as an analysis technique. The $\nu(\text{C-O})$ shift to higher wavenumbers then indicates that the alcohol acts as the *base*, donating negative charge through its lone pair electrons on the oxygen to hydroxyls on the oxide surface, which act as the *acid* [12].

The bonding mode of the amine group could not be determined due to absence of corresponding infrared bands. Marsh *et al.* [19] used XPS to determine bonding of the N-methyldiethanolamine with an aluminium oxide surface. XPS is more suitable to study bonding of amine functional groups than FTIR-RAS. They found that the amine bonds through Lewis acid-base interaction with the oxide surface, in which the nitrogen donates negative charge through its lone pair electrons to sites on the oxide surface. The results obtained here show that the N-methyldiethanolamine and 1,4-butanediol compounds do not differ in their bonding stability with the oxide surface, indeed indicating a not very strong bonding of the amine functional group. Also taking into account the results obtained for the other model adhesion compounds, the bonding of the amine is therefore likely via hydrogen-bonding to hydroxyls on the oxide surface.

In Fig. 6b, a schematic is shown of the bonding of the N-methyldiethanolamine compound with the oxide surface. The figure only serves as an illustration for the type of bonding and for example the orientation of the groups with respect to the surface plane is not taken well into account.

The results of the model adhesion compounds can be transferred back to the epoxy coating. Because all functional groups in the epoxy coating apparently only interact through hydrogen-bonding, it can be derived that the whole macroscopic bond between the epoxy-coating and the aluminium oxide surface will rely on hydrogen-bonding. The limited stability of the bonding of the compounds in water shows that the adhesion of the coating will likely be limitidly stable in the presence of water. As bonding with the oxide surface occurs to hydroxyls, an optimal adhesion of the epoxy coating is obtained for an oxide surface having a high density of hydroxyls.

8.5. Conclusion

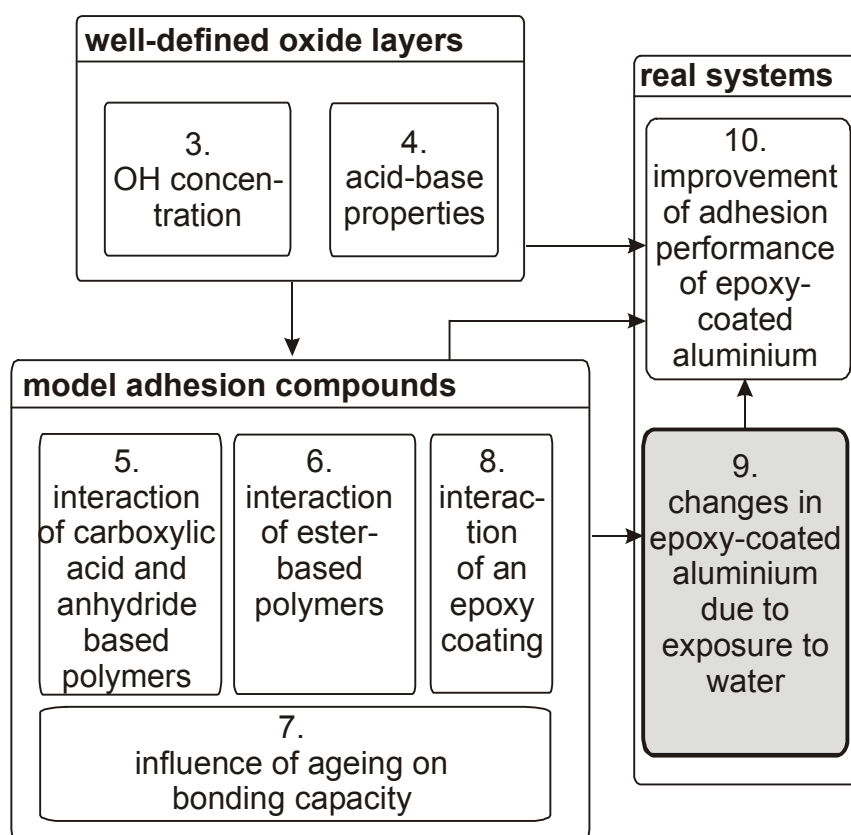
The epoxy coating that is studied in the next chapters was studied with respect to its bonding with the aluminium oxide surface using 3 different model compounds. It was found that bonding of the compounds occurred exclusively through hydrogen-bonding with hydroxyls on the oxide surface. The amide bonds via its carbonyl, donating negative charge through its oxygen lone pair electrons to hydroxyls on the oxide surface. The alcohol bonds through its oxygen, also donating negative charge through its oxygen lone pair electrons to hydroxyls on the oxide surface. The amine group bonds through its nitrogen, again donating negative charge through its oxygen lone pair electrons to hydroxyls on the oxide surface. None of the compounds showed a stable bonding to the oxide surface in the presence of water. Because only hydrogen-bonds are formed and these bonds are not stable in the presence of water, it can be expected that also the epoxy coating itself will not have an absolutely water-stable bonding. As bonding with the oxide surface occurs to hydroxyls, an optimal adhesion of the epoxy coating is obtained for an oxide surface having a high density of hydroxyls.

References

1. Ellis, B. *Chemistry and Technology of Epoxy Resins*; Blackie: London, 1993.
2. Bellamy, L. J. *The infrared spectra of complex molecules. Vol. 1*; 3rd ed.; Chapman and Hall: New York, 1978.
3. Roeges, N. P. G. *A guide to the complete interpretation of infrared spectra of organic structures*; Wiley: Chichester, 1994.
4. Maeda, Y.; Nakamura, T.; Ikeda, I. *Macromolecules* 2002, *35* 10172-10177.
5. Torii, H.; Tomoaki, T.; Tasumi, M. *Journal of Raman Spectroscopy* 1998, *29* 537-546.
6. Dahlqvist, M.; Hotokka, M.; Rasanen, M. *Chemical Physics* 1998, *229* 137-147.
7. Manzares, C. E.; Reynolds, D.; Lewis, E. K. *Journal of Molecular Structure* 2004, *689* 183-190.
8. Kubelka, J.; Keiderling, T. A. *Journal of Physical Chemistry A* 2001, *105* 10922-10928.
9. Gu, Y.; Shi, Z.; Nie, C. S. *Applied Spectroscopy* 1998, *52*(6), 855-862.
10. Hooper, A. E.; Werho, D.; Hopson, T.; Palmer, O. *Surface and Interface Analysis* 2001, *31* 809-814.
11. Burcham, L. J.; Briand, L. E.; Wachs, I. E. *Langmuir* 2001, *17*(6175), 6184.
12. Natal-Santiago, M. A.; Dumesic, J. A. *Journal of Catalysis* 1998, *175* 252-268.
13. Evans, H. E.; Weinberg, W. H. *Journal of Chemical Physics* 1979, *71*(4), 1537-1542.
14. Zaki, M. I.; Hassan, M. A.; Pasupuleti, L. *Langmuir* 2001, *17* 4025-4034.
15. Burcham, L. J.; Briand, L. E.; Wachs, I. E. *Langmuir* 2001, *17* 6164-6174.
16. Kagel, R. O.; Greenler, R. G. *The Journal of Chemical Physics* 1968, *49*(4), 1638-1647.
17. Besson, F.; Buchet, R. *Spectrochimica Acta Part A* 1997, *53* 1913-1923.
18. Dorval, C.; Zeegers-Huyskens, Th. *Spectrochimica Acta Part A* 1973, *29A* 1805-1814.
19. Marsh, J. *Applied Surface Science* 1998, *133* 270-287.

CHAPTER 9.

CHANGES IN EPOXY-COATED ALUMINIUM DUE TO EXPOSURE TO WATER ¹



¹ This chapter was published as a scientific paper:
J. van den Brand, S. Van Gils, H. Terryn, V.G.M. Sivel, J.H.W. de Wit,
Progress in Organic Coatings, 2004, accepted for publication

Synopsis

To be able to develop more durable metal-polymer bonds in the future, a thorough understanding of the changes occurring in the metal-polymer system due to exposure to water is important. In this chapter, an investigation is performed of the changes that occur in a typical epoxy-coated aluminium system when it is exposed to water of different temperatures. The adhesion of the coating is evaluated as a function of exposure time and temperature. It is found that upon exposure to water the adhesion is initially rapidly lost. After this however, the adhesion starts to improve again and even exceeds the initial adhesion. The changes that occur in the system as a result of exposure to water are investigated using various analytical techniques. Based on this, a model is developed. Initially, the adhesion of the coating is rapidly lost due to exposure to water because the bond with the oxide surface is not stable in the presence of water, see also Chapter 8. Water then accumulates at the epoxy-aluminium interface. As a result of this, a very thin aluminium oxyhydroxide layer starts to grow on the aluminium substrate due to the reaction between water and the aluminium metal. After some time, this growing oxyhydroxide layer re-establishes contact with the epoxy coating and the adhesion shows recovery – likely due to formation of a mixed epoxy-aluminium interphasial region – and becomes better than before exposure to water.

9.1. Introduction

When metal-polymer bonds are exposed to aqueous environments, the adhesion between the two is quite often weakened or sometimes even completely lost due to the accumulation of water at the interface. For structural adhesive bonds this can lead to failure of the structure [1] and for organic coatings, this can lead to corrosion of the underlying substrate [2-4].

Water is known to have a tendency to accumulate at the interface and thereby displaces the bond that exists between the metal and the polymer [5,6]. There can be several reasons for this. Most organic coatings contain functional groups that are only capable of forming comparably weak hydrogen-bonds with the oxide surface. Water molecules can displace these bonds as shown in Chapters 5 and 6, thereby causing a loss of adhesion of the coating [7,8]. Water can also condensate in existing microvoids at the interface where there is no adhesion between the coating and substrate [9]. Finally, there can be

accumulation of water at the interface as a result of osmotic pressures which are set-up due to hygroscopic contaminants on the oxide surface [9].

To be able to develop more durable metal-polymer bonds in the future, a thorough understanding of the changes occurring in the metal-polymer system and at the interface due to exposure to water is important. In this work, a detailed investigation is performed of the changes occurring in a typical epoxy-coated aluminium system due to exposure to water.

The adhesion of the epoxy-coating in an aqueous environment is investigated as a function of exposure time and temperature using the NMP adhesion test and using peel tests. TEM (transmission electron microscopy) cross section images are obtained of the epoxy-aluminium interface to visually inspect changes that have occurred in the system due to exposure. TGA (thermogravimetric analysis) measurements are performed to determine the amount of water absorbed by the system as a function of exposure time and temperature. To further investigate the changes that have occurred in the system, the coatings are manually peeled from the substrates and the separated parts are investigated using SEM (scanning electron microscopy), FTIR (infrared spectroscopy), XPS (X-ray photoelectron spectroscopy) and VISSE (visible spectroscopic ellipsometry).

9.2. Experimental

9.2.1. Sample preparation

For the investigation, a 99.5% pure AA1050 aluminium alloy (0.04 wt.% Fe and 0.25 wt.% Si) was used. The 30 cm x 25 cm x 1 mm size substrates were first wiped clean with tissues, soaked with acetone and ethanol. Then, the substrates were alkaline etched by immersion in a 5% NaOH solution for 5 minutes at room temperature, thereby etching away several microns of the material [10]. After this, the substrates were rinsed using deionised water. The smut layer caused by the alkaline etching was then removed by immersion in a 30% HNO₃ solution for 30 seconds and finally the substrates were thoroughly rinsed using deionised water and blown dry using compressed clean air.

On a number of substrates, the organic hydration inhibitor NTMP (nitrilotri methylene phosphonic acid) was subsequently adsorbed from a 1 g/l solution in water. NTMP was obtained from Sigma-Aldrich as a 97+% purity. The substrates were allowed to react with the organic compound for a period of 30 minutes, rinsed-off extensively using deionised water and then blown dry using compressed clean air.

Within 45 minutes after the surface treatments, the epoxy coatings were applied on the substrates, to prevent the adsorption of airborne organic contaminants, which occurs rapidly and is known to cause a decrease in reactivity of the aluminium substrates as was shown in Chapter 7. The epoxy coating that was used is a relatively simple, unmodified and transparent Resolution Epikote 1001 (based on bisphenol-A and epichlorhydrin). As a curing agent, a high molecular weight Versamid 115 polyamide-based curing agent was added in the appropriate ratio. An amount of 38 mass% of a solvent-mixture consisting of n-butanol (20 vol.%), xylene (54.2 vol.%) and n-butanon (25.8 vol.%) was added to make proper application of the coating possible. After thorough mixing, the resin mixture was applied on the substrates using a fully automated barcoater. During application the substrates were kept flat by using a vacuum table. Finally, the coated substrates were cured, first for 2 days at room temperature in a dust-free cabinet, then for 2 days at 50 °C and finally for 6 hours at 70 °C. The resulting final cured coating thickness was $80 \pm 5 \mu\text{m}$ across the substrates.

9.2.2. NMP adhesion testing and exposure conditions

For adhesion testing of the epoxy coatings the NMP-adhesion test was used [11-13]. NMP (N-methyl pyrrolidone, $\text{C}_5\text{H}_9\text{NO}$) is a highly polar solvent. It is capable of forming strong hydrogen-bonds, allowing it to rapidly diffuse into organic coatings and causing extensive swelling. Due to the swelling, shear stresses are imposed at the metal-coating interface. These shear stresses are in most cases relaxed by delamination of the coating, with a *longer* time until delamination indicating a *better* adhesion [11].

A square $4 \times 4 \text{ cm}^2$ coated sample was exposed at a circular 20 mm diameter region in the centre of the sample, using a cell filled with deionised water. This is shown schematically in Fig. 1. After the exposure period, the sample was taken out of its cell and cross-cuts were made through the coating using a knife, making a pattern of $5 \times 5 \text{ mm}^2$ squares. This has the advantage that delamination of the coating in NMP can proceed at independent sites. The sample was then immersed fully in the NMP solvent, heated to 60 °C. The time until all squares were removed was then recorded separately for the exposed and the not-exposed region.

To avoid the possible effects from coating thickness variations and ageing of the solvent on the NMP delamination time, the NMP delamination time of

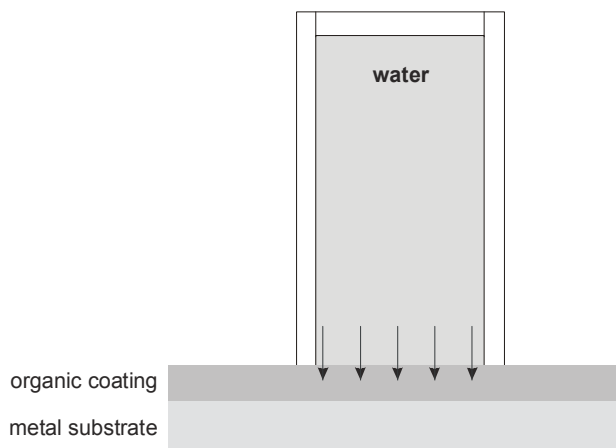


FIG.1. Schematic of the method of exposure used for the epoxy-coated aluminium samples.

the not-exposed region of the sample t_{notexp} was used to scale the delamination time of the exposed region of the sample t_{exp} . The scaling was done with respect to the average delamination time $t_{\text{av_notexp}}$ obtained for a large number of not-exposed samples, by using the relation: $t_{\text{exp}} \cdot (t_{\text{av_notexp}}/t_{\text{notexp}})$. This scaling is considered to be valid because variations in coating thickness were found to be limited within one sample and ageing of the solvent is expected to influence both the exposed and the not-exposed region.

9.2.3. Peel testing

To obtain knowledge on the numerical adhesion strength, the standardised floating roller test was performed [14]. The floating roller device was mounted in a Zwick tensile-machine, which was equipped with an appropriate loading cell. During the peeling, the force necessary for delamination was measured while maintaining a constant cross-head speed of 20 mm/min.

In the test, the coating was peeled from the substrates. To prevent rupture of the epoxy coating during peeling, a flexible metallised 3M tape was adhered on the coating after exposure of the coated substrates. Moreover, to prevent distortion of the aluminium substrate during peeling, a stiff backing was mounted on the backside of the substrates, using an adhesive. Then, strips having a size of 2.5 x 30 cm strips were cut from larger substrates for the experiments.

9.2.4. Analysis methods

SEM/TEM investigation

SEM (scanning electron microscopy) images were obtained on a JEOL JSM 6500F Field Emission Gun SEM, using an accelerating voltage of 5 kV for the epoxy coatings and 20 kV for the aluminium substrates.

TEM (transmission electron microscopy) cross section images of the epoxy-aluminium samples were obtained using a novel method. A detailed discussion on this work is given elsewhere [15,16]. First, the epoxy coatings were thinned to a few tens of micrometers using mechanical polishing. Then, a 1 μm thick platinum bar was deposited on the samples inside a FEI Strata DB 325 dual focussed ion beam (FIB) set-up. An electron-transparent electron lamella was then directly prepared in the FIB from the sample by milling away material using a focused ion beam. The milling was performed using Ga^+ ions which were extracted from a liquid metal ion source. Initially, high milling currents of 20 nA were used, which were reduced to 1 pA for the final steps because milling using a high current causes much damage. Outside of the FIB, this lamella was transferred onto a copper TEM grid, using the electrostatic force of a glass needle. The TEM images were obtained on a Philips CM30-TTEM using a voltage of 300 kV and having a point-to-point resolution of 0.23 nm.

XPS investigation

XPS (X-ray photoelectron spectroscopy) measurements were performed at a detection angle of 45 degrees with respect to the sample surface on both the coatings and the aluminium substrates. The Al $2p$, O $1s$ and C $1s$ photoelectron spectra were recorded with a step size of 0.1 eV, using a PHI 5400 ESCA instrument (base pressure $< 1 \cdot 10^{-8}$ Pa), set at a constant analyser pass energy of 35.75 eV, using unmonochromatised incident Mg X-ray radiation (Mg $K\alpha_{1,2} = 1253.6$ eV).

FTIR investigation

Infrared measurements were performed using a Thermo Nicolet Nexus, equipped with two liquid-nitrogen cooled detectors: MCT-A ($4000\text{-}700\text{ cm}^{-1}$) and a less sensitive MCT-B ($4000\text{-}400\text{ cm}^{-1}$). On the coatings, FTIR-ATR (infrared attenuated total reflectance spectroscopy) measurements were performed, using a Thermo Nicolet Golden Gate ATR accessory. On the aluminium substrates,

FTIR-RAS (infrared reflection absorption spectroscopy) measurements were performed, using a Specac variable angle reflection accessory, set at a near-grazing incident angle of 82 degrees with respect to the normal of the surface. The infrared radiation was p-polarised by employing a Specac grid-wire polarizer. For the infrared spectra of the oxide layers, a cleaned gold substrate was used as a reference. Approximately 128 scans with a resolution of 4 cm⁻¹ were co-added to obtain the final spectrum.

Spectroscopic ellipsometry investigation

Visible spectroscopic ellipsometry (VISSE) measurements were performed on the aluminium substrates at 65°, 75° and 85° angles of incidence on a J. A. Woollam Co. VASE system. The measurements were performed from 300 to 1700 nm with a stepwidth of 10 nm. The WVASE32 software was used to fit the ellipsometric data. The experiments were performed at the VU Brussel with the kind help of S. van Gils.

TGA measurements

TGA (thermogravimetric analysis) measurements were performed on a Perkin-Elmer TGA-7 to determine the amounts of water in the epoxy-coated aluminium system as a function of exposure time to water. Samples having a diameter of 6 mm were exposed at part of their surfaces to deionised water using a dedicated cell, which allowed very reproducible exposure conditions. Prior to exposure, the samples were kept dry by storing them in a drying stove, which was set at a temperature of 50 °C. After exposure to water, the samples were gently wiped dry using a tissue and then directly transferred into the TGA-apparatus. The temperature of the TGA-oven was ramped up to 60 °C and kept for 4 hours at this temperature while continuously measuring the mass. The free water that is present at the interface and in the coating evaporates at this temperature [17,18], resulting in a decrease in mass of the system. After 4 hours, the mass was found to have attained a constant value and also a further increase in temperature up to 70 °C did not lead to a significant decrease in the mass anymore. The amount of evaporated water for exposed samples was generally around 2·10⁻² mg. This is well within the sensitivity of the apparatus, which is 1·10⁻⁴ mg. The reproducibility among different samples for the same exposure period was found to be good, giving a spread of around 15%. Not-exposed samples that were kept dry in the drying stove were found to not show a significant decrease in mass upon heating.

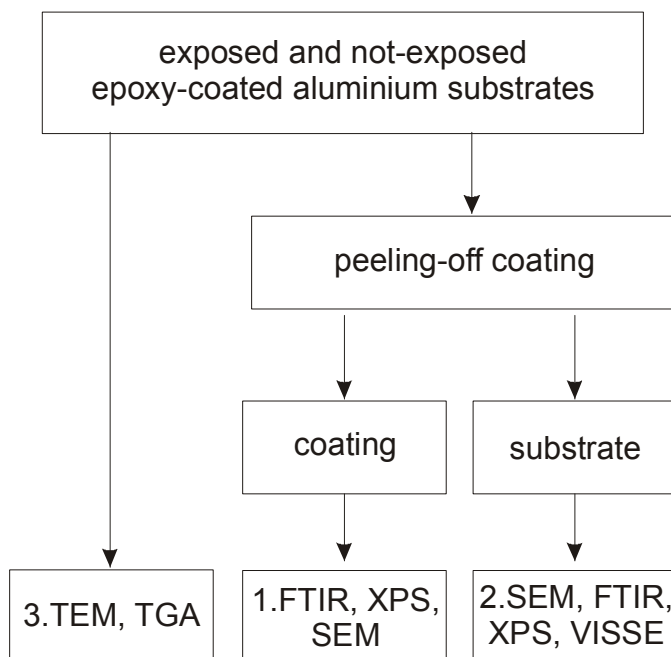


FIG. 2. Scheme of the experimental approach that was followed for investigating the changes that have occurred in the epoxy-coated aluminium system due to exposure to water.

9.3. Results

9.3.1. Introduction

First, the adhesion of the epoxy coatings due to exposure to water is studied as a function of time and temperature using the NMP adhesion test and using peel-testing. Then, the epoxy-coated aluminium system is investigated both before and after exposure using different analytical techniques. In Fig. 2, a scheme is shown of the approach followed. TGA measurements are performed to determine the amount of water absorbed by the system as a function of exposure time and temperature. TEM cross section images are obtained of the epoxy-aluminium interface before and after exposure to visually inspect changes that have occurred in the system due to exposure. To further investigate the changes, the coatings are separated from the substrates by manual peeling-off and the obtained parts are investigated separately. The coatings are investigated using SEM, XPS and FTIR to determine morphological changes, initial curing state and also chemical changes due to exposure to water. The aluminium substrates are investigated using SEM, XPS, FTIR and VISSE to determine morphological and chemical changes due to exposure to water.

9.3.2. NMP adhesion tests

NMP adhesion tests were performed at 3 different water exposure temperatures, RT (room temperature), 40 °C and 50 °C for exposure periods of up to 2000 hours. The results are summarised in the graphs in Fig. 3. In the graphs, each dot indicates a measurement performed on a different sample. The first 200 hours of exposure are shown expanded as an insert in the top right corner. Through the separate measurements, a solid line is plotted to indicate the observed trends. The NMP delamination time of the epoxy coating was 6 minutes for a not-exposed sample, which is indicated with the horizontal line in the plots. None of the samples showed discoloration or visual changes (i.e. blisters, corrosion products) in the exposed region. For exposure to RT deionised water, see Fig. 3a, the NMP delamination time of the coating becomes slightly shorter during the first 50 hours of exposure, indicating slight loss of adhesion of the coating. After around 100 hours of exposure, a minimum NMP delamination time of around 4 minutes and 50 seconds is obtained. Thereafter, the NMP delamination time increases again and above around 175 hours of exposure, becomes slightly higher than for the not-exposed coating. A maximum constant NMP delamination time of around 6 minutes and 40 seconds is then obtained, which remains roughly constant for the remaining exposure period. It indicates that eventually the adhesion of the coating becomes slightly better due to exposure to water.

In Fig. 3b, the results for exposure to 40 °C deionised water are given. Up until around 25 hours of exposure, the NMP delamination time decreases, indicating loss of adhesion of the coating. A minimum NMP delamination time of 1 minute and 50 seconds is obtained, which is considerably lower than for RT exposure. Above 25 hours of exposure, the NMP delamination time increases again and above 30 hours of exposure, the adhesion of the coating becomes better than before the exposure. After around 80 hours of exposure, the NMP solvent was no longer capable of delaminating the coating in the exposed region, as tested up until 60 minutes, indicating the adhesion of the coating has become very good due to exposure to water. The results are indicated on the top y-axis of the graph as 'infinite'. After this, no further change was observed as tested up until 2000 hours of exposure. For the 50 °C water exposure temperature, see Fig. 3c, a similar behaviour is observed. During the first 4 hours of water exposure, the coating loses its adhesion and a minimum NMP delamination time of around 1 minute and 15 seconds is obtained. Already after around 13 hours of exposure the adhesion in the exposed region becomes better than before

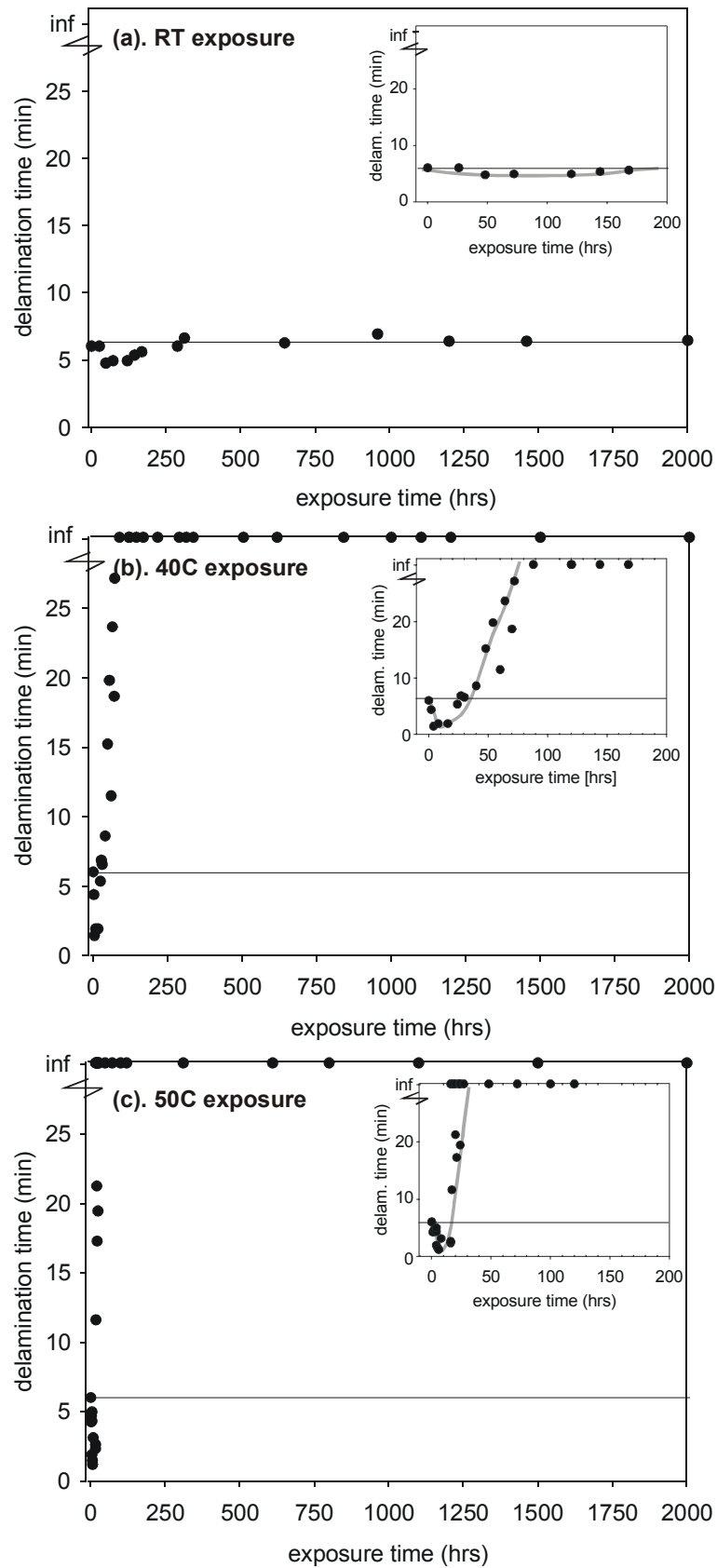


FIG. 3. NMP adhesion test results for exposure to water at (a) RT, (b) 40 °C and (c) 50 °C of the epoxy-coated aluminium system.

exposure and after around 25 hours of exposure, the coating could no longer be removed using NMP. After this, no further change was observed as tested up until 2000 hours of exposure. A summary of the NMP adhesion test results performed at the three exposure temperatures is given in Table 1.

9.3.3. Peel testing

Peel tests were performed to obtain knowledge on the numerical adhesion strengths after exposure to water of the epoxy-coated aluminium system. In contrast to the NMP adhesion tests, the time between exposure and adhesion testing was in this case several hours. For each of the three exposure temperatures, samples were exposed for 800 and 1500 hours. For each temperature and period, two samples were tested and the average values were determined. Based on this, the error in the results is estimated to be around 0.1 N/mm. The obtained results are shown in Fig. 4. Initially, the adhesion strength is comparably low at 0.2 N/mm. The used epoxy coating is relatively simple in composition and contains no adhesion promoting components. After exposure to RT deionised water, almost no change is observed. This corresponds well to the NMP adhesion test results, where for this exposure period only a slight increase in NMP delamination time was observed. For the 40 °C exposure temperature, a significant increase in adhesion strength is found, giving a value of around 0.6 N/mm. The NMP adhesion tests for these exposure periods showed similar results as there the coating could no longer be removed using NMP. For the 50 °C exposure temperature, an even further increase of the peel strength is observed, to a value of around 1.0 N/mm, which is a five-fold increase in adhesion strength as compared to a not-exposed sample.

TABLE 1. Summary of the results obtained using the NMP adhesion tests for exposure of the epoxy-coated aluminium system to water of different temperatures.

exposure temperature	minimum delamination time	time to minimum delamination time (hrs)	time until adhesion recovery (after initial loss of adhesion) (hrs)	maximum delamination time (after initial loss of adhesion)
RT (21 °C)	4m 50s	100	175	6m 40s
40 °C	1m 50s	20	30	∞
50 °C	1m 15s	6	13	∞

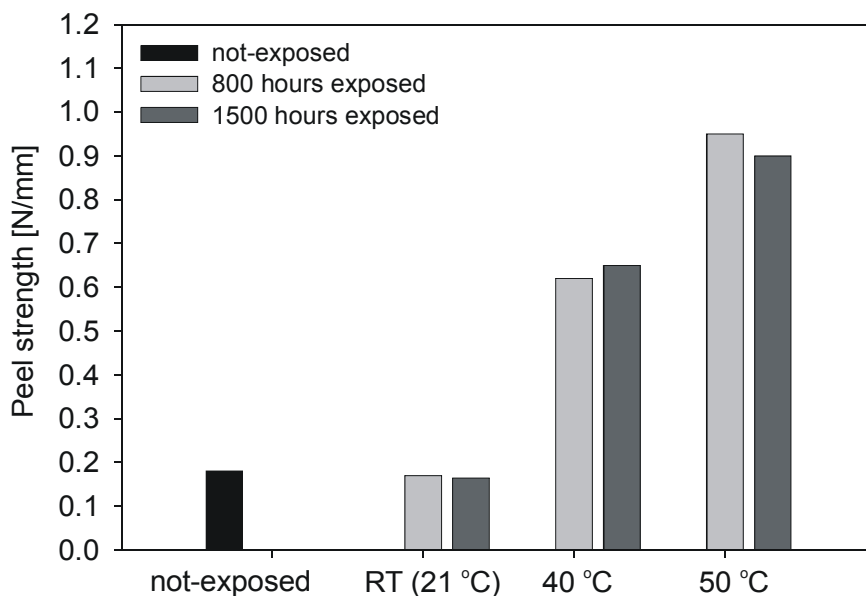


FIG. 4. Peel strength results obtained before and after exposure to water of the epoxy-coated aluminium system.

9.3.4. Investigation of the whole system

TGA (thermogravimetric analysis) measurements² were performed to investigate the amount of water that is absorbed by the epoxy-coated aluminium system as a function of exposure time and temperature. Measurements were also performed on free epoxy coatings, which were obtained by peeling from not-exposed epoxy-coated aluminium samples. The free coatings were exposed by full immersion in water.

The mass of evaporated water from the epoxy-aluminium samples was recalculated as a mass percentage of water in the coating by dividing by the mass of the coating in the exposed region. This results in a mass percentage of water in the exposed region and allows a comparison with the results of the free coatings.

The obtained results are summarised in Fig. 5 for both RT and 40 °C water exposure. The separate measurements are indicated by the dots, with each measurement performed on a different sample. A solid line is plotted through the results to indicate the observed trends. During the first 25 hours of exposure to 40 °C deionised water, see Fig 5a, the amount of water in the epoxy-coated aluminium system rapidly increases. A maximum water uptake of around 9% after around 75 hours of exposure is obtained. After this, the amount of water in the system decreases again and finally attains a more or less constant value

² TGA measurements were performed at the Polymer Materials and Engineering group of TU Delft with the kind help of B. Norder.

of 4% above around 200 hours. This behaviour is not observed for the free coating, which absorbs a constant amount of water of around 2 mass% throughout the exposure period, corresponding well to literature values for epoxies [9,19,20]. The room temperature exposed sample absorbs considerably less water, but a similar behaviour as for the 40 °C exposed samples is observed. The amount of water in the epoxy-coated aluminium system increases up to 3% during the first 100 hours of exposure. After this it decreases again. The amount of water absorbed by the free coating at RT is with around 1.3% lower than for 40 °C exposure, which is also expected [9], and does not change with exposure time.

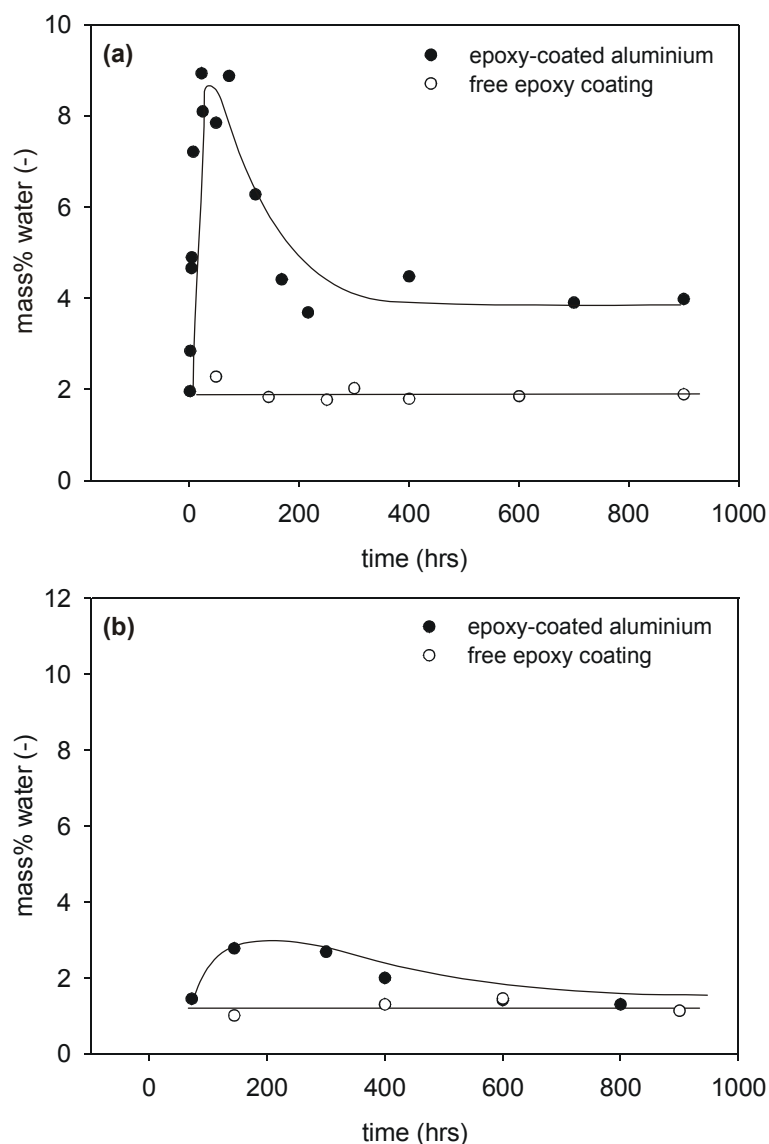


FIG. 5. TGA measurements showing the amount of water in the epoxy-coated aluminium system (closed dots) as a function of exposure time to (a) 40 °C and (b) RT deionised water. The results obtained for free coatings are indicated by the open dots.

To investigate the epoxy-aluminium interface, before and after exposure to water, a TEM investigation was performed³. For this purpose, cross section lamella were directly prepared from coated samples using a FIB apparatus. The procedure is illustrated in Fig. 6 in which a coated sample is shown on top. The lamella, shown in the centre, was prepared by milling away squares on both sides, all the way into the aluminium substrate, using a focussed ion beam. After some further thinning, this lamella was cut free and used directly as a TEM slice. The FIB/TEM work performed on these polymer-coated substrates is discussed elsewhere in detail [15,16]. In Figs. 7a and 7b, TEM cross section images are shown for respectively a sample which was exposed for 600 hrs to 50 °C deionised water and for a not-exposed sample. For the not-exposed sample, the interfacial region can be seen to be sharp with no apparent irregularities and also the epoxy coating appears homogeneous. The exposed sample on the other hand clearly shows a very thin layer, having a thickness of around 30 nm, to be present between the epoxy coating and the aluminium substrate. The layer is shown at a higher magnification in Fig 7c. Diffraction patterns obtained in the TEM on the layer showed it to be fully amorphous.

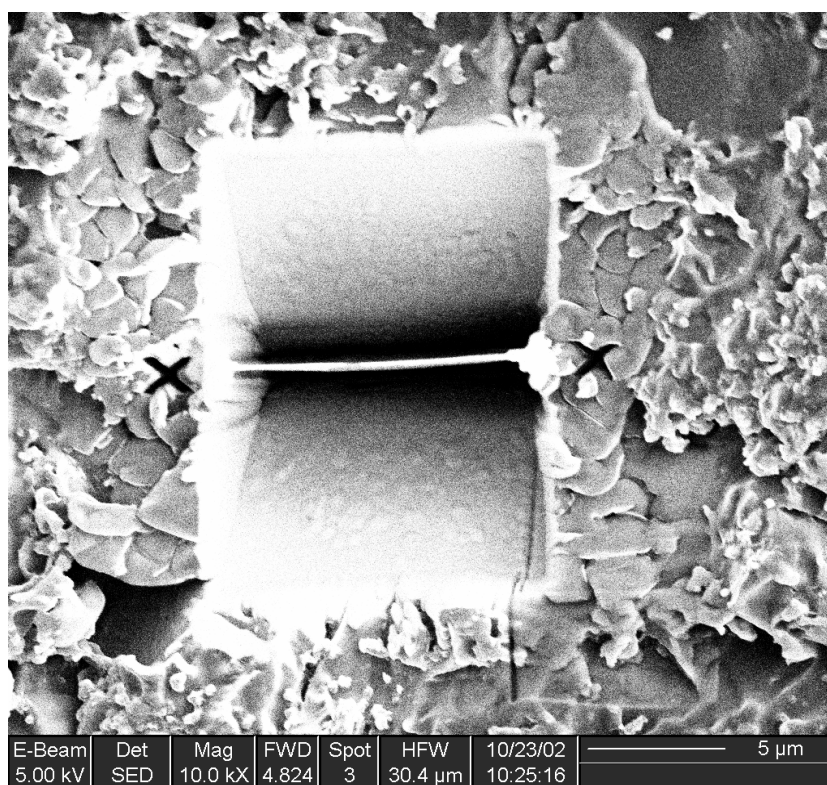


FIG. 6. SEM image obtained during FIB preparation of TEM cross section slices of the epoxy-coated aluminium system.

³ The TEM investigation was performed at the National Centre for High Resolution Electron Microscopy in Delft with the kind help of V.G.M. Sivel

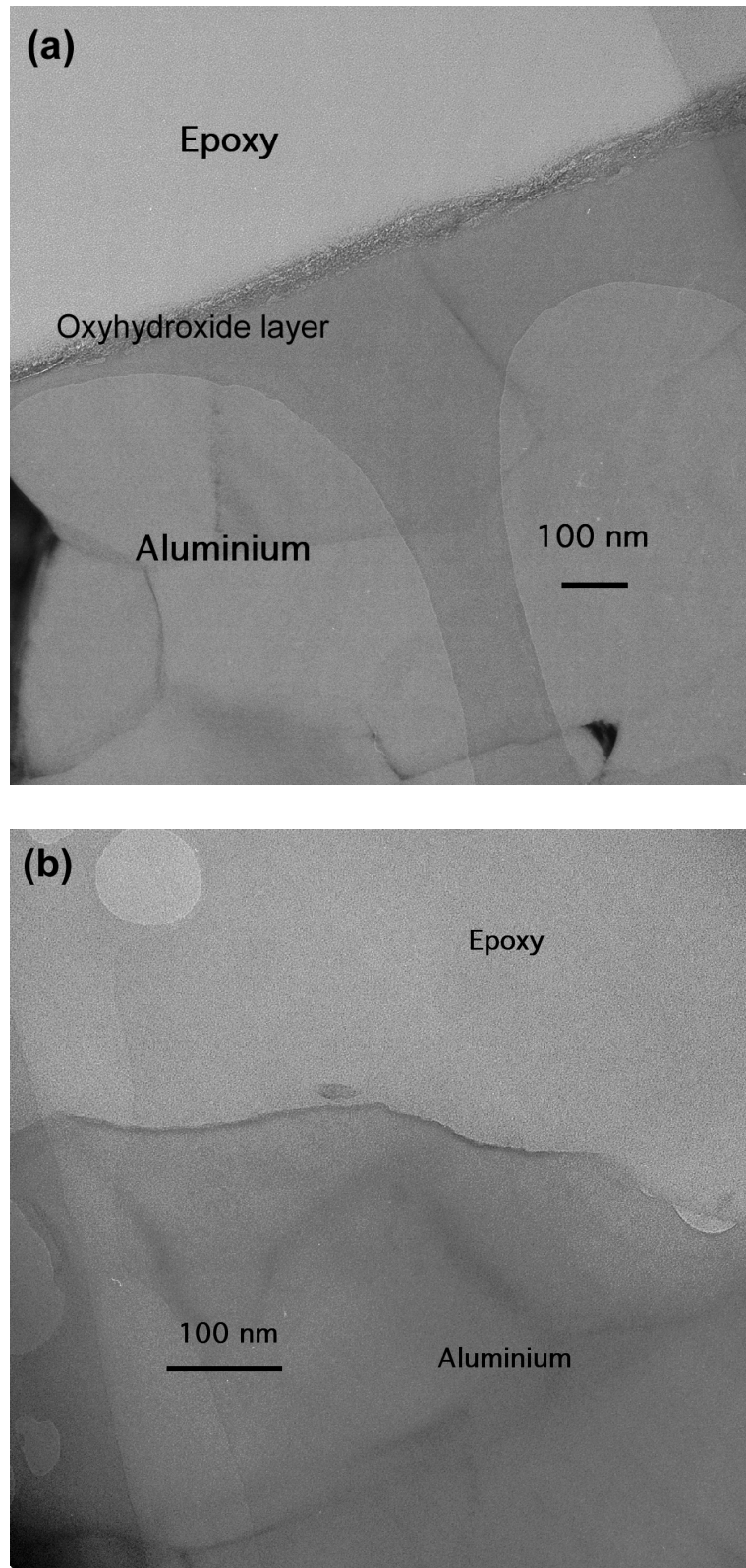


FIG. 7. TEM cross section images of (a) an epoxy-coated aluminium sample exposed for 600hrs to 50 °C deionised water, (b) a not-exposed sample and (c) the same as (a) only at a higher magnification. Continued on next page.

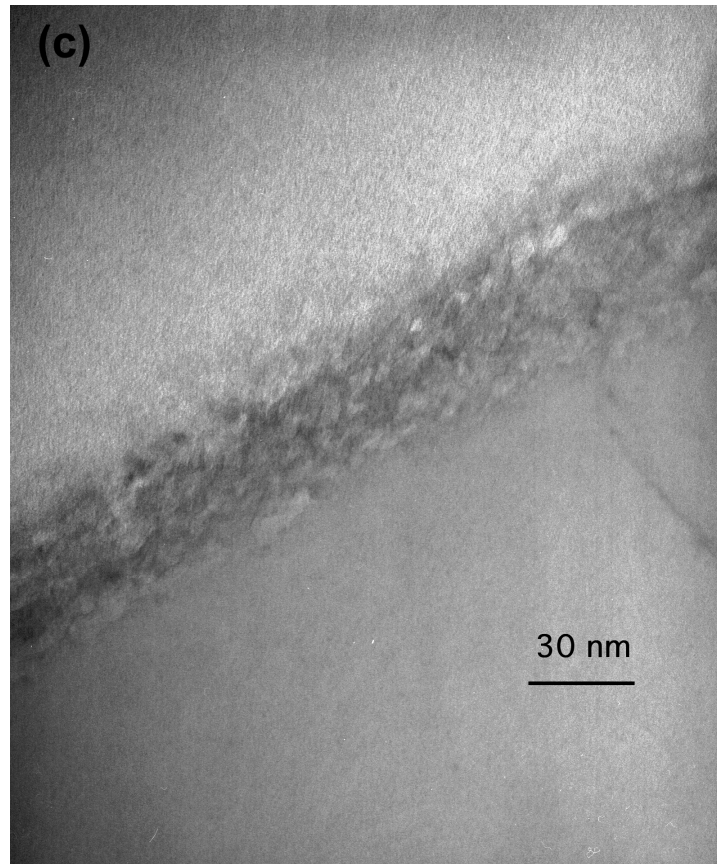


FIG. 7. Continued

9.3.5. Investigation of the peeled-off coatings

To allow for a detailed investigation of the coatings, they were separated from the substrates by peeling-off manually from exposed and not-exposed samples, see Fig. 2. In Fig. 8, SEM images of exposed and not-exposed coatings are shown, as obtained on the substrate-side of the coating (which is the side previously adhered to the aluminium substrate before peeling-off).

The not-exposed coating shows a surface with small globular protrusions. These are the opposite of shallow holes on the aluminium side and are due to the alkaline etching procedure, see also furtheron. The same globular protrusions are also visible on a sample exposed for 800 hours to 40 °C deionised water, but the coating surface appears rougher. This is because more force was necessary to remove the coating as a result of the improved adhesion due to exposure to water. This results in some deformation of the coating. Besides this, no clear morphological differences are observed between the exposed and the not-exposed coating, also not at higher magnifications.

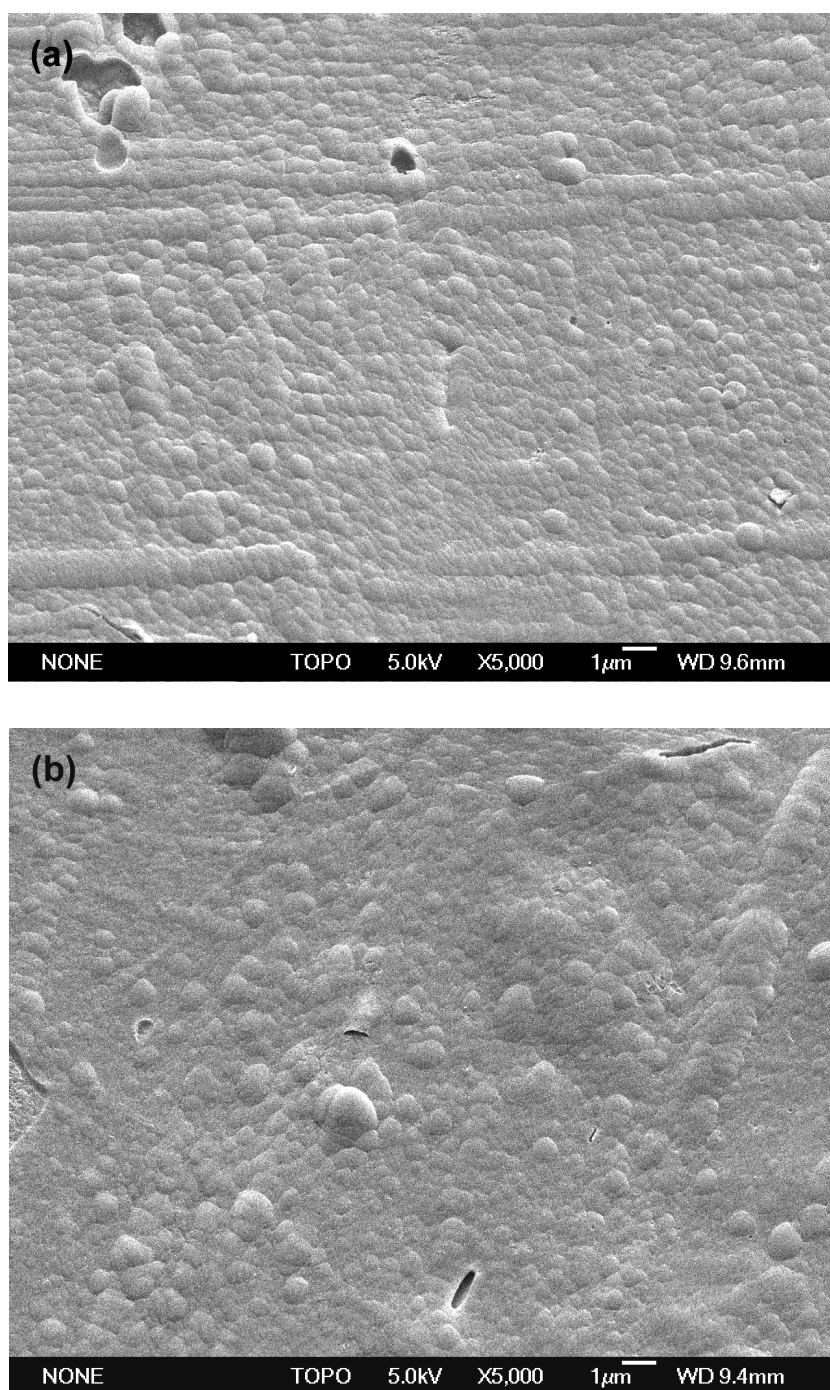


FIG. 8. SEM images of a not-exposed coating (top) and a coating exposed for 800hrs to 40 °C water (bottom). The coating is obtained by peeling-off from exposed and not-exposed epoxy-coated aluminium samples and is obtained on the substrate-side of the coatings (the side that was attached to the aluminium substrate).

A FTIR-ATR investigation of the peeled-off coatings was performed to find out any chemical changes that might have occurred due to the exposure to water and also to investigate the initial curing state of the epoxy coatings. The spectra are shown in Fig. 9. The use of the ATR technique allows studying the

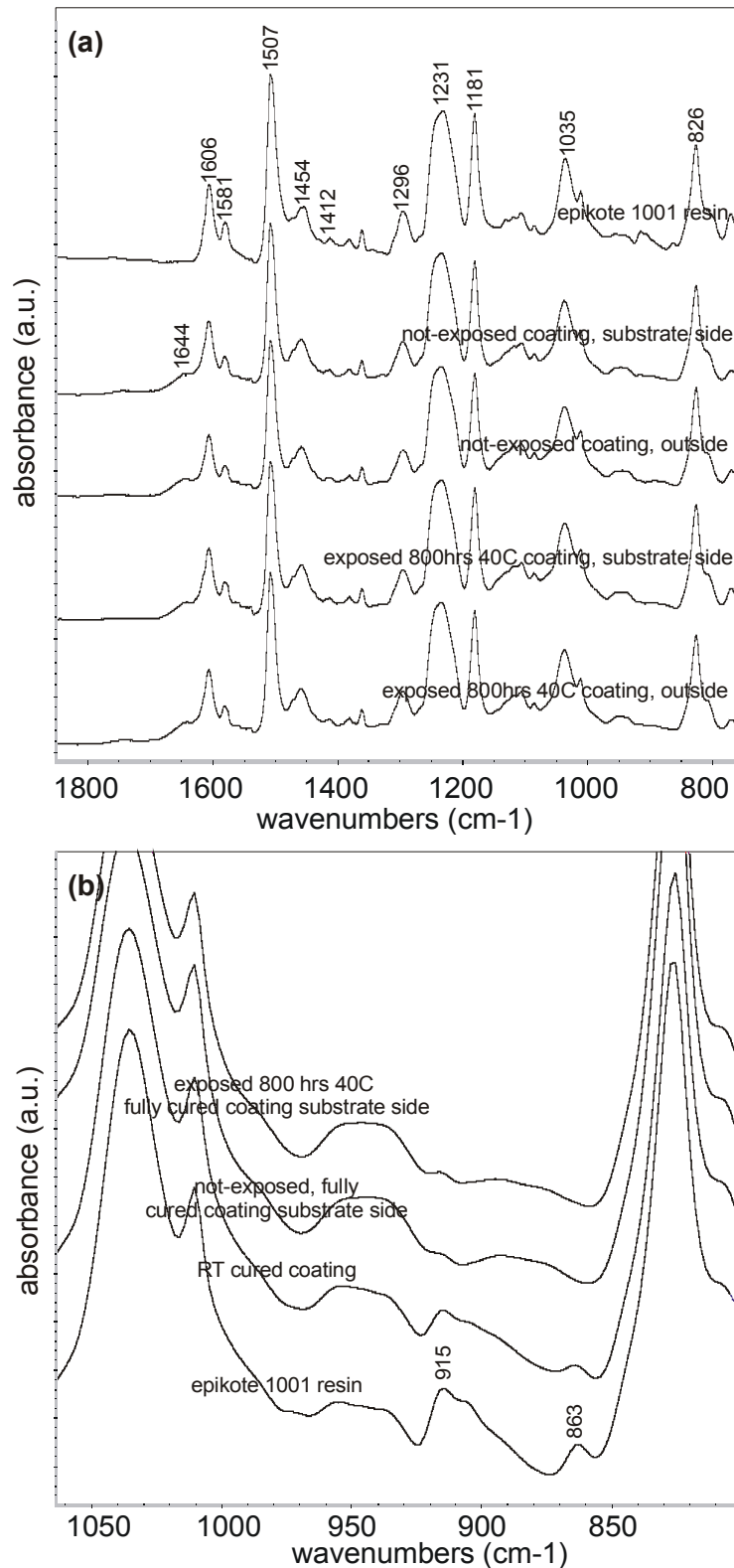


FIG. 9. FTIR-ATR spectra of (a) epoxy coatings and the initial resin in the 1800-750 cm^{-1} region and (b) in the 1100-750 cm^{-1} region, showing the epoxy ring infrared vibrations at 915 and 863 cm^{-1} .

outer surface region up to the micron range [21]. The measurements were performed on both the substrate side and the outside of the coating. In Fig. 9a,

infrared spectra obtained from a not-exposed coating and from an exposed coating (800 hrs, 40 °C deionised water) are shown in the 1800-750 cm^{-1} region. For comparison, the spectrum of the Epikote 1001 resin is also given. Most of the infrared bands of the coating originate from the epoxy resin. However, at around 1644 cm^{-1} , the coatings show an additional broad band, which is due to amide groups, resulting from the used polyamide-based hardener [22,23].

It is sometimes reported that epoxy coatings are incompletely cured close to the metal surface [24-26]. The curing state of epoxy coatings can be evaluated from the (comparably weak) epoxy ring infrared bands that are found at around 915 and 863 cm^{-1} [27,28]. For a properly cured coating, these bands are expected to be virtually absent. In Fig. 9b, the 800-1050 cm^{-1} region is shown expanded for the substrate-side of coatings obtained from exposed and not-exposed samples. Also, infrared spectra are shown of the epoxy resin and of a coating which was only cured at RT for 48 hours. The epoxy resin clearly shows the presence of epoxy ring bands. Also the spectrum of a coating cured only at RT shows the presence of epoxy bands, indicating the coating is not well-cured under these conditions. In contrast, the spectra of the coatings from exposed and not-exposed samples, which were additionally cured at 50 °C and 70 °C, do not show epoxy ring infrared bands. Based on the results it can therefore be concluded that the coatings in the studied epoxy-coated aluminium system are well-cured throughout.

The FTIR-ATR spectra of the coatings before or after exposure to water do not show any differences, see Figs. 9a and 9b. It can therefore be concluded that exposure to water does not lead to chemical changes in the coatings. To further investigate possible chemical changes as a result of exposure of the epoxy-coated aluminium samples to water, an XPS analysis was performed. In Fig. 10, the O *1s*, Al *2p* and C *1s* spectra are shown, obtained from the substrate-side of coatings of a not-exposed and an 800 hrs, 40 °C exposed sample. Both show very similar C *1s* and O *1s* core level peaks, indicating no chemical changes have occurred upon exposure to water. This confirms the FTIR-ATR measurements. However, for the coating of the exposed sample, a minor Al *2p* peak was additionally found to be present. The intensity of the peak corresponds to a concentration of around 2 atom%. The peak is located at around 74 eV and can therefore be ascribed to aluminium ions, present in an aluminium oxide or oxyhydroxide [29] which is apparently at a low concentration present in the exposed coatings.

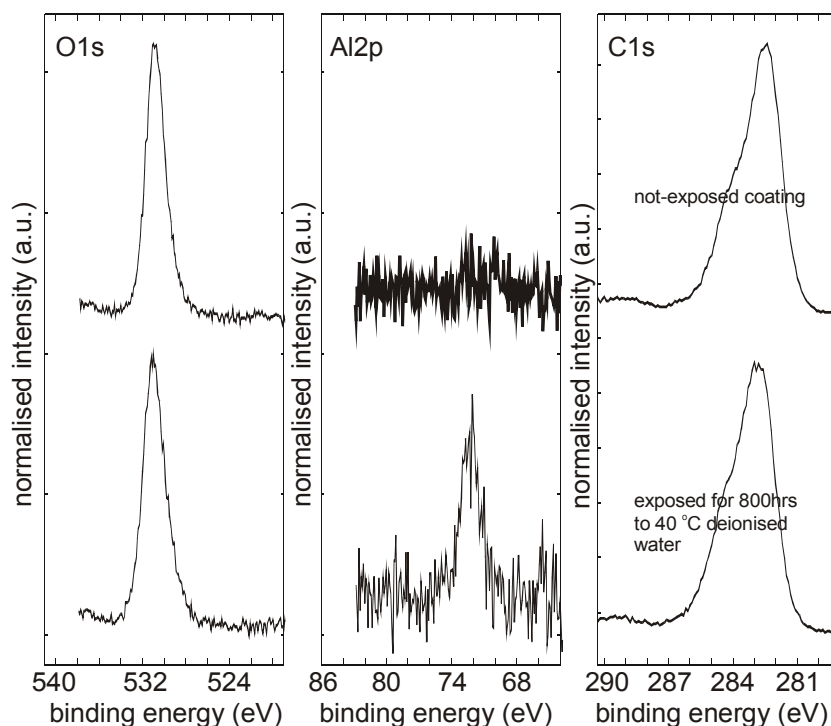


FIG. 10. XPS O 1s, Al 2p and C 1s spectra as obtained from coatings of not-exposed (top) and from exposed (800hrs, 40 °C) samples. Spectra are taken on the substrate-side of the coatings, which were peeled-off manually from the aluminium substrates. The regions are shown with a different vertical scaling.

9.3.6. Investigation of the aluminium substrates

Next, the results obtained from the investigation of the aluminium substrates obtained from exposed and not-exposed samples is discussed, see Fig. 2. In Fig. 11, SEM images are shown of the aluminium substrate after manually peeling-off the epoxy-coating. Images are shown for three different exposure times of samples to 40 °C deionised water. Fig 11a shows the aluminium substrate of a not-exposed sample. The large, shallow holes that are visible on the substrate are due to the alkaline etching pretreatment of the substrates. For the substrate of a sample exposed for 200 hrs to 40 °C deionised water, see Fig. 11b, inside these holes, small globular particles are present, having sizes smaller than 10 nm. For the substrate exposed for 800 hrs to 40 °C deionised water, see Fig. 11c, more of these globular particles are present. These globular particles likely correspond to the layer that is observed in the TEM images, see Fig. 7.

To identify the substance formed on the aluminium substrates, a FTIR-RAS investigation was performed. In Fig. 12, spectra are shown of aluminium substrates, obtained from samples exposed to RT and 40 °C water for different

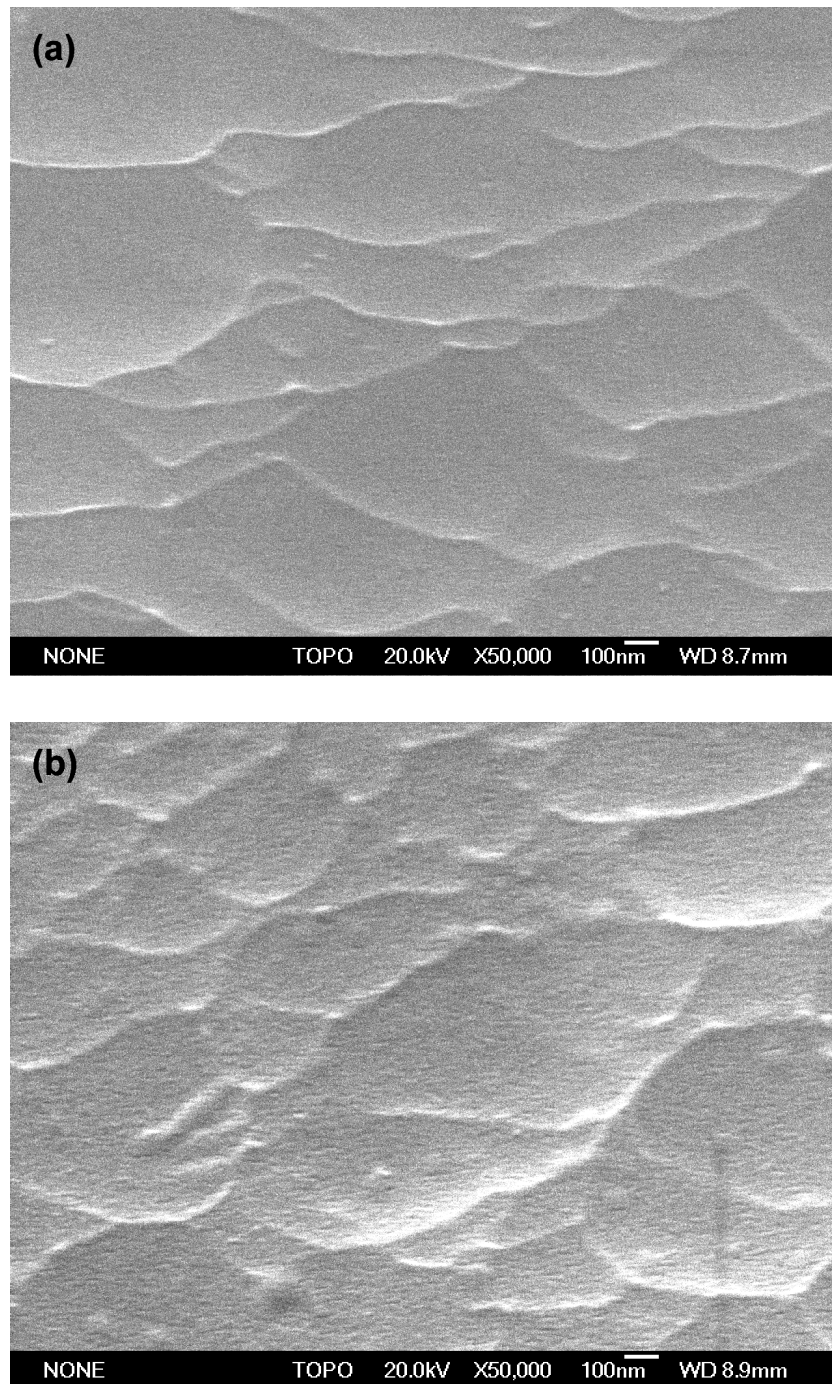


FIG. 11. SEM images for aluminium substrates, obtained from epoxy-coated aluminium samples (a) not-exposed and exposed to 40 °C water for (b) 200, (c) 800 hours. Continued on next page.

exposure periods. The infrared spectra on the aluminium substrates do not show the presence of peaks due to the epoxy coating, indicating peeling of the coating results in adhesive failure between coating and substrate. With increasing exposure time to 40 °C deionised water, the infrared spectra show the

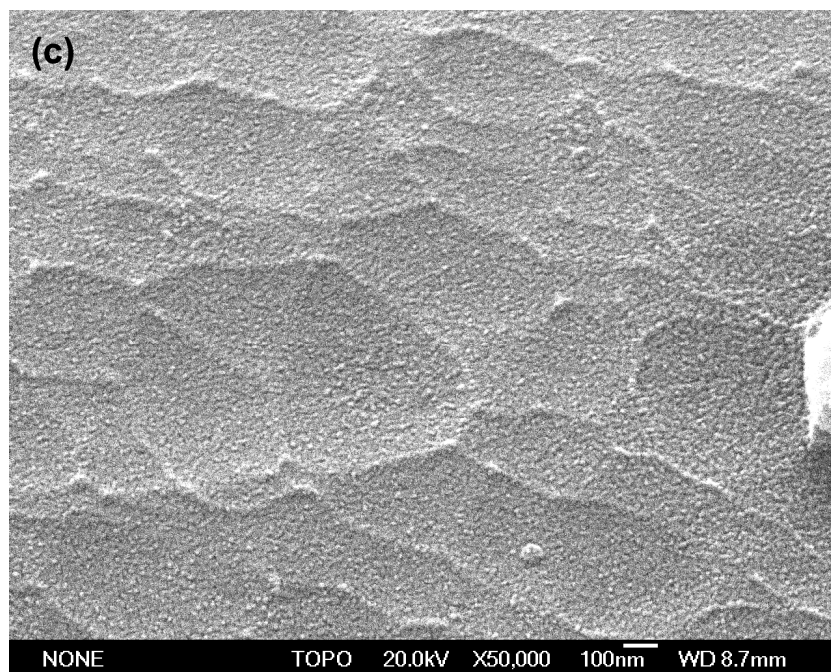


FIG. 11. Continued.

development of a broad band at 3450 cm^{-1} and bands at 1631 cm^{-1} and 1410 cm^{-1} .

Also there is the development of broad, not well-resolved bands at 1073 and 758 cm^{-1} around the main Al-O peak at 950 cm^{-1} . For the room temperature exposure, bands at the same positions also develop but considerably less intense. The $50\text{ }^{\circ}\text{C}$ exposure temperature (spectra not shown) also showed the development of infrared bands at the same positions, even more intense than for the $40\text{ }^{\circ}\text{C}$ exposure temperature.

The development of bands at around 1073 and 758 cm^{-1} indicates that hydroxylation of the oxide layer occurs. The bands can be ascribed respectively to $\delta(\text{OH})$ bending and $\gamma(\text{OH})$ twisting vibrations and their positions and broadness indicate the characteristics of an amorphous, pseudoboehmite-type aluminium oxyhydroxide [30-35]. The broad, asymmetrically shaped band at around 3450 cm^{-1} is partially due to the corresponding $\nu(\text{OH})$ stretching vibration. The band is however also partially due to the hydroxyl stretching vibrations of molecular water, giving also rise to the $\delta(\text{H}_2\text{O})$ bending vibration band at 1630 cm^{-1} [36-38]. This indicates the presence of water inside the structure.

VISSE⁴ is employed to determine the thickness of the aluminium oxyhydroxide layer formed on the aluminium substrates due to exposure of the coated samples to water. The technique requires the use of an optical model

⁴ The experiments were performed at the VU Brussel with the kind help of S. van Gils.

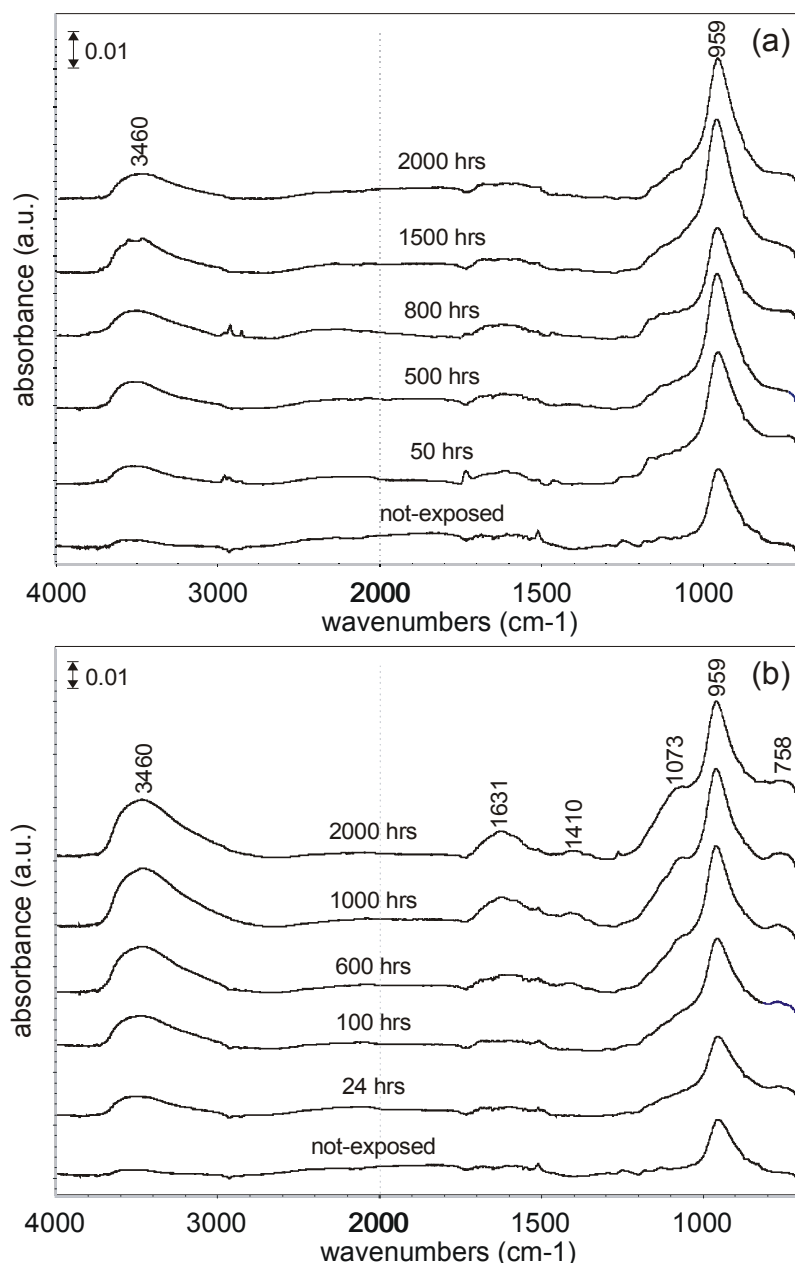


FIG. 12. FTIR-RAS spectra obtained from aluminium substrates, obtained from epoxy-coated aluminium samples exposed to (a) RT and (b) 40 °C deionised water. Exposure times as indicated.

onto which the ellipsometric measurement data is fitted. The used model consists of an aluminium substrate onto which the native oxide layer of a fixed thickness is placed. The substrate of a not-exposed sample was used as a reference for this. On top of this invariable system, an aluminium oxyhydroxide layer of a variable thickness is positioned. Further characteristics of this layer are discussed in a previous publication [37,38].

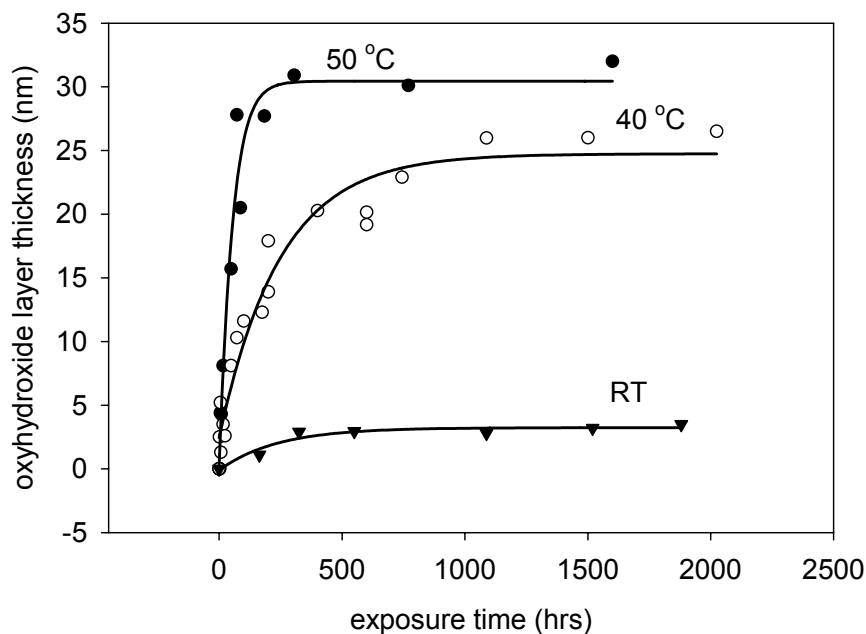


FIG. 13. VISSE measurements showing the thickness of the aluminium oxyhydroxide layer formed on the aluminium substrate as a function of exposure time of the epoxy-coated aluminium samples.

Subsequently, the oxyhydroxide layer thickness is adapted by iteration to fit the ellipsometric measurement data as obtained from the exposed aluminium substrates. The resulting oxyhydroxide layer thicknesses as a function of exposure time for the three exposure temperatures are summarised in Fig. 13. The separate measurements are indicated by the symbols. A solid line is plotted through the results to indicate the trends. At all exposure temperatures, a layer is observed to grow on the aluminium substrate, which attains a limiting thickness after a certain period. With higher exposure temperatures, the attained layer thickness is larger. For RT exposure, a limiting layer thickness of around 3 nm is attained, at 40 °C of 25 nm and at 50 °C of 30 nm. This latter thickness corresponds well to the interfacial layer thickness observed in the TEM cross section images, see Fig. 7. With a higher exposure temperature the layer is observed to grow faster. At RT, it is estimated that it takes around 1000 hours before the limiting layer thickness is attained, at 40 °C around 600 hours and at 50 °C around 250 hours.

An XPS analysis was performed on a not-exposed substrate and on the substrate from a sample that was exposed for 800 hrs to 40 °C deionised water to accurately determine composition of the oxyhydroxide layer and to determine the possible presence of a residual organic overlayer after the manual removal of the epoxy coatings. The hydroxyl fractions were determined by curve-fitting of the O *1s* core level spectra, and were corrected for the presence of oxygen-

functionalised contamination, following the procedure also used in Chapter 3. The oxide and contamination layer thicknesses were determined from the measured O *1s*, Al *2p* and C *1s* spectra, following the procedure also used in Chapter 3.

The aluminium substrate, obtained from the not-exposed sample, was found to have an oxide layer thickness of ~2.7 nm and ~7% of hydroxyls (of the total oxygen-content). The aluminium substrate of the sample exposed for 800 hrs to 40 °C deionised water was found to have an oxide layer thickness larger than 9 nm, as the Al *2p* spectra did not show the presence of an Al *2p* metal peak. This corresponds well with the VISSE measurements. The oxide layer was found to have 54% of hydroxyls, which corresponds to a layer having the stoichiometry of an oxyhydroxide (AlOOH), see also Chapter 3, as was also found from the FTIR-RAS measurements on the substrates. In contrast to the FTIR-RAS measurements however, a component due to water was found not to be present in the O *1s* peak. An explanation can be that the water might have become desorbed in the UHV environment of the XPS apparatus and is therefore not present anymore.

The oxide layers on the not-exposed and exposed aluminium substrates were found to be contaminated with organic overlayers, having effective thicknesses of around 0.3-0.5 nm. The contamination levels are thus comparably low [39,40]. This indicates that peeling-off the coating results in adhesive failure and occurs at the epoxy-aluminium interface both before and after exposure. This confirms the FTIR-RAS measurements where peaks due to the epoxy coating were not observed to be present.

9.3.7. Inhibition of hydration through the adsorption of NTMP

Add last, to clarify the role of the oxyhydroxide layer formed due to exposure of the coated system on the observed adhesion strengthening, additional NMP adhesion tests were performed. A thin layer of the organic hydration inhibitor NTMP (nitrilotri methylene phosphonic acid) was adsorbed on the aluminium substrates, prior to application of the epoxy coatings. This compound forms a strong bond with the oxide surface and prevents water from getting in contact with the oxide surface, thereby inhibiting the formation of an aluminium oxyhydroxide layer [41,42]. In Fig. 14, the NMP adhesion test results are shown for exposure of the epoxy-coated NTMP-aluminium system to 50 °C deionised water. In contrast with the results obtained for exposure of the normal epoxy-coated aluminium, see Fig. 3, the NMP delamination time for the epoxy coating rapidly drops to low values and also remains low for longer exposure

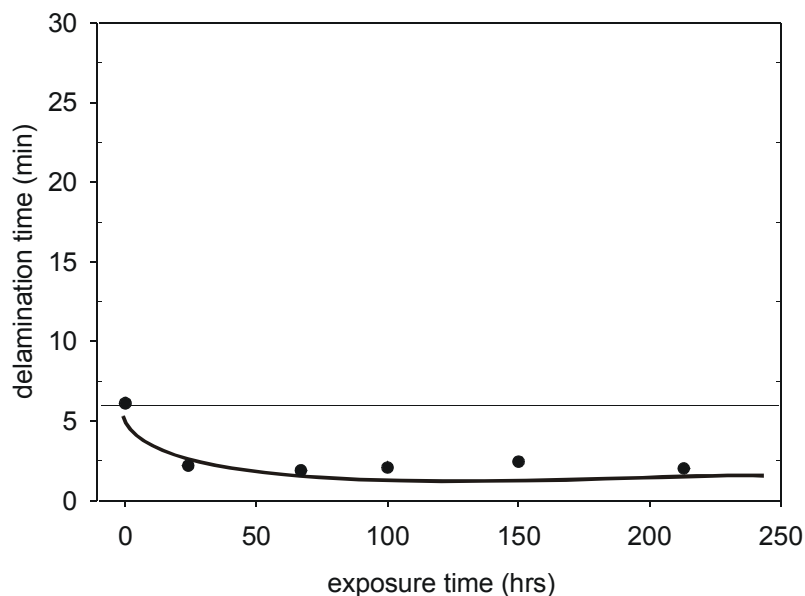


FIG. 14. NMP adhesion test results for exposure to 50 °C deionised water for an epoxy-coated aluminium system in which a layer of the NTMP hydration inhibitor is adsorbed on the aluminium substrate prior to epoxy-coating.

periods, indicating loss of adhesion of the coating occurs but recovery of the adhesion does not occur anymore. Infrared spectra performed on the aluminium substrates after peeling of the coating did not show the formation of an oxyhydroxide layer.

9.4. Discussion

Upon exposure to water, the epoxy coated aluminium first shows a loss of the adhesion but after this, the adhesion recovers and even exceeds the adhesion strength before exposure. This phenomenon has been reported before in the literature for polymer-coated aluminium substrates [9,43-48]. It was investigated in detail by Arslanov *et al.* for epoxy coatings on aluminium [45,46]. They ascribed it to the presence of an incompletely cured epoxy coating close to the aluminium substrate. Upon exposure to water, a hydroxide layer was observed to grow on the aluminium substrate. The incompletely cured region was found to cure in the presence of water. The growing hydroxide layer then formed a mixed interphasial region with the hydroxide layer, hence explaining the observed improvement of the adhesion. The phenomenon does however not appear to exclusively occur in presence of incompletely cured coatings, as it was also observed to occur for other types of polymers [43,44,47,48]. The results obtained here also clearly show that an incompletely cured epoxy is not a prerequisite.

Based on the results shown above, a three step model was developed for the processes occurring in the epoxy-coated aluminium system upon exposure to water. The different stages are shown schematically in Fig. 15.

9.4.1. First stage: the diffusion of water in the system and loss of adhesion

Upon exposure of the epoxy-coated aluminium, water diffuses into the epoxy coating. The TGA measurements show that the epoxy-aluminium system absorbs considerably more water than the free coating. Comparable differences in water absorption between free coatings and coated substrates were also found by others [4,49,50]. The additionally absorbed water can be attributed to water that accumulates at the interface [5,6,51], thereby causing a loss of adhesion of the coating. It was observed that when the epoxy coating was rapidly removed from the substrate directly after exposure, very small water droplets were present which almost instantly evaporated. This was found to be clearly visible at higher exposure temperatures. This phenomenon was also observed by others [5,9] and it indicates the presence of a significant amount of water at the

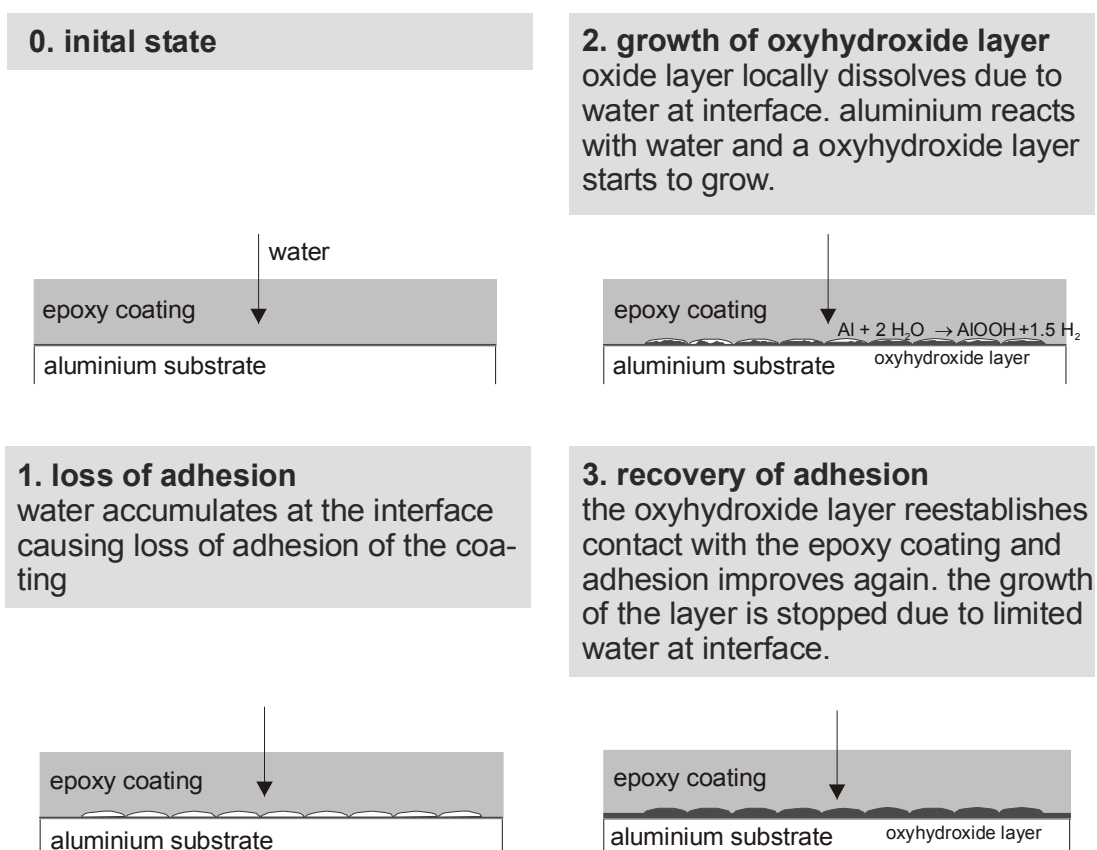


FIG. 15. Schematic of the processes occurring upon exposure of the epoxy-coated aluminium system to water.

interface. The rapid loss of adhesion of the coating upon exposure to water corresponds well with the fact that in Chapter 8 it was found that the epoxy coating only forms hydrogen-bonds with the epoxy-coating, and these bonds were found to be not stable in the presence of water.

The water-uptake curves closely correspond to the NMP adhesion results. The increase of water absorbed by the system for the short exposure times is directly reflected in the NMP adhesion tests as a decrease in adhesion of the coating. With a higher exposure temperature, the TGA measurements show that water is absorbed faster by the system and the NMP adhesion tests show that delamination occurs faster. Moreover, with a higher exposure temperature, more water accumulates at the interface and delamination occurs to a larger extent, as evidenced from smaller minimum NMP delamination times, see Table 1.

Water in epoxies can cause hydrolysis or other chemical changes to the network, eventually leading to macroscopic degradation of the coating [8,52,53]. However, no differences are observed in the FTIR-ATR or XPS spectra obtained from the coatings before and after exposure. This indicates that hydrolysis or any other chemical change to the coating does not occur under the studied exposure conditions. The epoxy coating therefore largely operates as an inert membrane, transporting water to the interface.

9.4.2. Second stage: the formation and growth of an aluminium oxyhydroxide layer

After or perhaps simultaneously to this initial loss of adhesion, a second mechanism starts to play a role. The water present at the interface causes Al-O bond breaking and localised dissolution of the oxide layer [30,54]. The dissolution allows passage of ions through the locally dissolved oxide layer, hydroxyl and oxygen ions inwards and aluminium ions outwards. This is followed by a precipitation of oxyhydroxides. Together this mechanism is known as the dissolution-precipitation mechanism [29,55,56]. Based on the FTIR-RAS, XPS and TEM results, the layer that is formed as a result of this could be identified as being as an amorphous, pseudoboehmite type of oxyhydroxide.

With a higher exposure temperature, the oxyhydroxide layer that is formed on the epoxy-aluminium interface becomes thicker, as shown by the VISSE measurements. This is in contrast with *bare* aluminium substrate immersed in water where it is reported that an oxyhydroxide layer is formed which becomes thinner with a higher exposure temperature [54]. For room temperature of bare substrates, a limiting layer thickness of several μm 's is reported [54] while for immersion in boiling water, a limiting layer thicknesses of around 400 nm is

reported to be formed [56]. The different behaviour for exposure of the epoxy-coated substrates is believed to be due to the limited availability of water at the epoxy-aluminium interface. With a higher exposure temperature, the TGA measurements show that more water is available at the interface and therefore the oxyhydroxide layer can grow thicker.

9.4.3. Third stage: the improvement of the adhesion of the coating

In the third and final stage, the growing oxyhydroxide layer gradually re-establishes and improves contact with the epoxy coating. Because a new bond is formed with the epoxy coating, the adhesion shows recovery after its initial loss. This is observed in the NMP adhesion tests as the increasing NMP delamination times. The NMP tests obtained on the NTMP hydration inhibitor-coated substrates prove the role of the oxyhydroxide layer in this adhesion recovery process. In absence of growth of the oxyhydroxide layer, adhesion recovery does not occur anymore. Also, there is a good correspondence between the growth speed of the oxyhydroxide layer as observed from the VISSE measurements at the different exposure temperatures and the speed at which the adhesion of the coating increases again, as shown by the NMP adhesion tests.

The newly formed bond is clearly much stronger than the initial bond between the native aluminium oxide layer and the epoxy coating as evidenced by the much higher peel adhesion strengths. A relation between the thickness of the oxyhydroxide layer formed and the final adhesion strength obtained is observed. At a higher exposure temperature, the oxyhydroxide layer grows thicker and the attained peel adhesion strengths are higher.

The exact nature of how the hydroxide layer is able to strengthen the adhesion and why there would be a relation between thickness of the oxyhydroxide layer and the adhesion strength is however currently not well understood. The XPS measurements performed on an exposed system show the presence of a limited amount of aluminium oxyhydroxide inside the epoxy coating after peeling. A possible strengthening mechanism can therefore be that the oxyhydroxide layer grows partially into the epoxy coating and forms a mixed epoxy/oxyhydroxide interphasial region. Upon peeling of the coating, rupture occurs partially through this mixed region, explaining the presence of aluminium oxyhydroxide in the coating. The observed higher adhesion strength upon formation of a thicker oxyhydroxide layer might then be due to a more extensive mixed region being formed. The TEM cross section images however do not show clear evidence for such a mixed interphasial region and also the SEM

images show relatively undamaged surfaces for both coating and aluminium substrates after peeling-off.

Alternately, the strengthening mechanism might be due to the oxyhydroxide layer formed underneath the coating having a more porous structure than the initial native oxide. This leads to possible mechanical interlocking, increased contact area and hence adhesion strength.

The newly formed bond is considerably more water-stable than the initial bond as the NMP adhesion tests show very high NMP delamination times, despite that the samples are in the 'wet' state. This explains the decreasing water concentrations in the epoxy-aluminium system, after the initial increase. Because of the water stability, additional water transported through the epoxy coating is not capable of entering the interface anymore. Moreover, the water that was present at the interface as a result of the initial loss of adhesion of the coating is consumed during formation of the oxyhydroxide layer. Therefore, the oxyhydroxide layer grows to attain a limiting thickness and further growth is stifled due to the limited availability of water at the interface. Some water however apparently remains present at the interface as also for very long exposure times still more water is absorbed by the system than by the free coating.

9.5. Conclusions

An analysis was performed of the adhesion and changes that occur for an epoxy-coated aluminium substrate exposed to water of different temperatures. First, the adhesion of the epoxy coating is lost upon exposure to water and a significant amount of water accumulates at the interface. The water at the interface causes formation and growth of a thin oxyhydroxide layer which after some time re-establishes contact with the coating and causes recovery and even considerable improvement of the adhesion. The improvement of the adhesion is likely due the formation of a limited but water-stable mixed epoxy-oxyhydroxide interphasial region. The whole process occurs faster and more extensively at higher temperatures, giving the accumulation of more water at the interface and the growth of a thicker oxyhydroxide layer.

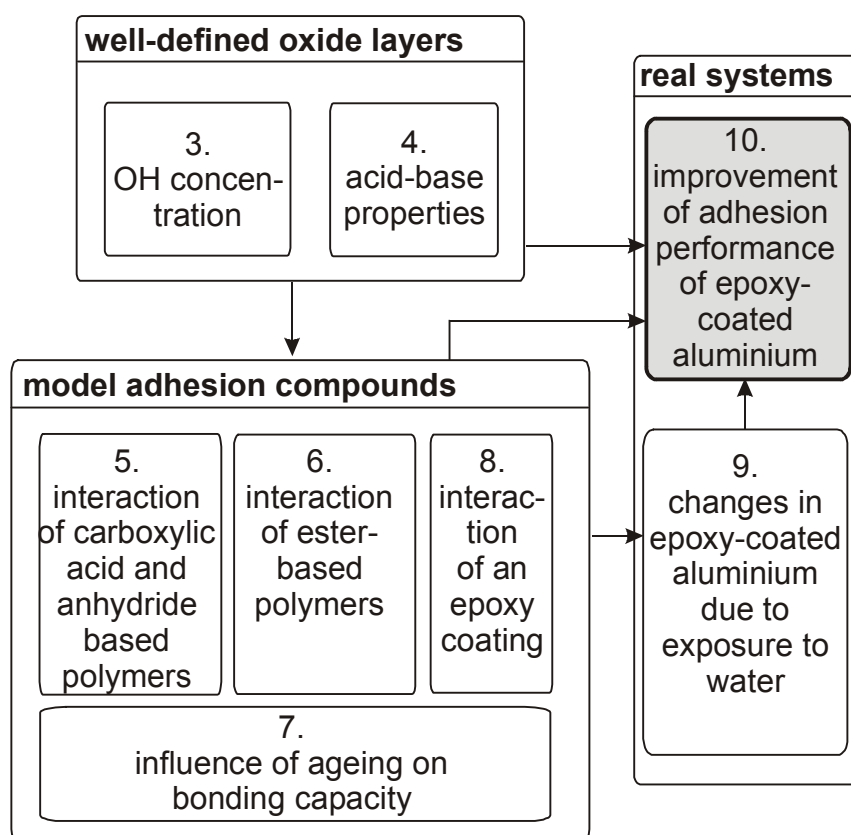
References

1. Kinloch, A. J. *Durability of structural adhesives*; Applied Science Publications: London, 1983.
2. van Westing, E. P. M. *Corrosion Science* 1993, *34*(9), 1511-1530.
3. van Westing, E. P. M. *Corrosion Science* 1994, *36*(6), 979-994.
4. Funke, W. *J.Oil Colour Chem.Assoc.* 1979, *62*(2), 63.
5. Nguyen, T.; Byrd, E.; Bentz, D. *Journal of Adhesion* 1995, *48* 169-194.
6. Nguyen, T.; Byrd, E.; Bentz, D.; Lin, C. *Progress in organic coatings* 1996, *27* 181-193.
7. Schneider, B. PhD Fraunhofer Institut fur Fertigungstechnik und Materialforschung, 2001.
8. Damian, C.; Espuche, E.; Escoubes, M. *Polymer degradation and stability* 2001, *72*(3), 447-458.
9. Leidheiser, H.; Funke, W. *J.Oil Colour Chem.Assoc.* 1987, *70* (5), 121-132.
10. Wernick, S.; Pinner, R.; Sheasby, P. G. *The surface treatment and finishing of aluminium and its alloys*; 5 ed.; Teddington: 1987; Vol. 1.
11. van Ooij, W. J.; Edwards, R. A.; Sabata, A.; Zappia, J. *Journal of Adhesion Science and Technology* 1993, *7*(8), 897-917.
12. Fedrizzi, L.; Rodriguez, F. J.; Rossi, S.; Deflorian, F.; DiMaggio, R. *Electrochimica Acta* 2001, *46*(24-25), 3715-3724.
13. Lowe, C.; Devos, L.; Lavaste, V.; Simmons, G. C.; Watts, J. F. *Journal of Coatings Technology* 2000, *72*(909), 135-144.
14. ASTM . Standard Test Method for Floating Roller Peel Resistance of Adhesives. D3167. 2003.
15. Sivel, V. G. M.; van den Brand, J.; Wang, W. R.; Mohdadi, H.; Tichelaar, F. D.; Alkemade, P. F. A.; Zandbergen, H. W. *Journal of Microscopy* 2004, *214*(3), 237-245
16. Sivel, V.G.M. "Dualbeam and FIB capability applied to metals research"; FEI Application Note, 2004.
17. Bajat, J. B.; Mikovic-Stankovic, V. B.; Kacarevic-Popovic, Z. *Progress in organic coatings* 2002, *45*(4), 379-387.
18. Miskovic-Stankovic, V. B.; Stanic, M. R.; Drazic, D. M. *Progress in organic coatings* 1999, *36*(1-2), 53-63.
19. Rouw, A. C. *Progress in organic coatings* 1998, *34* 181-192.
20. van Westing, E. P. M. *Corrosion Science* 1994, *36*(6), 957-977.
21. Smith, B. C. *Fundamentals of Fourier transform infrared spectroscopy*; CRC Press: Boca Raton, 1996.
22. Bellamy, L. J. *The infrared spectra of complex molecules. Vol. 1*; 3rd ed.; Chapman and Hall: New York, 1978.
23. Roeges, N. P. G. *A guide to the complete interpretation of infrared spectra of organic structures*; Wiley: Chichester, 1994.
24. Hong, S. G.; Tsai, J. S. *Journal of Thermal Analysis and Calorimetry* 2001, *63* 31-46.
25. Nakamae, K.; Nishino, T.; Airu, X.; Asaoka, S. *International Journal of Adhesion and Adhesives* 1995, *15* 15-20.
26. Arayasantiparb, D.; McKnight, S.; Libera, M. *Journal of Adhesion Science and Technology* 2001, *15*(12), 1463-1484.
27. *Chemistry and technology of epoxy resins*; Blackie: London, 1993.
28. Fraga, F.; Burgo, S.; Nunez, E. R. *Journal of Applied Polymer Science* 2001, *82*(13), 3366-3372.
29. Alexander, M. R. *Surface and Interface Analysis* 2000, *29* 468-477.
30. Vedder, W.; Vermilyea, D. A. *Transactions of the Faraday Society* 1969, *65* 561-584.
31. Kiss, A. B.; Kerezturny, G.; Farkas, L. *Spectrochimica Acta Part A* 1980, *36*(7), 653-658.
32. Frost, R. L.; Kloprogge, J. T.; Russell, S. C.; Szetu, J. *Applied Spectroscopy* 1999, *53*(7), 829-835.
33. Kloprogge, J. T.; Ruan, H. D.; Frost, R. L. *Journal of Materials Science* 2002, *37* 1121-1129.
34. Music, S.; Dragcevic, D.; Popovic, S. *Materials Letters* 1999, *40* 269-274.
35. Wefers, K.; Misra, C. "Oxides and hydroxides of aluminium"; 19; 1987.
36. Vlaev, L.; Damyanov, D.; Mohamed, M. M. *Colloids and Surfaces* 1989, *36* 427-437.
37. van Gils, S.; Melendres, C. A.; Terryn, H. *Surface and Interface Analysis* 2003, *35*(4), 387-394.

38. Melendres, C. A.; van Gils, S.; Terryn, H. *Electrochemistry Communications* 2001, *3*(12), 737-741.
39. McCafferty, E.; Wightman, J. *Journal of Colloid and Interface Science* 1997, *194*(2), 344-355.
40. Dartevelle, C.; McAlpine, E.; Thompson, G. E.; Alexander, M. R. *Surface and Coatings Technology* 2003, *173*(2-3), 249-258.
41. Davis, G. D. *Journal of Materials Science* 1985, *20* 975-988.
42. Davis, G. D.; Ahearn, J. S.; Venables, J. D. *Journal of Vacuum Science and Technology A* 1984, *2*(2), 763-766.
43. Walker, P. *Journal of the Oil and Colour Chemists Association* 1982, *65*(11), 415-423.
44. Walker, P. *Journal of the Oil and Colour Chemists Association* 1983, *66*(7), 188-192.
45. Arslanov, V. V.; Kalashnikova, I. V.; Gagina, I. A. *Colloid Journal* 1999, *61*(1), 20-25.
46. Arslanov, V. V. *Journal of Adhesion* 1994, *44* 257-269.
47. Arslanov, V. V.; Ogarev, V. A. *Progress in organic coatings* 1987, *15*(1), 1-31.
48. Schultz, J.; Carre, A.; Mazeau, C. *International Journal of Adhesion and Adhesives* 1984, *4* 163.
49. Walker, P. *Journal of Paint Technology* 1967, *31* 15.
50. Walter, G. W. *Corrosion Science* 1991, *32*(10), 1085-1103.
51. Funke, W.; Haagen, H. *Industrial and engineering chemistry product research and development* 1978, *17*(1), 50-53.
52. *Journal of Applied Polymer Science* 1984, *30*(4), 1573-1578.
53. Ivanova, K. I.; Pethrick, R. A.; Affrossman, S. *Journal of Applied Polymer Science* 2001, *82*(14), 3468-3476.
54. Alwitt, R. S. The aluminium-water system, in *Oxides and oxide films vol. 4*, Diggle, J. W., editor; Dekker: New York, 1976; Chapter 3, pp. 169-250.
55. Alexander, M. R.; Thompson, G. E.; Beamson, G. *ATB Metallurgy* 2000,(3-4), 133-141.
56. van Gils, S.; Terryn, H.; Stijns, E.; Thompson, G. E.; Alexander, M. R. *ATB Metallurgy* 2003, *43*(1-2), 358.

CHAPTER 10.

IMPROVING THE ADHESION BETWEEN EPOXY COATINGS AND ALUMINIUM SUBSTRATES BY EITHER USING THIN POLYMER LAYERS OR BY HYDRATION OF ALUMINIUM ¹



¹ This chapter was published as a scientific paper:
J. van den Brand, S. Van Gils, P.C.J. Beentjes, H. Terryn, V.G.M. Sivel, J.H.W. de Wit,
Progress in Organic Coatings, 2004, accepted for publication

Synopsis

In Chapter 9 it was shown that the adhesion between a typical epoxy coating and an aluminium substrate is initially lost upon exposure to water. This is likely caused by the fact that the epoxy coating bonds only through hydrogen-bonds with the oxide surface and these are found to be not stable in the presence of water, see Chapter 8. After the initial loss, the adhesion of the coating was observed to improve again due to the growth of a thin oxyhydroxide layer at the epoxy-aluminium interface. The stage of initial loss of adhesion should however be prevented from occurring as there can be situations where it could lead to failure of the system, for example in structural adhesive bonds. Moreover, for coatings containing a scratch, exposed to chloride-containing electrolytes, the initial loss of adhesion could allow chloride diffusion across the interface, ultimately causing undercoating corrosion to occur. Throughout this thesis, knowledge was obtained of how the adhesion performance of the epoxy coating can be improved. This knowledge is used in this chapter to develop an epoxy-coated aluminium system having an improved adhesion performance. Two different methods are considered. In the first method, a thin polymeric layer is added between epoxy coating and the aluminium substrate. The functional groups of this layer are chosen to be capable of chemisorption to the oxide surface and are also capable of being involved in the curing reaction with the epoxy, thereby linking the epoxy coating strongly to the aluminium substrate. In the second method, the aluminium substrate is hydrated by immersion in boiling water. This results in the formation of a pseudoboehmite oxyhydroxide layer, which is one of the substrate treatments studied throughout this thesis. The layer is porous, consequently has a large surface area and has a high density of hydroxyls on its surface. If the epoxy coating can fully penetrate into this layer, a good adhesion performance is expected. It is found that both methods indeed give a significantly improved adhesion performance. The best results are obtained using a polymeric interfacial layer containing anhydride functional groups and with the pseudoboehmite layer.

10.1. Introduction

When metal-polymer bonds are exposed to aqueous environments, the adhesion between the two is quite often weakened or sometimes even completely lost. Water is known to have a tendency to accumulate at the interface, thereby replacing the bonds that exist between the metal and the polymer [1,2]. A

corrosion protective coating will then no longer be protective towards the underlying metallic substrate and for a structural adhesive bond this will result in failure of the structure.

In Chapter 9 it was shown that due to exposure to water, the adhesion between a typical epoxy coating and an aluminium substrate is rapidly lost and a significant amount of water accumulates at the interface. Similar results were also found by others [3,4]. As was shown in Chapter 8, this is due to the fact that the studied epoxy is only capable of forming hydrogen-bonds with the aluminium oxide surface and these are not stable in the presence of water. For exposure of intact coatings, after this initial loss, the adhesion of the coating was observed to improve again due to the growth of a thin oxyhydroxide layer at the epoxy-aluminium interface. The stage of initial loss of adhesion should however be prevented from occurring as there can be situations where it can lead to complete failure of the system, for example in structural adhesive bonds. Also, for coatings containing a scratch, exposure to chloride-containing electrolytes can lead to undercoating corrosion to occur as a result of the initial loss of adhesion.

The aim of the current work is to improve the adhesion and durability of the adhesion (i.e. the adhesion performance) of such a typical epoxy coating on an aluminium substrate by following two different methods which can be readily applied in industry and which do not require a modification of the epoxy coating itself.

In the first method, a thin polymeric interfacial layer with a thickness of around 10 nm is added between the epoxy coating and the aluminium substrate. The functional groups in this polymeric layer are chosen to be capable of chemisorption to the oxide surface while on the other side they should be capable of being involved in the curing reaction with the epoxy, thereby also forming a strong bond with the coating. Three differently functionalised polymers are studied here for such interfacial polymeric layers: poly(acrylic acid), poly(ethylene-alt-maleic anhydride) and poly(vinyl phosphonic acid). The reactions of the carboxylic acid and anhydride functional groups with the oxide surface was studied and discussed extensively in Chapter 5. For the poly(acrylic acid) polymer, the carboxylic acid groups react with the oxide surface to form a chemisorbed carboxylate. For the poly(ethylene-alt-maleic anhydride), upon adsorption on the oxide surface, the anhydride groups hydrolyse and two carboxylic acid groups are formed. Both carboxylic acid groups subsequently react with the oxide surface to form a chemisorbed carboxylate, just as for poly(acrylic acid). Finally, the phosphonic acid groups in the poly(vinyl phosphonic acid) polymer react with the oxide surface to form a

chemisorbed phosphonate [5-7]. Both anhydride and carboxylic acid groups are known to be able to take part in the curing reaction of the epoxy coating [8,9]. For the poly(vinyl phosphonic acid) polymer this is unknown. Besides studying different organic functionalities for the interfacial polymeric layer, also the influence of the polymeric interfacial layer thickness and of the molecular weight on the adhesion performance of the system is investigated. The influence of the layer thickness is investigated by studying the adhesion performance resulting from two different polymeric interfacial layer thicknesses. The influence of the molecular weight is investigated by studying the adhesion performance of two different molecular weight poly(acrylic acid) polymeric interfacial layers.

In the second method of adhesion improvement, the aluminium substrate is hydrated by immersion in boiling water. A pseudoboehmite layer (AlOOH with some interlamellar water) is then formed on the aluminium substrate through a dissolution-precipitation reaction between aluminium ions and water [10-13]. This very hydroxyl-rich layer is porous and has a large surface area, see Chapter 5. In that Chapter it was also shown that the layer has a 15-fold increase in surface area as compared to the native aluminium oxide layer surface. The high density of hydroxyls gives the surface the capacity to form a large number of bonds with organic functional groups, as was shown in Chapters 5 and 6. Moreover, the porous surface and consequently the large surface area facilitate adhesion and durability through the large epoxy coating-oxide layer contact area and through mechanical interlocking between epoxy coating and oxide layer. These characteristics make it a very suitable candidate as an aluminium surface treatment for giving strong and durable bonds with organic overlayers [14-17].

The polymeric and pseudoboehmite layers are investigated prior to application of the epoxy coating using FTIR-RAS (infrared reflection absorption spectroscopy) and VISSE (visible spectroscopic ellipsometry) to determine composition and layer thicknesses. The chemical reactions between the epoxy and the interfacial polymeric layers are studied by manually removing the epoxy coating after curing and then studying the interphasial region using FTIR. For the pseudoboehmite system, TEM (transmission electron microscopy) cross section images are obtained to study morphology of the layer and the extent of penetration of the epoxy coating. The adhesion strength and durability of adhesion of the epoxy coating for the improved systems is evaluated initially and after exposure to water and to 5% acetic acid and compared with the results for the unmodified systems. Finally, a TGA (thermogravimetric analysis) investigation is performed of the amount of water absorbed by the pseudoboehmite system as a function of exposure time.

10.2. Experimental

10.2.1. Thin polymeric interfacial layers

The repetition units for the three polymers used as thin interfacial layers are shown in Fig. 1. Poly(ethylene-alt-maleic anhydride) polymer was obtained from Sigma-Aldrich, having an average molecular weight of about 100,000. To study the influence of the molecular weight on the adhesion performance, two different poly(acrylic acid) polymers were obtained from Sigma-Aldrich, having average molecular weights of 5,000 and 100,000. The poly(vinyl phosphonic acid) polymer was obtained from Polysciences as a 30% solution in water, having an average molecular weight of 20,000. The polymers were applied on the freshly prepared aluminium substrates by dip-coating from a 1 mass% solvent solution. For poly(acrylic acid) and poly(vinyl phosphonic acid), methanol (99% purity) was used and for poly(ethylene-alt-maleic anhydride), acetone (97% purity) was used. To investigate the influence of the polymeric interfacial layer thickness on the adhesion performance, for half of the substrates, the initially adsorbed

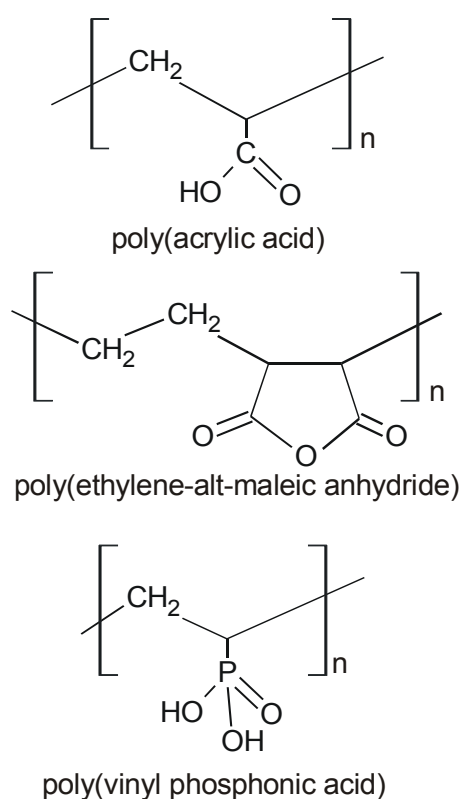


FIG. 1. Repetition units of the polymers used for the thin interfacial layers between the epoxy coating and aluminium substrate for the purpose of adhesion performance improvement.

polymeric layers were rinsed-off by dipping 3 times in clean methanol.

10.2.2. Coated substrate preparation

The 99.5% pure AA1050 aluminium alloy (0.04 wt.% Fe and 0.25 wt.% Si) substrates were prepared following the same procedure as in Chapter 9, see paragraph 9.2.1 on page 147. The pseudoboehmite oxyhydroxide layer was made by immersion of the aluminium substrates in boiling water for 60 seconds, directly after the alkaline/acid surface treatment. The substrates were blown dry using compressed clean air and within 45 minutes after preparation of the substrates, the epoxy coating was applied.

After preparation, the epoxy coating was applied on the substrates onto which either a thin polymeric layer or the pseudoboehmite surface treatment was applied. The epoxy coating and the application procedure were the same as used in Chapter 9, see paragraph 9.2.1 on page 147.

10.2.3. Adhesion testing

For determination of the adhesion strength of the coatings, pull-off tests were performed [18,19]. The tests were performed using a P.A.T. GM 01 hydraulic pull-off tester. A circular dolly, having a diameter of 20 mm, was mounted on top of the epoxy coating using an adhesive. A 5 mm thick steel plate was adhered on the backside to prevent distortion of the 1 mm thick aluminium substrates. After curing of the adhesive, the coating was cut around the dolly. Then, the dolly was pulled-off vertically while measuring the necessary force.

For determination of the adhesion of the coating after exposure to water and 5% acetic acid, the NMP adhesion test was used, see paragraph 9.2.2 on page 148 for details.

10.2.4. Analytical techniques

The used analytical techniques were the same as used in Chapter 9, see paragraph 9.2.4 on page 150 for the experimental details.

10.3. Results

10.3.1. Thin polymeric coatings

FTIR analysis

In Fig. 2, FTIR-RAS spectra are shown of the aluminium substrates, after application of the polymeric layers but prior to application of the epoxy coating. The low and high molecular weight poly(acrylic acid) polymers gave the same spectra and therefore only one of them is shown. For each type of polymer, a set of two spectra is shown. The top spectrum shows the initially adsorbed polymeric layer. The bottom spectrum shows the thinner layer which is made from the thicker layer by rinsing-off excess polymer. Rinsing was performed three times and continued rinsing was found to not result in a further decrease in the amount of adsorbed polymer.

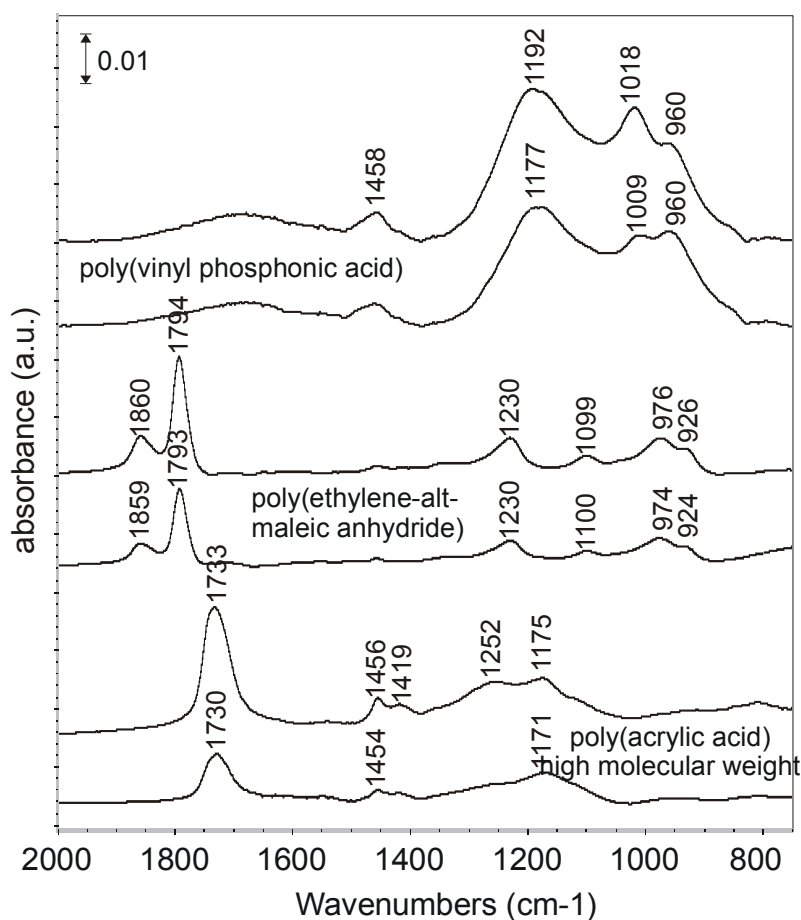


FIG. 2. FTIR-RAS spectra of the polymeric layers as freshly applied on the aluminium substrates. For each type of polymer, a set of two spectra is shown. The top spectrum shows the results without and the bottom spectrum with rinsing-off using clean solvent.

An assignment of the various bands in the spectra is given in Table 1. The high molecular weight poly(acrylic acid) polymer shows its main band at 1730 cm^{-1} , which is due to the $\nu(\text{C}=\text{O})$ carbonyl stretching band of the carboxylic acid groups. The asymmetry observed in the carbonyl band is an optical effect, resulting from a contribution of the refractive index $n(\nu)$ to the measured spectrum [20-22] and see also Chapter 2. The effect is stronger for more intense bands and it also causes the generally observed slightly higher wavenumbers for the thicker layers as compared to the thinner layers. The poly(ethylene-alt-maleic anhydride) polymer shows its main bands at 1860 and 1794 cm^{-1} , which are respectively the $\nu_{\text{as}}(\text{C}=\text{O})$ and $\nu_{\text{s}}(\text{C}=\text{O})$ carbonyl stretching vibrations of the anhydride functional groups. The poly(vinyl phosphonic acid) polymer shows its main bands at 1180 , 1010 and 960 cm^{-1} which are respectively due to the $\nu(\text{P}=\text{O})$, $\nu_{\text{as}}(\text{P}-\text{O})$ and $\nu_{\text{s}}(\text{P}-\text{O})$ stretching vibrations of the phosphonic acid functional groups.

Infrared bands due to bonding of the polymers with the substrates could not be distinguished from the infrared spectra. This is due to the comparably intense infrared bands resulting from the bulk and the comparably lower optical quality of the substrates due to the increased roughness, both making the interfacial contribution limited. The bonding of these functional groups with the oxide surface is however rather well-established and is discussed in the Introduction.

TABLE 1. Infrared peak assignments for the polymers used for the polymeric interfacial layers [5-7,38-42].

poly(acrylic acid)	poly(vinyl phosphonic acid) (cm^{-1})	poly(ethylene-alt-maleic anhydride)	assignment
		1860	$\nu_{\text{as}}(\text{C}=\text{O})$ [asym C=O stretch anh]
		1794	$\nu_{\text{s}}(\text{C}=\text{O})$ [sym C=O stretching anh]
1730			$\nu(\text{C}=\text{O})$ [C=O stretching]
1456/1410	1458	1456	$\delta(\text{CH}_2)$ [CH_2 deformation]
1252			$\delta\text{OH}\dots\text{O}$ [OH bend, coupled]
		1230	$\omega(\text{CH}_2)$ [CH_2 wagging]
1175			$\nu(\text{C}-\text{O})$ [CO stretch, coupled]
	1180		$\nu(\text{P}=\text{O})$
		1099	$\nu(\text{COC})$ [ring stretch]
	1010		$\nu_{\text{as}}(\text{P}-\text{O})$
	960		$\nu_{\text{s}}(\text{P}-\text{O})$
		974/924	ring vibrations

10.3.2. Visible spectroscopic ellipsometry

Visible spectroscopic ellipsometry measurements have been performed to investigate the layer thicknesses of the polymeric layers. The technique requires the use of an optical model to derive the thickness from the ellipsometric measurement data. The model used consisted of an aluminium substrate with on top an oxide layer having a fixed thickness. The results of a measurement performed on an aluminium substrate without a polymeric layer were used as a reference for this. On top of this, a polymeric layer having a variable thickness was positioned in the optical model. A Cauchy dispersion relation was used for this: $n=A+B/\lambda^2$ with λ the wavenumber, n the refractive index and $A = 1.45$ and $B = 0.01$, which are typical values for polymers [23]. The polymeric layer thickness was varied in the model until the best possible fit with the ellipsometric measurement data was obtained. The layer thicknesses resulting from this are summarized in Table 2. The polymeric layer thicknesses are roughly constant in the 12-17 nm range. This is because the layers were applied using dipcoating, starting from the same concentrations in solution. After rinsing, layer thicknesses in the 5-10 nm range are obtained and so roughly half of the initially adsorbed polymer is removed again. The low molecular weight poly(acrylic acid) polymer layer is almost completely removed upon rinsing. It is known that for a low molecular weight polymer, it is easier to dissolve polymer molecules from the bulk of the layer. The very low thickness makes it questionable whether a homogeneously covering polymeric layer can be considered to be still present, see also furtheron.

10.3.3. FTIR analysis of the system after coating

An investigation was performed to determine whether the polymeric interfacial layers were involved in the curing reaction after application and

TABLE 2. Layer thicknesses of applied polymeric layers as determined using spectroscopic ellipsometry.

polymer	layer thickness	layer thickness
	before rinsing	after rinsing
	(nm)	(nm)
poly(acrylic acid) high molecular weight	16.8	9.7
poly(acrylic acid) low molecular weight	16.0	0.7
poly(ethylene-alt-maleic anhydride)	15.1	7.1
poly(vinyl phosphonic acid)	11.9	4.6

curing of the epoxy. To allow this, the cured epoxy coatings were manually peeled from the substrates, thus exposing the interface. Not much force was necessary to remove the coatings for the poly(acrylic acid) and poly(vinyl phosphonic acid) based systems while more force was necessary for the poly(ethylene-alt-maleic anhydride) based system. Subsequently, FTIR-ATR measurements were performed on the coatings and FTIR-RAS on the aluminium substrates. The use of the FTIR-ATR technique allows studying the outer surface region of the coating up to the micron range [24]. The FTIR-ATR measurements, performed on the substrate-side of the coatings (i.e. the side of the coating that used to be attached to the aluminium substrate), only showed infrared bands originating from the epoxy coating (not shown) while bands originating from the polymeric layer were not found. In Fig. 3, FTIR-RAS spectra obtained from the aluminium substrates are shown. For comparison, a FTIR-ATR spectrum of a well-cured epoxy-coating is also included in the Figure. The spectra obtained for the modified systems show infrared bands due to an organic overlayer remaining on the substrate. The intensity of the infrared bands is well-comparable to those of the freshly prepared polymeric layers. For this reason, it can be derived that manual removal of the epoxy coating results in *cohesive failure* at a position close to the epoxy-polymeric interfacial layer interface. For the unmodified system, see the top spectrum, the spectrum only shows infrared bands originating from the aluminium oxide layer and thus *adhesive failure* occurs in this case.

The bands in the spectra are clearly different from those in the spectra of the freshly applied polymeric layers; compare Figs. 2 and 3, indicating that significant chemical changes occur to the layer upon application and curing of the epoxy.

For the freshly applied poly(acrylic acid) polymeric layer, the main band is observed at around 1730 cm^{-1} , due to the $\nu(\text{C}=\text{O})$ of carboxylic acid groups, see Fig. 2. The layer remaining on the substrate does not show the presence of this band anymore but a minor band at 1716 cm^{-1} is observed, which can be ascribed to ester functional groups [8,25,26]. The spectrum contains various bands, which are due to the epoxy, compare with the bottom spectrum, obtained from the coating. Besides this, the spectrum shows a broad band at 1580 cm^{-1} , which does not originate from the original polymeric interfacial layer or from the epoxy. The band can be ascribed to the $\nu_{\text{as}}(\text{COO}^-)$ asymmetric carboxylate stretching vibration of a carboxylate [8,25,26]. This species is being formed as a result of deprotonation of the carboxylic acid. The corresponding $\nu_{\text{s}}(\text{COO}^-)$ symmetric carboxylate stretching vibration, which should be found in the $1420\text{-}1350\text{ cm}^{-1}$ region [8,25,26], is likely hidden below other bands. From this it can be

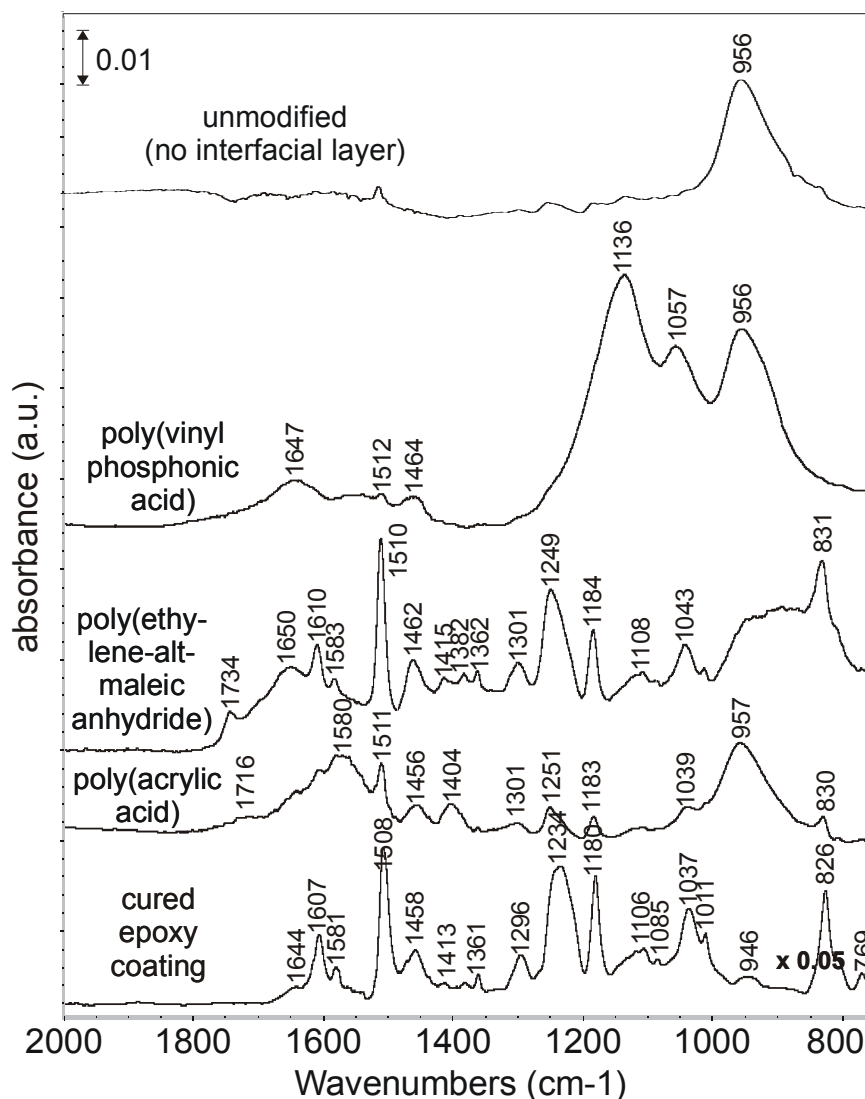


FIG. 3. FTIR-RAS spectra of the polymeric layers as found on the aluminium substrates after peeling-off the epoxy coatings. Samples were chosen onto which the thicker layer of polymer was adsorbed initially and for the poly(acrylic acid) polymer, the high molecular weight type was chosen. The top spectrum shows the results for the unmodified epoxy-coated aluminium system. The bottom spectrum is a FTIR-ATR spectrum performed on the cured epoxy coating.

concluded that the initially applied polymeric layer is transformed into a mixed *interphasial region*, which consists of epoxy, carboxylates and esters. The system is shown schematically in cross section in Fig. 4a. Upon manual removal of the epoxy coating from the aluminium substrate, cohesive failure then occurs and the interphasial region remains on the aluminium substrate as the organic overlayer observed in the FTIR-RAS spectra.

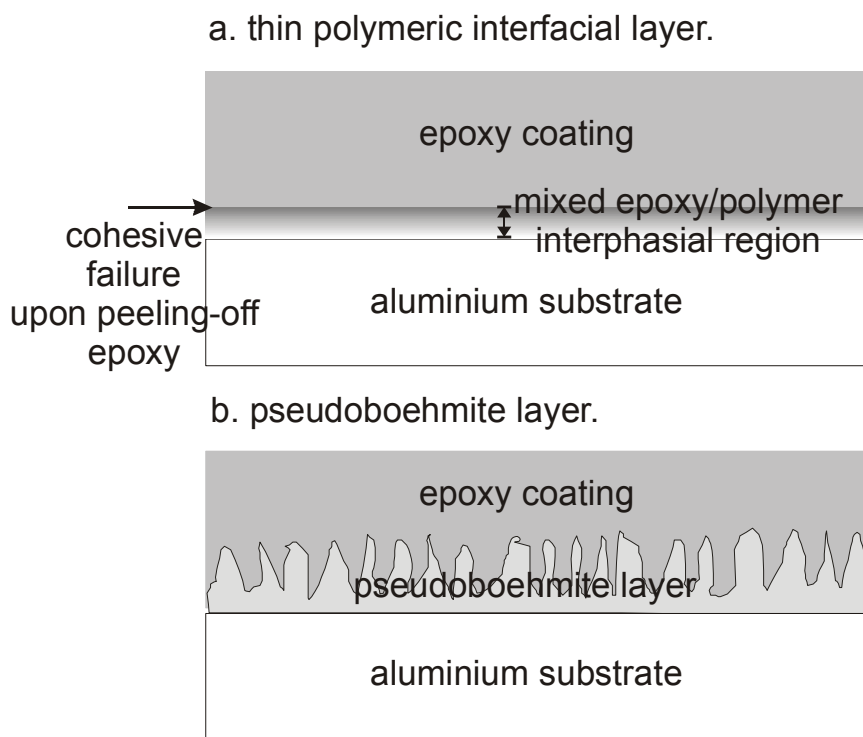


FIG. 4. Schematic of the systems developed using the two methods of adhesion performance improvement. (a). Adding a thin polymeric layer between aluminium and epoxy. As a result of reaction between epoxy and the polymeric layer, this results in the formation of a mixed epoxy/polymer interphasial region. (b). Hydration of the aluminium substrate by immersion in boiling water, resulting in the formation of a porous pseudoboehmite oxyhydroxide layer. The epoxy coating fully penetrates into this porous structure.

Cherdoud-Chihani *et al.* [8] studied curing of epoxies in presence of poly(acrylic acid-co-styrene) polymers. The reaction is initiated by acid-base complexes, formed between an alcohol (originating from the solvent) and an amine catalyst. These complexes cause deprotonation of the carboxylic acid groups, to form intermediate carboxylates. The carboxylates in turn react further with epoxy rings to form ester groups and ultimately resulting in a network structure. The reaction is terminated by reacting with an alcohol from the solvent [8]. A fully cured coating results in the complete consumption of the epoxy groups. The state of curing of epoxies can be evaluated from the (comparably weak) epoxy ring infrared bands, which are found at around 915 and 863 cm^{-1} and are thus expected to be absent for a well-cured coating [27,28]. The curing state of the interphasial region between epoxy and aluminium substrate (so, the layer remaining on the aluminium substrate) can however not be evaluated, because of the large contribution of the Al-O stretching vibration at 950 cm^{-1} , resulting from the aluminium oxide layer. The clear presence of both ester groups and carboxylates in the interphasial region however indicates that the curing

reaction between epoxy and the poly(acrylic acid) interfacial layer has initiated, but likely the curing has not been completed, as otherwise carboxylates would not be present anymore [8].

For the poly(ethylene-alt-maleic anhydride) polymeric layer, the main bands are observed at 1794 and 1860 cm^{-1} , due to the anhydride functional groups, see Fig. 2. In the layer remaining on the substrate, these bands are completely absent, see Fig. 3. The spectrum shows a band at 1734 cm^{-1} , which for this polymer can be ascribed to ester functional groups [9,25,26]. Just as for the poly(acrylic acid) layer, various infrared bands resulting from the epoxy are present. The curing reaction of an epoxy by an anhydride-based polymer proceeds similar to that with carboxylic acid groups [9]. In contrast to the results for the poly(acrylic acid) polymer however, bands due to carboxylates are not observed. It can therefore be concluded that in this case the curing reaction has proceeded further than for the poly(acrylic acid) polymer. A mixed and cured epoxy/polymer interphasial region is therefore formed in which the poly(ethylene-alt-maleic anhydride) polymer is directly incorporated into the epoxy network. Differences between curing of epoxies with either carboxylic acid-based or anhydride-based polymers were also found by others. Cherdoud-Chihani *et al.* noted the presence of residual intermediate carboxylates for curing with a poly(acrylic acid-co-styrene) [8] polymer, but not for curing with a poly(styrene-alt-maleic anhydride) [9].

For the freshly prepared poly(vinyl phosphonic acid) polymeric layer, bands due to the phosphonic acid groups are found at 1192, 1018 and 960 cm^{-1} , see Fig. 2. For the interphasial region, bands are observed at 1136, 1057 and 956 cm^{-1} , see Fig. 3. The bands at 1057 and 1136 cm^{-1} can be assigned respectively to the $\nu_s(\text{PO}_3^{2-})$ and $\nu_{\text{as}}(\text{PO}_3^{2-})$ phosphonate stretching vibrations [7]. Their presence indicates that deprotonation of the phosphonic acid groups has occurred and phosphonate groups are formed throughout the layer. Besides this, minor bands due to the epoxy are present. Corresponding with the results for poly(acrylic acid), the results for the poly(vinyl phosphonic acid) polymer also suggest that a mixed epoxy/polymer interphasial region is formed in which the phosphonic acid groups were involved in curing with the epoxy coating. The reaction has however also not been fully completed and a cured interphasial region is not formed.

10.3.4. Pseudoboehmite layer

Infrared analysis

In Fig. 5, the infrared spectrum is shown of the pseudoboehmite aluminium oxyhydroxide layer, made by boiling of the aluminium substrates for 60 seconds in water. In Table 3, the assignment of the various infrared bands is given. The bands at 3094, 1089 and 748 cm^{-1} are respectively the $\nu(\text{OH})$ hydroxyl stretching, $\delta(\text{OH})$ hydroxyl bending and $\gamma(\text{OH})$ hydroxyl twisting vibrations [29-32] due to hydroxyls in the pseudoboehmite matrix. The bands at 3440, 1642, 1492 and 1381 cm^{-1} are water-related bands and indicate the presence of water inside the pseudoboehmite structure [33,34]. Finally, the bands at 860, 798 and 672 cm^{-1} originate from oxide lattice vibrations [29].

Visible spectroscopic ellipsometry

The thickness and porosity of the pseudoboehmite layer were obtained from VISSE measurements. The optical model used to fit the ellipsometric measurement data is discussed in detail elsewhere, where it was used to study the formation of pseudoboehmite as a function of immersion time in boiling water [33]. A Cauchy-layer is used to model the pseudoboehmite layer itself. An effective medium approximation (EMA) layer is added between the aluminium substrate and the pseudoboehmite layer to describe the interfacial roughness [33]. Fitting of the optical model onto the ellipsometric measurement data gave

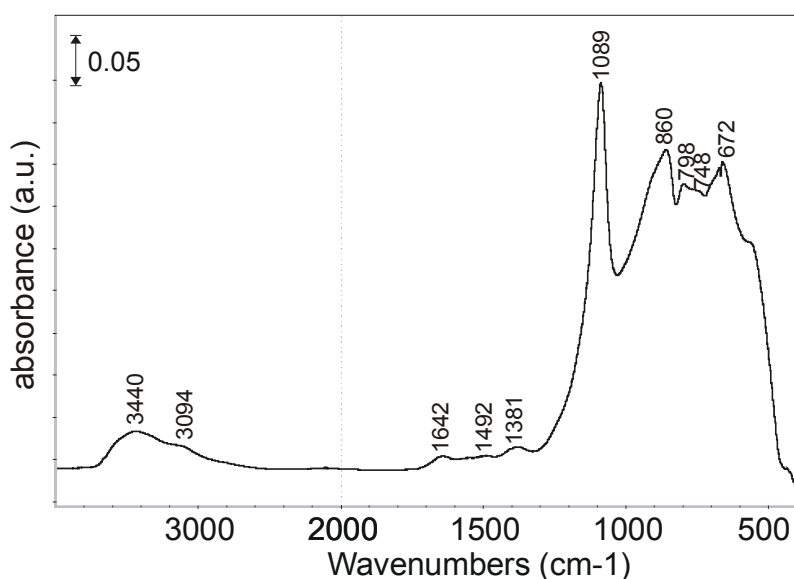


FIG. 5. FTIR-RAS spectra of the pseudoboehmite layer, made by hydration of the aluminium substrates by immersion in boiling water for 60 seconds.

TABLE 3. Infrared peak assignments for the pseudoboehmite oxyhydroxide layer [29-34].

peak position (cm^{-1})	assignment
3440	$\nu(\text{OH})$ [hydroxyl stretch due to water]
3094	$\nu(\text{OH})$ [hydroxyl stretch due to AlOOH]
1642, 1492, 1381	$\delta(\text{H}_2\text{O})$ [water bend due to water in AlOOH]
1089	$\delta(\text{OH})$ [hydroxyl bend due to AlOOH]
860	$\nu(\text{AlO}_6)$ [stretch due to oxide lattice]
798	$\nu(\text{AlO}_6)$ [stretch due to oxide lattice]
748	$\gamma(\text{OH})$ [hydroxyl twist due to AlOOH]
672	$\nu(\text{AlO}_6)$ [stretch due to oxide lattice]

a total pseudoboehmite layer thickness of 265 ± 5 nm. The refractive index was found to have a value of 1.23 at 630 nm, which is rather low and indicates a porous structure. An estimate of the porosity can then be obtained using reference optical constants for aluminium oxide and assuming that the porosity is present homogeneously throughout the depth [33]. This resulted in a value of 63% for the porosity in the layer.

SEM/TEM investigation

In Fig. 6, a SEM top view image at a magnification of 40,000x is shown of the pseudoboehmite layer. The layer can be seen to be porous and having a ‘hairy’, ‘cornflake’-like structure [10]. The full aluminium substrate was found to be homogeneously and well-covered with pseudoboehmite.

For optimal adhesion, it is important that the epoxy coating fully penetrates into the pores of the layer. To investigate whether this occurs, a TEM investigation was performed. In Fig. 7, a cross section image of the epoxy-pseudoboehmite-aluminium system is shown. On top is the epoxy coating, in the centre the porous pseudoboehmite layer and on the bottom the aluminium substrate. The pseudoboehmite layer can be seen well-resolved. It consists of an inner, dense region having a thickness of around 80 nm and an outer, porous region consisting of protruding ‘needles’, having a length of around 200 nm. The total thickness of the layer corresponds well to the VISSE measurements. The TEM image also clearly shows that the epoxy coating has fully penetrated into the pseudoboehmite layer, ensuring an optimal adhesion. The pseudoboehmite based system is shown schematically in Fig. 4b.

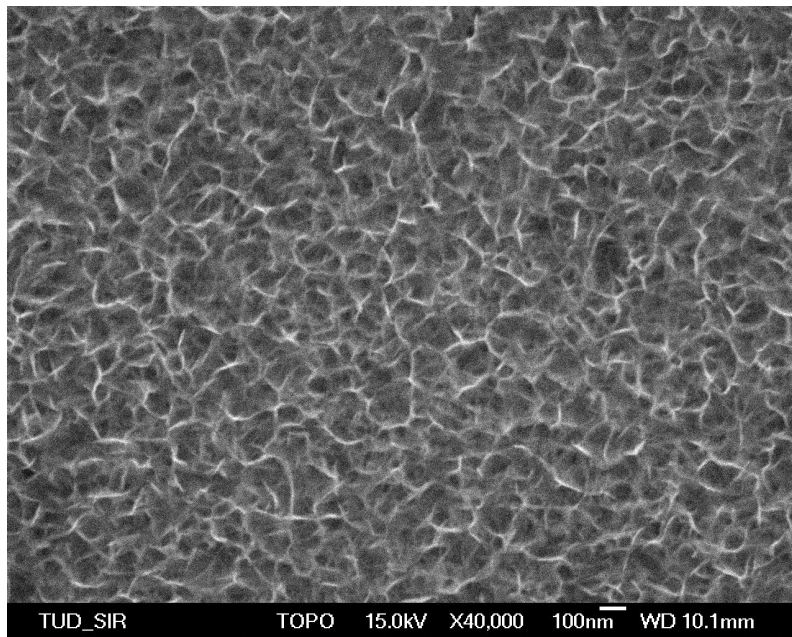


Fig. 6. SEM image of the surface of an aluminium substrate after immersion in boiling water for 60 seconds.

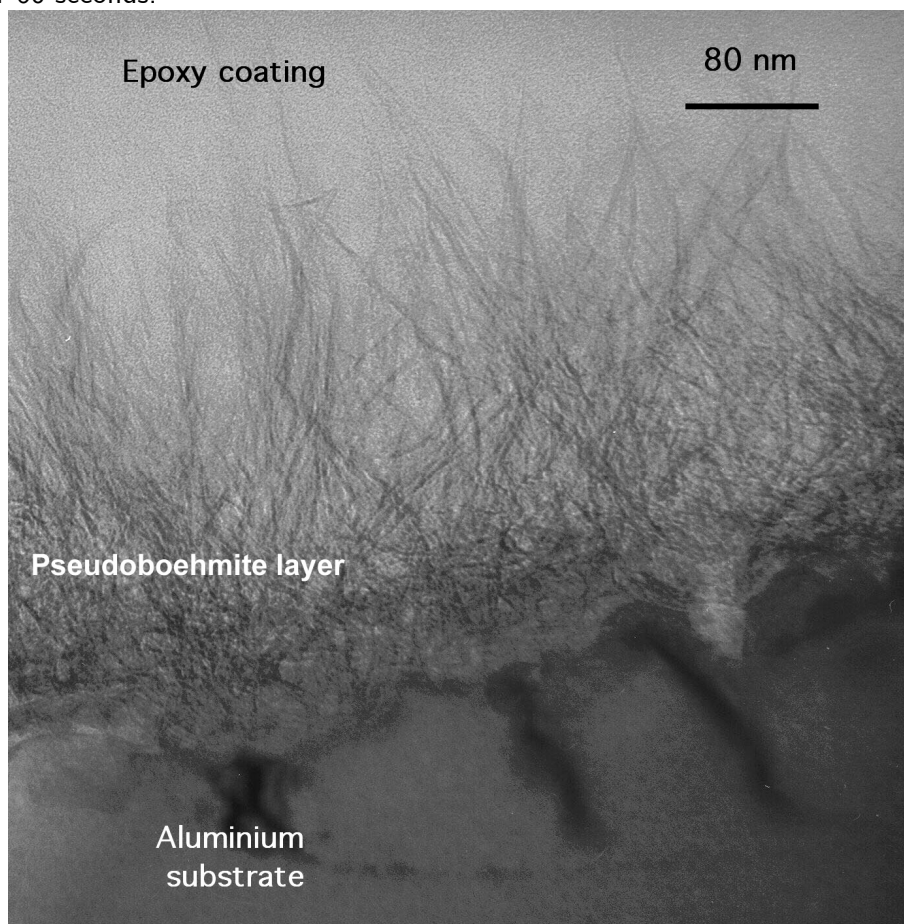


FIG. 7. TEM cross section image of the epoxy-pseudoboehmite-aluminium system. In the centre the pseudoboehmite oxyhydroxide layer is visible. The epoxy coating is observed to have fully penetrated into the porous layer.

10.3.5. Adhesion testing

Initial adhesion strength

To test the adhesion strength of the epoxy coating for the different systems, pull-off tests were performed. For each type of aluminium-epoxy system, three samples were tested and the average value of this was taken. Based on this, the error in the results is estimated to be 1 MPa. For all systems, a limited FTIR investigation showed that delamination occurred cohesively in the interphasial region that is formed, just as for the manually removed coatings, see above, and through the epoxy coating for the pseudoboehmite system.

The pull-off test results are shown in Fig. 8. For the unmodified system (without a polymeric or pseudoboehmite layer) a value of around 9 MPa is obtained. For the modified systems, the best performance is obtained for the pseudoboehmite based system, which shows a pull-off strength of around 17 MPa. Below that is the result obtained for the poly(ethylene-alt-maleic anhydride) based system, giving a value of around 12 MPa. The poly(acrylic acid) based system shows lower pull-off strengths of 10 MPa, which are only slightly higher than with no interfacial layer. The high molecular weight poly(acrylic acid) based system gives a higher adhesion strength than the low molecular weight poly(acrylic acid) based system. The rinsed, low molecular weight polymer appears to contradict this, but it is doubtful whether an

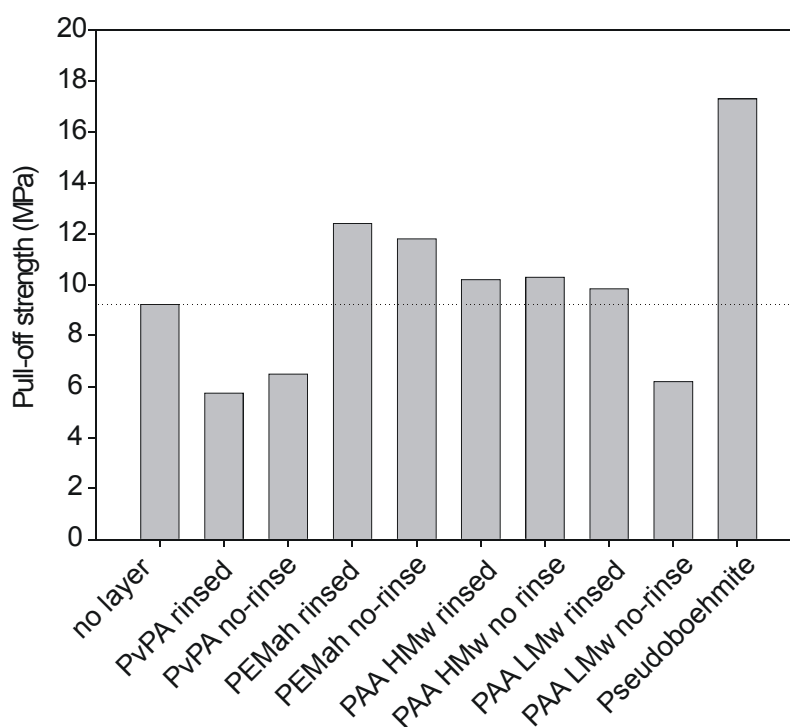


FIG. 8. Pull-off strengths for the different improved epoxy-aluminium systems.

homogeneously covering polymeric layer was initially present, see also Table 2, hence giving the same pull-off strength as with no interfacial layer being present. Finally, the poly(vinyl phosphonic) acid based system gives very low values of 6 MPa, which are even lower than the unmodified system.

NMP adhesion testing

NMP adhesion tests were performed initially, after exposure of the various types of epoxy-aluminium systems for 750 hours to 40 °C water and after 750 hours of exposure to 5% acetic acid at 40 °C. The results are shown in Fig. 9.

With respect to the NMP delamination times obtained before exposure, the highest NMP delamination time is obtained for the poly(ethylene-alt-maleic anhydride) (PEMah) and pseudoboehmite based systems. For both, the epoxy coating could not be removed using NMP as tested up until 1 hour of immersion. Their results are therefore indicated as infinite.

For the poly(acrylic acid) (PAA) based system, the delamination times are slightly higher than for the unmodified system. The low molecular weight polymer gives slightly worse results than the high molecular weight polymer. The lowest performance is obtained for the poly(vinyl phosphonic acid) (PvPA)

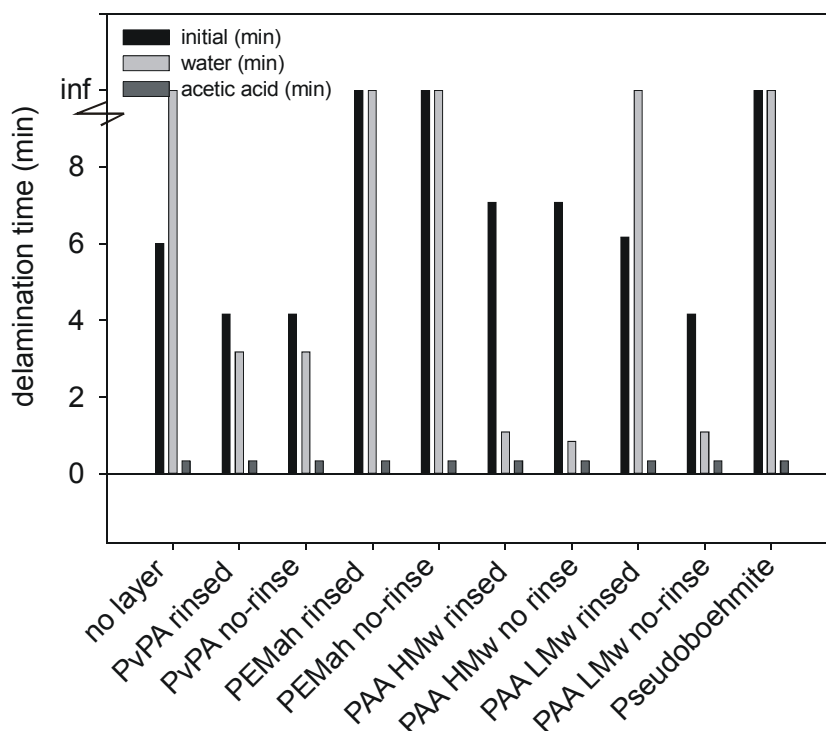


FIG. 9. NMP delamination times for the different improved epoxy-aluminium systems. Results are shown as obtained initially and after exposure for 750 hours to 40 °C deionised water and 5% acetic acid.

based system, which gives NMP delamination times even lower than for the unmodified system. In general, these NMP delamination times compare well with the results obtained using the pull-off tests.

After exposure to 40 °C water, for the unmodified system, the coating could no longer be removed using NMP. Exposure to water thus results in improvement of the adhesion. This phenomenon is investigated and discussed in detail in Chapter 9. Upon exposure to water, the adhesion between the coating and the aluminium substrate is rapidly lost and water accumulates at the interface. An aluminium oxyhydroxide layer starts to grow, which eventually re-establishes contact with the coating and forms a new, stronger and water-stable bond, causing an improvement of the adhesion of the epoxy coating as compared to the not-exposed system. For the modified systems, the best performance after exposure to water is obtained for the poly(ethylene-alt-maleic anhydride) (PEMah) and pseudoboehmite based systems. Just as prior to exposure, the epoxy coating could not be removed using NMP. Also, at intermediate times (results not shown) the coating could not be removed using NMP. The poly(vinyl phosphonic acid) (PvPA) based system shows a slight decrease in delamination time, indicating slight loss of adhesion of the coating. The worst performance is obtained for the poly(acrylic acid) based system. The epoxy coatings were almost instantly removed upon immersion in NMP. In contrast to this, the rinsed, low molecular weight poly(acrylic acid) polymer also showed an increase in adhesion quality upon exposure to water. This is likely because a homogeneously covering polymeric layer cannot be considered present initially, see Table 2, and therefore the same phenomena as for the unmodified system occurs.

Exposure for 750 hours to 5% acetic acid at 40 °C resulted for all epoxy-aluminium systems in the presence of a large amount of tiny blisters underneath the epoxy-coating, except for the pseudoboehmite system. As an illustration, photographs of the exposed region are shown in Fig. 10 for the unmodified and the pseudoboehmite system. Upon immersion in NMP, instant delamination of the coating occurred, also for the pseudoboehmite system. After removal of the coating it was observed that significant corrosive attack of the aluminium had occurred and a whitish salt layer was present on the substrates.

Water uptake measurements

The pseudoboehmite and poly(ethylene-alt-maleic anhydride) based systems give a very good adhesion stability of the epoxy coating in the presence of water. Because of this, it would be expected that also a limited amount of water

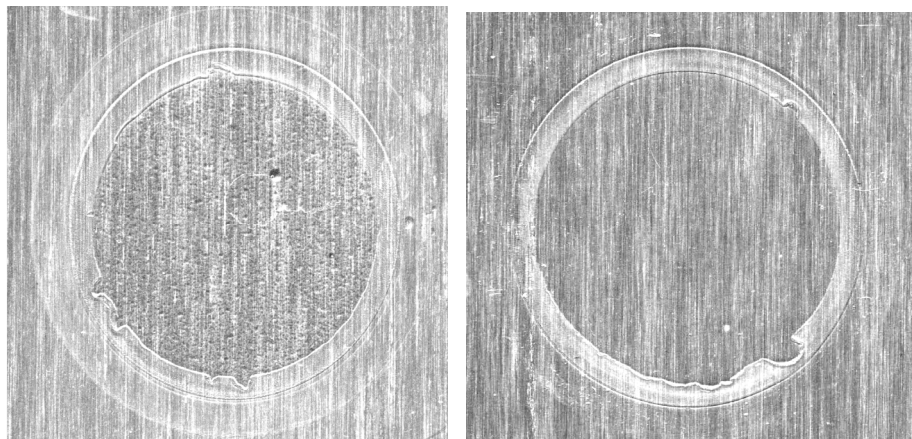


FIG. 10. Photographs of the exposed region for samples exposed to 5% acetic acid for 750 hours at 40 °C. Left photograph is for an unmodified epoxy-aluminium system. In the exposed circular region, tiny blisters are observed to be present underneath the epoxy coating. Right photograph is for an epoxy-pseudoboehmite-aluminium system which does not show the presence of blisters.

is absorbed by the system as a function of exposure time. In Chapter 9, the unmodified epoxy-aluminium system was already investigated with respect to its water uptake as a function of exposure time using TGA (thermogravimetric analysis). In Fig. 11, TGA results are shown for the pseudoboehmite based system and for the unmodified system. The mass of evaporated water from the epoxy-aluminium samples, as obtained from the TGA measurements, was recalculated as a mass percentage of water in the coating by dividing by the mass of the coating in the exposed region. This results in a mass percentage of water in the exposed region and allows a comparison with the results of the free coatings which are also included in the Figure for comparison.

For the unmodified system, the total amount of water in the system increases up to around 9 mass% during the first 25 hours of exposure to 40 °C water owing to loss of adhesion of the coating and the accumulation of a significant amount of water at the interface, see Chapter 9. After this, the amount of water in the system decreases as a result of the formation of a new, water-stable bond with the oxyhydroxide layer that forms on the substrate, see above, preventing the further accumulation of water at the interface.

For the pseudoboehmite system, there appears to be a slight increase in water concentration during the first 300 hours of exposure although probably more measurements need to be performed to confirm this trend. As the percentage of adsorbed water is higher than for the free coating, it can be derived that some water accumulates at the interface. After this however, a stationary value of around 3.5 mass% of water in the system is obtained. The amount of water absorbed by the system can be considered to be low, especially

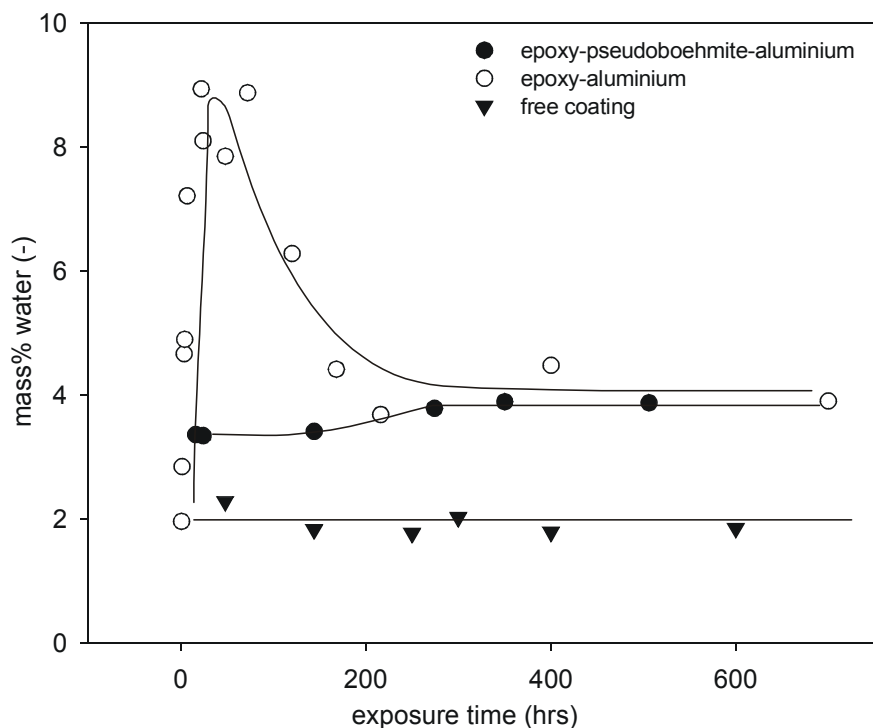


FIG. 11. TGA measurements showing the water uptake of the epoxy-aluminium system as a function of exposure time to 40 °C deionised water.

when considering the large interfacial area between epoxy coating and pseudoboehmite layer at which water can accumulate. The limited amount of water that accumulates at the interface confirms the very good aqueous stability of the adhesion that is obtained for this system, see Fig. 9.

10.4. Discussion

Two different methods were followed to improve the adhesion performance of an epoxy-coating on an aluminium substrate. In Fig. 4, a schematic of these two systems is shown.

The first method studied of improving adhesion and durability was by adding a thin polymeric layer (i.e. an interfacial layer) between aluminium substrate and epoxy coating. The groups were deliberately chosen so as to be able to chemisorb onto the oxide surface and to be capable of being involved in the curing reaction with the epoxy. The bond between the organic overlayer and the substrate is indeed found to be improved. Removal of the epoxy coating after curing results for all improved systems in *cohesive* failure in an interphasial region while for the unmodified system *adhesive* failure occurs between epoxy and aluminium, see Chapter 9.

For all types, significant chemical changes to the polymeric interfacial layer are observed after application and curing of the epoxy coating. The following process is likely to take place at the interface after application of the resin. First, the polymeric layer is largely dissolved due to the solvents. Mixing of the polymer and the epoxy resin constituents can then take place and the functional groups of the polymeric interfacial layer are directly involved in the curing reaction with the epoxy. This eventually results in the formation of a mixed epoxy/polymer interphasial region, see Fig. 4a.

For the poly(ethylene-alt-maleic anhydride) based system, a cured interphasial region is formed, which has become part of the epoxy coating. As a result, this system shows a very good initial adhesion strength and stability in the presence of water.

The poly(acrylic acid) based system shows the presence of carboxylates throughout the interphasial region. This indicates that a curing reaction with the epoxy has started but has not been fully completed [9]. The interphasial region is therefore likely weakly cured and consequently without a large internal strength. Moreover, a hydrophilic, weakly cured region acts as a sponge and can absorb a considerable amount of water. Therefore, despite that a chemisorptive carboxylate-oxide bond is present on the aluminium side, this system does not show a good adhesion strength and durability in the presence of water.

A very similar reasoning can likely also explain the comparably bad adhesion performance obtained for the poly(vinyl phosphonic acid) based system, which shows the formation of phosphonates, likely also indicating the presence of a weakly cured region.

The results obtained using the two different molecular weight poly(acrylic acid) polymers appear to show that a higher molecular weight results in better initial adhesion strength. These results are however likely also because of the incompletely cured interphasial layer, which will be even weaker for a low molecular weight polymer. Differences in durability of the adhesion are not observed. Considering all polymers, not much difference in adhesion performance is observed between a thicker or thinner polymeric interfacial layer.

The second method of adhesion improvement was by hydration of the aluminium substrates by immersion in boiling water, see Fig. 4b. A pseudoboehmite oxyhydroxide layer is formed on the aluminium substrate, having a large number of hydroxyls on its surface and being porous with consequently a large surface area. The epoxy coating was found to be well-capable of penetrating this porous structure. In Chapters 5 and 6 it was shown that most types of organic functional groups bond through hydroxyls on the oxide surface. But, the bonding mechanism itself with organic functional groups

is however not different for pseudoboehmite as compared to other typical aluminium oxides. The large number of hydroxyls on the pseudoboehmite surface and the large surface area will therefore result in a high density of bonds with the epoxy coating. This will result in high initial adhesion strength and water can then not easily accumulate at the interface, because there are a minimum number of sites at which there is no adhesion. Indeed, the pseudoboehmite system shows a significant improvement of the initial adhesion strength and a very good durability in aqueous environments. Upon exposure to water of 40 °C, only limited water is absorbed by the system and the adhesion of the coating remains stable. Apparently, the fact that chemisorptive bonds are not formed between the epoxy coating and the pseudoboehmite layer is compensated by the other beneficial properties of the layer.

Although a good performance was obtained with respect to aqueous exposure, none of the improved systems could resist exposure to 5% acetic acid at 40 °C. Electrolytes containing organic acids are known to be extremely aggressive towards adhesion of organic layers. Although epoxy coatings are effective barriers towards ions, acetic acid can diffuse through the coating in its molecular form [35,36]. Upon arriving at the interface, dissociation of the acid occurs in the aqueous phase and a significant lowering of the pH results. This causes dissolution of the aluminium oxide and severe corrosion of the underlying aluminium with precipitation of an aluminium-acetate salt [15,37].

10.5. Conclusions

An analysis was made of the adhesion performance initially and after exposure to 40 °C water and 5% acetic acid for a number of improved epoxy-aluminium systems. Two methods were followed: application of a thin polymeric interfacial layer between aluminium and epoxy and hydration of the aluminium substrate by immersion in boiling water. The thin polymeric interfacial layers are found to be involved in curing with the subsequently applied epoxy coating. For a poly(ethylene-alt-maleic anhydride) based system, this results in the formation of a cured and mixed epoxy/polymer interphasial region, while in both the poly(acrylic acid) and poly(vinyl phosphonic acid) based systems only a weakly cured epoxy/polymer interphasial region is formed. As a result, the poly(ethylene-alt-maleic anhydride) based system shows a good adhesion strength and durability while the systems based on the two other polymers do not give a very good adhesion performance. The initially applied polymeric layer thickness is not found to have an influence on the adhesion performance. The use of a poly(acrylic acid) polymer having a lower molecular weight as the

interfacial layer is found to result in worse initial adhesion strength. This can however also be due to weakly cured region that is formed. Differences in durability were not observed.

Hydration of the aluminium substrate by immersion in boiling water for 60 seconds results in the formation of a pseudoboehmite oxyhydroxide layer, having a porous structure. The epoxy coating is found to fully penetrate into the layer. The high hydroxyl density on this oxide surface, the large surface area and the porous nature are found to lead to a very good adhesion performance for this system. Upon exposure to water, only very limited water is absorbed by the system.

None of the methods used to improve the adhesion of the epoxy coating are found to be able to resist exposure to 5% acetic acid and delamination of the epoxy coatings and severe blistering occurs.

References

1. Nguyen, T.; Byrd, E.; Bentz, D. *Journal of Adhesion* 1995, 48 169-194.
2. Nguyen, T.; Byrd, E.; Bentz, D.; Lin, C. *Progress in organic coatings* 1996, 27 181-193.
3. Arslanov, V. V. *Journal of Adhesion* 1994, 44 257-269.
4. Leidheiser, H.; Funke, W. *J.Oil Colour Chem.Assoc.* 1987, 70 (5), 121-132.
5. Pellerite, M. J.; Dubar, D. B.; Boardman, L. D.; Wood, E. J. *Journal of Physical Chemistry B* 2003, 107 11726-11736.
6. Tusek-Bozic, L. *Vibrational Spectroscopy* 2002, 28 235-241.
7. Kuys, K. J.; Roberts, N. K. *Colloids and Surfaces A* 1987, 24 1-17.
8. Cherdoud-Chihani, A.; Mouzali, M.; Abadie, M. J. M. *Journal of Applied Polymer Science* 1998, 69(9), 1167-1178.
9. Cherdoud-Chihani, A.; Mouzali, M.; Abadie, M. J. M. *Journal of Applied Polymer Science* 2003, 87(13), 2033-2051.
10. Alwitt, R. S. The aluminium-water system, in *Oxides and oxide films vol. 4*, Diggle, J. W., editor; Dekker: New York, 1976; Chapter 3, pp. 169-250.
11. Strålin, A. *Applied Surface Science* 1994, 74 263-275.
12. Wefers, K.; Misra, C. "Oxides and hydroxides of aluminium"; 19; 1987.
13. Alexander, M. R. *Surface and Interface Analysis* 2000, 29 468-477.
14. Strålin, A. *Journal of Adhesion Science and Technology* 1992, 6(11), 1233-1250.
15. Strålin, A.; Hjertberg, T. *Journal of Adhesion Science and Technology* 1993, 7(11), 1211-1229.
16. Strålin, A.; Hjertberg, T. *Journal of Applied Polymer Science* 1993, 49(3), 511-521.
17. Rider, A. N. *Journal of Adhesion Science and Technology* 2001, 15(4), 395-422.
18. Roche, A. A. *Journal of Adhesion Science and Technology* 1994, 8(6), 587-609.
19. International Organisation for Standardisation "Paints and varnishes -- Pull-off test for adhesion"; ISO 4626; 2004.
20. Brogly, M.; Grohens, H.; Labbe, C.; Schultz, J. *International Journal of Adhesion and Adhesives* 1997, 17(3), 257-261.
21. Brogly, M.; Nardin, M.; Schultz, J. *Journal of Adhesion* 1996, 58(3-4), 263-279.
22. Röseler, A. *Infrared spectroscopic ellipsometry*; Akademie Verlag: Berlin, 1990.
23. J.A.Woollam *Manual WVASE32*; Lincoln USA, 1997.
24. Smith, B. C. *Fundamentals of Fourier transform infrared spectroscopy*; CRC Press: Boca Raton, 1996.
25. Bellamy, L. J. *The infrared spectra of complex molecules. Vol. 1*; 3rd ed.; Chapman and Hall: New York, 1978.
26. Roeges, N. P. G. *A guide to the complete interpretation of infrared spectra of organic structures*; Wiley: Chichester, 1994.
27. Ellis, B. *Chemistry and technology of epoxy resins*; Blackie: London, 1993.
28. Fraga, F.; Burgo, S.; Nunez, E. R. *Journal of Applied Polymer Science* 2001, 82(13), 3366-3372.
29. Kiss, A. B.; Kerezury, G.; Farkas, L. *Spectrochimica Acta Part A* 1980, 36(7), 653-658.
30. Frost, R. L.; Kloprogge, J. T.; Russell, S. C.; Szetu, J. *Applied Spectroscopy* 1999, 53(7), 829-835.
31. Kloprogge, J. T.; Ruan, H. D.; Frost, R. L. *Journal of Materials Science* 2002, 37 1121-1129.
32. Music, S.; Dragcevic, D.; Popovic, S. *Materials Letters* 1999, 40 269-274.
33. van Gils, S.; Melendres, C. A.; Terry, H. *Surface and Interface Analysis* 2003, 35(4), 387-394.
34. Vlaev, L.; Damyanov, D.; Mohamed, M. M. *Colloids and Surfaces* 1989, 36 427-437.
35. Scantlebury, J. D.; Galik, K. *Progress in organic coatings* 1997, 31(3), 201-207.
36. Dutheliet, Y.; Mantle, M.; Vesely, D.; Gladden, L. *Journal of Polymer Science: Part B Polymer Physics* 1999, 37(23), 3328-3336.
37. Olafsson, G.; Jagerstad, M.; Oste, R.; Wesslen, B.; Hjertberg, T. *Food Chemistry* 1993, 47(3), 227-233.
38. Berrada, K.; Dumas, P. *Journal of Electron Spectroscopy and Related Phenomena* 1990, 54-55 1153-1162.
39. Thery, S. *Journal of Adhesion* 1996, 56 1-13.
40. Allara, D. L. *Abstracts of papers of the american chemical society* 1979, april 751-756.

41. Wu, H. S.; Jone, H. C.; Hwang, J. W. *Journal of Applied Polymer Science* 1997, *63* 89-101.
42. Vermohlen, K.; Lewandowski, H.; Narres, H. D.; Koglin, E. *Colloids and Surfaces A* 2000, *170* 181-189.

CHAPTER 11.

PHOTOTHERMAL IMAGING OF LOCALISED DELAMINATION BETWEEN ORGANIC COATINGS AND METALLIC SUBSTRATES USING A SCANNING PHOTOPYROELECTRIC (PPE) MICROSCOPE ¹

Synopsis

In this final chapter, a new experimental technique is discussed which is highly suitable for studying macroscopic delamination below organic coatings with a high spatial resolution. Although the technique was not used in this thesis further, it is discussed here as the work was also performed within the scope of the PhD project and it is relevant for the subject of adhesion and delamination between organic coatings and metallic substrates in general. In the technique, a pyro-electric sensor is mounted on top of the investigated sample. A focussed, intensity-modulated laser beam is scanned across the sensor-surface. This induces a thermal wave in the sample. The thermal wave will experience transmission and reflection at buried interfaces, causing a change in phase and amplitude. At sites of macroscopic delamination between the coating and the substrate, at which air is entrapped below the coating, the resulting thermal wave will be different with respect to phase and amplitude as compared to a region of intact adhesion. The resulting thermal wave is now detected again using the attached pyro-electric sensor, which converts it back into an AC current. The background behind this technique is discussed and its applicability is shown for studying macroscopic delamination. Moreover, a numerical model is developed which allows predicting the capability of the technique and also the attainable lateral resolution.

¹ This chapter was published as a scientific paper, in a more extended form:
J. van den Brand, M. Chirtoc, M.R. Wubbenhorst, J.H.W. de Wit, *Journal of Applied Physics*,
93(4), 2019-2027, 2003

11.1. Introduction

The identification and investigation of localised delamination spots between polymeric coatings and metallic substrates is an important task since they are the most likely starting points for corrosion at the interface and eventually for propagation of delamination [1]. Their origin can be the contamination of the substrate before coating or imperfections (scratches) in the metal substrate where the adhesion between coating and substrate is compromised.

Thermal waves are currently used for non-destructive evaluation (NDE) of various types of subsurface features [2-5]. The measurement principle relies on the fact that the surface temperature of a periodically heated sample carries tomographic information on its structure. Photothermal (PT) methods are highly suitable for the analysis of air-filled defects, which represents a large thermal inhomogeneity [4, 6]. In the photoacoustic method, the sample is introduced in an air-tight chamber. Heating of the sample surface generates a pressure wave in the gas, which is detected by a microphone. With photothermal radiometry the surface temperature of the sample is measured in a non-contact way by using an infrared detector. Imaging and microscopy based on these methods have been reported before [7-11]. Both methods yield results in which the optical properties (absorption coefficient and emissivity) of the sample surface are mixed with the depth profiles of thermal properties.

Unlike these, there are few reports on imaging applications using a pyroelectric/piezoelectric sensor [12, 13]. Imaging of the thermal wave field with

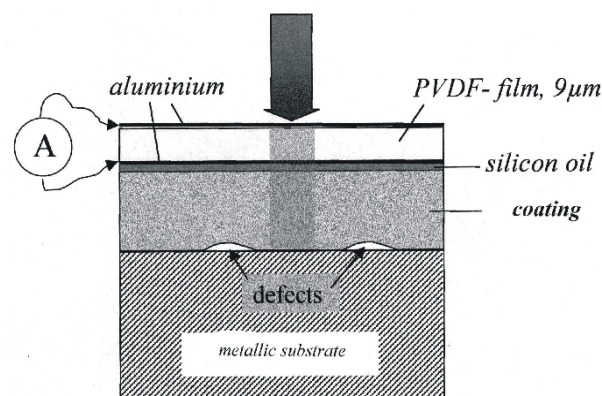


FIG. 1. Schematic of the use of the scanning photopyroelectric microscope (SPPEM) for studying delamination between organic coatings and metallic substrates. The investigated sample is irradiated on top using a focussed modulated laser beam, resulting in localised heating of the material. The resulting thermal response of the sample is converted back into an AC current, using a PVDF pyroelectric sensor which is mounted on top of the coating surface using silicon oil

a PVDF pyroelectric sensor in back-detection configuration was demonstrated [14, 15], where the spatial resolution was obtained by replacing one of the sensor's electrodes by a metal tip. In an earlier work, the scanning photopyroelectric microscope (SPPEM) was applied to a sample that had itself pyroelectric properties [16]. In this work, the same SPPEM is used, but this time in a slightly different configuration. The principle is shown in Fig. 1. On top of the coating surface, a pyroelectric (PE) sensor is mounted using silicon oil. On this same surface (front-detection configuration), the sample is irradiated using a focussed, modulated laser beam. The thermal ac response of the sample to the modulated localised heating contains localised information on the possible presence of subsurface features below the coating. This response is converted back into an electrical signal by the PE sensor. By two-dimensional (2-D) scanning of the focused beam across the surface, a thermal image of the sample can be obtained. Furthermore, by varying the modulation frequency of the laser, information can be obtained on the depth below the surface at which these features are present. The drawback of the PPE method of requiring direct contact with the sample is compensated for by the fact that it yields easy-to-interpret thermal information that is not altered by optical properties of the sample (in the front-detection configuration). The surface temperature of a sample depends on the temperature field within the whole system. Analytical solutions can be found only for simple cases assuming 1-D heat propagation [17].

In general, a full 3-D characterization of the temperature field is necessary [18]. Various approaches have been extensively reported in the literature based on Fourier-optics analogy [6], on direct solutions in integral form [19] using Green's functions [20, 21], on the point spread function [22], or on finite-difference methods [13, 23]. In this work, a more versatile 3-D finite-element model was developed for the analysis of the thermal response of geometrically more complex systems. It allows to estimate the attainable lateral resolution in the measurement and to calculate surface temperature maps for geometrically complex systems with sub-surface flaws.

The SPPEM technique was applied for spatially localised analysis of delamination sites between organic coatings and metallic substrates. Experimental results are shown of measurements performed on model systems. The first one consists of an artificial air gap made in a polished stainless steel sample covered by a polymeric layer. The second one consists of a flat stainless steel substrate covered by an adhesive tape of which the adhesive layer was partially removed.

Next, SPPEM measurements performed on realistic systems are shown: a corrosion spot and surrounding disbonded region inside a polymer coated

drinking can, and a detail with possible starting points of corrosion on the uncoated drinking can substrate. It is demonstrated experimentally that it is possible to detect non-destructively and with a high spatial resolution small air gaps ($\leq 1 \mu\text{m}$) below polymeric coatings and to estimate their position below the surface.

11.2. Theoretical background

Heating of an isotropic solid by a periodically modulated heat flux results in general in a 3-D temperature profile $T(\mathbf{r},t)$ (depending on position \mathbf{r} and time t) which is the solution of the following heat diffusion equation:

$$\rho c \frac{\partial T(\mathbf{r}, t)}{\partial t} - k \nabla^2 T(\mathbf{r}, t) = Q(t) \quad (1)$$

where ρ is the specific density of the material, c is the specific heat capacity, k the thermal conductivity and $Q(t)$ the heat source. The PPE cell for the case considered here can be modelled by the schematic structure of Fig. 2. Because of the harmonic nature of the excitation: $Q(t) = Q_0[1 + \cos(\omega t)]/2$, the time- and space-dependent parts of the steady-state solution can be factorized as $T(\mathbf{r})\exp(j\omega t)$. In the absence of internal heat sources within the layers of Fig. 2,

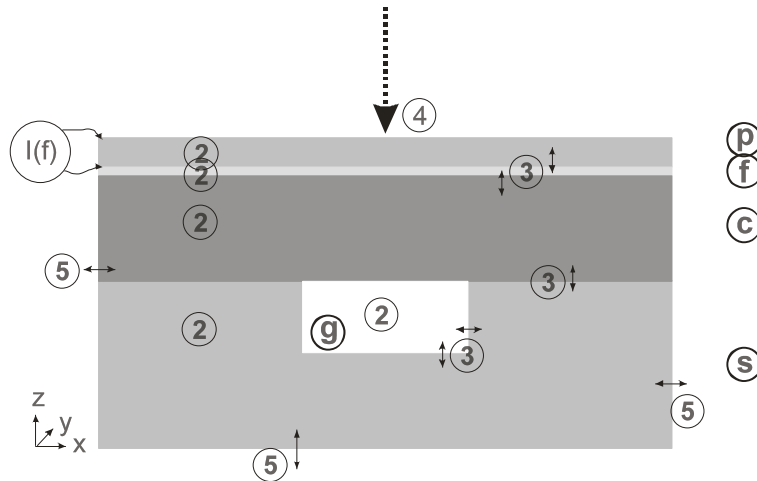


FIG. 2. Cross section of the considered system. The opaque PVDF sensor (p) is applied using coupling fluid (f) to the sample consisting of polymer coating (c) and steel substrate (s). The substrate contains an air gap (g) representing a local delamination. The PVDF sensor and underlying parts are locally heated using a modulated laser beam (indicated by arrow). The imaging feature is achieved by recording the PPE current $I(f)$ while scanning the laser spot over the surface. Numbers indicate locations where the respective equations apply for the finite-element model.

Eq. 1 becomes:

$$\nabla^2 T(\mathbf{r}) - j(\omega / \alpha)T(\mathbf{r}) = 0 \quad (2)$$

where $\alpha=k/\rho c$ is the thermal diffusivity of the respective layer and $\omega=2\pi f$ is the angular modulation frequency. It is reasonable to neglect ac heat exchanges with the ambient in Eqs. 1 and 2, as long as the system boundaries are far away as compared to the thermal diffusion length $\mu = \sqrt{\alpha / \pi f}$. It is assumed that transport of heat across the air gap occurs only by heat conduction.

For the determination of $T(\mathbf{r})$ additional boundary conditions must be specified for heat flux and temperature continuity at interfaces (ij) between layers, respectively:

$$\mathbf{n} \cdot (k_i \nabla T_i) = \mathbf{n} \cdot (k_j \nabla T_j) \quad \text{and} \quad T_i = T_j \quad (3a,b)$$

with \mathbf{n} the outward normalized unit vector. At the irradiated surface the heat flux is:

$$\mathbf{n} \cdot (k \nabla T) = Q_0 / 2 \quad (4)$$

with Q_0 the heat deposition. At the other outer boundaries of the model adiabatic conditions are considered:

$$\mathbf{n} \cdot (k \nabla T) = 0 \quad (5)$$

In Fig. 2, the locations are indicated where each of Eqs. 2-5 apply. The set of equations were implemented in the commercially available finite-element modelling software FEMLAB 2.1. For the modelling, it was assumed that the whole top sensor surface is irradiated by a uniform radiation flux, instead of the focused heating in the actual experiment. The finite-element calculation results in a full 3-D complex temperature profile across the modelled system in one computation step, and in particular in a 2-D temperature map of the sample surface below the sensor. In order to measure this temperature, the sensor must be thermally thin ($\mu_p > L_p$ with L_p the thickness of the PVDF sensor) meaning a low enough modulation frequency. Consider an element of the sample surface $\Delta A = \Delta x \Delta y$, centered at coordinates (x,y) . The current signal of the corresponding abovelying pyroelectric element is proportional to the time derivative of the temperature profile $T(z,t)$ averaged over the sensor thickness L_p [16]:

$$I(x, y) = \frac{j\omega p \Delta A}{L_p} \int_0^{L_p} T(z) dz \quad (6)$$

where p is the pyroelectric coefficient and $T(z)$ is the temperature field $T(\mathbf{r})$ averaged over the intervals Δx and Δy . As a result of the assumption of uniform radiation, the spatial resolution in the finite-element model will be limited to $\Delta A = \Delta x \Delta y \approx 2\mu_p$, due to lateral diffusion of heat. Consider now that in the actual experiment, the whole sensor surface area A is locally irradiated by a laser beam, having a cross-section smaller than ΔA . Also in this case, as a result of lateral diffusion of heat, the PPE signal is a measure of the local temperature averaged over a surface with a diameter of the order of $2\mu_p$. Therefore, the ensemble of signals $I(x, y)$ for all finite elements of the sensor can be determined in one numerical computation step yielding the theoretical surface map of the PPE signal.

Obtaining 3-D numerical solutions with the finite-element model may become calculation-intensive for complex systems. If the lateral dimensions of the defect are larger than μ_c and L_c (coating thickness), meaning the edges of the defect are far away, the use of a 1-D analytical solution is justified and probably more appropriate. In the publication related to this chapter, a set of Eqs. are derived for such a 1-D model. In Fig. 3, theoretically calculated

TABLE I. Thermal properties of PVDF sensor and of materials (at room temperature), composing the investigated samples

symbol in Fig. 2	material	density (ρ) (kg/m ³)	specific heat (c) (J/kgK)	thermal conductivity (k) (W/mK)	thermal effusivity (e) (W ^{1/2} s/m ² K)
(p)	PVDF polymer	1780	1260	0.13	530
(f)	silicon oil polymeric layer	845	2020	0.14	489
(c)	(polyolefi ne type)	1200	1300	0.15	484
(g)	air	1.2	1007	0.03	5.5
(s)	stainless steel	8238	468	13.4	7188

thermal wave amplitude and phase contrast plots are shown for an organic coating applied onto a steel substrate with air gaps of different thickness below the organic coating. These plots were calculated using this 1-D model. The vertical axes are ratioed with respect to the result obtained with no air defect present. The Figure shows that the air gaps are visible in the amplitude plot at very low frequencies and at much higher frequencies for the phase plot. In the actual experiment, the amplitude signal is however also influenced by local variations in roughness, absorption coefficient and laser power while the phase signal is not. Moreover, with a lower frequency, lateral resolution is lost which can be estimated to be $2 \mu_c$, see above. For this reason, the phase signal is most often used to study subsurface features [15]. At high frequency, (above ~ 10 Hz

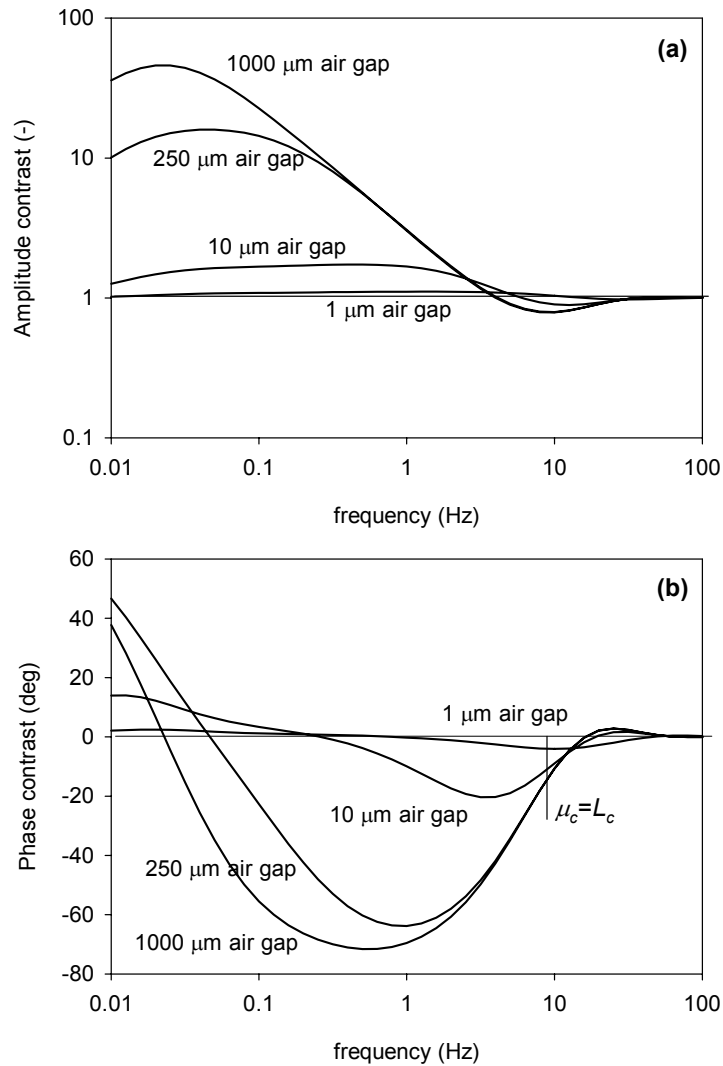


FIG. 3. PPE amplitude (a) and phase (b) of contrast plots, calculated using a 1-D analytical model. Results for different air gap thicknesses L_g embedded between 60 μm thick adhesive tape and 5 mm thick stainless steel substrate are shown.

where $\mu_c < L_c$) and at very low frequency, the air gap is not visible. The optimum frequency is in the region where $\mu_c \approx L_c$. It should be emphasized that an air gap of only $1 \mu\text{m}$ thickness produces a phase contrast of about 5 deg , which is readily detectable as will be shown further on.

11.3. Experimental set-up

The SPPEM set-up is shown schematically in Fig. 4. It is discussed in detail elsewhere [16]. The set-up consists of readily available components. The excitation source is a laser diode type LISA HL25/M2 emitting 5 mW at 635 nm , modulated in intensity at a given frequency by the reference oscillator of a DSP lock-in amplifier (Stanford Research model 850). The latter processes the PPE signal that is first fed to a current-to-voltage converter (Keithley model 428 with 10^8 V/A gain). The laser beam is guided through a normal optical microscope provided with a semi-transparent internal mirror positioned at 45 deg . By looking through the microscope, it is possible to inspect and locate the laser spot (minimum size is $20 \mu\text{m}$) at the sample surface. The sample is mounted on a x-y translation stage driven by stepping motors, which has a positioning accuracy of better than $1 \mu\text{m}$ over a surface of $5 \times 5 \text{ cm}$. The whole set up is controlled by PC computer using GPIB interfaces. Typical signals were in the range between 10^{-2} and 10^2 pA , requiring shielding the PPE cell with a copper grid.

The cross-section of the considered system is shown schematically in Fig. 2. The pyroelectric sensor of $1 \times 3 \text{ cm}^2$ was made of $9 \mu\text{m}$ thick PVDF polymer

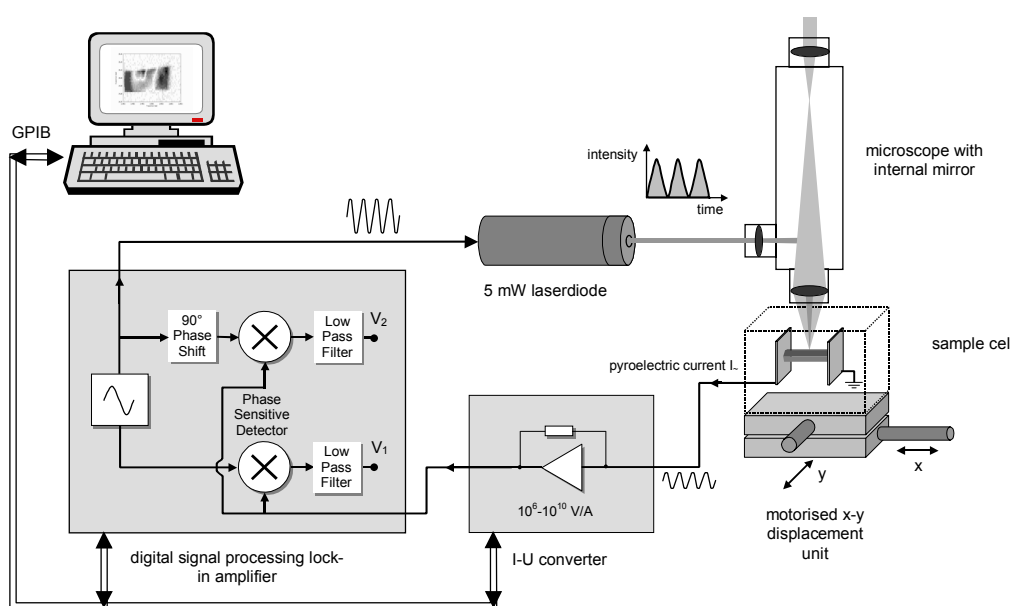


FIG. 4. Schematic of the different components of the SPPEM set-up

(produced by Solvay S.A., Brussels, Belgium) provided on both sides with vacuum-evaporated aluminium electrodes (approximately 40 nm thick), which can be neglected in the thermal transport analysis. Thin copper wires were attached by conductive epoxy adhesive (Comma Electrocure). The sensor was blackened on one side using a permanent marker. The backside was uniformly covered with a thin and homogeneous layer of silicon oil to ensure proper thermal contact. Subsequently, the sensor was applied to the surface of the sample and slightly moved laterally to remove possible air bubbles. The flexible PVDF foil followed the surface of the sample due to capillary forces exerted by the oil film. The latter had an estimated thickness of the order of few microns.

The thermal properties of materials composing the PPE cell are listed in Table 1 and were used for all theoretical simulations.

The metallic drinking cans that were investigated were made of chromium coated steel (ECCS). The production process consists of applying a thin chromium layer by electrolytic deposition for corrosion protection onto rolled steel sheet. Then, a transparent polymer coating with thickness of 40 μm is extruded directly onto the steel sheet. After deep-drawing to obtain the final product, the thickness of the polymeric coating reduces to 30 μm .

11.4. Results and discussion

11.4.1. Validation of finite element model

The first experiment aimed at checking the validity of the finite-element model in the simple case of the sensor attached directly to a flat and polished metallic substrate. In Fig. 5 one can see that within the experimental frequency range (limited by electronics) there is good agreement. The laser beam was defocused to a diameter of 100 μm only for this measurement in order to level out possible local inhomogeneities of the surface. The thickness of the coupling oil layer was a fit parameter in the numerical model. The best fit value $L_f = 2$ μm was considered in all subsequent simulations, despite the fact that L_f might be neglected when it couples the sensor to a polymer coating (from Table 1, silicon oil and polymer coating have practically the same effusivity).

The condition $\mu_p = L_p$ is satisfied at about 200 Hz. At higher frequency ($\mu_p < L_p$) the temperature oscillation is confined in the vicinity of the front face of the sensor and then Eq. 6 yields the maximum signal amplitude and phase $\varphi = 0$) [25].

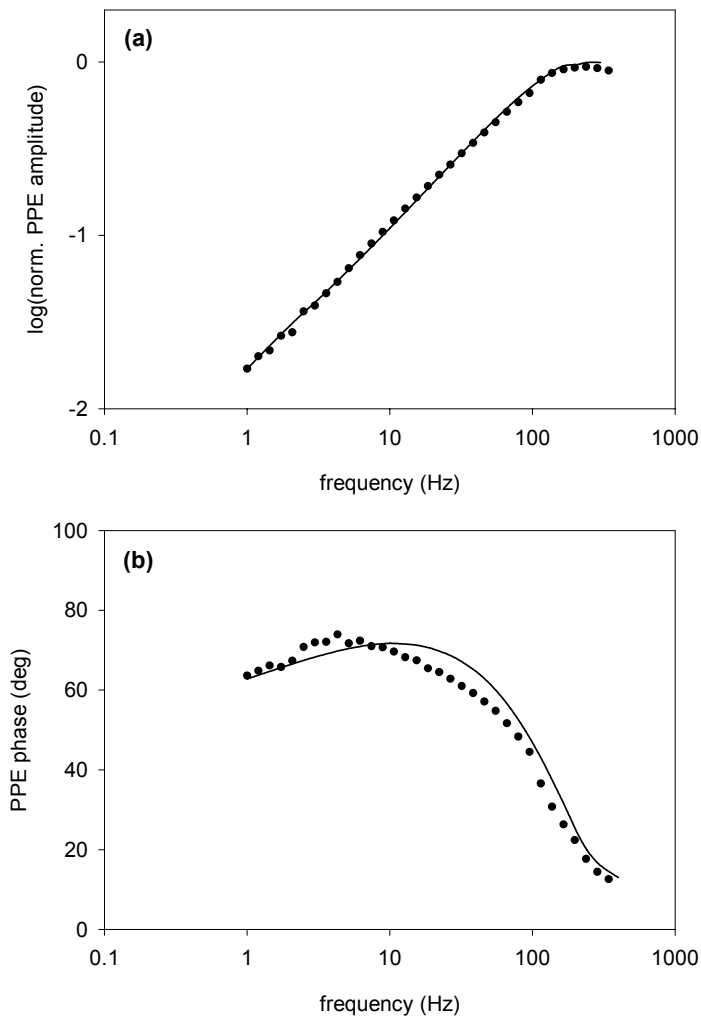


FIG. 5. Experimental signal amplitude (a) and phase (b) for PVDF sensor attached onto 5 mm thick stainless steel substrate (points) and simulation with the finite-element model (solid lines). Signals are normalized to their values at high frequency. The condition $\mu_p > L_p$ required by Eqs. 7-11 is satisfied below about 200 Hz.

The lateral resolution of the set up and the capability of the finite-element model to predict it were tested on an artificial defect. A circular cavity with a depth of 1 mm and a diameter of 2 mm was made by spark erosion into a similar stainless steel sample as above. A polymeric layer was applied onto it, thereby mimicking an air gap below an organic coating. In Fig. 6a,b the results are shown of SPPEM line scans across the diameter of the air gap and the simulations with the finite-element model, respectively. One can see that the trends of the experimental results and finite-element simulations as a function of frequency are similar. The measured contrast between the air gap and the surrounding phase level (Fig. 6a) is in good agreement with the 1D predictions

of Fig. 3. The finite-element curves (Fig. 6b) overestimate the contrast by about 20%. At 21 Hz and at 33 Hz the absolute measured phase is shifted by about

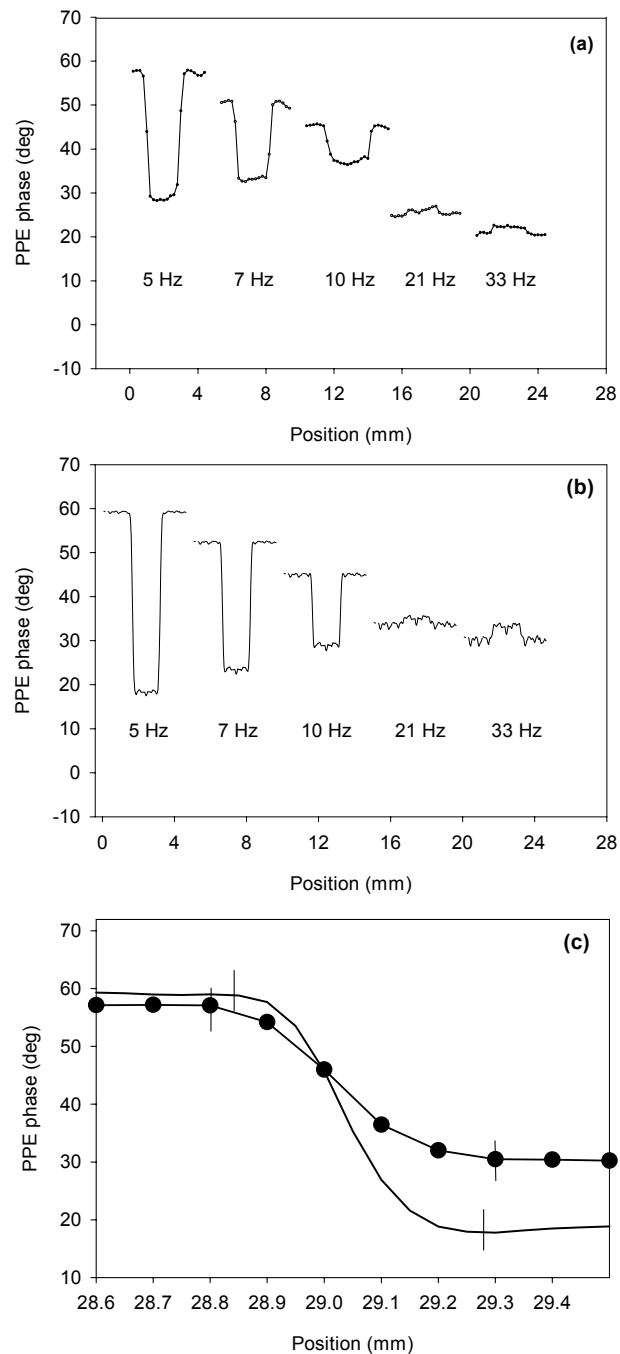


FIG. 6. Experimental (a) and simulated with the finite-element model (b) signal phase upon scanning a 2 mm in diameter artificial air gap. In (c) is shown a detail at the air gap - steel edge with both, experiment and finite-element model, at $f=5$ Hz. Sample structure consists of 60 μm thick adhesive tape, 1 mm thick air gap and 5 mm thick stainless steel substrate (see also Fig. 1). Experimental scanning step size is 100 μm . The positions of scans at different frequencies are shifted for clarity. The phase reversal with increasing frequency is consistent with Fig. 3.

-10 deg compared to the simulation, probably due to higher sensitivity of the signal to the detailed structure of the PPE cell at high frequency (coupling fluid, adhesive layer, accurate thickness of layers, thermal properties, etc.). Nevertheless, the contrast due to the presence of the air gap is not lost. The inversion that occurs between 10 Hz and 21 Hz is consistent with the zero-phase crossing point situated at 15 Hz in Fig. 3.

As discussed in the theoretical section, the lateral resolution for surface temperature imaging is limited to $2 \mu_c$. When imaging defects buried at the coating-steel interface the resolution is therefore degraded to some extent. In Fig. 6c details are shown of experimental and theoretical line scans across the edge of the artificial defect investigated in Fig. 6a,b.

At 5 Hz, $\mu_c = 78 \mu\text{m}$ and is slightly larger than L_c . From the theoretical curve, the lateral resolution (half distance of step function) is about $200 \mu\text{m}$. As expected because the sample does not have infinitely sharp edges like the numerical model, the experimental lateral resolution is larger, of about $250 \mu\text{m}$. At higher frequencies both, theoretical and experimental resolutions (determined from Fig. 6a,b) are somewhat better because μ_c decreases and the only limit remains is L_c .

11.4.2. Mapping of artificial subsurface defects

Next a surface mapping test was performed on a sample similar to the previous one. The artificial defect was a circular cavity with a depth of $250 \mu\text{m}$ and a diameter of $500 \mu\text{m}$ made by spark-erosion into the stainless steel substrate. Onto this, a $60 \mu\text{m}$ thick polymeric coating was applied. In Fig. 7a, the defect is clearly resolved with a phase contrast of about 17 deg. In the region surrounding the defect, some minor inhomogeneities are most probably present as the phase is not flat. At $f = 7 \text{ Hz}$, $\mu_c \approx L_c$ so that the theoretical and experimental lateral resolutions are practically the same as those determined in Fig. 6c. As a result, the apparent diameter of the defect at the level of the surrounding surface is about $800 \mu\text{m}$ (Fig. 7a). For comparison, on the phase surface computed with the finite-element model the diameter of the defect appears to be of about $700 \mu\text{m}$ (Fig. 7b). As for the line scans discussed in the previous section, the finite-element model overestimates to some extent the phase contrast, which also causes the defect to appear sharper in the computed plot.

A more realistic delamination defect consisted of an artificial blister made between an adhesive tape and the polished steel substrate by locally rubbing away the adhesive layer using a Q-tip soaked in ethanol, Fig. 8a. From the

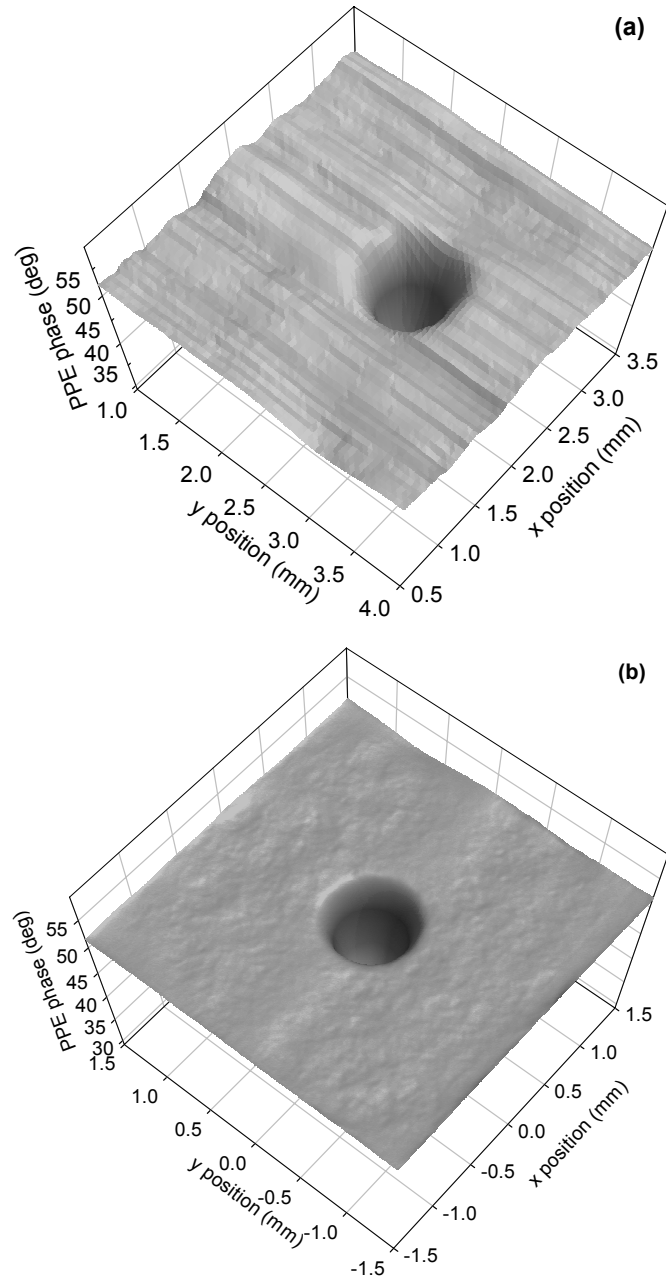


FIG. 7. Experimental (a) and simulated with the finite-element model (b) map of an artificial air gap ($500\ \mu\text{m}$ in diameter and $250\ \mu\text{m}$ thick) made in $5\ \text{mm}$ thick stainless steel substrate and covered by $60\ \mu\text{m}$ thick adhesive tape. Experimental scanning step size is $100\ \mu\text{m}$ and $f=5\ \text{Hz}$.

thickness of the locally removed adhesive layer one could estimate that the air gap trapped at the interface was approximately $10\ \mu\text{m}$ thick. The SPPEM surface map is shown in Fig. 8b. The contour of the region with the accumulated adhesive (on the left hand side) is clearly visible, but inside that region the phase does not differ from that of the surrounding background

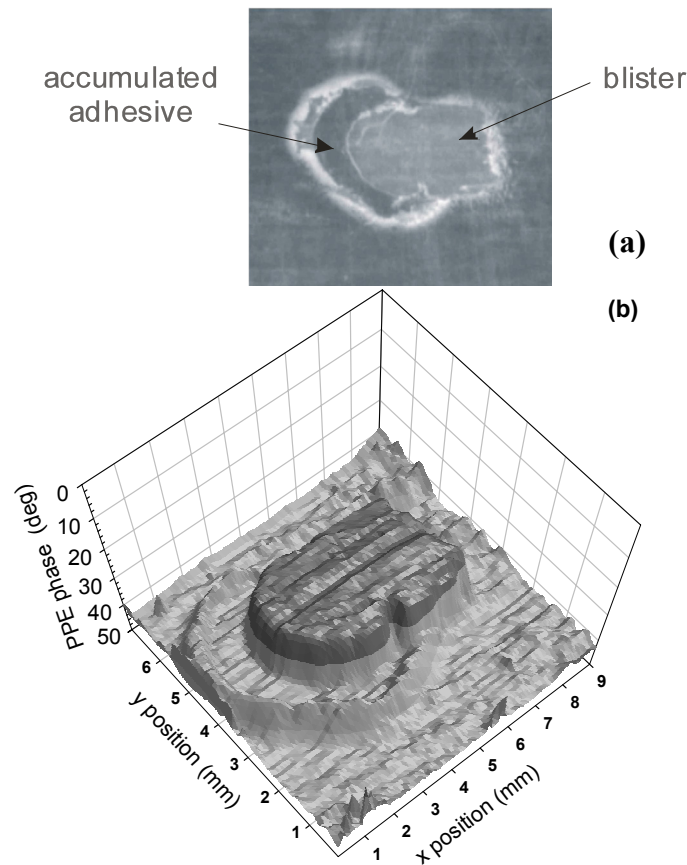


FIG. 8. Photograph (a) and measured phase map (b) of artificial blister (estimated $10\ \mu\text{m}$ thick air gap) between adhesive tape ($50\ \mu\text{m}$ thick without adhesive layer) and $5\ \text{mm}$ thick stainless steel substrate. Experimental scanning step size is $100\ \mu\text{m}$ and $f=10\ \text{Hz}$. Z-axis is reversed for clarity.

because there is still good contact between coating and steel layers. Unlike this, in the region with ablated adhesive the phase contrast is about $-15\ \text{deg}$.

This is in agreement with the calculated phase contrast for an air gap of $10\ \mu\text{m}$ (Fig. 3b) and corresponds to the thickness of the removed adhesive layer. This example shows that the SPPEM method is sensitive in the first place to delamination defects filled with air and to a less extent to variations of coating layer thickness.

11.4.3. Blisters and corrosion spots inside a drinking can

The last example is a real-life sample cut from a drinking can made of polymer-coated ECCS steel. After a sterilization test it was noted that several

corrosion spots appeared at seemingly random positions. Delamination regions were formed around some of them, probably due to mechanical pressure exerted by growing corrosion products that are porous and contain air voids, Fig. 9a. Fig. 9b shows the corresponding SPPEM phase map. At $f \cong 30$ Hz, $\mu_c \approx L_c = 30$ μm for this sample, which is the best trade-off between depth-profiling sensitivity and lateral resolution contrast. The corrosion products are clearly visualized by a more negative phase in the top right hand side of the plot.

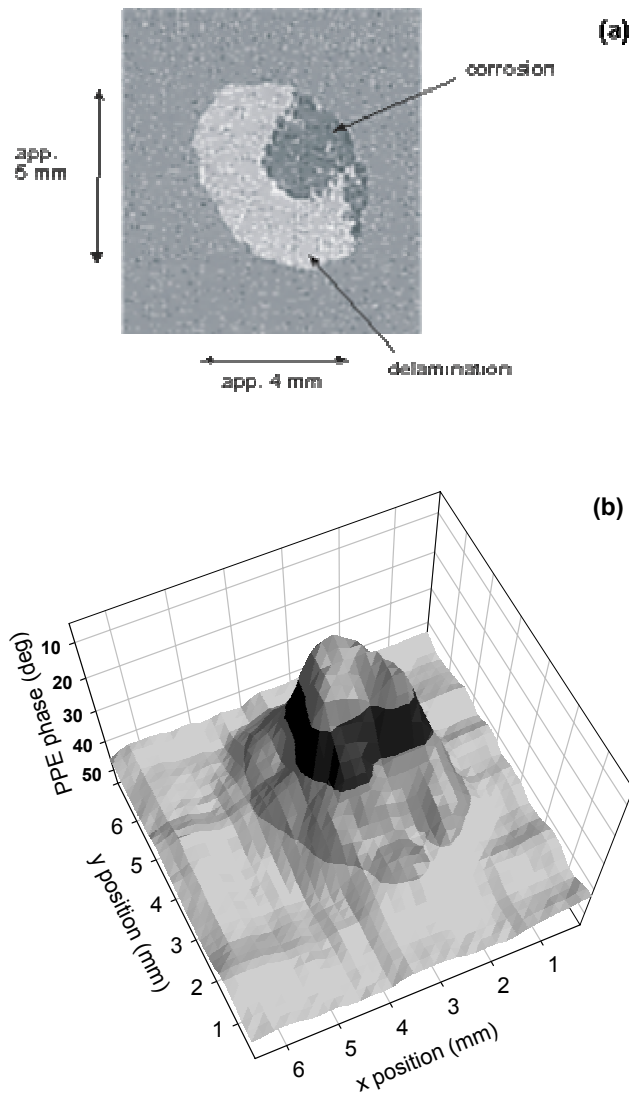


FIG. 9. Photograph (a) and measured phase map (b) of corrosion spot with surrounding delamination region inside drinking can. Sample structure consists of 30 μm thick polymer coating, some tens of microns thick air gap and 500 μm thick ECCS steel substrate (see also Fig. 1). Experimental scanning step size is 200 μm and $f=31$ Hz. Z-axis is reversed for clarity.

Based on the phase difference relative to the background, their thickness can be estimated to be of the order of some tens of microns. Surrounding this, the disbanded region can also be clearly distinguished.

The investigation of this sample was more difficult than the previously discussed model samples. The coating was somewhat lifted by the corrosion products and it might have been thinner or even discontinuous in that region. Furthermore, the sample as a whole was curved due to the fact that it was cut from a drinking can. However, the results prove that it is feasible to study

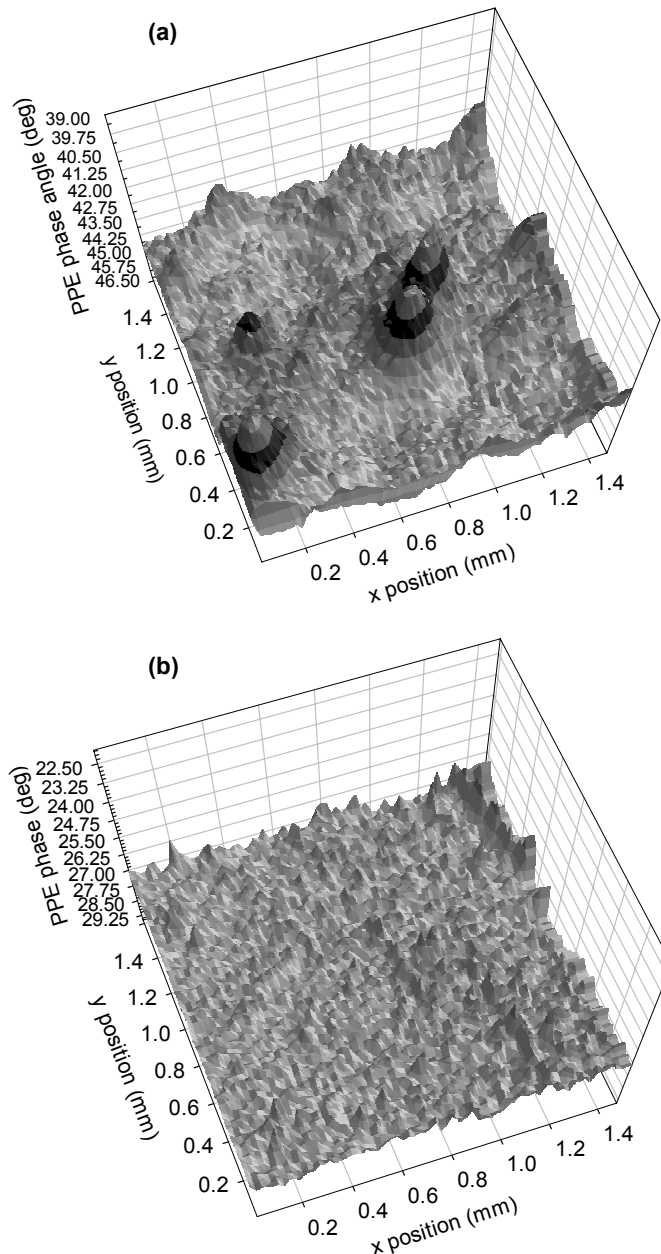


FIG. 10. Signal phase map of ECCS steel before the deep-drawing process, at 21 Hz (a) and 120 Hz (b). Sample structure consists of 40 μm thick polymer coating and 500 μm thick ECCS steel substrate (see also Fig. 1). Experimental scanning step size is 20 μm . Z-axis is reversed for clarity. See the text for details.

curved and/or rough surfaces using the SPPEM method. It should be noted that if the coating were not optically transparent, only the position of the corrosion products could be seen by optical methods, as a slightly lifted coating at that location. With the SPPEM, the fully disbonded region becomes visible. Although all measurements shown here were performed on optically transparent coatings, this is not a prerequisite for the method.

In search for an explanation for the apparently random development of corrosion spots, a small part of the polymer-coated ECCS material was investigated before the deep-drawing process. The SPPEM phase image recorded with the highest scanning resolution (20 μm) is shown in Fig. 10a. At $f \cong 20$ Hz, $\mu_c \approx L_c$ (in this case $L_c = 40$ μm) meaning again the best imaging conditions. The plot reveals some circular spots having a phase contrast of -3 ... -5 deg implying delamination of the order of 1 μm (see Fig. 3b). The apparent lateral size of the spots of approximately 100 - 200 μm is probably overestimated due to the limited lateral resolution. Phase images recorded at higher frequency (at 120 Hz where $\mu_c < L_c$) do not show these features (Fig. 10b), proving that the defects are situated at the coating-steel interface and neither inside the coating (i.e. air bubbles) nor underneath the PVDF sensor (i.e., small dust particles, etc.).

Figs. 11a,b show a line scan and a topographic image performed with an AFM (atomic force microscope) on the bare ECCS sample before application of the polymeric coating. As one can see, the substrate contains small indentations with lateral sizes in the range between 50 μm and 150 μm and average depths of 0.5 - 1 μm . The indentations are introduced in the surface by one of the rolling steps of the steel during its manufacturing. The size of the indentations is consistent with the air gaps determined from Fig. 10a using the SPPEM. By combining the theoretical and experimental SPPEM results with those obtained by AFM, one concludes that the small indentations produced in

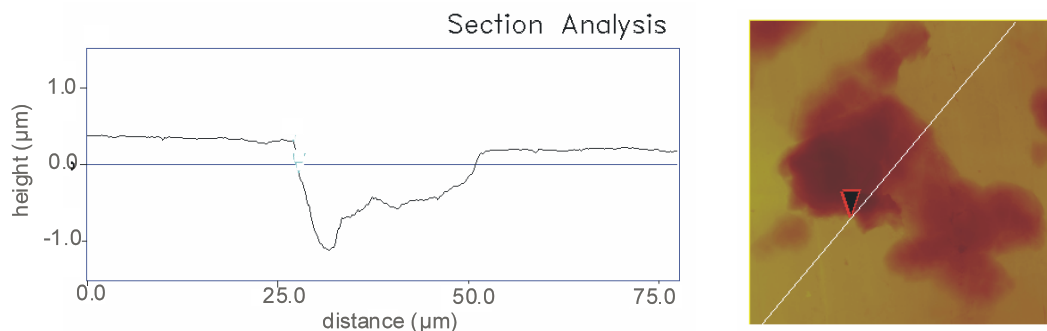


FIG. 11. Atomic force microscopy (AFM) height profile (left) and topographic image (right) of a typical indentation in the bare ECCS steel surface produced by sand blasting treatment before coating.

the steel substrate by the shot-blasting procedure are not completely filled with polymer in the coating process. This leaves air gaps at the coating-steel interface with dimensions of about 50 - 150 μm and depths of 0.5 - 1.0 μm . Water that penetrates through the coating can freely condensate in these indentations without the necessity to first break the adhesive bonds. If small defects exist in the protective chromium layer, for example due to the deep-drawing process, corrosion of the underlying steel can freely start. For this reason, it is very likely that the origin of the observed randomly occurring corrosion spots can be found in these air-filled gaps.

11.5. Conclusion

In this work the scanning photopyroelectric microscopy (SPPEM) method and instrument was investigated as a new imaging tool for non-destructive evaluation (NDE) and subsurface characterization of materials. It combines laser photothermal imaging with microscopy in a simple set up, using the photopyroelectric method in front detection configuration. The method requires direct contact between sensor and sample via a coupling fluid, but nevertheless it can be applied to curved samples with relatively rough surface, due to the use of a flexible PVDF polymer sensor. Unlike non-contact imaging photothermal methods, with the SPPEM the interpretation of results is facilitated by the fact that only the thermal properties of the sample have to be considered while the optical properties are irrelevant.

A 3-D finite-element model was developed and implemented in the commercially available FEMLAB software. This model allowed modelling complex and irregularly shaped systems and in particular, to predict the lateral resolution of the set up. The model was validated by comparison with measurements performed on well-defined polymer-coated steel substrates with artificial sub-surface defects. It was found that the model is well-capable of predicting the phase contrast maps and the attainable lateral resolution.

SPPEM maps were obtained on well-defined polymer-coated steel substrates, clearly showing the capabilities of the technique. Also, microscopic corrosion sites on the inner side of drinking cans were investigated. In combination with atomic force microscopy (AFM) data, the origin of the corrosion spots was identified. They arise from small air gaps trapped between the polymer coating and the steel substrate. The air gaps were found to be caused by small indentations in the ECCS substrate caused by the rolling process which apparently are not filled with polymer during direct extrusion.

References

1. Nguyen, T., *Materials Characterization*, 1992, 28, 291
2. Patel, P.M. *Applied Physics*. 1987 B-43, 9
3. Moksini, M. M. *Journals of Materials Science*. 1995 30, 2251
4. Parthasarathi, S. *Materials and Manufacturing Processes* 1995, 10, 1077
5. Busse, G.; Renk, K. F. *Applied Physics Letters* 1983, 42, 366
6. Vaez Iravani, M.; Wickramasinghe, H. K. *Journal of Applied Physics*. 1985, 58, 122
7. Rosencwaig, A. *American Lab* 1979, 11, 39
8. Nordal, P. E.; Kanstad, S. O. "Photothermal radiometry for spatial mapping of spectral and material properties", in *Scanned Image Microscopy*, E. A. Ash, ed. (Academic, London, 1980), p. 331.
9. Thomas, R. L.; Favro, L. D.; Grice, K. R.; Inglehart, L. J.; Kuo, P. K.; Lhota, J.; Busse, G. "Thermal wave imaging for nondestructive evaluation," in *Proceedings of the Institute of Electrical and Electronics Engineers Ultrasonic Symposium* (IEEE, New York, 1982), 586.
10. Busse, G.; Walther, H. G. in *Progress of Photothermal and Photoacoustic Science and technology*, A. Mandelis, ed., Vol. 1. (Elsevier, New York, 1992), 206.
11. Munidasa, M.; Mandelis, A. in *Progress of Photothermal and Photoacoustic Science and technology*, A. Mandelis, ed., Vol. 1. (Elsevier, New York, 1992), 300.
12. Luukkala, M. "Photoacoustic microscopy at low modulation frequencies", in *Scanned Image Microscopy*, E. A. Ash, ed. (Academic, London, 1980), 273
13. Petts, C. R.; Wikramasinghe, H. K. "Photothermal spectroscopy on a microscopy scale", in *Proceedings of the Institute of Electrical and Electronics Engineers Ultrasonic Symposium* (IEEE, New York, 1981), 832.
14. Mieszkowski, M.; Leung, K. F.; Mandelis, A. *Review of Scientific Instruments* 1989, 60, 306
15. Mieszkowski, M.; Mandelis, A. *Journal of the Optical Society of America*. A 1990, 7, 552
16. Wübbenhorst, M.; Turnhout, J. van; Quintel, A.; Hulliger, J. *Journal of Applied Physics* 2000, 88, 2108
17. Bozóki, Z.; Miklós, A. *Applied Physics Letters* 1994, 64, 1362
18. Mandelis, A. *Journal of the Optical Society of America*. A 1989, 6, 298
19. Aamodt, L. C.; Murphy, J. C. *Journal of Applied Physics* 1981, 52, 4903.
20. Padé, O.; Mandelis, A. *Inverse Problems* 1994, 10, 185
21. Thibaud, J.-B.; Carminati R.; Greffet, J.-J. *Journal of Applied Physics* 2000, 87, 7638
22. Seidel, U.; Haupt, K.; Walther, H. G.; Burt, J. A.; Munidasa, M. *Journal of Applied Physics* 1995, 78, 2050
23. O. O. Diniz Neto and C. A. S. Lima, *J. Phys. D: Applied Physics* 1994 27, 1795.
24. Mandelis, A.; Zver, M. M. *Journal of Applied Physics* 1985, 57, 4421
25. Chirtoc, M.; Mihailescu, G. *Physical Review* 1989, B40, 9606
26. Chirtoc, M.; Antoniow, J. S.; Egée, M. Photoacoustic and Photothermal Phenomena X-th Int. Conf., Rome, Italy 1998, Conference Proceedings 643, F. Scudieri and M. Bertolotti, Eds., (American Institute of Physics, Woodbury, New York, 1999) 84-86.
27. *Handbook of Chemistry and Physics*, 78th ed. edited by D. R. Lide, CRC, Boca Raton, Florida, 1998.
28. Gerliczy, G.; Betz, R. *Sensors and Actuators* 1987, 12, 207-233

GENERAL OVERVIEW AND DISCUSSION.

In Chapters 3 until 7 of this thesis, an investigation was performed of how polymers in general bond to aluminium oxide surfaces, how this is influenced by the chemistry of the oxide surface and whether the bonds that are formed are stable in the presence of water.

In Chapter 3, an angle-resolved XPS investigation was performed to determine the amount of hydroxyls on five differently pretreated aluminium substrates. These surface treatments were an alkaline and an acidic pretreatment, oxidising of aluminium in vacuum, dehydroxylation of aluminium at 275 °C and boiling in water, resulting in the formation of a pseudoboehmite oxyhydroxide layer. The same set of different pretreatments was used throughout Chapters 3 until 7. To determine the amount of hydroxyls, restricted curve-fitting of the O 1s core level peak was performed and by using an additional method, it was demonstrated that the used restrictive fitting procedure provides correct and accurate results.

The differently pretreated aluminium substrates were found to be enriched in hydroxyls towards their surface region and showed clear variations in the amount of hydroxyls on their surfaces. The highest hydroxyl fraction was obtained for pseudoboehmite, namely 50% (of the total oxygen content present on the oxide layer surface), corresponding well to its composition, AlOOH. Below that was the alkaline pretreated aluminium, which had a hydroxyl fraction of 43% on its surface. The lowest hydroxyl fraction was found for dehydroxylated aluminium, which had a hydroxyl fraction of 9%, see Chapter 5.

In Chapter 4, the same set of differently pretreated aluminium substrates were investigated with respect to the acid-base properties of the Al, O and OH sites on their surfaces. For this purpose, the shifts in the O 1s and Al 2p core level binding energies were evaluated, while taking into account the factors that might contribute to this.

It was found that for *structurally comparable* oxides, the core level binding energies can be *directly* used to evaluate the acid-base properties of the various surface sites. Despite that quite different pretreatments were used to prepare the different aluminium substrates it was, quite surprisingly, found that their Al, O and OH sites had the same acid-base properties. The pseudoboehmite oxide deviated, having more basic Al, O and OH sites on its surface. This could

be explained by the fact that the localised coordination structure in this oxide is different from the other oxides.

The aim of Chapters 5 and 6 was to study the same set of pretreated aluminium substrates with respect to their bonding with polymers. To allow for a detailed investigation, a model adhesion compound approach was followed. A given polymer is simplified to a small molecule, containing the same, for bonding relevant, functional groups. The compounds were adsorbed on the aluminium substrates as a thin layer. Subsequently, bonding of the compounds was studied using infrared reflection absorption spectroscopy (FTIR-RAS). The bonding of two general classes of organic functional groups was investigated: functional groups capable of *chemisorption* with the oxide surface and functional groups capable of *physisorption*. From a macroscopic adhesion point of view, chemisorptive bonding is preferred over physisorptive bonding because the bonding energy is roughly an order of magnitude larger. Model compounds based on carboxylic acids were chosen to represent functional groups capable of chemisorption and model compounds based on ester groups were chosen to represent functional groups capable of physisorption.

Despite the different surface treatments, the organic functional groups interacted very similarly with the different substrates. The carboxylic acid functional groups reacted to form a (strongly) *chemisorbed* carboxylate and the ester functional groups showed (weaker) *physisorptive* bonding. This corresponds well with the XPS measurements discussed in Chapter 4, where it was demonstrated that the sites on the different oxide layer surfaces have in fact the same acid-base properties. Surprisingly however, also bonding with the pseudoboehmite type of oxide was found to be the same as for the other oxides, while this oxide was found to have more basic hydroxyls. This discrepancy was ascribed to the fact that in XPS not the true outer surface, but approximately the outer five Al-O layers are being investigated and so also a portion of the internal hydroxyls are being measured, which for pseudoboehmite have deviating properties as a result of internal hydrogen-bonding.

Clear differences were found among the differently pretreated substrates with respect to the *amount* of organic functional groups that could bond to their surfaces. It was found that the substrates with more hydroxyls on their surfaces were capable of bonding both more carboxylic and also more ester functional groups. This clearly showed that interaction of both classes of organic functional groups occurs through the hydroxyls on the oxide surface. It is believed that this can be extrapolated and that most probably all organic functional groups will interact with the studied aluminium substrates through

their hydroxyls. It is sometimes suggested in the literature that interaction of organic functional groups with ambient-exposed aluminium substrates can also occur through incompletely coordinated cations, which would be much stronger bonding sites than the hydroxyls. However, despite that a range of differently pretreated aluminium substrates was investigated, no evidence could be found supporting this. It is believed here that although incompletely coordinated cations can be present on the oxide surfaces of strongly dehydroxylated oxide layers and under vacuum conditions, they rapidly react away with water and oxygen when exposed to the ambient.

Based on these results it can be concluded that with the studied, relatively simple but commonly used surface treatments, it is not possible to achieve a different type of bonding with the studied organic functional groups. However, the *amount* of bonds that can be formed can be modified through the amount of hydroxyls on the oxide surface. For this reason, for optimal bonding between a polymeric overlayer (e.g. a coating or an adhesive) and an aluminium oxide surface, one should try to maximise the number of hydroxyls on the oxide surface through a suitable surface treatment. A very elegant and simple surface treatment by which such a surface can be obtained is considered to be boiling in water, with which the studied pseudoboehmite oxyhydroxide layer is obtained.

The fact that bonding of organic functional groups proceeds through hydroxyls probably also has implications for the durability of the macroscopic bond between a polymeric overlayer and an aluminium oxide surface. The interfacial area between an aluminium substrate with a low number of hydroxyls and a polymeric overlayer will likely be a ‘patchwork’ of sites at which there is no bonding and sites at which there is organic functional group/hydroxyl interaction. At sites where there is no bonding, water can be imagined to be capable of freely condensating, causing the onset of macroscopic delamination of the polymer.

Both the chemisorbing carboxylic acid and the physisorbing ester functional groups were found to *not* give an absolutely stable bonding with the aluminium oxide surface in the presence of water. Differences among the oxides were not observed. Some differences in bonding stability of the different studied compounds were however observed. A chemisorbed *monocarboxylic acid* model compound was rapidly displaced by water but a chemisorbed *bicarboxylic acid* could resist water for a prolonged period. A physisorbed *bifunctional ester* was rapidly displaced by water, but a physisorbed *tetrafunctional ester* showed a better stability, although not as good as the bicarboxylic acid. A molecule thus

shows a better bonding stability when it can form more bonds with the oxide surface. These differences are considered to be a purely kinetic effect. With more bonds per molecule, more bonds need to be displaced simultaneously by water before the whole molecule can be displaced from the surface. This also directly applies to polymers. For a polymer, a large number of bonds with the oxide surface need to be simultaneously displaced by water before delamination occurs. The limited stability of the adsorbed molecules however demonstrates that eventually this will happen. The results indicate some differences in bonding stability between the carboxylic acid and the ester functional group. The carboxylic acid based molecule with two chemisorptive bonds with the oxide surface shows a stable bonding, while an ester molecule having four physisorptive bonds with the oxide surface does not show a stable bonding. This implies that a polymer, capable of chemisorption, will show a more water-stable bonding with an aluminium oxide surface than a polymer only capable of physisorption. For this reason, when selecting polymers for organic overlayers, for an optimal adhesion performance, one should select polymers capable of chemisorption.

In Chapter 7 it was demonstrated that an initially ‘clean’ aluminium oxide surface, exposed to the ambient atmosphere, quite rapidly adsorbs air-borne contamination and water. These adsorbed species cannot be displaced anymore using solvents, as are widely used in industry to clean metallic substrates. It was found that within 20 hours of ageing in the ambient, the oxide surface was found to have irreversibly lost 60% of its initial bonding capacity towards organic functional groups. This has a direct influence on the adhesion of applied polymeric overlayers. As a result of the adsorbed species, the interfacial region between the polymeric overlayer and the substrate will be a patchwork of sites at which there is bonding and sites at which there is no bonding because contamination is strongly adsorbed on the oxide surface. Water can be imaged to be capable of freely condensating at the non-bonding sites, causing the onset of macroscopic delamination of the polymeric overlayer.

From an experimental point of view, the combined use of infrared spectroscopy for studying bonding of organic molecules and XPS for studying the chemistry of the aluminium oxide surface is considered to be the most suitable for the kind of research performed in this thesis.

This thesis is considered to clearly demonstrate that infrared spectroscopy can be used to study the type of bonding with the oxide surface for a wide range of organic functional groups. The technique is comparably cheap, easy to

employ, does not require a vacuum environment and is non-destructive. It allows to readily distinguish between esters and carboxylates and can also determine their bonding with the oxide surface. Studying bonding with for example XPS is considered to be less accurate. All oxygen-functionality (including that of the oxide) will be contained in the O *1s* core level peak and all carbon-functionality in the C *1s* core level peak. Accurate curve-fitting and detailed knowledge of the peak positions is then a requirement. The results in Chapter 3 on the hydroxyl concentration determination show that already for the oxide layer itself, this is not an easy task.

For the quantitative determination of the composition and chemistry of the oxide layer, the XPS is however very suitable, as was demonstrated in Chapters 3 and 4. It should however be kept in mind that even under the experimental conditions at which maximum surface sensitivity is obtained, still the outer 5 Al-O layers are being investigated. This turned out to be a disadvantage in the current thesis for the determination of the acid-base properties of the pseudoboehmite type of oxide layer, see above. FTIR is considerably less suitable for this purpose. For example, hydroxylation of the oxide layer only shows up as broad shoulders around the main Al-O peak, see for example Chapter 5 and information on the amount of hydroxylation cannot be readily obtained.

Some points were not addressed in this model compound and oxide layer work, which might be suitable topics for future research. First, the bonding of model compounds was only studied with a 99.5% pure AA1050 aluminium alloy. In practice however, alloyed aluminium is often being used. Alloys can for example have exposed precipitates, intermetallics and magnesium enrichment at their surfaces. On these sites, the bonding with the polymeric overlayer can deviate from that of the aluminium matrix. It might for example be that certain types of sites have a significantly lower bonding capacity than the aluminium matrix. A polymeric organic overlayer will then macroscopically only bond weakly at the position of these sites, generating starting sites for macroscopic delamination of a polymeric overlayer. An investigation of these phenomena requires the use of analytical methods, which are capable of performing spatially highly localised measurements, like a Scanning Auger Microscope.

Promising replacements for commonly used corrosion-improving surface treatments are self-assembling monolayers (SAM's). A SAM layer is made by adsorbing small aliphatic organic molecules on the surface which forms a closely packed, dense monolayer. This layer prevents the penetration of water and aggressive ions like chlorides, hence protecting the metal surface towards

corrosion. Moreover, the layers are also considered suitable for improving bonding between an organic polymeric overlayer and a metallic substrate. In this case, the molecules are chosen to have two functional end groups, separated by a central aliphatic spacer. Although also in this thesis thin organic layers were investigated, a translation towards SAM's has not been made. For example, the structural organisation of the adsorbed model compounds was not investigated and the extent of surface coverage was also not determined. The work performed in this thesis is however considered to provide a good starting point for such an investigation.

In Chapter 9 until 11, adhesion and delamination is investigated for polymeric overlayers on metallic substrates.

In Chapter 9, the adhesion of a typical epoxy-coated aluminium system was investigated for exposure to water of different exposure temperatures. The coating was found to quite rapidly lose its adhesion upon exposure to water. At higher exposure temperature, this occurred faster and more extensively. This rapid loss of adhesion corresponds well with the results in Chapter 8, where it was demonstrated that the studied epoxy-coating only bonds through physisorptive hydrogen-bonding and these bonds are not stable in the presence of water. After the initial loss, the adhesion of the coating was however found to recover again and even exceeded the adhesion prior to exposure. At a higher exposure temperature, the extent of adhesion improvement was larger. The improvement could be ascribed to the growth of a thin oxyhydroxide layer on the aluminium substrate, which forms a new, water-stable and stronger bond with the epoxy coating. Generally, in the structural adhesive bonding industry, the formation of an oxyhydroxide layer in an adhesive bond is considered to be detrimental. The differences with the epoxy-coated aluminium studied in this thesis can likely be found in large differences in initial adhesion strength. Structural adhesives are heavily chemically modified and as a result bond strongly with the oxide surface. If an oxyhydroxide layer is formed in this system as a result of exposure to water, also here the bond with the adhesive is expected to further improve. However, the adhesion of the oxyhydroxide layer on the aluminium substrate becomes the weakest link in the system. System failure then occurs at a lower than the initial strength with the detachment of the oxyhydroxide layer from the substrate. In contrast, the studied, chemically unmodified, epoxy coating only gives very low initial adhesion strength. Improvement of adhesion occurs with the epoxy but not so extensively that the

adhesion between the oxyhydroxide layer and the aluminium substrate becomes the weakest link.

In general, the immersion of polymer-coated aluminium in hot water, resulting in adhesion improvement, is considered to be a very elegant method of improving the adhesion. For example, deformation of a polymer-coated substrate is known to cause large interfacial stresses or even delamination of the polymer. It might be possible to 'recover' the adhesion of the substrates by immersion in hot water.

Although the adhesion improves upon exposure to water, the initial stage of loss of adhesion should be prevented, because it could for example allow diffusion of chlorides across the interface for exposure of not intact coatings to chloride-containing solutions. Based on the knowledge acquired throughout the thesis, in Chapter 10, two methods were followed to improve the adhesion performance of the epoxy coated-aluminium system. The methods were deliberately chosen to be easy to apply and without requiring a chemical modification of the epoxy coating.

Because the epoxy-coating only bonds through physisorption with the oxide surface, see Chapter 8, it appears logical to try to improve the adhesion by modifying the system so that the epoxy-coating bonds forms a chemisorptive bond with the oxide surface, which was found to be more stable in presence of water, see above. To achieve this, in the first method of adhesion improvement, an interfacial polymeric layer, having a thickness of around 10 nm, is added between the epoxy coating and the aluminium substrate. The functional groups of this thin interfacial layer were chosen to be able to chemisorb on the oxide surface but also to be capable of being involved in the curing reaction with the epoxy coating, hence strongly linking epoxy and aluminium substrate together. Polymeric interfacial layers based on anhydride, carboxylic acid and phosphonic acid functional groups were chosen for this purpose. The best adhesion performance was obtained using the anhydride based polymeric interfacial layer. The layer was involved in the curing reaction with the epoxy coating and a cured and mixed epoxy/polymer interphasial region was formed. The other two polymers also showed involvement in the epoxy curing reaction, but a weakly cured mixed epoxy/polymer interphasial region was formed. As a result, for the other two polymers, the adhesion performance of the system as a whole was only limitedly improved or even showed a decrease. Although not attempted, by optimising the curing parameters, also for these two other polymers it might be possible to form a well-cured interphasial region. The results obtained for the other two polymers emphasize the disadvantages of this method of adhesion

improvement. Adding an extra layer also causes the addition of extra uncertainties in the system. The same types of interfacial polymeric layers are considered to be also useful to improve the adhesion performance for other types of polymeric overlayers.

In the second method of adhesion performance improvement, the aluminium substrates were hydrated by immersion in boiling water, prior to application of the epoxy, resulting in the formation of a pseudoboehmite oxyhydroxide layer. This surface treatment was also studied in Chapters 3 until 6 of this thesis, and was identified as being very suitable for giving a good adhesion performance because of the large number of hydroxyls on the surface, see above. Additionally, the pseudoboehmite layer is very porous, providing the capability of improvement of adhesion performance through mechanical interlocking between epoxy-coating and aluminium substrate. The studied epoxy coating was found to be capable of fully penetrating the porous layer. The pseudoboehmite-based system showed a very good adhesion performance, which was even better than the results obtained with the polymeric interfacial layers. Apparently, although a chemisorbed bond is not formed with the oxide surface, this is compensated by the other beneficial properties of the pseudoboehmite layer.

In Chapter 11 of this thesis, a new experimental technique was discussed, which is capable of studying delamination with a high spatial resolution. The technique is based on the transport of thermal waves through matter and their reflection at buried interfaces. In the Chapter, it was shown that the technique can very accurately study localised, macroscopic delamination. Some model samples and also more realistic samples were studied to demonstrate the capabilities of the technique. Optically invisible delamination spots, having a size of 100 μm were clearly identified on the inside of a drinking can. These spots were due to holes on the steel substrate which were not filled with polymer during the application process. In these delamination spots, water can freely condensate, making them likely starting points for corrosion occurring beneath the organic coating.

SUMMARY.

The aim of this PhD work was to obtain knowledge on the adhesion between polymers and aluminium and the influence of water on this.

The first part of this thesis (chapters 3 until 8) describes a relatively fundamental investigation of these phenomena. With the current experimental techniques it is not possible to directly investigate the metal-polymer interface. For this reason, a model approach was followed in which the polymer is simplified to a molecule, having the same, for adhesion relevant, functional groups. This molecule is adsorbed on the aluminium oxide surface as a thin layer. It is then possible to directly investigate the bonding between the molecule and the oxide surface. The model investigation focussed on some specific aspects. First, it is investigated how polymers in general bond with the aluminium oxide surface. Also, the relation is investigated between the composition and chemistry of the oxide surface and the way this influences bonding of the polymers. Finally, it is investigated whether the bond between the polymer and the aluminium oxide surface is stable in the presence of water. The investigation shows that specifically the hydroxyls (OH) on the oxide surface are crucial for the adhesion between polymers and aluminium. The investigation has also shows that the bonds between the polymer and the oxide surface are only limitly stable in the presence of water.

The second part of the thesis (chapters 9 and 10) describes an investigation into adhesion and loss of adhesion in the presence of water for a real epoxy coating on an aluminium substrate. This system is commonly found in drinking cans, cars and planes. The investigation shows that the epoxy/aluminium adhesion is not stable in the presence of water and that already quite rapidly a significant amount of water accumulates at the interface. After the initial loss however, the adhesion recovers and becomes even better than prior to exposure. This is due to the formation of a very thin oxyhydroxide layer on the aluminium substrate, as a result of the reaction between aluminium and water. The initial loss of adhesion should be prevented in practice. For this reason, two different methods were followed to improve the adhesion and durability between the epoxy coating and the aluminium substrate. This resulted in the development of two types of epoxy-coated aluminium systems, having an improved adhesion and durability. Finally, in this thesis, a new experimental technique is discussed, based on a focussed laser beam, which is very suitable for

studying delamination between polymeric coatings and metallic substrates with a high spatial resolution.

SAMENVATTING.

Het doel van dit promotie-onderzoek was het verkrijgen van kennis op het gebied van de hechting tussen polymeren en aluminium en de invloed die water hier op heeft.

Het eerste stuk van het proefschrift (hoofdstukken 3 tot en met 8) beschrijft een relatief fundamenteel onderzoek hiernaar. Met de huidige experimentele technieken is het niet goed mogelijk om direct op het grensvlak tussen een polymeer en een metaalsubstraat te kijken. Om dit toch mogelijk te maken is een modelbenadering gevolgd, waarin het polymeer wordt vereenvoudigd tot een enkel modelmolecuul met dezelfde, voor hechting relevante, functionele groepen. Dit modelmolecuul wordt vervolgens geadsorbeerd op het aluminium-oxide oppervlak als een zeer dun laagje. Hiermee is het mogelijk om de binding tussen het molecuul en het oxide oppervlak te bestuderen. Het model-onderzoek heeft zich op een aantal punten geconcentreerd. Allereerst is onderzocht hoe polymeren in het algemeen met aluminium-oxide oppervlakken binden. Ook is de relatie onderzocht tussen de samenstelling en chemie van het oxide oppervlak en de manier waarop dit de binding met het polymeer beïnvloedt. Tenslotte is onderzocht of een binding tussen een functionele groep in een polymeer en een aluminium oxide oppervlak stabiel is in aanwezigheid van water. Het onderzoek heeft aangetoond dat met name de hydroxyl (OH) groepen aan het oxide oppervlak van cruciaal belang zijn voor hechting tussen polymeren en aluminium. Daarnaast heeft het onderzoek ook aangetoond dat de bindingen tussen een polymeer en een aluminiumsubstraat beperkt stabiel zijn in aanwezigheid van water, maar na verloop van tijd loslaten.

Het tweede stuk van het proefschrift (hoofdstukken 9 en 10) beschrijft een onderzoek naar hechting en verlies van hechting onder invloed van water voor een echte epoxy-coating op een aluminium substraat. Dit systeem komt veelvuldig voor in de praktijk, bijvoorbeeld in aluminium blikjes, auto's en vliegtuigen. Het onderzoek laat zien dat de epoxy/aluminium binding niet stabiel is bij blootstelling aan water en dat er zich al vrij snel significante hoeveelheden water ophopen op het grensvlak. Na dit initiële verlies herstelt de hechting zich en wordt zelfs beter dan voor blootstelling aan water. Dit is het gevolg van de groei van een dun hydroxide-laagje op het aluminium substraat door de reactie tussen aluminium en water. Het initiële verlies van hechting moet in de praktijk voorkomen worden. Er zijn daarom 2 methodes toegepast om te zorgen voor een sterkere en meer stabiele hechting tussen de epoxy-coating en het aluminium substraat. Dit resulteerde in twee typen van epoxy-

gecoate aluminium systemen met een significant betere hechting en duurzaamheid. Tenslotte wordt in dit proefschrift nog een nieuwe meettechniek besproken die zeer geschikt is om met een hoge resolutie macroscopische onthechting tussen polymeren en metaalsubstraten te onderzoeken, met behulp van een gefocusseerde laserbundel.

PUBLICATIONS.

Scientific papers.

J. van den Brand, M. Chirtoc, M. R. Wubbenhorst, and J. H. W. de Wit. "Photothermal imaging of localized delamination between organic coatings and metallic substrates using a scanning photopyroelectric microscope". *Journal of Applied Physics* 93(4),2019-2027, 2003.

J. van den Brand, W. G. Sloof, H. Terryn, and J. H. W. de Wit. "Correlation between hydroxyl fraction and O/Al atomic ratio as determined from XPS spectra of aluminium oxide layers". *Surface and Interface Analysis* 36 (1),81-88, 2004.

J. van den Brand, P. C. Snijders, W. G. Sloof, H. Terryn, and J. H. W. de Wit. "Acid-base properties of aluminium oxide surfaces as studied using XPS". *Journal of Physical Chemistry B* 108 (19),6017-6024, 2004.

J. van den Brand, O. Blajiev, P.C.J. Beentjes, H. Terryn and J. H. W. de Wit. "Interaction of anhydride and carboxylic acid compounds with aluminium oxide surfaces". *Langmuir*, 20(15), 6308-6317, 2004.

J. van den Brand, O. Blajiev, P. C. J. Beentjes, H. Terryn and J. H. W. de Wit, "Interaction of ester functional groups with aluminium oxide surfaces". *Langmuir*, 20(15), 6318-6326, 2004.

J. van den Brand, S. van Gils, P. C. J. Beentjes, H. Terryn, and J. H. W. de Wit. "Ageing of aluminium oxide surfaces and their subsequent reactivity towards bonding with organic functional groups". *Applied Surface Science* accepted for publication, 2004.

J. van den Brand, S. van Gils, H. Terryn, W. G. Sloof, and J. H. W. de Wit. "Changes at the epoxy-aluminium interface due to exposure to water". *Progress in organic coatings*, accepted for publication, 2004.

J. van den Brand, S. van Gils, P. C. J. Beentjes, H. Terryn, and J. H. W. de Wit. "Improving the adhesion between epoxy coatings and aluminium substrates by either using thin polymer layers or by hydration of the aluminium". *Progress in organic coatings*, accepted for publication, 2004.

J. van den Brand, H. Terryn and J.H.W. de Wit. "Interaction between carboxylic acid based model adhesive molecules and aluminium substrates with different surface treatments", *ATB Metallurgy*, 43(1-2),72-78, 2003

S. van Gils, J. van den Brand, C.A. Melendres, H. Terryn and E. Stijns, "Chemical composition of thin oxide films on aluminium studied with infrared and visible spectroscopic ellipsometry", *ATB Metallurgy*, 43(1-2),66-71, 2003

V. G. M. Sivel, J. van den Brand, W. R. Wang, H. Mohdadi, F. D. Tichelaar, P. F. A. Alkemade, and H. W. Zandbergen. "Application of the dual beam Focused Ion Beam to metals research" *Journal of Microscopy*, 214(3), 237-245, 2004

Presentations, poster presentations and proceedings.

J. van den Brand, H. Terryn, J.H.W. de Wit, "Interaction of carboxylic acid and ester functionalized model adhesion compounds with different aluminium oxide layers", ECASIA 2003, 5-10 October 2003, Bonn, Germany, Poster

J. van den Brand, H. Terryn, J.H.W. de Wit, "Interaction between carboxylic acid based model adhesion molecules and aluminium substrates with different surface treatments", The 3rd Conference on Aluminium Surface Science and Technology (ASST 2003), Bonn, Germany, 18-22 May 2003, Oral presentation

J. van den Brand, H. Terryn, J.H.W. de Wit, "Interaction between model adhesion molecules and aluminium oxide surfaces", University of Paris, Paris, France, 28 april 2003, Oral presentation

J. van den Brand, H. Terryn, J.H.W. de Wit, "Undercoating hydration in aluminium-epoxy systems due to exposure to water", XXVI FATIPEC Congress on "Quo Vadis - Coatings", Dresden, Germany, 9-11 September 2002, Oral presentation

J. van den Brand, H. Terryn, J.H.W. de Wit, "Undercoating hydration in aluminium-epoxy systems due to exposure to water", Building Bridges in Metallurgy, NIMR Conference, Noordwijkerhout, 8-9 December 2001, Oral presentation

S. van Gils, J. van den Brand, C.A. Melendres, H. Terryn, E. Stijns, "Chemical composition of thin oxide films on aluminium studied with infrared and visible spectroscopic ellipsometry" The 3rd Conference on Aluminium Surface Science and Technology (ASST 2003), Bonn, Germany, 18-22 May 2003, Oral presentation by S. van Gils

A. Franquet, J. van den Brand, S. van Gils, H. Terryn, J. Vereecken, J.H.W. de Wit, "Study of protection films on Al by means of optical reflection methods (SE UV-VIS-IR, FTIR-RAIRS and Raman)", International symposium "Corrosion science in the 21st century", UMIST, Manchester, UK, 2003, Oral presentation by H. Terryn.

A. Franquet, J. van den Brand, S. van Gils, H. Terryn, J. Vereecken, J.H.W. de Wit, "Study of protection films on Al by means of optical reflection methods (SE UV-VIS-IR, FTIR-RAIRS and Raman)", International symposium "Corrosion science in the 21st century", ICEPAM, Oslo, Norway, 2004, Oral presentation by H. Terryn.

ACKNOWLEDGEMENTS.

Er zijn een hele hoop mensen die ik wil bedanken omdat ze een bijdrage hebben geleverd aan de totstandkoming van dit proefschrift. De lijst is zo lang dat je bijna zou gaan denken dat ik niks zelf heb hoeven te doen.... Allereerst wil ik natuurlijk Professor Hans de Wit bedanken voor de enorme vrijheid die ik heb gekregen in mijn onderzoek en de vele interessante discussies (die niet alleen over werk gingen). Professor Herman Terryyn wil ik ook graag bedanken. Herman, je bent precies op het juiste moment in mijn promotie gekomen om een zeer belangrijke bijdrage te leveren en de zaak in de juiste richting te sturen. Ik vond het een eer om door jou begeleid te mogen worden! Erik van Westing wil ik heel, heel erg bedanken voor zijn vriendschap en duizend-en-een dingen in zijn rol als een soort begeleider achter de schermen. Daarnaast wil ik ook Professor Radelaar bedanken voor het in mij gestelde vertrouwen en vooral voor de goedkeuring van het investeringsvoorstel voor de aanschaf van het infrarood-apparaat. Ik zou niet weten hoe mijn proefschrift er zonder dat apparaat uitgezien zou hebben.

Ik wil ook graag Bart Norbart bedanken. Onze zeer prettige samenwerking de afgelopen jaren is moeilijk in woorden te vatten. Misschien dat haat-liefde verhouding de lading het beste dekt. Het aantal projecten dat wij succesvol hebben voltooid is denk ik nauwelijks te tellen (backflow, dr-blade, sch&pol, dubbelzijdig, nowaa, pp ;-). Het was me ook een waar genoegen om je aan te mogen sturen in de dagelijkse werkzaamheden!

Ook Peter Beentjes wil ik bedanken. Zonder jou was dit proefschrift zeker niet geworden wat het nu is. Je bijdrage is bijna niet te overschatten. Zoals je al zei in jouw proefschrift, er zijn vele, vele e-mailtjes (1614 om precies te zijn) heen en weer geflitst tussen Corus en de TU met bijvoorbeeld uitleg en lange discussies over Lewis zuur/basen, OH groepen op oxide-oppervlakken, nog uit te voeren experimenten maar ook discussies op het persoonlijke vlak. De mailtjes waarin je geduldig een tipje van de chemie-sluier oplicht voor een domme Materiaalkundige heb ik vele malen opnieuw gelezen. Het ga ook jou goed Peter!!

Paul Snijders en Sake van Gils wil ik bedanken voor de hulp en de diverse discussies op het gebied van XPS, infrarood, ellipsometrie maar ook op het persoonlijke vlak. Met beiden heb ik zeer prettig samengewerkt en beiden

hebben zij met hun eigen expertise een zeer belangrijke bijdrage geleverd aan dit proefschrift.

Wim Sloof wil ik bedanken voor het feit dat hij mij geduldig en in vele iteraties heeft ‘leren schrijven’. Ik hoop dat de overige hoofdstukken net zo weldoordacht zijn als Hoofdstuk 3 en 4. Lars Jeurgens wil ik bedanken voor zijn uitleg van de XPS en voor het mogen gebruiken van zijn XPS-software. I would like to thank Orlin Blaijev for his contribution to Chapters 5 and 6. I also would like to thank Bernhard Schneider of IFAM (Fraunhofer-Institut für Fertigungstechnik und Angewandte Materialforschung) in Bremen and Professor Wulff Possart of the University of Saarland for the interesting discussions on monolayers. Ben Norder wil ik bedanken voor de TGA-metingen en voor het feit dat hij altijd klaar stond voor nog weer een meting, Valerie Sivel for the fantastic FIB/TEM work. Thank you for putting so much effort in my samples! Michaël Wübbenhorst and Mihai Chirtoc I would like to thank for the SPPEM measurements and their significant contributions to Chapter 11.

I would like to sincerely thank Francesco and Paola for being very nice roommates. I think we stimulated each other well in being very productive and getting the most out of our PhD’s (The best room in the group! ;-), while still having a lot of nice laughs and discussions. Paola, I wish you all the best for your life! After Paola’s leaving for Agfa, the “talking” in our room really started (and also the temperature in the room dropped by 10 degrees or more). Francesco, it was a pleasure to spend this time with you. I hope you will find what you are looking for, both in job and in personal life.

I would also like to thank the other group members for the very pleasant collaboration over the past few years and making my PhD a very nice period. Wouter (het ga je goed!), Siu Fai, Jose, Laetitia, Premendra, Mae, Xiaolong, Saskia, Jaco, Natalya, Gerrit, Peter, thank you very much. En natuurlijk ook mijn afstudeerders (die mij helaas ‘overleefd’ hebben): Tjitte en Frederik.

Tenslotte, maar zeker niet als minste, wil ik Ellen bedanken voor haar zeer belangrijke rol op de achtergrond. Ik heb dit proefschrift mede voor jou geschreven om nu eens eindelijk uit te leggen wat ik de afgelopen 4 jaar heb uitgespookt ;-). Als je begint op bladzijde 1 en je leest door tot het einde, dan weet je het tot in de fijnste details. (De vast&zeker zeer belangrijke rol van UV op hechting heb ik helaas niet kunnen onderzoeken, misschien een volgende keer dan maar?).

CURRICULUM VITAE.

The author of this thesis was born on May 28th 1974 in Tilburg. In 1995, he started a MSc study in Materials Science and Engineering in Delft. In 2000, he graduated cum laude and was awarded best Materials Science and Engineering Student of TU Delft 2000. His MSc final project was performed as a project within the Netherlands Institute for Metals Research (NIMR). The topic of his thesis was the diffusion of water in Hylite, a commercially available aluminium-polymer laminate of Corus. After this, he started a PhD project within the Netherlands Institute for Metals Research. The topic of the PhD project was “delamination in metal-polymer interfaces” (project no. ME97026B). This study is described in this PhD thesis.